

POLYTECHNIQUE



L.A.D.H.Y.
Laboratoire d'Hydrodynamique
École polytechnique CNRS
91128 Palaiseau Cédex FRANCE
Tél. 01 69 33 49 89

École polytechnique

Laboratoire d'hydrodynamique

Thèse présentée pour obtenir le grade de

DOCTEUR DE L'ÉCOLE POLYTECHNIQUE

spécialité : mécanique

par

Benoît PIER

Comportement non linéaire synchronisé dans les écoulements cisaillés

---

soutenue le 16 décembre 1999 devant le jury composé de :

Patrick Huerre	directeur de thèse
Patrice Le Gal	
Rebecca Lingwood	
Peter Monkewitz	rapporteur
Marc Rabaud	
Wim van Saarloos	
Olivier Thual	rapporteur

Comportement non linéaire synchronisé dans les écoulements cisaillés



ÉCOLE POLYTECHNIQUE



École polytechnique

Laboratoire d'hydrodynamique

Thèse présentée pour obtenir le grade de

DOCTEUR DE L'ÉCOLE POLYTECHNIQUE

spécialité : mécanique

par

Benoît PIER

Comportement non linéaire synchronisé dans les écoulements cisaillés

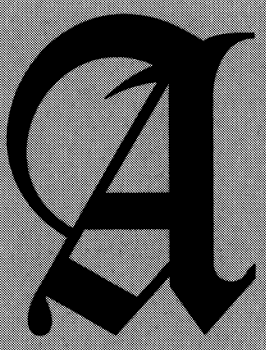
---

soutenue le 16 décembre 1999 devant le jury composé de :

Patrick Huerre	directeur de thèse
Patrice Le Gal	
Rebecca Lingwood	
Peter Monkewitz	rapporteur
Marc Rabaud	
Wim van Saarloos	
Olivier Thual	rapporteur

Rien n'est beau comme la pesanteur
dans les plis fugitifs des ondulations de la mer
ou les plis presque éternels des montagnes.

Simone Weil



Avant-propos

La dynamique des fluides étudie des écoulements aussi divers que le mouvement de magma à l'intérieur de la Terre ou dans les cheminées des volcans, les courants océaniques, la circulation atmosphérique, les flots actionnant les turbines ou arrachant les ponts, les jets propulsant les fusées spatiales, et même le milieu interstellaire très dilué. Parmi tous les écoulements possibles, certains sont créés par l'homme, d'autres sont incontrôlables, certains sont bénéfiques, d'autres sont extrêmement destructeurs, certains peuvent rapporter de l'argent, d'autres sont simplement beaux à regarder. La science des fluides a pour objet de comprendre les écoulements existants, d'en créer ou d'en imaginer d'autres, de prédire leur comportement ou de le modifier. La plupart d'entre eux sont trop complexes ou trop riches en propriétés pour que leur étude directe permette d'isoler des phénomènes qui ont lieu simultanément et s'imbriquent les uns dans les autres. Pour analyser un écoulement donné, il est souvent nécessaire d'en étudier ou d'en inventer plusieurs autres. Le recours à des situations simplifiées ou idéalisées permet d'étudier isolément un aspect d'un phénomène sans qu'il soit camouflé par des effets secondaires. C'est ce travail d'analyse qui permet de comprendre les briques élémentaires constituant la mécanique des fluides.

Certaines propriétés, comme par exemple une apparition régulière de tourbillons, se retrouvent dans des situations très diverses. Ainsi, le vent soufflant sur un câble téléphonique tendu entre deux pylônes produit une note par émission périodique de tourbillons. Ces mêmes tourbillons peuvent être observés derrière le pilier d'un pont plongeant dans un fleuve. La vapeur d'eau s'élevant d'une tasse de thé brûlant peut également être le siège d'un battement régulier. Ce sont des exemples où des instabilités de l'écoulement se synchronisent pour donner lieu à des oscillations globales à une fréquence bien déterminée. Cette fréquence est une caractéristique intrinsèque du système considéré : elle n'est pas la conséquence d'une action extérieure, mais le résultat des instabilités et de leurs interactions au sein même du système. Les exemples cités font tous partie d'une classe d'écoulements produisant spontanément des structures oscillatoires. Puisqu'un tel phénomène se produit dans des cas très divers, sa source doit se situer au niveau des propriétés fondamentales de ces systèmes et non pas dans les détails superficiels extrêmement variables d'un écoulement à un autre. Le but du présent travail est d'identifier les causes d'un tel comportement globalement synchronisé, de comprendre le mécanisme de sélection et de prédire la fréquence ainsi que la structure spatiale de ces oscillations.

Différentes méthodes ont été utilisées. Dans un premier temps, j'ai étudié un modèle simplifié (dit de Ginzburg–Landau) qui ne prend pas en compte la complexité des équations de la mécanique des fluides mais qui, par le passé, s'est révélé très utile pour appréhender la dynamique d'un grand nombre d'écoulements. L'étude théorique de ce modèle m'a permis de montrer qu'il existe deux types de structures synchronisées, appelées modes "chapeau" et modes "éléphant". Ce sont deux critères différents qui déterminent la fréquence de chacun de ces modes. Cette étude est guidée et confirmée par les simulations numériques directes. Après avoir identifié, à l'aide de ce modèle, les principes de sélection de ces structures globalement synchronisées,

j'ai pu généraliser ces résultats aux équations complètes de la dynamique des fluides (dites de Navier–Stokes). J'en ai principalement conclu qu'une structure comme la génération périodique de tourbillons dans un sillage est un mode de type "éléphant" dont la fréquence est correctement prédite par le critère développé dans le cadre du modèle de Ginzburg–Landau. Ceci constitue l'un des premiers résultats théoriques complets donnant la fréquence des oscillations d'amplitude finie produites dans des écoulements cisaillés ouverts.

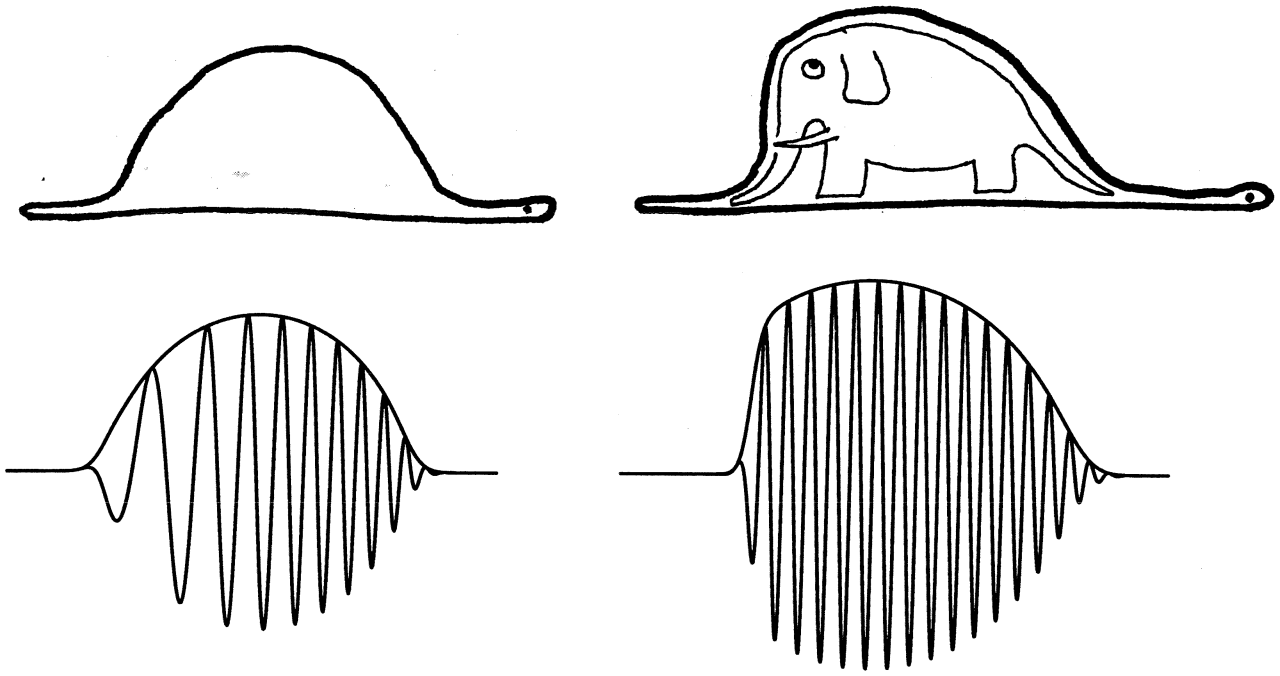
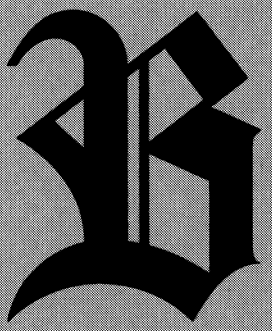
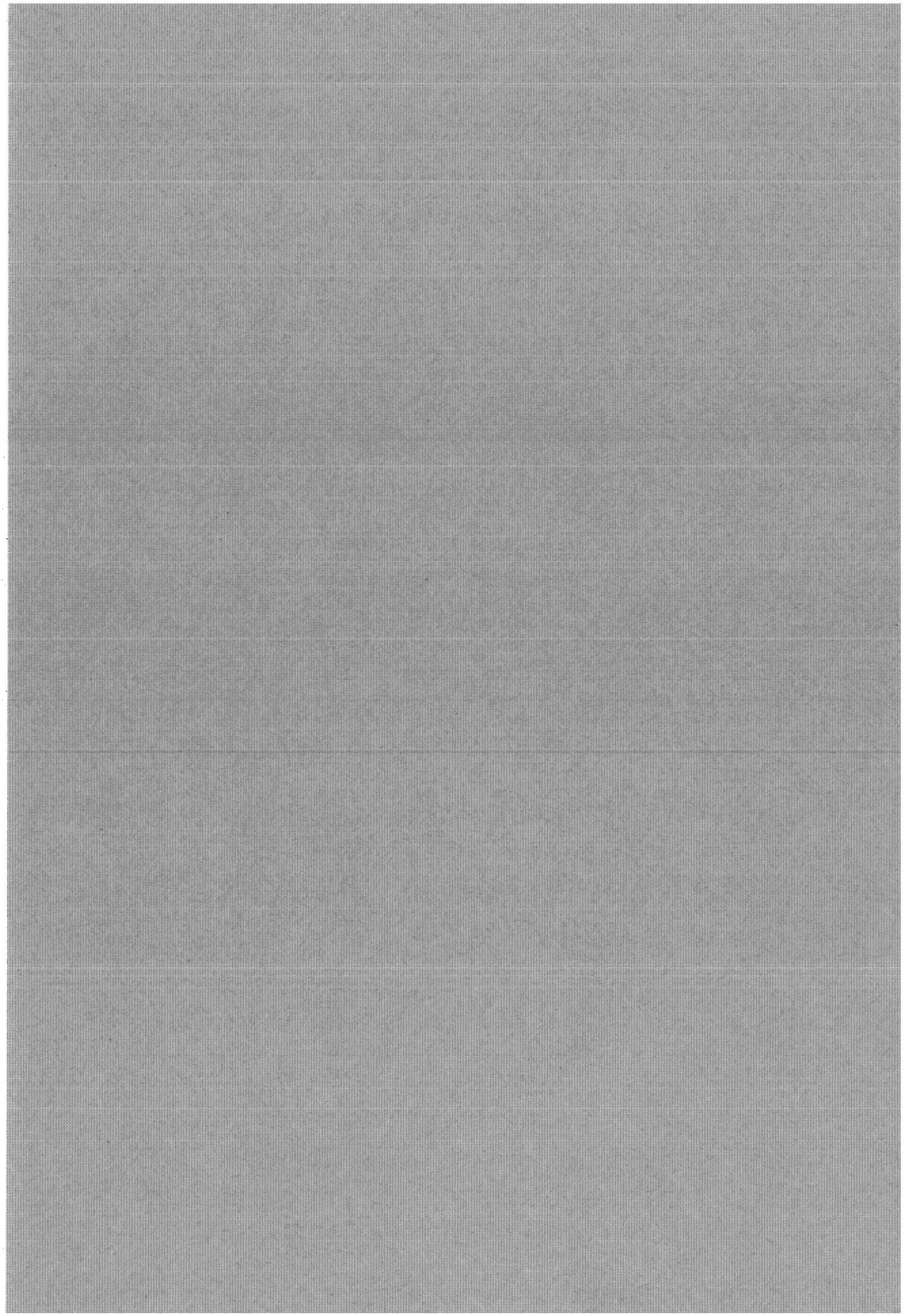


FIGURE 0.1. Modes chapeaux et modes éléphants, d'après [76].





Balade le long d'une allée de tourbillons

1. À propos des écoulements

Les écoulements observés dans la nature ou produits artificiellement sont très variés. Avant d'aborder le type de situation considérée dans cette étude, il convient d'introduire quelques termes couramment utilisés.

Écoulements ouverts ou fermés. Dans des écoulements fermés, c'est le même fluide qui circule dans un récipient clos, alors que dans les écoulements ouverts le fluide entre d'un côté et ressort de l'autre. Ces deux types d'écoulements ont des dynamiques très différentes, et, par conséquent, leur étude nécessite des approches bien distinctes. Les écoulements fermés sont caractérisés par la recirculation du même fluide due au confinement ; il n'y a pas de direction privilégiée et tout se passe "sur place". Dans les écoulements ouverts, au contraire, le sens du courant introduit les notions d'amont et d'aval, et la dynamique s'organise autour de cette direction de l'amont vers l'aval.

Écoulements homogènes ou inhomogènes. Un exemple d'écoulement homogène est produit dans un tuyau rectiligne de section constante dans lequel un débit constant est imposé (écoulement de Poiseuille). Dans ce cas, le profil de vitesse ainsi que toutes les autres caractéristiques sont les mêmes en chaque position le long du courant. Il suffit alors d'étudier un endroit donné pour en déduire toutes les propriétés du système. L'inhomogénéité de la plupart des écoulements est due à la présence de parois ou d'obstacles, à la viscosité qui tend à arrondir les profils de vitesse, au changement des propriétés du fluide : écoulement autour d'une aile d'avion, étalement d'un jet loin de l'orifice, refroidissement des gaz de combustion. Dans ce cas, le comportement global ne peut être obtenu qu'à partir de l'ensemble des propriétés en chaque point du système. Souvent ces configurations comportent des régions où les perturbations sont amplifiées et des régions où elles sont amorties. Cette variation spatiale des propriétés donne lieu à un type de dynamique qui n'existe pas dans les écoulements homogènes.

Oscillateurs ou amplificateurs. Certains écoulements ouverts peuvent se comporter comme des amplificateurs : dans ce cas les fluctuations observées à la sortie reproduisent celles toujours présentes à l'entrée, amplifiées d'une certaine façon. De tels écoulements ont un comportement *extrinsèque* : les structures observées sont imposées de l'extérieur, dues aux conditions régissant l'entrée du fluide. En revanche, pour d'autres écoulements, la dynamique des instabilités à l'intérieur même du domaine dicte le comportement global. Dans ce cas, la dynamique globale est *intrinsèque* et peu sensible aux conditions d'entrée. En outre, des résonances peuvent entrer en jeu pour accorder l'ensemble des fluctuations à une même fréquence. Alors l'écoulement peut se comparer à un oscillateur.

Écoulements réguliers ou turbulents. De très nombreux écoulements, comme par exemple une cascade en montagne, ont un comportement désordonné et imprévisible. Leur description complète nécessite une grande quantité d'information car ils sont structurés à toutes les échelles. Dans ce cas, on se limite souvent à une approche statistique qui ignore les détails trop riches et essaie de dégager les propriétés valables en moyenne. À ce jour, aucune définition précise d'un écoulement turbulent n'a été

donnée. Un écoulement est considéré régulier s'il peut être caractérisé par un petit nombre de paramètres. C'est en étudiant des écoulements assez réguliers qu'on peut obtenir des résultats théoriques complets. Mais ces résultats restent souvent valables dans des cas plus désordonnés...

2. Comportement synchronisé

Cette étude est consacrée aux écoulements qui se mettent à osciller de façon spontanée. Sans action extérieure, de petites fluctuations aléatoires, inévitables dans un système physique, sont amplifiées dans certaines régions. Ces perturbations peuvent croître sur place ou être emportées par l'écoulement vers l'aval tout en continuant à se développer. Si l'instabilité du milieu est suffisamment forte, ces perturbations ne seront jamais évacuées vers l'aval mais contamineront tout le système. Ces fluctuations puisent leur énergie dans l'écoulement sous-jacent ; leur amplitude saturera forcément puisque les ressources disponibles sont limitées. Ce scénario peut conduire à un comportement désordonné et imprévisible : c'est le cas des écoulements turbulents. En revanche, une croissance transitoire des perturbations peut aussi aboutir à un régime stationnaire où les fluctuations s'installant aux différents endroits sont toutes accordées à une même fréquence. Une telle synchronisation est le fruit d'une résonance au sein de l'écoulement. Ce mémoire cherche à établir les causes de cette résonance.

Avant de passer en revue différentes explications pour ce phénomène, nous allons présenter un exemple d'écoulement simple qui engendre des oscillations spontanées.

3. Un archétype : l'allée tourbillonnaire de Bénard–Kármán

Les sillages autour de différents obstacles comme des câbles téléphoniques, des piliers d'un pont ou des ailes d'avion présentent des caractéristiques communes, indépendantes du système considéré. Pour étudier leurs propriétés en s'affranchissant de la complexité géométrique, l'expérience très largement utilisée est l'écoulement autour d'un obstacle de forme cylindrique.

Strouhal [82] a été le premier à étudier la production de son par le mouvement d'un corps cylindrique dans l'air. De ses observations expérimentales il a déduit la loi selon laquelle la fréquence du son f est proportionnelle à la vitesse U et inversement proportionnelle au diamètre D, de sorte que le *nombre de Strouhal* défini par

$$\mathrm{St} = \frac{fD}{U} \tag{1.1}$$

est constant. En fait, des mesures plus précises et beaucoup plus récentes ont montré que le nombre de Strouhal varie.

Ensuite, Bénard [2] a mis en évidence que la structure du sillage d'un barreau cylindrique déplacé dans l'eau prend la forme d'une allée tourbillonnaire (figure 1.1) : deux rangées de tourbillons contra-rotatifs s'installent de part et d'autre du plan de symétrie du sillage. Bénard a constaté que les tourbillons sont parfaitement équidistants, leur production est donc périodique.

Puis von Kármán [43] a étudié différentes configurations d'allées tourbillonnaires, leur stabilité et la traînée exercée sur l'obstacle. Jusqu'à nos jours, cette expérience continue à poser des problèmes intéressants et à être étudiée expérimentalement,

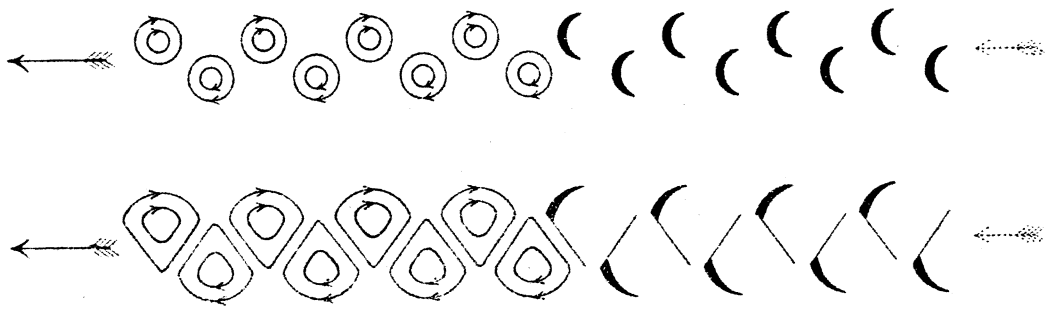


FIGURE 1.1. Centres de giration observés par Henri Bénard à l'arrière d'un obstacle en mouvement [2]. N.B. Le sens de rotation indiqué pour les tourbillons pairs (comptés à partir de la gauche de la figure) est erroné : en réalité ils tournent dans le sens anti-horaire.

numériquement et théoriquement. Les transitions entre différents types de comportements du sillage sont maintenant bien établies, la fréquence d'émission des tourbillons est connue expérimentalement sur une large gamme de paramètres [92], mais la détermination de sa valeur par la théorie n'est pas encore une chose acquise.

Le paramètre de contrôle dont dépend le régime observé expérimentalement est le nombre de Reynolds (Re), basé sur le diamètre du cylindre et la vitesse du fluide loin de l'obstacle. En augmentant Re, par exemple en augmentant la vitesse du fluide incident, l'écoulement obtenu varie et à certaines valeurs particulières de Re sa structure change radicalement. Le scénario de transition en fonction de Re est le suivant [87].

Pour de très faibles valeurs de Re, le fluide ne fait que contourner l'obstacle sans s'en détacher (figure 1.2*a*). En augmentant Re au-delà de 4, une première bifurcation, un premier changement de nature de l'écoulement se produit (figure 1.2*b*) : le fluide qui arrive sur le cylindre en amont le contourne, s'en détache à un certain point et n'atteint donc pas le point le plus en aval du cylindre. Il en résulte une zone de recirculation en aval du cylindre, où une partie du fluide reste piégée et circule dans deux tourbillons contra-rotatifs attachés au cylindre. En augmentant Re dans ce régime, cette région d'eau morte s'étend vers l'aval sans qu'il y ait changement de nature de l'écoulement. L'écoulement est toujours permanent, le champ de vitesse n'évolue pas au cours du temps.

Une transition plus intéressante a lieu à $\mathrm{Re}_c = 48.5$. Au-delà de cette valeur, l'écoulement varie au cours du temps : les deux tourbillons à l'aval du cylindre s'en détachent alternativement et sont emportés par l'écoulement. Pendant que l'un des tourbillons se détache, l'autre se reforme pour quitter le cylindre un peu plus tard. Ce phénomène produit la célèbre allée tourbillonnaire de Bénard–Kármán (figure 1.2*c*). Le processus est périodique : la période d'émission des tourbillons dans le sillage est responsable du son entendu par Strouhal [82].

Mathis, Provansal & Boyer [55] ont étudié en détail la nature de la transition à $\mathrm{Re} = \mathrm{Re}_c$ et ont montré qu'il s'agit d'une bifurcation de Hopf super-critique [54]. Pour $\mathrm{Re} < \mathrm{Re}_c$, l'état stationnaire avec une région de recirculation est stable. Même si de petites perturbations sont présentes, elles sont évacuées vers l'aval et le milieu retourne à son état indépendant du temps. Cet état se déstabilise à $\mathrm{Re} = \mathrm{Re}_c$ quand les tourbillons commencent à se détacher de l'obstacle. Pour $\mathrm{Re} > \mathrm{Re}_c$, un régime périodique est obtenu : le champ de vitesse varie au cours du temps. Ce nouveau régime est caractérisé par sa fréquence et par l'amplitude des fluctuations de vitesse. Près du seuil d'instabilité, la fréquence est presque constante alors que l'amplitude des fluctuations est proportionnelle à la racine carrée de l'écart au seuil $\mathrm{Re} - \mathrm{Re}_c$.

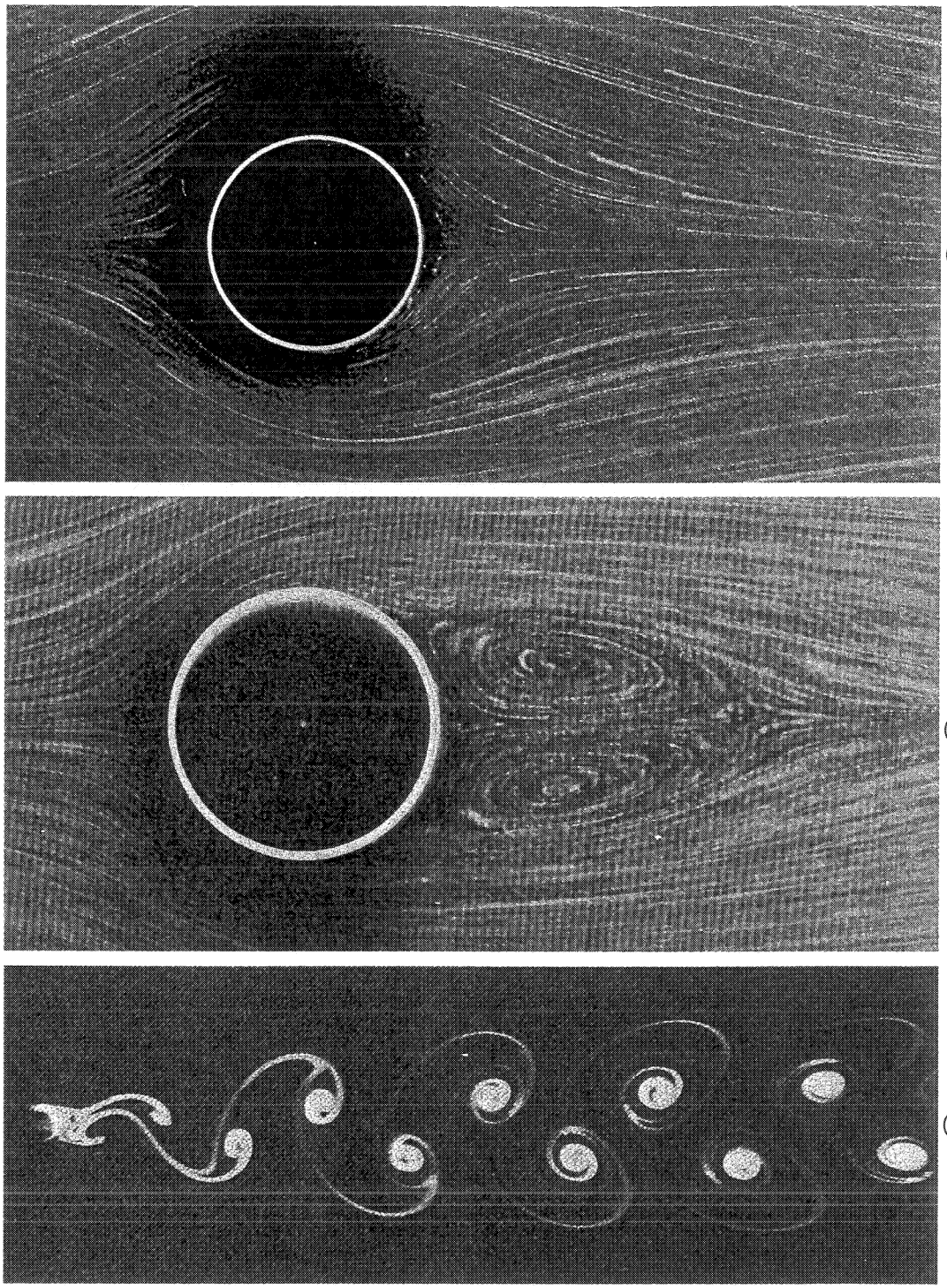


FIGURE 1.2. (*a*) Écoulement attaché autour d'un cylindre à Re = 1.54. (*b*) Écoulement avec zone de recirculation à Re = 26. (*c*) Allée tourbillonnaire de Bénard–Kármán à Re = 105. [28]

La nature de la transition vers un état parfaitement périodique est dorénavant bien comprise, mais les valeurs caractéristiques comme la période des oscillations ne peuvent être obtenues qu'à partir de mesures expérimentales et non par des raisonnements théoriques.

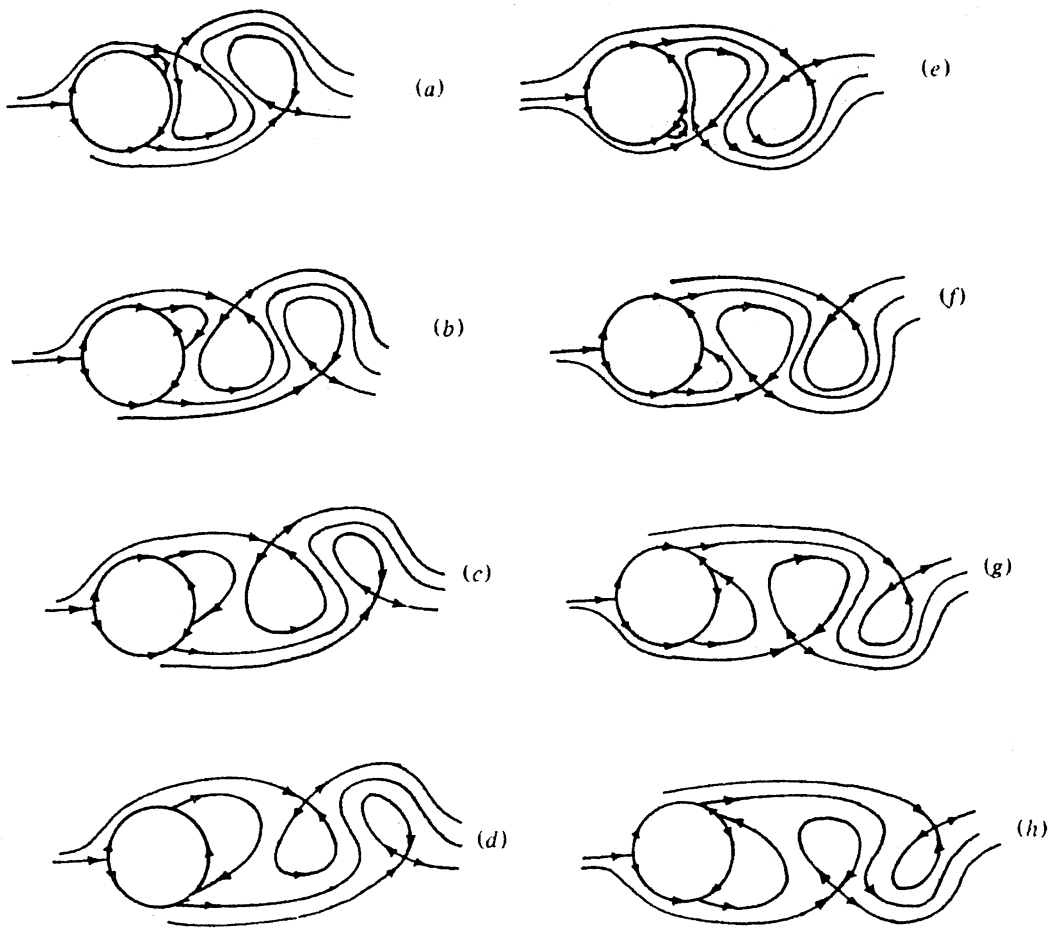


FIGURE 1.3. Modélisation de la formation des vortex dans le sillage d'un cylindre sur une période. Seules les séparatrices sont indiquées [64].

4. Quelques principes de sélection

Depuis que ce phénomène d'émission périodique de tourbillons a été observé, de nombreuses explications ont été avancées pour rendre compte de la structure spatiale et de la fréquence sélectionnée. Les différentes théories se répartissent en deux tendances selon que l'accent est mis sur la présence de l'obstacle ou sur la structure du sillage.

L'analyse détaillée du voisinage immédiat de l'obstacle permet de suivre la naissance de chaque tourbillon et d'essayer de relier la fréquence de l'allée tourbillonnaire au processus de formation (p.ex. [31, 64]). Des méthodes expérimentales ingénieuses ont révélé l'évolution de la géométrie des lignes de courants au cours du mouvement (figure 1.3). Mais la connaissance détaillée des formations et déformations des vortex avant leur décollement n'a pas abouti à une prédiction précise de la fréquence. Au mieux des ordres de grandeur ont été obtenus.

En raison des difficultés rencontrées au voisinage immédiat de l'obstacle, d'autres recherches se sont tournées vers l'aval du sillage dans le but d'y trouver le mécanisme de sélection. Cette approche est motivée par la structure périodique en espace et en temps de l'allée tourbillonnaire. Même si la périodicité spatiale n'est qu'approximativement vérifiée, une analyse du sillage en termes d'ondes propagatives semble appro-

priée. La propagation d'ondes suivant une certaine vitesse de phase est bien connue dans des milieux spatialement homogènes. Ici, à cause de l'obstacle, cette invariance spatiale n'est plus exacte, mais, en aval, les propriétés du milieu varient suffisamment lentement pour qu'une telle description puisse s'appliquer. C'est ainsi que l'on cherche à relier la dynamique globale de l'écoulement aux propriétés locales des ondes progressives qui peuvent exister en chaque point du système.

Avant d'être en mesure de prédire la fréquence globale, il est indispensable de connaître les propriétés locales de stabilité et d'instabilité de l'écoulement étudié. Ces notions seront exactement définies au chapitre ℭ ; pour le moment il suffit de mentionner les différents types d'instabilité : un milieu est dit *stable* si toutes les petites perturbations sont atténuées, *convectivement instable* (CI) s'il existe des perturbations amplifiées mais qui sont emportées par l'écoulement, *absolument instable* (AI) s'il existe des perturbations qui croissent sur place. Dans un milieu fermé, l'instabilité coïncide généralement avec l'instabilité absolue. Dans les écoulements ouverts, en revanche, l'advection de l'amont vers l'aval fait qu'un écoulement peut être instable (convectivement) alors qu'un observateur immobile voit les perturbations décroître : il faudrait courir le long de l'écoulement pour rattraper la perturbation qui continue à croître en aval. C'est ainsi qu'on définit le *taux de croissance absolu* comme mesure de la croissance d'une perturbation localisée par rapport à un repère fixe. Dans des cas où le profil de vitesse se développe le long du courant, ces notions s'appliquent localement et permettent d'identifier des régions stables, convectivement instables ou absolument instables.

Depuis les débuts de l'analyse en termes d'instabilité convective ou absolue, l'idée s'est imposée que ce sont ces notions qui déterminent l'évolution des écoulements ouverts plutôt que la distinction classique entre stabilité et instabilité. En effet, dans un écoulement convectivement instable, de petites perturbations qui entrent en amont quittent le système après avoir subi une amplification. Un tel écoulement, bien que localement instable, n'a pas de dynamique propre et ne peut entretenir un comportement temporellement non trivial. En revanche, pour conduire à des oscillations auto-entretenues, des perturbations doivent se développer sur place sans être emportées par le courant ; il faudrait donc une région absolument instable. Ce raisonnement simpliste suppose que toute l'évolution du système est déterminée par les propriétés linéaires des petites perturbations. Or, dans des systèmes étendus, ces perturbations sont considérablement amplifiées avant de quitter le domaine. Alors des effets non linéaires reliés à leur forte amplitude peuvent modifier l'évolution ultérieure. Ce n'est qu'à la fin de ce travail que nous serons en mesure d'évaluer le rôle joué par l'amplitude des perturbations.

Ces notions ont été mises à profit par Pierrehumbert [69] dans le cadre d'un modèle de circulation atmosphérique pour rendre compte des cycles produits par les régions de forte baroclinicité. Il a suggéré que le point de taux de croissance absolu le plus élevé l'emporte et produit la fréquence des oscillations globales observées. C'est à cet endroit, en effet, que les perturbations croissent le plus rapidement *in situ* et imposeraient donc leur fréquence à l'ensemble du système.

Koch [47] a été parmi les premiers à vouloir expliquer le comportement synchronisé des sillages en termes d'instabilité absolue. Pour cela, il a utilisé une famille analytique de profils de vitesse pour décrire le sillage d'une plaque rectangulaire. Il en a déduit que le voisinage immédiat de l'obstacle est absolument instable alors que plus loin le sillage n'est que convectivement instable. Koch a invoqué un mécanisme de résonance localisé au bord *aval* de la région absolue comme cause de l'émission

régulière de tourbillons dans le sillage. Quand le régime permanent est établi, il n'y a plus ni amplification ni atténuation et à l'endroit où le sillage passe de AI à CI, le taux de croissance absolu est précisément nul. Les perturbations marginalement amplifiées à cet endroit seraient responsables de la fréquence globale.

Dans une autre étude de sillages, Monkewitz & Nguyen [60] ont proposé un *critère de résonance initiale,* basé également sur une famille de profils de vitesse pour modéliser le sillage. D'après ce critère, c'est le premier endroit AI rencontré dans l'écoulement qui impose sa fréquence absolue à l'ensemble du système et en particulier à toutes les structures qui se développent en aval de cette position. Alors que Pierrehumbert [69] a justifié son résultat par des simulations numériques du modèle et une analyse asymptotique, les critères de Koch [47] et de Monkewitz & Nguyen [60] sont des conjectures qui demandent à être vérifiées.

Depuis lors, les progrès dans la compréhension des comportements synchronisés ont eu lieu en procédant en deux étapes : une étude de modèles simplifiés a d'abord permis d'identifier un critère de sélection, qui ensuite a pu être généralisé à des écoulements réels. C'est par une telle approche que le problème de sélection *linéaire* a été résolu ; la même stratégie s'est avérée efficace pour résoudre le problème *non linéaire* étudié dans ce mémoire.

L'équation de Ginzburg–Landau à coefficients complexes (GLC) constitue la drosophile de la physique non linéaire [20]. C'est le modèle de dynamique unidimensionnelle le plus simple possible qui donne lieu à des ondes propagatives de propriétés similaires à celles couramment rencontrées en mécanique des fluides. Pour rendre compte d'écoulements inhomogènes, les coefficients de l'équation de GLC sont choisis avec une lente variation en espace. Un bon jeu de coefficients permet alors d'imiter presque toutes les propriétés des écoulements réels.

Dans le cadre de ce modèle en milieu infini, Chomaz, Huerre & Redekopp [13] et Le Dizès *et al.* [51] ont obtenu des solutions globalement synchronisées (*modes globaux*) dans l'approximation linéarisée. Ce critère de sélection (rappelé à la section ℭ.5) fait intervenir la variation spatiale du taux de croissance absolu $\omega_0(X)$ en fonction de la variable X dans la direction de l'écoulement : la fréquence complexe d'un mode global est donnée par un point-selle de la fonction $\omega_0(X)$ prolongée analytiquement dans le plan des X complexes. L'analyse démontre qu'une région AI est une condition nécessaire pour l'instabilité linéaire globale. Ce n'est pas une condition suffisante : si la région AI n'est pas assez étendue, le milieu peut être globalement stable alors qu'il est localement absolument instable.

Ce critère a ensuite été généralisé par Monkewitz, Huerre & Chomaz [59] aux équations de Navier–Stokes linéarisées autour d'un écoulement de base faiblement divergent. Toutes les conclusions obtenues avec GLC restent valables pour Navier–Stokes.

Traditionnellement, le pas suivant vers la non-linéarité consiste à se placer près de la transition où les modes globaux linéaires sont marginalement instables et à faire une étude faiblement non linéaire. Une telle approche permet généralement d'identifier la nature de la transition et d'obtenir les premières solutions non linéaires en supposant que leur amplitude est encore relativement faible. Ce travail a été entrepris par Le Dizès *et al.* [50] qui ont montré que, pour une fois, cette méthode ne permet pas d'accéder au régime non linéaire. En effet, la constante de Landau qui détermine si la transition est super-critique ou sous-critique n'a pas de limite bien définie ni de signe constant dans la limite de faible non-parallélisme. Par ailleurs, la théorie faiblement non linéaire ne s'applique que dans un voisinage exponentiellement étroit du

seuil de l'instabilité. Pour contourner les difficultés liées à l'approche faiblement non linéaire des modes globaux mises en évidence par ces auteurs, il semble indiqué de se placer d'emblée dans un cadre où les fluctuations sont d'amplitude finie.

5. Objectifs

La plupart des écoulements donnant lieu à des oscillations globalement synchronisées se développent spatialement : les profils de vitesse, et donc les caractéristiques locales de stabilité, varient le long de l'écoulement. Pour pouvoir relier le comportement global de ces systèmes à leurs propriétés locales, il est indispensable que l'échelle des variations spatiales soit grande devant l'échelle typique des instabilités. En effet, sous cette hypothèse de **faible inhomogénéité spatiale**, une structure spatialement étendue peut être approchée par des trains d'onde dont la forme, le nombre d'onde et l'amplitude varient lentement en espace. C'est cette hypothèse qui permet d'obtenir les critères de sélection de manière analytique. Elle sera complètement justifiée dans la suite.

L'étude linéaire caractérise les propriétés de stabilité d'un état de base. Dans le cas d'un système instable, une approche faiblement non linéaire permet de décrire son évolution aussi longtemps que l'amplitude des perturbations reste faible. Une telle approche n'est donc valable que très près du seuil d'instabilité globale ou dans les premiers moments d'un régime transitoire menant à des solutions d'amplitude croissante. Ces méthodes ne permettent pourtant pas de prédire l'état final des systèmes où les fluctuations ne sont plus d'amplitude négligeable. Ainsi, pour pouvoir rendre compte des structures stationnaires qui s'installent avec une amplitude finie après un régime transitoire, il est indispensable de développer une **théorie non linéaire non perturbative**, puisque les fluctuations sont du même ordre de grandeur que l'état de base.

Une structure auto-entretenue s'installant sur un écoulement se développant en espace résulte des caractéristiques locales de l'état de base et des conditions aux bords. Pour isoler les effets dus aux propriétés de l'écoulement de base nous ne considérerons que des **milieux doublement infinis** vers l'amont comme vers l'aval. Cette approche permet de tenir compte de l'effet déstabilisant de l'écoulement engendré autour de l'obstacle matériel en évitant les complications dues aux parois.

Le but de ce travail est d'étudier des écoulements réels régis par les équations de **Navier–Stokes**. Nous allons montrer que les mécanismes de sélection s'appliquant aux jets, aux sillages et aux couches de mélange ne sont pas spécifiques aux équations de la dynamique des fluides : ils peuvent être obtenus dans le cadre d'équations modèles de type Ginzburg–Landau qui permettent d'identifier les mécanismes fondamentaux. Ensuite, il sera montré que ces principes de sélection restent valables pour des écoulements réels.

Tout au long de cette étude, l'accent est mis sur les **critères de sélection de la fréquence**. À chaque fois qu'un tel critère est dégagé, la **structure spatiale** associée au mode est également obtenue. Mais le détail de cette structure spatiale n'est que la conséquence du mécanisme déclencheur de l'oscillation. Aussi notre intérêt principal concerne-t-il la prédiction de la fréquence des comportements synchronisés observés.

6. Plan

Après un bref rappel, au chapitre ℭ, des notions fondamentales de la dynamique des fluides, le mémoire est organisé autour de quatre articles. Les trois premiers

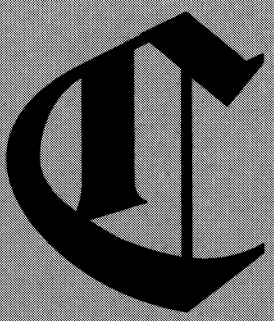
étudient l'équation modèle de GLC alors que le dernier concerne les équations de Navier–Stokes.

Le premier mode global non linéaire découvert est de type "chapeau" ; son enveloppe spatiale varie lentement partout. Le chapitre 𝔇 en démontre l'existence et donne l'expression de sa fréquence ainsi que le détail de sa structure spatiale.

Ensuite un deuxième type de structure synchronisée a été obtenu : les modes de type "éléphant" sont caractérisés par un front raide tourné vers l'amont alors qu'ils ressemblent aux modes chapeaux partout ailleurs. Leur principe de sélection est donné au chapitre 𝔈.

Après la démonstration de l'existence de ces deux variétés de modes globaux non linéaires, le chapitre 𝔉 étudie comment ils apparaissent lorsqu'on fait varier les paramètres de contrôle globaux. Les différentes transitions sont analysées, ainsi que la compétition entre les deux types de modes.

Finalement, les résultats précédents sont généralisés aux équations de Navier–Stokes bidimensionnelles au chapitre 𝔊. Il est montré que les méthodes ayant fait leurs preuves dans le modèle simplifié restent valables pour les écoulements réels.



Courte introduction aux instabilités hydrodynamiques

1. Les équations de Navier–Stokes

Dans toute cette étude nous ne considérons que des écoulements bidimensionnels et incompressibles. Supposer que l'écoulement est bidimensionnel signifie que la troisième direction est une direction d'invariance : tous les champs en sont indépendants et il n'y a pas de vitesse dans cette direction. D'emblée on utilisera des grandeurs sans dimension basées sur des échelles caractéristiques de longueur et de vitesse $\ell^\star$ et $U^\star$. La dynamique du système ne dépend alors plus que d'un seul paramètre, le *nombre de Reynolds*

$$\mathrm{Re} = \frac{U^\star \ell^\star}{\nu}, \tag{2.1}$$

où ν est la viscosité cinématique du fluide en question.

La coordonnée dans la direction du courant est notée x, le sens des x croissants étant celui du fluide. La direction transverse est mesurée par y. On désigne par u et v les composantes du champ de vitesse dans les directions x et y respectivement, par p le champ de pression. Les équations de Navier–Stokes [49] pour cet écoulement bidimensionnel s'écrivent alors

$$\left(\frac{\partial}{\partial t} + u\frac{\partial}{\partial x} + v\frac{\partial}{\partial y}\right) u = -\frac{\partial p}{\partial x} + \frac{1}{\mathrm{Re}}\Delta u, \tag{2.2a}$$

$$\left(\frac{\partial}{\partial t} + u\frac{\partial}{\partial x} + v\frac{\partial}{\partial y}\right) v = -\frac{\partial p}{\partial y} + \frac{1}{\mathrm{Re}}\Delta v. \tag{2.2b}$$

La condition d'incompressibilité

$$\frac{\partial u}{\partial x} + \frac{\partial v}{\partial y} = 0 \tag{2.3}$$

montre que les champs de vitesse dérivent d'une fonction courant $\Psi(x, y, t)$ telle que $u = \partial\Psi/\partial y$ et $v = -\partial\Psi/\partial x$. La vorticité $\varpi = \partial v/\partial x - \partial u/\partial y$ s'écrit alors $-\Delta\Psi$. Pour la fonction de courant, les équations de Navier–Stokes (2.2) prennent la forme de l'équation de la vorticité

$$\left(\frac{\partial}{\partial t} + \frac{\partial\Psi}{\partial y}\frac{\partial}{\partial x} - \frac{\partial\Psi}{\partial x}\frac{\partial}{\partial y}\right)\Delta\Psi = \frac{1}{\mathrm{Re}}\Delta^2\Psi. \tag{2.4}$$

Cette équation scalaire est plus pratique à manier que le système d'équations (2.2) et sera largement utilisée dans ce travail.

2. Stabilité et instabilités

Les mécanismes de sélection envisagés par différents auteurs sont déduits des propriétés d'instabilité des écoulements étudiés. Ces notions sont maintenant présentées.

Considérons un écoulement homogène dans la direction x dont le profil de vitesse $U(y)$ ne dépend que de la direction transverse y. Pour étudier l'évolution temporelle et spatiale des perturbations de ce profil, la fonction de courant totale $\Psi(x,y,t)$ est décomposée en la contribution de l'écoulement de base et celle des perturbations. Elle s'écrit

$$\Psi(x,y,t) = \int_0^y U(\eta)d\eta + \psi(x,y,t). \tag{2.5}$$

La substitution de cette expression dans l'équation maîtresse (2.4) donne

$$\left(\frac{\partial}{\partial t} + U(y)\frac{\partial}{\partial x}\right)\Delta\psi - U''(y)\frac{\partial\psi}{\partial x} + \left(\frac{\partial\psi}{\partial y}\frac{\partial}{\partial x} - \frac{\partial\psi}{\partial x}\frac{\partial}{\partial y}\right)\Delta\psi = \frac{1}{\mathrm{Re}}\Delta^2\psi. \tag{2.6}$$

Du moment que la perturbation est de faible amplitude, les termes d'ordre supérieur en ψ sont négligeables ce qui conduit à l'équation linéarisée

$$\left(\frac{\partial}{\partial t} + U(y)\frac{\partial}{\partial x}\right)\Delta\psi - U''(y)\frac{\partial\psi}{\partial x} = \frac{1}{\mathrm{Re}}\Delta^2\psi. \tag{2.7}$$

Pour un tel système linéaire, homogène dans la direction x et indépendant du temps t, une perturbation $\psi(x,y,t)$ peut se décomposer en une somme de perturbations élémentaires (modes normaux) de la forme

$$\phi(y)\mathrm{e}^{\mathrm{i}(kx-\omega t)} + \text{c.c.} \tag{2.8}$$

de nombre d'onde k et de pulsation ω *a priori* complexes. Ainsi, l'évolution de la perturbation totale s'obtient par superposition de ces perturbations élémentaires qui se propagent chacune indépendamment des autres. En exigeant que ces modes normaux vérifient l'équation (2.7), on obtient l'équation d'Orr–Sommerfeld [9,25]

$$(kU(y)-\omega)(\phi'' - k^2\phi) - kU''(y)\phi = \frac{-\mathrm{i}}{\mathrm{Re}}(\phi'''' - 2k^2\phi'' + k^4\phi). \tag{2.9}$$

Pour les écoulements non visqueux ($\mathrm{Re} = \infty$) elle se réduit à l'équation de Rayleigh

$$(kU(y)-\omega)(\phi'' - k^2\phi) - kU''(y)\phi = 0. \tag{2.10}$$

Avec des conditions de décroissance exponentielle en $y = \pm\infty$, ces modes ϕ satisfont un problème aux valeurs propres : il n'existe de solutions que si les valeurs complexes de ω et de k satisfont une relation de dispersion

$$D(k,\omega) = 0, \tag{2.11}$$

et alors les modes $\phi(y)$ s'obtiennent comme la fonction propre associée au couple (k,ω) vérifiant la relation de dispersion. La relation de dispersion implicite (2.11) admet un grand nombre de solutions pour ω à un k donné ou pour k à un ω donné. Mais parmi tous ces modes, il y en a en général un qui est beaucoup plus instable que les autres. Il n'est donc pas utile de connaître tous les modes (et de toute façon c'est pratiquement impossible), car toute la dynamique est correctement décrite par un ou tout au plus deux modes.

Trois cas ont un intérêt particulier : la réponse du système à une perturbation initiale spatialement périodique, à une impulsion très brève appliquée à un endroit précis, ou à un forçage harmonique en temps appliqué à une certaine position. L'étude de ces trois cas permet d'introduire les notions essentielles de la théorie des instabilités hydrodynamiques.

2.1 Problème temporel et relation de dispersion non linéaire

Le *problème temporel* est l'étude de l'évolution d'une perturbation initiale de faible amplitude spatialement périodique, soit

$$\psi(x,y,t=0) = A\phi(y;k)\mathrm{e}^{\mathrm{i}kx} + \text{c.c.}, \tag{2.12}$$

où ϕ est un mode propre associé au nombre d'onde k et $A \ll 1$. Dans cette approche, le nombre d'onde k est *réel*. En toute généralité il faudrait considérer une fonction $\phi(y)$ quelconque et la décomposer sur tous les modes propres de l'écoulement associés au nombre d'onde k. Pour des jets ou des sillages symétriques par rapport à la ligne centrale désignée par $y = 0$, les modes se divisent en modes *sinueux* (ϕ impaire) et modes *variqueux* (ϕ paire). Dans la plupart de ces configurations, le mode le plus instable est un mode sinueux. Pour simplifier la présentation, nous n'utiliserons donc que ce meilleur des modes possibles $\phi(y;k)$ et écrivons la relation de dispersion sous la forme

$$\omega = \Omega^{\ell}(k). \tag{2.13}$$

L'évolution de la perturbation (2.12) est alors donnée par

$$\psi(x,y,t) = A\phi(y;k)\exp \mathrm{i}\left[kx - \Omega^{\ell}(k)t\right] + \text{c.c.} \tag{2.14}$$

L'amplitude de cette perturbation varie avec un taux de croissance[1] $\Omega_i^{\ell}(k) \equiv \operatorname{Im}\Omega^{\ell}(k)$. Selon le signe de Ω_i^{ℓ}, la perturbation est atténuée ($\Omega_i^{\ell} < 0$) ou amplifiée ($\Omega_i^{\ell} > 0$) au cours du temps. La pulsation est donnée par $\Omega_r^{\ell}(k)$.

L'hypothèse d'un seul mode "dominant" peut maintenant être précisée : si parmi tous les modes associés au nombre d'onde k, il y en a un avec un taux de croissance beaucoup plus élevé que les autres, c'est celui-là qui va être observé et dominer l'évolution à long terme de la perturbation.

S'il n'existe aucune valeur de k réelle associée à un taux de croissance positif, l'écoulement est *linéairement stable* : toute perturbation décroît au cours du temps et le système retourne toujours à son état de base. En revanche, le système est *linéairement instable* s'il existe au moins un nombre d'onde amplifié. Dans ce cas il existe généralement toute une gamme $k_1 < k < k_2$ de nombres d'ondes instables.

Un mode linéairement instable ($\Omega_i^{\ell}(k) > 0$) croît exponentiellement et les non-linéarités vont forcément entrer en jeu aux temps longs. Pour connaître l'évolution ultérieure, la relation de dispersion linéaire (2.13) ne suffit plus et il faut recourir à l'équation non linéaire (2.6) au lieu de la version linéarisée (2.7). Lorsque l'instabilité est *super-critique*, les effets non linéaires limitent rapidement la croissance à une certaine amplitude et, en l'absence d'instabilités secondaires, la perturbation converge vers un train d'ondes non linéaires périodique dont le nombre d'onde k est imposé par la perturbation initiale. Dans les cas d'instabilité *sous-critique*, les non-linéarités peuvent modifier profondément l'état final du système et des perturbations

[1] Dans la suite, les indices i et r indiquent toujours respectivement les parties imaginaire et réelle d'une quantité complexe : $z_i \equiv \operatorname{Im} z$ et $z_r \equiv \operatorname{Re} z$.

non linéaires persistent éventuellement dans des situations linéairement stables. Dans les systèmes super-critiques, l'état final même non linéaire est en grande partie déterminé par les caractéristiques de stabilité linéaire ; alors que ces mêmes caractéristiques n'apportent pas beaucoup de renseignements sur la dynamique non linéaire dans les systèmes sous-critiques. Comme nous le verrons au cours de cette étude, la dynamique des écoulements considérés est de nature super-critique.

Ces trains d'ondes d'amplitude finie, vers lesquels l'évolution d'un mode instable converge, sont explicitement connus dans le cas du modèle GLC. Mais dans les écoulements réels, ils ne peuvent en général être obtenus que par des simulations numériques, ce qui sera fait au chapitre 6. Ces ondes non linéaires sont de la forme

$$\psi(x,y,t) = \Psi^{n\ell}(\theta,y;k) \quad \text{avec} \quad \theta = kx - \omega t, \tag{2.15}$$

où ω est une pulsation réelle et $\Psi^{n\ell}$ est 2π-périodique en θ. Ces ondes sont l'équivalent non linéaire des modes normaux (2.8). La fréquence ω des ondes non linéaires propagatives vers laquelle le problème temporel converge définit la *relation de dispersion non linéaire*

$$\omega = \Omega^{n\ell}(k). \tag{2.16}$$

Dans des systèmes super-critiques, ces ondes non linéaires n'existent que pour des nombres d'onde k linéairement amplifiés ; la relation de dispersion non linéaire (2.16) n'est donc définie que pour les k tels que $\Omega_i^\ell(k) > 0$.

2.2 Réponse impulsionnelle et instabilité absolue

Une autre façon d'étudier les caractéristiques de stabilité linéaire est d'étudier la réponse à une impulsion locale et instantanée appliquée à $t = 0$ en un point,

$$\left(\frac{\partial}{\partial t} + U(y)\frac{\partial}{\partial x}\right)\Delta\psi - U''(y)\frac{\partial\psi}{\partial x} - \frac{1}{\mathrm{Re}}\Delta^2\psi = \delta(x-x_f)\delta(y-y_f)\delta(t), \tag{2.17}$$

où δ est la fonction de Dirac et (x_f, y_f) l'endroit où l'impulsion est appliquée. En toute rigueur, il faut suivre l'évolution en x et y du paquet d'ondes créé par cette impulsion initiale ; mais en général la direction transverse ne joue pas de rôle important et un suivi du comportement dans le sens de l'écoulement suffit pour illustrer les propriétés essentielles.

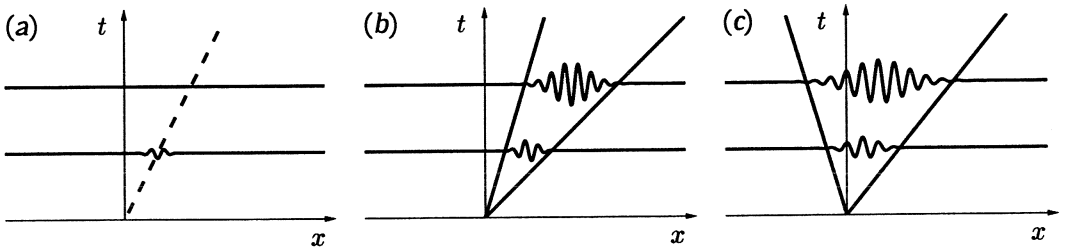


FIGURE 2.1. Évolution spatio-temporelle d'une impulsion initiale dans un milieu (*a*) stable, (*b*) convectivement instable, (*c*) absolument instable.

Trois comportements sont alors possibles (figure 2.1) : le paquet d'ondes créé par l'impulsion initiale (*a*) décroît (milieu *stable*), (*b*) croît mais est en même temps emporté par le courant jusqu'au bord du domaine de telle sorte que le milieu retourne finalement à l'état non perturbé (milieu *convectivement instable*), (*c*) croît sur place en s'étendant vers l'aval et vers l'amont pour envahir tout le système (milieu *absolument instable*). Les notions d'instabilité convective et absolue ont été introduites

par Briggs [6] et Bers [5] dans le contexte de la physique des plasmas ; elles se sont également avérées très utiles en mécanique des fluides pour l'étude des écoulements ouverts [39]. C'est dans ces références qu'on trouvera une discussion détaillée de la théorie des instabilités absolue et convective.

Les trois types de stabilité sont facilement déduits de la relation de dispersion linéaire (2.13). Le milieu est *linéairement stable* si la réponse impulsionnelle décroît sur tous les rayons $x/t = \text{const.}$ (figure 2.1*a*). Ceci se vérifie si $\Omega_i^\ell(k) < 0$ pour tout k réel.

Dans le cas contraire, une paquet d'ondes d'amplitude croissante se développe à partir de l'impulsion initiale. Le caractère convectif (figure 2.1*b*) ou absolu (figure 2.1*c*) de l'instabilité dépend de la *pulsation absolue* ω_0 et du *nombre d'onde absolu* k_0 complexes du paquet d'ondes de vitesse de groupe nulle, définis par

$$\omega_0 = \Omega^\ell(k_0) \quad \text{avec} \quad \frac{d\Omega^\ell}{dk}(k_0) = 0. \tag{2.18}$$

Le milieu est absolument instable si des perturbations croissent sur place, donc si $\omega_{0,i} > 0$, et convectivement instable si $\omega_{0,i} < 0$.

Dans un milieu CI ou AI, le paquet d'ondes amplifié est finalement régi par les équations non linéaires qui peuvent modifier le comportement ultérieur du système. Les notions d'instabilité convective ou absolue ont été généralisées par Chomaz [10] à des systèmes non linéaires.

2.3 Problème spatial et causalité

La notion de causalité est illustrée par l'étude de la réponse spatiale du milieu à un forçage périodique en temps et localisé en espace. Dans ce cas, le système est régi par

$$\left(\frac{\partial}{\partial t} + U(y)\frac{\partial}{\partial x}\right)\Delta\psi - U''(y)\frac{\partial\psi}{\partial x} + \left(\frac{\partial\psi}{\partial y}\frac{\partial}{\partial x} - \frac{\partial\psi}{\partial x}\frac{\partial}{\partial y}\right)\Delta\psi$$
$$= \frac{1}{\mathrm{Re}}\Delta^2\psi + \left[A_f\delta(x - x_f)\delta(y - y_f)H(t)\mathrm{e}^{-\mathrm{i}\omega_f t} + \text{c.c.}\right], \tag{2.19}$$

où $H(t)$ est la fonction de Heaviside, A_f et ω_f désignent respectivement l'amplitude et la pulsation du forçage appliqué en (x_f, y_f). Pour une faible amplitude de forçage $A_f \ll 1$, la réponse spatiale dans le voisinage du forçage est donnée par le problème linéarisé associé à (2.19). Quand le forçage périodique est branché à $t = 0$, il se développe un paquet d'ondes transitoire qui accompagne la réponse à la fréquence du forçage. Si le milieu est stable ou convectivement instable, ce transitoire est atténué ou emporté loin de la source, et finalement la réponse à la fréquence du forçage s'installe partout. En revanche, si le milieu est absolument instable, le transitoire croît sur place et contamine tout l'écoulement. Dans ce dernier cas, le forçage n'arrive pas à imposer sa fréquence au milieu et le problème spatial est mal posé. Nous n'allons donc étudier la réponse spatiale que pour des milieux au plus convectivement instables.

Dans la mesure où la réponse au forçage a une amplitude faible, elle obéit à la relation de dispersion linéaire (2.13). Les ondes d'instabilité se développant en aval et en amont oscillent à la pulsation ω_f, leurs nombres d'onde sont donc des solutions de $\omega_f = \Omega^\ell(k)$. Cette équation admet en général plusieurs branches de solutions $k_m^\ell(\omega_f)$ indexées par m et leur nombre dépend beaucoup de la forme particulière de $\Omega^\ell(k)$. Mais dans la plupart des cas il n'y a que deux branches qui jouent un rôle actif.

Comme l'effet ne peut se produire avant la cause, il faut que $\psi = 0$ pour $t < 0$. En utilisant un calcul de résidus dans le plan complexe ω, et en supposant que les taux de

croissance temporels ($\Omega_i^\ell(k)$ avec k réel) sont bornés, on déduit [6, 5] de ces raisons de causalité que les branches spatiales k^ℓ se rapportent ou bien à la réponse en aval ($x > x_f$) ou bien à la réponse en amont ($x < x_f$) du point de forçage. C'est pourquoi on peut noter $k^{\ell+}$ et $k^{\ell-}$ les branches correspondant à l'aval et à l'amont respectivement. Alors, après évacuation des transitoires, la solution du problème (2.19) s'écrit

$$\begin{aligned}\psi(x,y,t) \propto\ & H(-x)\,\phi[y;k^{\ell-}(\omega_f)]\exp i[k^{\ell-}(\omega_f)x-\omega_f t]+\text{c.c.}\\ & +H(x)\,\phi[y;k^{\ell+}(\omega_f)]\exp i[k^{\ell+}(\omega_f)x-\omega_f t]+\text{c.c.}\end{aligned}\tag{2.20}$$

Puisque cette répartition des branches spatiales en branches + et branches − est basée sur des arguments de causalité, on parlera toujours de branches spatiales causales en référence à un problème de forçage.

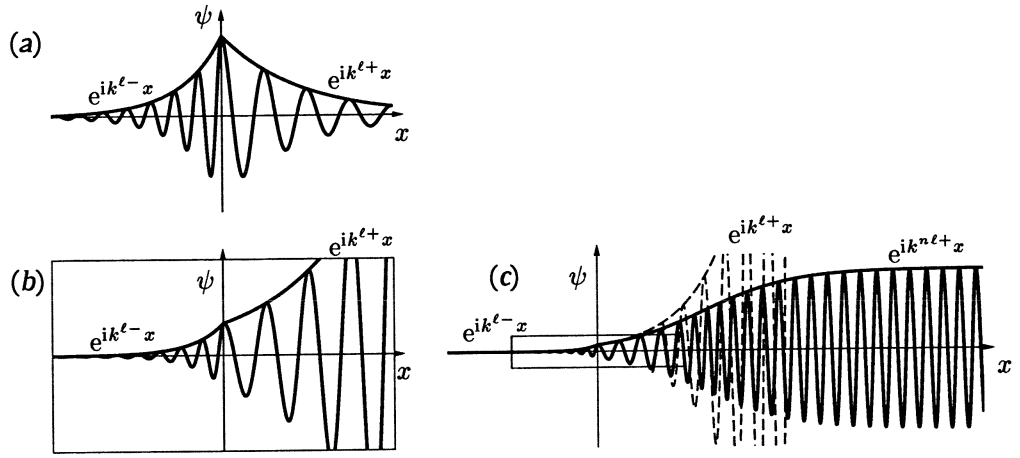


FIGURE 2.2. Réponse à un forçage harmonique en temps. Représentation schématique de la fonction de courant ψ et de son enveloppe en $y = 0$. (*a*) Réponses atténuées en aval et en amont. (*b*) Réponse amplifiée en aval ($k_i^{\ell+} < 0$) et (*c*) train d'ondes saturées obtenu plus loin en aval.

La croissance spatiale de ces ondes dépend du signe de $k_i^\ell = \operatorname{Im} k^\ell$. Pour distinguer entre une branche amplifiée et une branche atténuée, il est donc essentiel de savoir si elle est obtenue en aval ou en amont de la source. La réponse en aval est spatialement atténuée si $k_i^{\ell+} > 0$ et amplifiée si $k_i^{\ell+} < 0$. Au contraire, la décroissance spatiale vers l'amont coïncide avec $k_i^{\ell-} < 0$, alors que l'amplification a lieu quand $k_i^{\ell-} > 0$.

Dans un milieu stable, toutes les branches sont atténuées. Quelle que soit la fréquence de forçage ω_f réelle, on a alors $k_i^{\ell+}(\omega_f) > 0$ et $k_i^{\ell-}(\omega_f) < 0$ (figure 2.2*a*).

Dans un milieu CI, la réponse peut être amplifiée vers l'aval. Comme on suppose l'écoulement de base de $x = -\infty$ vers $x = +\infty$, ce sont les branches $k^{\ell+}(\omega)$ qui peuvent se déstabiliser. Lorsqu'une branche linéaire est amplifiée (figure 2.2*b*), il faut prendre en compte les termes non linéaires à une certaine distance du forçage, même pour des amplitudes de forçage A_f très faibles. Lorsque la réponse atteint une amplitude finie, la saturation non linéaire arrête la croissance et conduit, en l'absence d'instabilités secondaires, vers une onde non linéaire se propageant à la fréquence d'excitation avec un nombre d'onde *réel* $k^{n\ell}$ (figure 2.2*c*). Comme ce train d'ondes est obtenu en aval de la source, on note cette branche non linéaire $k^{n\ell+}(\omega_f)$. Ce train d'ondes non linéaire étant périodique en temps et en espace, la fréquence de forçage ω_f et le nombre d'onde $k^{n\ell+}$ vérifient la relation de dispersion non linéaire (2.16). Mais

il faut remarquer que toutes les solutions non linéaires ne sont pas accessibles par un problème de forçage. La relation précise entre branches spatiales linéaires et non linéaires sera établie au chapitre 𝔉, et des exemples de réponse spatiale non linéaire dans les sillages sont donnés au chapitre 𝔊.

En conclusion de cette section, les propriétés de stabilité linéaire d'un milieu sont entièrement décrites par la relation de dispersion linéaire (2.13). Les ondes non linéaires existent pour des nombres d'onde linéairement instables et elles peuvent toutes être obtenues dans un problème temporel. Leur fréquence est alors régie par la relation de dispersion non linéaire (2.16). Dans les systèmes stables ou convectivement instables, les branches spatiales se répartissent en branches aval $k^{\ell+}(\omega)$ et branches amont $k^{\ell-}(\omega)$ selon des critères de causalité. Dans les systèmes CI, les branches spatiales non linéaires $k^{n\ell+}(\omega)$ ont également un sens causal.

Dans le cadre de l'approximation linéaire, les problèmes temporel et spatial sont de nature différente : un nombre d'onde k réel est associé à une fréquence complexe ω dans le cas temporel, dans le cas spatial la fréquence est réelle et les nombres d'ondes sont complexes. En revanche, en tenant compte des non-linéarités, les approches spatiales et temporelles se rejoignent : l'onde progressive non linéaire observée en aval par forçage harmonique en temps est exactement la même que celle obtenue par une perturbation initiale de même nombre d'onde. Les cas spatiaux et temporels non linéaires associent les mêmes fréquences réelles aux mêmes nombres d'onde réels.

3. Milieux inhomogènes

Les résultats précédents s'appliquent à des écoulements homogènes. Or, dans la plupart des systèmes étudiés, le profil de vitesse évolue le long de l'écoulement.

Les notions précédentes peuvent être généralisées dans les cas où l'écoulement de base varie suffisamment lentement pour que les ondes d'instabilité vivant dans les différentes régions de l'écoulement ne voient qu'un milieu homogène. Ceci est le cas si la distance caractéristique L sur laquelle l'écoulement est modifié est très grande devant l'échelle typique des instabilités λ. Soit

$$\epsilon = \lambda/L \ll 1 \tag{2.21}$$

le rapport entre ces deux échelles. L'hypothèse de faible inhomogénéité spatiale permet alors de définir une variable lente dans le sens du courant

$$X = \epsilon x. \tag{2.22}$$

Sous l'hypothèse de séparation des échelles, les deux variables x et X sont comme décorrélées : x régit les oscillations rapides sur l'échelle des instabilités tandis que X rend compte de la lente variation sous-jacente de l'écoulement de base. Les propriétés locales de l'écoulement sont alors obtenues en figeant X et en étudiant l'écoulement strictement parallèle obtenu en prolongeant vers $x = \pm\infty$ le profil de vitesse de la position X. C'est dans ce sens que le terme *local* sera utilisé dans la suite.

Ainsi la relation de dispersion linéaire est définie *localement* en chaque point X de l'écoulement comme

$$\omega = \Omega^{\ell}(k, X), \tag{2.23}$$

et les modes propres associés sont de la forme $\Psi^{\ell}(y; k, X)$. On en déduit la fréquence absolue $\omega_0(X)$ et le nombre d'onde absolu $k_0(X)$ locaux comme en (2.18) et les régions

localement stables, convectivement instables ou absolument instables de la configuration étudiée. Dans les régions instables, la relation de dispersion non linéaire locale

$$\omega = \Omega^{n\ell}(k, X) \tag{2.24}$$

est définie pour des nombres d'ondes réels tels que $\Omega_i^\ell(k, X) > 0$. L'amplification temporelle aboutit alors aux ondes non linéaires locales $\Psi^{n\ell}(\theta, y; k, X)$, qui sont obtenues en chaque point le long de l'écoulement.

Une structure globale couvrant toute l'étendue de l'écoulement s'obtient alors en suivant de proche en proche des solutions valables à chaque position. Des développements asymptotiques de type WKBJ [3] seront utilisés pour justifier rigoureusement cette méthode. C'est grâce à cette hypothèse de faible inhomogénéité (2.21) que les comportements globaux des écoulements se déduisent de leurs propriétés locales. Dans les équations modèles de type Ginzburg–Landau utilisées dans les chapitres 𝔅, ℭ et 𝔉, cette hypothèse est vérifiée par construction. Sa validité dans le cas des équations de Navier–Stokes sera démontrée au chapitre 𝔊.

4. Formulation du problème de comportement synchronisé

Ce mémoire étudie des oscillations globales : les fluctuations observées en chaque point de l'écoulement sont toutes accordées à une même fréquence. La fréquence globale ω_g est encore inconnue, mais elle est constante dans tout le domaine. Ainsi, il faut résoudre les relations de dispersion (2.23,2.24) pour $\omega = \omega_g$ donné. Le nombre d'onde local s'obtient alors sous la forme $k^{\ell\pm}(X, \omega_g)$ ou $k^{n\ell\pm}(X, \omega_g)$ dans les régions où les fluctuations sont de faible amplitude ou d'amplitude finie respectivement.

Pour le moment, nous ignorons quel est le moteur de ces fluctuations synchronisées, mais nous avons supposé que le comportement est intrinsèque : les oscillations globales résultent d'un mécanisme de résonance qui trouve sa cause au cœur du système étudié, et elles sont indépendantes de perturbations venant de l'extérieur. Le principe de causalité énoncé à la section 2.3 permet alors de préciser les branches spatiales obtenues dans les régions situées loin en amont et loin en aval. En effet, dans ces régions éloignées, les trains d'ondes trouvent leur origine dans la région centrale et sont donc associés à des branches spatiales k^- en amont et des branches k^+ en aval (figure 2.3). Si le milieu est stable aux extrémités, c'est la relation de dispersion linéaire qui s'applique et la structure globale est faite d'une branche $k^{\ell-}$ loin en amont et d'une branche $k^{\ell+}$ loin en aval. Mais si le système reste convectivement instable jusqu'à l'infini, l'amplitude des perturbations ne décroît pas forcément et alors la branche non linéaire $k^{n\ell+}$ peut s'étendre jusqu'au bord aval. Ainsi, les conditions aux limites sont déterminées par des considérations de causalité plutôt que de décroissance à l'infini, quelle que soit la dynamique qui régit la région centrale. En effet, une décroissance des perturbations aux bords du système n'est pas nécessaire.

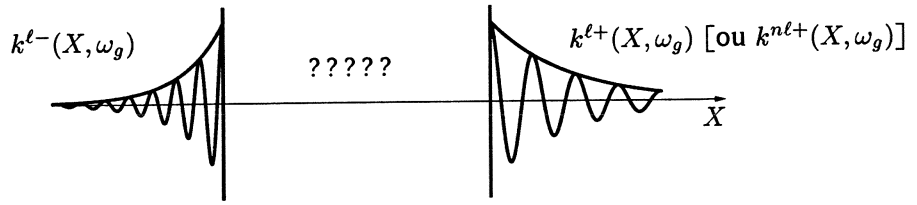


FIGURE 2.3. La synchronisation globale comme un problème de valeur propre non linéaire : la fréquence globale ω_g doit permettre le passage entre les branches $k^-(X, \omega_g)$ en amont et $k^+(X, \omega_g)$ en aval à travers une région centrale dominée par une dynamique non linéaire.

Ainsi, le comportement synchronisé se formule comme un problème de valeur propre non linéaire : il faut trouver la fréquence globale ω_g qui autorise le passage entre les branches spatiales – et + de part et d'autre de la région centrale. L'analyse précise de cette région centrale permettra d'identifier le mécanisme de résonance.

5. Modes globaux linéaires

Avant d'aborder les structures non linéaires, il est utile de rappeler les résultats obtenus dans un cadre strictement linéaire par Chomaz, Huerre & Redekopp [13] et Le Dizès *et al.* [51].

Dans l'approximation linéaire, le problème de synchronisation globale (figure 2.3) ne fait intervenir que les branches spatiales $k^{\ell-}$ et $k^{\ell+}$. Un mode global linéaire connecte donc directement la branche spatiale amont $k^{\ell-}$ à la branche aval $k^{\ell+}$ sans région non linéaire intermédiaire. Par définition de la fréquence absolue locale $\omega_0(X)$, les branches $k^{\ell-}$ et $k^{\ell+}$ sont connectées en $k_s^\ell \equiv k^{\ell-}(X_s^\ell,\omega_g) = k^{\ell+}(X_s^\ell,\omega_g)$ au point X_s^ℓ précisément quand $\omega_g = \omega_0(X_s^\ell)$. Un tel point est appelé *point tournant* [3,90] de la relation de dispersion locale. Mais un simple point tournant ne suffit pas pour donner naissance à un mode global linéaire. L'étude approfondie menée par Le Dizès *et al.* [51] a montré la nécessité d'avoir un point tournant double ou deux points tournants simples de même fréquence. Si X_s^ℓ est un point tournant double, *i.e.*, si

$$\frac{d\omega_0}{dX}(X_s^\ell) = 0, \tag{2.25}$$

il existe alors un mode global linéaire de fréquence

$$\omega_g = \omega_s^\ell \equiv \omega_0(X_s^\ell). \tag{2.26}$$

En amont et en aval de X_s^ℓ la structure spatiale globale est respectivement décrite par les branches $k^{\ell-}(X,\omega_s^\ell)$ et $k^{\ell+}(X,\omega_s^\ell)$ issues de k_s^ℓ (figure 2.4*a*). Nous ne considérerons ici que les modes globaux avec un point tournant double X_s^ℓ.

En général, les conditions (2.25,2.26), ou de façon équivalente

$$\omega_s^\ell = \Omega^\ell(k_s^\ell, X_s^\ell) \quad \text{et} \quad \frac{\partial\Omega^\ell}{\partial k}(k_s^\ell, X_s^\ell) = \frac{\partial\Omega^\ell}{\partial X}(k_s^\ell, X_s^\ell) = 0, \tag{2.27}$$

ne peuvent être vérifiées sur l'axe des X réels. Mais, dans une théorie linéaire, la relation de dispersion $\Omega^\ell(k,X)$ peut être prolongée analytiquement pour des valeurs complexes de X. La fréquence absolue $\omega_0(X)$ est alors définie dans tout le plan complexe $X_r + \mathrm{i}X_i$ et un point tournant double correspond à un col de la surface définie par $\omega_{0,i}(X_r + \mathrm{i}X_i)$ (figure 2.4*b*).

L'évolution temporelle du mode global dépend de $\omega_{s,i}^\ell \equiv \mathrm{Im}\omega_s^\ell$. Si $\omega_{s,i}^\ell < 0$, le mode est atténué et le système est *linéairement globalement stable*. En revanche, si $\omega_{s,i}^\ell > 0$, le milieu est *linéairement globalement instable*. Ainsi, pour qu'il y ait instabilité globale linéaire, il faut que le col (figure 2.4*b*) soit à une altitude $\omega_{s,i}^\ell > 0$. Ceci n'est possible que s'il existe un intervalle AI sur l'axe réel X_r. L'intervalle hachuré de la figure 2.4(*b*) correspond à la portion de l'écoulement dont le taux de croissance absolu local $\omega_{0,i}(X_r)$ est plus grand que $\omega_{s,i}^\ell$. L'instabilité absolue locale est donc une condition nécessaire pour avoir une instabilité globale linéaire. Comme en général le col n'est pas situé sur l'axe réel, cette condition n'est pas suffisante : il faut une région AI *d'extension finie* pour qu'un écoulement soit instable au sens des modes globaux linéaires.

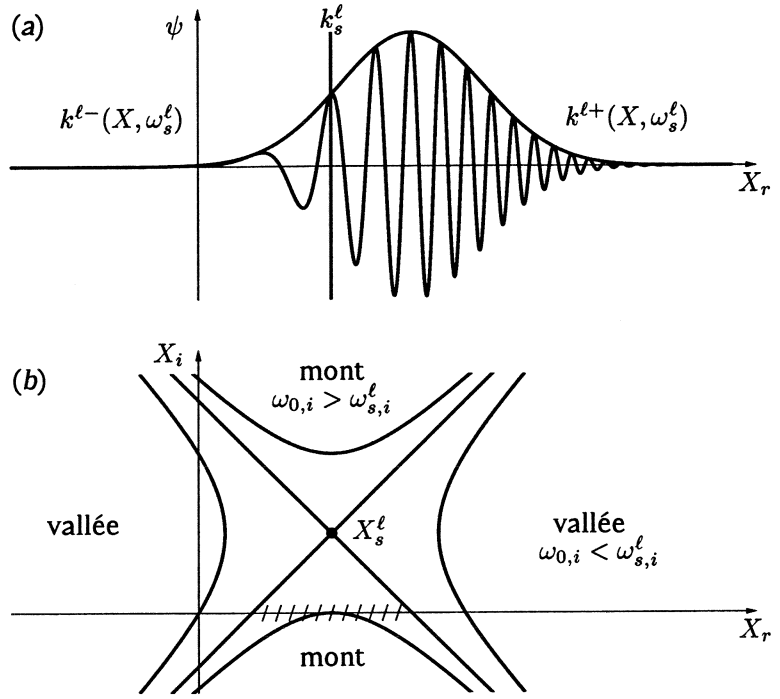


FIGURE 2.4. (*a*) Structure spatiale du mode global linéaire de fréquence ω_s^ℓ. Les branches spatiales amont $k^{\ell-}$ et aval $k^{\ell+}$ sont connectées en k_s^ℓ. Le maximum d'amplitude n'est généralement pas atteint en ce point tournant. (*b*) Courbes de niveau $\omega_{0,i}(X) = \text{const.}$ dans le plan des X complexes. Le point tournant double X_s^ℓ correspond à un col d'altitude $\omega_{s,i}^\ell$. L'intervalle de l'axe réel X_r situé au-dessus du col est hachuré.

6. Approche faiblement non linéaire

L'étape suivante vers le régime non linéaire a été réalisée par Le Dizès *et al.* [50] en étudiant les modes globaux faiblement amplifiés, *i.e.*, les situations où $0 < \omega_{s,i}^\ell \ll 1$. Cette étude a révélé de sérieuses limitations à une théorie faiblement non linéaire des modes globaux.

Pour comprendre l'origine de ces difficultés, il faut se reporter à la structure spatiale des modes linéaires (figure 2.4*a*). Au point-selle X_s^ℓ, les deux branches spatiales se rejoignent, $k^{\ell+}(X_s^\ell,\omega_s^\ell) = k^{\ell-}(X_s^\ell,\omega_s^\ell) = k_s^\ell$. Si $k_{s,i}^\ell < 0$, l'amplitude du mode global croît exponentiellement dans le sens de l'écoulement au point X_s^ℓ. Le maximum de l'amplitude est alors atteint en aval du point-selle, lorsque le taux de croissance spatial $-k_i^{\ell+}(X,\omega_s^\ell)$ change de signe et devient négatif.

L'approche faiblement non linéaire reste valable aussi longtemps que l'amplitude maximale du mode est faible. Or, à cause du décalage entre le point tournant X_s^ℓ et le point d'amplitude maximale et à cause de la croissance exponentielle de l'amplitude entre ces deux positions, une faible amplitude maximale requiert une amplitude exponentiellement petite en X_s^ℓ. Ainsi, le domaine de validité de la théorie faiblement non linéaire est extrêmement restreint : il faut que $|\omega_{s,i}^\ell| < \mathrm{e}^{-1/\epsilon}$ où ϵ est le petit paramètre mesurant l'inhomogénéité (2.21). En outre, la constante de Landau qui détermine la nature de la transition à $\omega_{s,i}^\ell = 0$ n'a pas de limite bien définie ni de signe constant quand $\epsilon \to 0$. Tous ces effets pernicieux sont le signe qu'une théorie faiblement non linéaire est mal adaptée aux écoulements ouverts. D'où la nécessité d'élaborer une théorie non perturbative pouvant traiter des non-linéarités pleinement développées pour comprendre le comportement synchronisé des écoulements cisaillés.



Doux chapeaux

Les équations de Navier–Stokes me paraissant trop difficiles à étudier au départ, je me suis d'abord tourné vers l'équation modèle de Ginzburg–Landau à coefficients complexes et spatialement variables. Le choix de ce modèle était motivé par le fait que Chomaz, Huerre, Redekopp et Le Dizès [13, 51] avaient obtenu dans ce même cadre le critère de sélection de *modes globaux linéaires*. Les résultats de Le Dizès *et al.* [50] semblaient indiquer qu'on ne peut pas atteindre le régime pleinement non linéaire en passant par une analyse faiblement non linéaire, mais qu'il faut passer directement à des solutions d'amplitude finie sans essayer de les obtenir par continuité à partir des solutions linéaires.

Ainsi, il faut d'abord pouvoir analyser correctement des solutions d'amplitude finie évoluant dans un milieu faiblement inhomogène. Pour des systèmes linéaires régis par une équation dépendant d'une variable d'espace lente, la théorie WKBJ classique [3] permet d'obtenir des approximations asymptotiques uniformément valables des solutions. Bernoff [4] utilise un développement en échelles multiples (à la fois spatiales et temporelles) pour obtenir des solutions d'ondes non linéaires lentement modulées en espace et en temps dans un *milieu homogène*. M'inspirant de ces résultats, j'ai généralisé la technique WKBJ à des solutions oscillantes d'amplitude finie évoluant dans un milieu faiblement inhomogène. Cette technique non linéaire est analogue au cas linéaire, mais elle ne fait intervenir que des quantités réelles.

L'approche WKBJ part de la constatation qu'en chaque point une solution globale ressemble à une solution locale, obtenue en figeant en ce même point la variation du milieu le long de l'écoulement. Dans des systèmes linéaires, ces solutions locales sont des ondes planes de la forme $\mathrm{e}^{\mathrm{i}(kx-\omega t)}$, où le nombre d'onde complexe k et la fréquence complexe ω sont reliés par la relation de dispersion linéaire (2.23), obtenue avec les valeurs des coefficients de l'équation en chaque point X. En exigeant que la solution globale soit synchronisée à une fréquence globale ω_g, il faut résoudre la relation de dispersion précédente pour $\omega = \omega_g$. On en déduit ainsi le nombre d'onde local $k^\ell(X,\omega)$, mais l'amplitude locale (complexe) des solutions reste indéterminée à cet ordre. C'est à l'ordre d'approximation suivant que le raccord des solutions obtenues en chaque point conduit à une condition de solvabilité qui donne l'évolution de cette amplitude complexe.

Cette technique, classique dans le cas des équations linéaires, se généralise à des systèmes non linéaires, s'ils admettent également des solutions locales ondulatoires. Dans le cas de GLC, les solutions oscillantes non linéaires sont simplement des ondes planes d'amplitude finie, $R\mathrm{e}^{\mathrm{i}(kx-\omega t)}$. Cette fois-ci, le nombre d'onde k et la fréquence ω sont des quantités *réelles*, ainsi que l'amplitude R. Ces quantités réelles sont reliées entre elles par des relations de dispersion non linéaires (2.24), obtenues en chaque point. Comme dans le cas linéaire, la condition que la fréquence ne dépende pas de l'espace donne le nombre d'onde local $k^{n\ell}(X,\omega)$. Mais ici cette condition fixe également l'amplitude des trains d'onde non linéaires.

On a désormais à notre disposition des familles de solutions locales linéaires et non linéaires et on sait comment suivre spatialement une branche linéaire ou une

branche non linéaire. Avant de poursuivre notre analyse, il faut préciser les conditions aux limites utilisées. Quand on étudie des milieux stables loin en amont et loin en aval, on s'attend à ce que la solution décroisse quand $X \to -\infty$ et quand $X \to +\infty$. Donc, dans un voisinage des bords, l'amplitude sera négligeable et la solution sera correctement décrite par les équations linéarisées. En fait, la relation de dispersion linéaire admet deux branches spatiales : $k^{\ell+}(X,\omega)$ et $k^{\ell-}(X,\omega)$. La branche $k^{\ell-}$ correspond à un train d'onde décroissant exponentiellement quand $X \to -\infty$ et exponentiellement amplifié quand $X \to +\infty$; et l'inverse est vrai pour la branche $k^{\ell+}$. D'où la nécessité de passer de la branche $k^{\ell-}$ en amont à la branche $k^{\ell+}$ en aval pour satisfaire les conditions aux limites. Nous verrons au chapitre $\mathfrak{F}$ (section 4.1 de l'article) que la condition de décroissance en $X = +\infty$ n'est pas nécessaire : il suffit que le système soit stable ou convectivement instable aux bords.

La théorie des modes globaux linéaires [13] permet de joindre les deux branches spatiales $k^{\ell-}$ et $k^{\ell+}$ par un point-selle de la relation de dispersion linéaire. Mais cette méthode oblige de prolonger analytiquement cette relation de dispersion pour des valeurs complexes de X, ce qui est exclu dans notre cas puisque nous recherchons des solutions non linéaires. Nous ne pouvons donc directement passer de la branche $k^{\ell-}$ à la branche $k^{\ell+}$.

En revanche, les solutions linéaires sont naturellement reliées à leurs homologues non linéaires aux points d'amplification marginale. En effet, aux points de stabilité neutre, l'amplitude des ondes non linéaires tombe à zéro et les solutions non linéaires se transforment alors continûment pour devenir des ondes linéaires de même nombre d'onde. La relation de dispersion linéaire y est précisément vérifiée avec des valeurs *réelles* pour la fréquence et pour le nombre d'onde. Ce sont ces mêmes valeurs qui vérifient la relation de dispersion *non linéaire* avec une amplitude nulle. Ceci établit que les branches spatiales non linéaires $k^{n\ell-}$ et $k^{n\ell+}$ viennent se raccrocher aux branches linéaires $k^{\ell-}$ et $k^{\ell+}$ aux points respectifs de stabilité linéaire marginale.

Nous savons qu'il faut des branches $k^{\ell-}$ et $k^{\ell+}$ loin en amont et en aval. Chacune de ces branches linéaires est prolongée vers la région centrale par la branche associée $k^{n\ell-}$ ou $k^{n\ell+}$. Le problème de l'obtention d'un mode global se réduit alors à savoir relier ces deux branches non linéaires : il faut passer de la branche $k^{n\ell-}$ à la branche $k^{n\ell+}$ pour obtenir une solution valable sur toute l'étendue du domaine étudié.

Fully Nonlinear Global Modes in Spatially Developing Media

Benoît Pier and Patrick Huerre

Laboratoire d'hydrodynamique (LadHyX), École polytechnique, F-91128 Palaiseau cedex, France.

Abstract

Global modes on a doubly-infinite one-dimensional domain $-\infty < X < +\infty$ are studied in the context of the complex Ginzburg-Landau equation with slowly spatially varying coefficients. A fully nonlinear frequency selection criterion is derived for global-mode solutions under the assumption of weak inhomogeneity of the medium. The global mode is found to be governed by the fully nonlinear equations in a region of finite size, and by the linearized equations in the vicinity of $X = \pm\infty$. Asymptotic matching techniques are used to relate the WKBJ approximations in the linear and nonlinear regions through appropriate transition layers. The *real* global frequency is determined by requiring that spatial branches issuing from $X = -\infty$ and $X = +\infty$ be continuously connected at a saddle point of the local nonlinear dispersion relation $\omega = \Omega^{nl}(k, R^2, X)$ between the frequency ω, the wavenumber k and amplitude R at a given station X. The results constitute a fully nonlinear generalization of the linear frequency selection criteria previously obtained by Chomaz *et al.* [13], Monkewitz *et al.* [59], and Le Dizès *et al.* [51].

1 Introduction

Our present understanding of hydrodynamic instabilities relies, to a great extent, on the scientific achievements of Fritz Busse and his colleagues. For instance, an intimate knowledge of the Busse balloon [8] has indeed become prerequisite reading to any serious student of Rayleigh-Bénard convection in a fluid layer heated from below, one of the most widely studied closed flow systems. This is just one example of Fritz Busse's fundamental and lasting contributions to hydrodynamics. Fritz has devoted a relatively small portion of his boundless energy to the study of open shear flows, which may explain why our comprehension of instabilities in open flows may have not reached the same fully mature stage. This contribution, which is dedicated to Fritz Busse in

Article published in Physica D 97 (1996) 206–222

celebration of his 60th birthday, illustrates one possible approach which could be successful in spatially developing open flows exhibiting a global resonance.

Spatially developing flows may, under certain conditions, develop self-sustained oscillations. Fluctuations saturate at a finite amplitude in the locally unstable regions of the flow and become tuned at an overall frequency. The intrinsic frequency and the associated spatial distribution of fluctuations define a *global mode*. Relatively little is known regarding the nonlinear evolution stage of such objects. Chomaz [10] and Couairon & Chomaz [16] have recently introduced generalized definitions of absolute, convective and global instability applicable to the fully nonlinear case and demonstrated that linear absolute instability is not always synonymous with global instability. Furthermore, these authors have brought to light the close relationship existing between the dynamical systems point of view and the more classical description in terms of a dispersion relation. The goal of the present study is the derivation of a *fully nonlinear* global mode selection criterion in the context of the one-dimensional complex Ginzburg-Landau equation with slowly varying coefficients.

The main stability concepts pertaining to spatially developing open flows have been reviewed by Huerre & Monkewitz [39]. Recent developments have been discussed in Le Dizès *et al.* [51]. It is here sufficient to recall that specific classes of spatially developing open flows such as bluff-body wakes [55,35,44,84], low density jets [80,58] and counterflow mixing layers [83] may sustain in specific parameter ranges synchronized periodic oscillations over an extended region of the flow. In other words, such systems undergo a Hopf bifurcation as some control parameter is continuously varied. Global mode concepts have precisely been introduced to account for this peculiar behavior of open flows.

In most basic flows of interest, the velocity profile is nonuniform in the streamwise direction, and in order to distinguish between local and global properties it is essential to assume that streamwise variations are slow over a typical instability wavelength. Under this hypothesis, local stability properties are obtained within the parallel flow approximation by freezing the slow streamwise coordinate X. At the local level of description, linear stability properties of normal modes $e^{i(kx-\omega t)}$ are then characterized by a local dispersion relation $D(k,\omega,X)=0$ between complex wavenumber k and frequency ω. The goal of a global analysis is to construct in a self-consistent manner a global spatial distribution made up of saturated instability waves governed by the local properties of the flow. The global frequency ω_g is then considered as an eigenvalue to be determined by requiring that perturbations decay at $X=\pm\infty$. The resulting global mode is viewed as a theoretical analogue of the self-sustained oscillatory structures that are observed experimentally.

The analysis by Chomaz *et al.* [13] of the linearized Ginzburg-Landau equation with slowly varying coefficients has demonstrated that a region of absolute

instability is a necessary condition for linearly unstable global modes to exist. The dominant complex global frequency ω_g is obtained, at leading order in the WKBJ approximation, for a saddle point of the local linear dispersion relation $\omega = \Omega^\ell(k, X)$, *i.e.*,

$$\omega_g \sim \omega_s = \Omega^\ell(k_s, X_s), \tag{1}$$

where the complex pair (k_s, X_s) satisfies

$$\frac{\partial \Omega^\ell}{\partial k}(k_s, X_s) = \frac{\partial \Omega^\ell}{\partial X}(k_s, X_s) = 0. \tag{2}$$

The same linear frequency selection criterion has been derived by Monkewitz *et al.* [59] in the framework of the Navier-Stokes equations linearized around an arbitrary weakly nonparallel basic flow. More recently, the frequency selection criterion pertaining to the Ginzburg-Landau equation over a doubly infinite domain has been examined anew by resorting to a comparison equation method (Le Dizès *et al.* [51]). It has been shown that global modes are either of type 1, with two simple turning points in the complex X-plane, or type 2, with a double turning point as defined in (2). The validity of the selection criterion (2) has further been confirmed by the exact Green function calculations of Hunt & Crighton [41].

The extension of these concepts to the nonlinear régime has until recently appeared somewhat problematic. It seems, at first sight, natural to perform a weakly nonlinear analysis in the vicinity of the global mode onset. Such an approach is straightforward for nonparallel effects of *order unity*, as shown by Chomaz *et al.* [12] in the case of the Ginzburg-Landau equation with a linearly or quadratically varying control parameter. Paradoxically, the introduction of a weakly nonparallel assumption in addition to the weakly nonlinear one leads to unexpected difficulties [51]: in the limit of zero nonparallelism, the Landau constant does not converge to a well defined limit of *constant* sign. In other words, the Landau equation formalism which purportedly describes a Hopf bifurcation near onset does not apply unless drastic conditions are met. In order to circumvent these difficulties, we choose in the present study to jump to the fully nonlinear régime while keeping the weakly nonparallel assumption. Thus we implement a nonlinear WKBJ approximation scheme which remains valid for amplitudes of order unity, as encountered in the phase dynamics of patterns [70,21,48,54] or in the description of slowly varying fully nonlinear wavetrains [36,4].

The main objective of the paper is the generalization of the linear frequency selection criterion (1,2) to fully nonlinear global modes provided that the local nonlinear dispersion relation of the weakly inhomogenous flow is given. We should emphasize that, in contrast to the linear criterion, the present formulation will only involve purely real values of the wavenumber, frequency

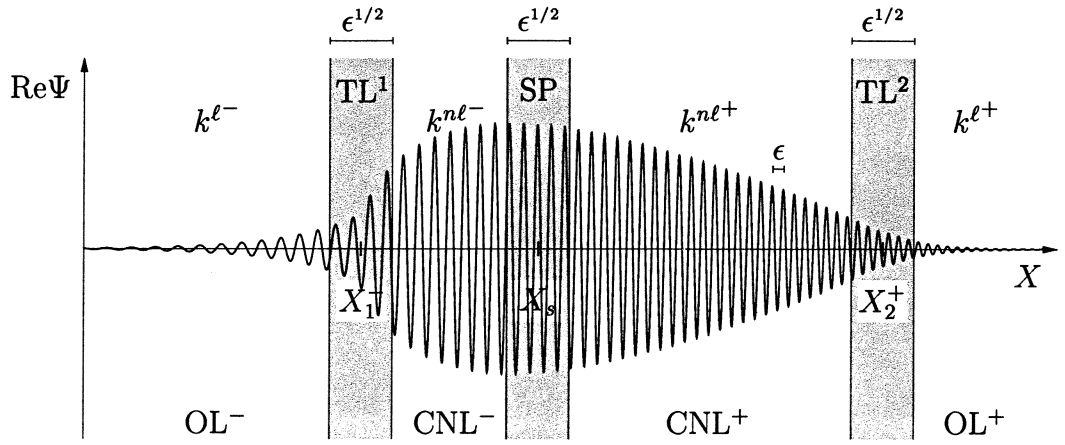


Fig. 1. Fully nonlinear global mode spatial structure: $\mathrm{OL}^{\pm}$, outer semi-infinite linear regions close to $X = \pm\infty$; $\mathrm{TL}^{1,2}$, transition layers of thickness $O(\epsilon^{1/2})$ connecting linear and nonlinear regions; $\mathrm{CNL}^{\pm}$, central nonlinear regions of size $O(1)$; SP, saddle-point region of thickness $O(\epsilon^{1/2})$.

and local streamwise variable. In the present study there is no need to extend analytically the dispersion relation in the complex k-plane and X-plane, a feature which considerably simplifies the analysis.

The inhomogeneities of the medium are characterized by a small parameter

$$\epsilon \sim \frac{\lambda}{L} \ll 1, \tag{3}$$

where L is a typical evolution length scale of the basic flow and λ a typical wavelength of the instability. Under the assumption $\epsilon \ll 1$, global mode solutions depend on two different length scales: a fast space variable x related to the rapid spatial oscillations of the carrier wave and a slow variable $X = \epsilon x$ describing the slow spatial evolution of the "basic flow". Fluctuations $\Psi(x,t)$ around a given basic state are governed by a partial differential equation, the coefficients of which depend on the slow variable X. The local properties of the flow are then recovered by freezing X. This separation of scales calls for an analysis in terms of nonlinear WKBJ approximations: the slowly evolving local characteristics may be exploited to construct global mode solutions composed of slowly varying nonlinear wavetrains.

In the course of the study, we are led to distinguish different regions characterizing the global mode spatial structure, as sketched in fig.1. In central nonlinear regions of finite size ($\mathrm{CNL}^{\pm}$) the wave has finite amplitude and satisfies the fully nonlinear governing equation of the problem. These central nonlinear regions are surrounded by two semi-infinite outer linear regions ($\mathrm{OL}^{\pm}$) where the global mode satisfies the linearized equation and is exponentially decaying towards infinity, as required by the boundary conditions. Transition lay-

ers ($TL^{1,2}$) of size $\epsilon^{1/2}$ (measured in units of X) allow a smooth crossover from the central nonlinear regions ($CNL^{\pm}$) into the outer linear regions ($OL^{\pm}$). As shown later, the existence of a nonlinear global mode requires two wavenumber branches to meet in the core of the nonlinear regions, at a saddle point of the local nonlinear dispersion relation. An additional internal layer (SP) of size $\epsilon^{1/2}$ around this saddle point needs to be introduced in order to generate the nonlinear frequency selection criterion at arbitrary order. The selection mechanism is therefore entirely determined by the saddle point structure. Thus this inner transition layer (SP) is surrounded by nonlinear regions of finite extent ($CNL^{\pm}$) which in turn are connected through transition layers ($TL^{1,2}$) to the outer linear regions ($OL^{\pm}$) extending towards infinity.

The organization of the present paper reflects the global mode structure. The global mode problem is stated in §2 and the linear WKBJ approximations pertaining to the outer regions ($OL^{\pm}$) are recalled in §3. Corresponding nonlinear WKBJ solutions relevant to the central nonlinear regions ($CNL^{\pm}$) are derived in §4. In §5 the leading order nonlinear frequency selection criterion is obtained in the following form: *a global mode can only be constructed if two wavenumber branches meet at a saddle point in the bulk of the nonlinear regions*. The structure of the transition layers connecting linear and nonlinear regions is analyzed in §6. In closing we summarize the main conclusions and address some future developments.

2 Nonlinear Eigenvalue Problem

Throughout the study, complex scalar fluctuations $\Psi(x,t)$ around a given basic state are assumed to be governed by a nonlinear equation of the form

$$i\frac{\partial \Psi}{\partial t} = \Omega^{n\ell}\left(-i\frac{\partial}{\partial x}, |\Psi|^2, X\right)\Psi, \tag{4}$$

where $X = \epsilon x$ is a slow space variable which describes the inhomogeneities of the medium and ϵ is the WKBJ parameter introduced in (3). The operator $\Omega^{n\ell}$ is the physical space counterpart of the local nonlinear dispersion relation $\omega = \Omega^{n\ell}(k, R^2, X)$ to be defined later.

A nonlinear global mode is then defined as a time-periodic solution of eq.(4) of *real* frequency ω, satisfying vanishing boundary conditions at infinity. Thus it can be written as

$$\Psi(x,t) = \psi(x,\omega)e^{-i\omega t},$$

where the global frequency ω and the amplitude ψ are governed by the differential equation

$$\left[\omega - \Omega^{n\ell}\left(-i\frac{\partial}{\partial x}, |\psi|^2, X\right)\right]\psi = 0, \tag{5}$$

with the boundary conditions

$$\lim_{x\to\pm\infty} \psi(x,\omega) = 0. \tag{6}$$

In the particular case of the complex Ginzburg-Landau equation [39],

$$i\frac{\partial\Psi}{\partial t} = \left(\omega_0(X) + \frac{1}{2}\omega_{kk}(X)k_0(X)^2\right)\Psi + i\omega_{kk}(X)k_0(X)\frac{\partial\Psi}{\partial x} - \frac{1}{2}\omega_{kk}(X)\frac{\partial^2\Psi}{\partial x^2} + \gamma(X)|\Psi|^2\Psi, \tag{7}$$

the nonlinear dispersion operator $\Omega^{n\ell}$ may be separated into linear and nonlinear parts as

$$\Omega^{n\ell}\left(-i\frac{\partial}{\partial x}, |\Psi|^2, X\right) \equiv \Omega^{\ell}\left(-i\frac{\partial}{\partial x}, X\right) + \gamma(X)|\Psi|^2,$$

where the linear dispersion operator Ω^{ℓ} reads

$$\Omega^{\ell}\left(-i\frac{\partial}{\partial x}, X\right) \equiv \omega_0(X) + \frac{1}{2}\omega_{kk}(X)k_0(X)^2 + i\omega_{kk}(X)k_0(X)\frac{\partial}{\partial x} - \frac{1}{2}\omega_{kk}(X)\frac{\partial^2}{\partial x^2}. \tag{8}$$

The complex functions $\omega_0(X)$, $\omega_{kk}(X)$, $k_0(X)$, and $\gamma(X)$ which solely depend on the slow space variable X account for the weak inhomogeneities of the medium and their meaning is discussed in §3.

The goal of the present study is to solve the nonlinear eigenvalue problem (5,6) where the global mode amplitude ψ is $O(1)$ in an interval of finite extent. We construct such global mode solutions in the régime $\epsilon \ll 1$ and determine how the global frequencies ω_g depend on the characteristics of the "basic flow", as specified by the nonlinear dispersion relation.

Since global modes must decay at infinity, they are governed by the linearized equation for sufficiently large X. The solutions of the associated linear equation are therefore required in outer linear regions ($\mathrm{OL}^{\pm}$), as reviewed in the next section.

3 Outer Linear WKBJ Regions OL$^{\pm}$

In the present section we examine the structure of outer linear regions (OL$^{\pm}$) in fig.1 and recall the main features of the solutions of the linearized equation

$$i\frac{\partial \Psi}{\partial t} = \Omega^{\ell}\left(-i\frac{\partial}{\partial x}, X\right)\Psi, \tag{9}$$

for an arbitrary frequency ω of order unity, as studied by Chomaz *et al.* [13] and Le Dizès *et al.* [51].

Upon substituting $\partial/\partial x \to ik$ and $\partial/\partial t \to -i\omega$ in (8,9) one obtains the associated local linear dispersion relation of the Ginzburg-Landau model in the form

$$\omega = \Omega^{\ell}(k, X) \equiv \omega_0(X) + \frac{1}{2}\omega_{kk}(X)\big(k - k_0(X)\big)^2. \tag{10}$$

In order to enforce causality we assume throughout that sufficiently large wavenumbers are damped, *i.e.*, $\omega_{kk,i}(X) \equiv \mathrm{Im}[\omega_{kk}(X)] < 0$ for all X. According to (10) the frequency ω is a simple quadratic function of the complex wavenumber k. Thus there exist for each value of the frequency two linear spatial branches given by

$$k^{\ell\pm}(X, \omega) \equiv k_0(X) \pm \sqrt{2\frac{\omega - \omega_0(X)}{\omega_{kk}(X)}}. \tag{11}$$

Under the assumption $\omega_{kk,i}(X) < 0$ for all X, the square root branch in (11) can always be chosen such that $k_i^{\ell+}(X) > 0$ and $k_i^{\ell-}(X) < 0$ for large enough ω. The introduction of the functions $k_0(X)$ and $\omega_0(X)$ may now be justified: at each station X, k_0 and ω_0 denote the complex absolute wavenumber and frequency defined by $\frac{\partial \Omega^{\ell}}{\partial k}(k_0, X) = 0$, $\omega_0 = \Omega^{\ell}(k_0, X)$, as extensively discussed in [39]. In other words, $\omega_0(X)$ is a branch point of the function $k^{\ell}(X, \omega)$ in the complex ω-plane, as clearly displayed in (11).

Under the slowly varying medium hypothesis ($\epsilon \ll 1$) a solution of eq.(9) with frequency ω can be obtained in terms of WKBJ approximations [3]. The spatial behavior of the solution is described by a rapidly varying phase, corresponding to the local wavenumber, and a slowly varying envelope which, for a given value of the frequency ω, read

$$\psi^{\ell}(X, \omega) = A^{\ell}(X, \omega) \exp \frac{i}{\epsilon}\int^{X} k^{\ell}(s, \omega) ds, \tag{12}$$

where $k^{\ell}(X, \omega)$ is one of the spatial branches (11).

In classical WKBJ fashion, the envelope [1] $A^\ell(X)$ is expanded in powers of ϵ

$$A^\ell(X) \sim A_0^\ell(X) + \epsilon A_1^\ell(X) + \epsilon^2 A_2^\ell(X) + \ldots, \tag{13}$$

and the spatial derivative operator is decomposed into

$$\partial_x = ik^\ell(X) + \epsilon\partial_X. \tag{14}$$

Upon substituting (12,13,14) into the governing equation (9), one obtains

$$\omega\left(A_0^\ell + \epsilon A_1^\ell + \ldots\right) = \Omega^\ell\left(k^\ell(X) - i\epsilon\partial_X, X\right)\left(A_0^\ell + \epsilon A_1^\ell + \ldots\right). \tag{15}$$

Note that differentiation with respect to the fast variable, *i.e.*, multiplication by $ik^\ell(X)$, does not commute with the slow derivative operator ∂_X [45]. Thus $\Omega^\ell\left(k^\ell(X) - i\epsilon\partial_X\right)$ admits the expansion

$$\begin{aligned}\Omega^\ell\left(k^\ell(X) - i\epsilon\partial_X\right) &= \Omega^\ell - i\epsilon\frac{1}{2}\left(\Omega_k^\ell\partial_X + \partial_X\Omega_k^\ell\right) + O(\epsilon^2)\\ &= \Omega^\ell - i\epsilon\left(\Omega_k^\ell\partial_X + \frac{1}{2}\Omega_{kk}^\ell k_X^\ell(X)\right) + O(\epsilon^2).\end{aligned} \tag{16}$$

On the r.h.s. of these equations, Ω^ℓ and its derivatives with respect to k are evaluated at $k^\ell(X)$. In eq.(15) the slow derivative operator ∂_X only applies to the wavefunction, hence to $k^\ell(X)$, but *not* to the second argument X of $\Omega^\ell(k, X)$.

At lowest order, eq.(15) reduces to the dispersion relation (10), which yields the local wavenumber $k^\ell(X)$ in terms of ω, as given by (11).

At order ϵ, we obtain

$$\left[\omega - \Omega^\ell\left(k^\ell(X), X\right)\right] A_1^\ell = -i\Omega_k^\ell(X)\frac{dA_0^\ell}{dX} - \frac{i}{2}\Omega_{kk}^\ell(X)k_X^\ell(X)A_0^\ell,$$

with the notations

$$\Omega_k^\ell(X) = \frac{\partial\Omega^\ell}{\partial k}\left(k^\ell(X), X\right) \quad \text{and} \quad \Omega_{kk}^\ell(X) = \frac{\partial^2\Omega^\ell}{\partial k^2}\left(k^\ell(X), X\right).$$

By invoking the local dispersion relation (10), one obtains the obvious solvability condition for A_0^ℓ

$$\frac{dA_0^\ell}{dX} = -\frac{1}{2}k_X^\ell(X)\frac{\Omega_{kk}^\ell(X)}{\Omega_k^\ell(X)}A_0^\ell(X).$$

[1] For simplicity we no longer explicitly mention the frequency dependence.

Thus, at first order, the solution of the linearized equation reads

$$\psi^\ell(X) \sim A_0^\ell(X_1) \exp\left(-\frac{1}{2}\int_{X_1}^{X} k_X^\ell(s)\frac{\Omega_{kk}^\ell(s)}{\Omega_k^\ell(s)}ds\right)\exp\left(\frac{i}{\epsilon}\int_{X_1}^{X} k^\ell(s)ds\right), \quad (17)$$

where X_1 is some arbitrarily specified reference point.

The linear Ginzburg-Landau equation admits two spatial branches $k^{\ell\pm}(X)$ given by (11); thus eq.(17) yields two WKBJ approximations $\psi^{\ell\pm}(X)$ for two linearly independent solutions of eq.(9). Let us assume that $k_i^{\ell+}(X) > 0$ and $k_i^{\ell-}(X) < 0$ for sufficiently large $|X|$ (for a discussion of the relationship between this assumption and causality see [51]). Under this assumption the WKBJ approximation $\psi^{\ell-}(X)$ is subdominant when $X \to -\infty$, *i.e.*, exponentially small with respect to $\psi^{\ell+}(X)$; similarly the solution $\psi^{\ell+}(X)$ becomes subdominant for $X \to +\infty$. Boundary conditions (6) require the choice of $\psi^{\ell\pm}(X)$ for $X \to \pm\infty$. A global mode solution is thus solely composed of the branch $k^{\ell-}$ for $X \to -\infty$ and of the branch $k^{\ell+}$ for $X \to +\infty$. In the following sections a nonlinear solution is derived which allows a smooth crossover from one linear branch to the other as X varies from $-\infty$ to $+\infty$.

4 Central Nonlinear WKBJ Regions CNL$^\pm$

In this section a *fully nonlinear* solution of equation (4) is constructed in the central regions (CNL$^\pm$) of fig.1 by means of the nonlinear dispersion relation, for an arbitrary frequency of order unity.

Let us first consider in the same notations as eq.(4) the *homogenous* nonlinear equation with *constant* coefficients

$$i\frac{\partial \Psi}{\partial t} = \Omega^{n\ell}\left(-i\frac{\partial}{\partial x}, |\Psi|^2\right)\Psi.$$

This equation admits nonlinear travelling wave Stokes solutions of the form

$$\Psi(x,t) = Re^{i(kx-\omega t)}, \quad (18)$$

where the amplitude R, wavenumber k, and frequency ω are *real* parameters bound by the *nonlinear* dispersion relation

$$\omega = \Omega^{n\ell}(k, R^2). \quad (19)$$

This complex equation completely defines the family of solutions (18). It is also convenient to introduce a *reduced nonlinear dispersion relation* as follows.

Taking the imaginary part of complex equation (19) shows that the amplitude R^2 is slaved to the wavenumber k and is implicitly given by

$$0 = \Omega_i^{n\ell}(k, R^2).$$

Replacing the amplitude R^2 as a function of k in the real part of (19),

$$\omega = \Omega_r^{n\ell}(k, R^2),$$

yields the reduced nonlinear dispersion relation in the form

$$\omega = \Omega^{NL}(k) \equiv \Omega_r^{n\ell}\left(k, R^2(k)\right).$$

This reduced form clearly demonstrates that Stokes travelling waves (18) indeed constitute a one-parameter family of finite amplitude solutions, of real parameter k.

In the context of the complex Ginzburg-Landau model (7), the *complete* nonlinear dispersion relation reads

$$\omega = \Omega^{n\ell}(k, R^2) \equiv \omega_0 + \frac{1}{2}\omega_{kk}(k - k_0)^2 + \gamma R^2 = \Omega^{\ell}(k) + \gamma R^2, \tag{20}$$

and the reduced dispersion relation may explicitely be determined by following the procedure outlined above. Extracting R^2 from the imaginary part of (20), one finds

$$R^2 = \frac{\mathrm{Im}[\Omega^{\ell}(k)]}{\mathrm{Im}[\gamma^{\star}]}, \tag{21}$$

and by substitution into the real part of (20), one readily obtains the reduced nonlinear dispersion relation

$$\omega = \Omega^{NL}(k) = \frac{\mathrm{Im}[\gamma^{\star}\Omega^{\ell}(k)]}{\mathrm{Im}[\gamma^{\star}]}. \tag{22}$$

Since (22) is quadratic in k, to each frequency ω are associated, under suitable conditions, two nonlinear spatial branches $k^{n\ell^{\pm}}(\omega)$, and, via (21), two amplitudes $\mathcal{R}^{2^{\pm}}(\omega)$. Thus the complete nonlinear dispersion relation (20) is seen to possess two pairs of solutions

$$(k, R^2) = \left(k^{n\ell^{\pm}}(\omega), \mathcal{R}^{2^{\pm}}(\omega)\right).$$

Such pairs of solutions only exist if (20) can be solved for *real* k and *real non-negative* R^2. For given coefficients in (20) these conditions correspond to a range of allowable frequencies.

In a *weakly inhomogenous* medium where the coefficients of the nonlinear equation are now functions of the slow space variable X (equations (4,7)), a *local* nonlinear dispersion relation may still be derived of the form

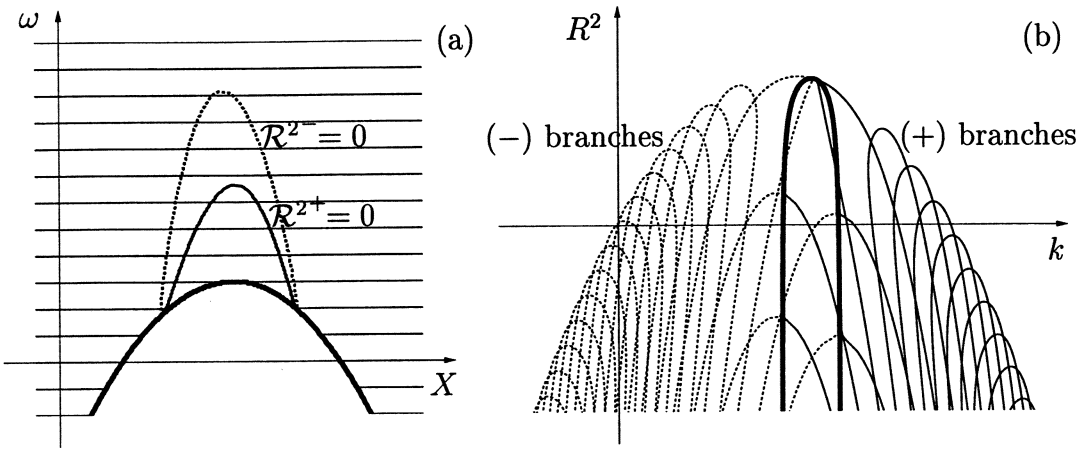


Fig. 2. Nonlinear spatial branches in the X-ω and k-R^2 planes. In (a) the horizontal lines ω = const. indicate in the X-ω plane the allowable domain, delineated by the bold critical curve, where the nonlinear dispersion relation (23) admits real solutions in the k-R^2 plane sketched in (b). Each of the lines ω = const. is mapped into two spatial branches $\left(k^{n\ell\pm}(X), \mathcal{R}^{2\pm}(X)\right)$ in the k-R^2 plane: the (+) branches are represented by solid curves, the (−) branches by dotted curves. For frequencies such that the line ω = const. intersects the boundary of the allowable domain (bold curve in (a)), the two branches in the k-R^2 plane meet at the corresponding image critical curve (bold curve in (b)). The subregions of the allowable domain corresponding to $R^2 > 0$ are delimited in (a) by the curves $\mathcal{R}^{2+}(X,\omega) = 0$ (solid) and $\mathcal{R}^{2-}(X,\omega) = 0$ (dotted).

$$\omega = \Omega^{n\ell}(k, R^2, X) \equiv \omega_0(X) + \frac{1}{2}\omega_{kk}(X)\left(k - k_0(X)\right)^2 + \gamma(X)R^2 \qquad (23)$$
$$= \Omega^{\ell}(k, X) + \gamma(X)R^2,$$

and the corresponding local reduced nonlinear dispersion relation may be formally expressed as

$$\omega = \Omega^{NL}(k, X) \equiv \frac{\mathrm{Im}[\gamma^\star(X)\Omega^{\ell}(k, X)]}{\mathrm{Im}[\gamma^\star(X)]}. \qquad (24)$$

Local wavenumber and amplitude are obtained in the same way as in the homogenous case; they are real functions of the frequency and the slow space variable:

$$(k, R^2) = \left(k^{n\ell\pm}(X,\omega), \mathcal{R}^{2\pm}(X,\omega)\right), \qquad (25)$$

solutions of (23) and (24).

Let us now examine the properties of the double-valued mapping between the X-ω and k-R^2 planes defined by solution pairs (25). The X-ω plane separates into an allowable region where two *real* solution pairs (25) satisfy the local nonlinear dispersion relation (23) and a region where no such real solutions are obtained (fig.2-a). For given X, real wavenumber solutions of the quadratic

equation (24) are found to exist when $\omega \to +\infty(-\infty)$ if $\omega_{kk,r} - \omega_{kk,i}\gamma_r/\gamma_i > 0(< 0)$. Let us assume that $\omega_{kk,r}(X) - \omega_{kk,i}(X)\gamma_r(X)/\gamma_i(X) > 0$ for all X. As ω decreases for a given X, the two pairs merge at a critical value of ω when the discriminant of the quadratic equation (24) vanishes. The set of such points in the X-ω plane defines the critical line (bold curve of fig.2-a), *i.e.*, the boundary of the allowable domain indicated by the hatched region of fig.2-a. Below this critical line the nonlinear dispersion relations (23) or (24) admit no real solutions. Each point (X, ω) of the allowable domain then maps into two points in the k-R^2 plane (fig.2-b) through the mapping functions (25). A solution of real uniform frequency is in fact represented in the X-ω plane by a straight horizontal line $\omega = \text{const.}$ As X varies for a given ω, solutions of eq.(25) move along two distinct branches $\left(k^{n\ell^+}(X), \mathcal{R}^{2^+}(X)\right)$ and $\left(k^{n\ell^-}(X), \mathcal{R}^{2^-}(X)\right)$ in the k-R^2 plane, as indicated by the continuous and dashed curves in fig.2-b. If the line $\omega = \text{const.}$ is high enough and does not meet the critical line delimiting the allowable domain in the X-ω plane, the two corresponding branches in the k-R^2 plane do not intersect; if by contrast the horizontal line $\omega = \text{const.}$ is not entirely contained in the allowable hatched domain, spatial branches in the k-R^2 plane are not defined for the portion of the line situated outside the allowable domain. In fact, upon hitting the critical line in the X-ω plane, $(+)$ and $(-)$ branches in the k-R^2 plane meet along the image of the critical line (bold curve of fig.2-b) and cease to exist.

Note also that each branch of (25) has physical meaning only if $R^2 \geq 0$. Thus the subregions of the allowable domain, where meaningful nonlinear solutions are obtained, are further restricted to $\mathcal{R}^{2^\pm}(X, \omega) \geq 0$. These regions are located within the curves labelled $\mathcal{R}^{2^+} = 0$ and $\mathcal{R}^{2^-} = 0$ on fig.2-a. If one assumes $\gamma_i(X) < 0$ uniformly in X (locally supercritical behavior) the condition $\mathcal{R}^{2^\pm}(X, \omega) \geq 0$ corresponds to linearly unstable wavenumbers $k^{n\ell^\pm}(X, \omega)$, as seen by inspection of (21). Elsewhere in the X-ω plane, $\mathcal{R}^{2^\pm}(X, \omega) < 0$, nonlinear solutions pertaining to $(+)$ or $(-)$ branches do not exist and only linear solutions are allowed.

As in the outer linear regions, the spatial distribution is taken to be a rapidly oscillating wave modulated by a slowly varying envelope

$$\psi^{n\ell}(X) = A^{n\ell}(X) \exp \frac{i}{\epsilon} \int^X k^{n\ell}(s) ds. \tag{26}$$

Upon expanding the envelope in powers of ϵ

$$A^{n\ell}(X) \sim A_0^{n\ell}(X) + \epsilon A_1^{n\ell}(X) + \epsilon^2 A_2^{n\ell}(X) + \ldots,$$

interpreting the spatial derivatives as

$$\partial_x = ik^{n\ell}(X) + \epsilon \partial_X,$$

and substituting these expansions into eq.(4), one readily obtains the nonlinear counterpart of (15), *i.e.*,

$$\omega\left(A_0^{n\ell}+\epsilon A_1^{n\ell}+\ldots\right)=\Omega^{n\ell}\Big(k^{n\ell}(X)-i\epsilon\partial_X\,,|A_0^{n\ell}+\epsilon A_1^{n\ell}+\ldots|^2,X\Big)\Big(A_0^{n\ell}+\epsilon A_1^{n\ell}+\ldots\Big). \tag{27}$$

At lowest order, we recover the local nonlinear dispersion relation (23), *i.e.*,

$$\omega=\Omega^{n\ell}\Big(k^{n\ell}(X),|A_0^{n\ell}(X)|^2,X\Big), \tag{28}$$

which determines the local wavenumber $k^{n\ell}(X)$ and the leading order amplitude $|A_0^{n\ell}(X)|^2=\mathcal{R}^2(X)$ as functions of the slow space variable X for a given frequency ω. Note that the phase $\theta_0(X)$ of $A_0^{n\ell}(X)$ is as yet undetermined.

After expanding the operator $\Omega^{n\ell}$ in powers of ϵ in the same fashion as in (16), the ϵ terms of (27) yield

$$\left(\omega-\Omega^{n\ell}\right)A_1^{n\ell}=-i\Omega_k^{n\ell}\frac{dA_0^{n\ell}}{dX}-\frac{i}{2}\Omega_{kk}^{n\ell}k_X^{n\ell}A_0^{n\ell}+\Omega_{R^2}^{n\ell}\left(A_0^{n\ell\star}A_1^{n\ell}+A_1^{n\ell\star}A_0^{n\ell}\right)A_0^{n\ell},$$

where $\Omega^{n\ell}$ and its partial derivatives are evaluated at $\Big(k^{n\ell}(X),\mathcal{R}^2(X),X\Big)$. In the following, $\Omega^{n\ell}(X)$ stands for $\Omega^{n\ell}\Big(k^{n\ell}(X),\mathcal{R}^2(X),X\Big)$.

Upon exploiting the identity $\omega=\Omega^{n\ell}(X)$, the fact that $\frac{dA_0^{n\ell}}{dX}=\left(i\frac{d\theta_0}{dX}+\frac{\mathcal{R}_X^2}{2\mathcal{R}^2}\right)A_0^{n\ell}$, and the real nature of $A_0^{n\ell\star}A_1^{n\ell}+A_1^{n\ell\star}A_0^{n\ell}$, we readily obtain a solvability condition for $\theta_0(X)$ of the form

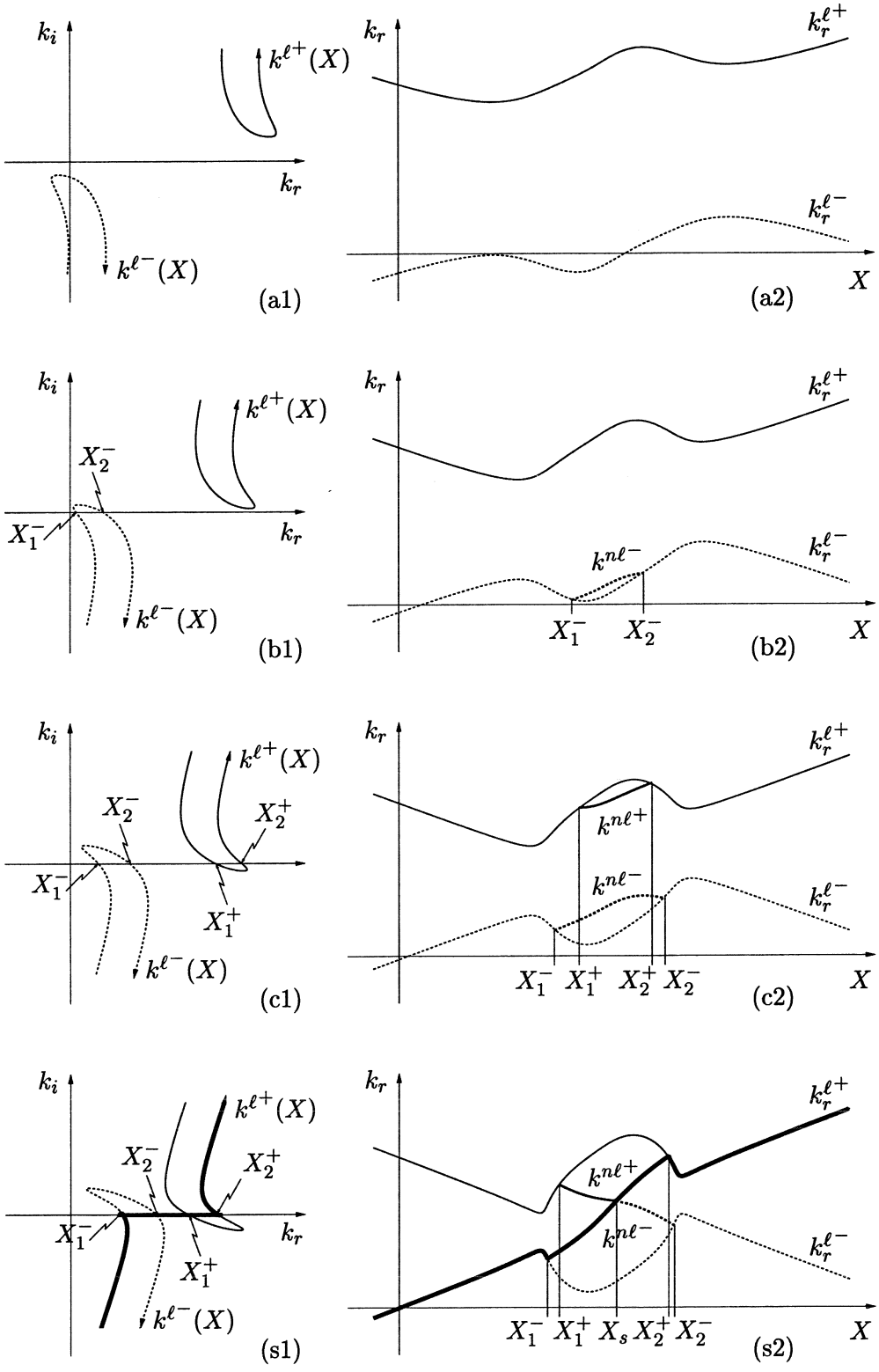
$$\frac{d\theta_0}{dX}=\frac{1}{2}\frac{\mathrm{Re}[\Omega_{R^2}^{n\ell}(X)^\star\Omega_k^{n\ell}(X)]}{\mathrm{Im}[\Omega_{R^2}^{n\ell}(X)^\star\Omega_k^{n\ell}(X)]}\frac{\mathcal{R}_X^2(X)}{\mathcal{R}^2(X)}-\frac{1}{2}\frac{\mathrm{Re}[\Omega_{R^2}^{n\ell}(X)^\star\Omega_{kk}^{n\ell}(X)]}{\mathrm{Im}[\Omega_{R^2}^{n\ell}(X)^\star\Omega_k^{n\ell}(X)]}k_X^{n\ell}(X). \tag{29}$$

Equations (26,28,29) entirely specify the nonlinear solution at leading order.

5 Saddle Point Region SP: Leading-Order Nonlinear Frequency Selection Criterion

In this section the global frequency ω_g is obtained at lowest order by matching the nonlinear spatial branches $k^{n\ell+}(X)$ and $k^{n\ell-}(X)$.

Solving the linear dispersion relation (10) yields local complex wavenumbers $k^{\ell\pm}(X,\omega)$ as functions of the frequency at any location. By contrast, the nonlinear dispersion relation (23) admits solution pairs $\Big(k^{n\ell\pm}(X,\omega),\mathcal{R}^{2\pm}(X,\omega)\Big)$ only in the allowable region of the X-ω plane. Moreover only nonlinear solutions with $\mathcal{R}^{2\pm}(X,\omega)>0$ have physical meaning.


k_i
k_r
$k^{\ell+}(X)$
$k^{\ell-}(X)$
(a1)
k_r
$k_r^{\ell+}$
$k_r^{\ell-}$
X
(a2)
X_2^-
X_1^-
(b1)
$k^{n\ell-}$
X_1^- X_2^-
(b2)
X_2^+
X_1^+
(c1)
$k^{n\ell+}$
X_1^- X_1^+ X_2^+ X_2^-
(c2)
X_s
(s1)
(s2)

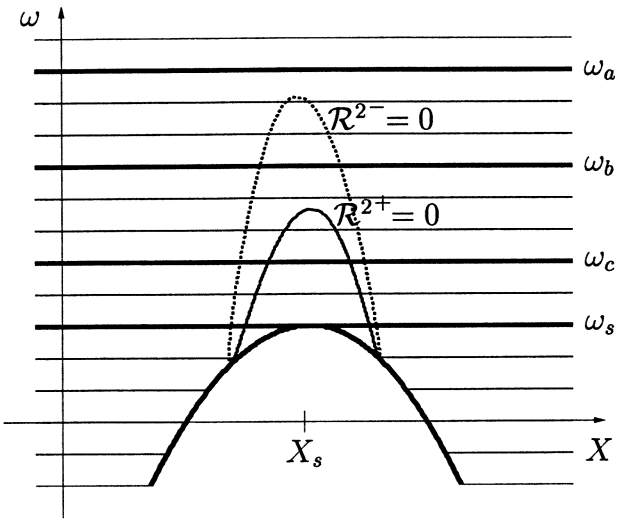


Fig. 3. Relationship between linear and nonlinear spatial branches for different values of the frequency. For a large frequency ω_a, the line $\omega = \omega_a$ does not intersect the regions $\mathcal{R}^{2\pm}(X,\omega) \geq 0$ in the X-ω plane, the linear branches $k^{\ell\pm}(X)$ do not cross the k_r-axis in the complex k-plane (a1), and nonlinear branches do not exist; the real parts $k_r^{\ell\pm}(X)$ are represented in (a2). For ω_b such that the line $\omega = \omega_b$ intersects the region $\mathcal{R}^{2^-}(X,\omega) \geq 0$ in the X-ω plane, the branch $k^{\ell^-}(X)$ crosses the k_r-axis for $X = X_1^-$ and $X = X_2^-$ in (b1); as a result, the nonlinear $k^{n\ell^-}(X)$ exists for $X_1^- < X < X_2^-$ and is connected to $k_r^{\ell^-}(X)$ in (b2). The line $\omega = \omega_c$ intersects both regions $\mathcal{R}^{2\pm}(X,\omega)$, thus both linear branches cross the k_r-axis in (c1); both nonlinear branches exist in the ranges $X_1^\pm < X < X_2^\pm$ respectively (c2). When the frequency equals ω_s such that the line $\omega = \omega_s$ is tangent to the boundary of the allowable domain at X_s in the X-ω plane, the nonlinear branches meet at X_s (s2), and the crossover between branches is possible; the global spatial branch selected by the global mode is indicated in bold in (s1,2).

The relationship between linear and nonlinear spatial branches as a function of frequency is illustrated in fig.3. In the X-ω plane a solution of uniform frequency is represented by the line $\omega = \text{const}$. This line is mapped, in the complex k-plane, into two linear spatial branches $k^{\ell\pm}(X)$ defined in (11).

Let us recall that, for large enough frequencies $\omega = \omega_a$ (see X-ω plane of fig.3), the linear branches do not cross the k_r-axis in the complex k-plane as long as $\omega_{kk,i}(X) < 0$ for all X (fig.3-a1), and that $k^{\ell\pm}(X)$ denotes the linear branch located in the $k_i > 0$ and $k_i < 0$ half-planes respectively. Corresponding variations of $k_r^{\ell\pm}$ with X are displayed on fig.3-a2.

When the frequency is decreased to $\omega = \omega_b$ (see X-ω plane of fig.3), the linear branches move about in the complex k-plane. The branch $k^{\ell\pm}(X)$ crosses the k_r-axis (fig.3-b1) whenever the frequency is such that the line $\omega = \omega_b$ intersects, in the X-ω plane, the region $\mathcal{R}^{2\pm}(X,\omega) > 0$. Indeed a local solution of the nonlinear dispersion relation with $R^2 = 0$ is precisely a solution of

the linear dispersion relation, and this linear solution happens to have a *real* wavenumber. Thus at locations where $R^2 = 0$, linear and nonlinear branches meet. Let us denote by $k^{n\ell^\pm}(X,\omega)$ the nonlinear branches that match to the corresponding linear branches $k^{\ell^\pm}(X,\omega)$. In the specific case of fig.3-b, the line $\omega = \omega_b$ is partly contained within the region $\mathcal{R}^{2^-} > 0$ of the X-ω plane and, as a result, the nonlinear branch $k^{n\ell^-}$ is seen to take over from $k_r^{\ell^-}$ in a finite X-subinterval.

For frequencies such that the line $\omega = \omega_c$ in the X-ω plane intersects both regions $\mathcal{R}^{2^\pm}(X,\omega) > 0$, both linear branches cross the k_r-axis (fig.3-c1) and are connected to the corresponding nonlinear branches (fig.3-c2). Let $X_1^\pm(\omega)$ and $X_2^\pm(\omega)$ be the locations where $\mathcal{R}^{2^\pm}(X,\omega) = 0$, whereby $k^{\ell^\pm}(X_{1,2}^\pm) = k^{n\ell^\pm}(X_{1,2}^\pm)$. A nonlinear solution with local wavenumber $k^{n\ell^\pm}(X,\omega)$ then exists in the range $X_1^\pm < X < X_2^\pm$. The locations $X_{1,2}^\pm$ depend on the frequency, and in §6 we show that, for any frequency, the linear and nonlinear solutions can be matched at all orders in ϵ through transition layers centered around $X_{1,2}^\pm(\omega)$. Recall that boundary conditions (6) require keeping only the linear branch $k^{\ell^\pm}(X)$ in the regions $X \to \pm\infty$ respectively. At the locations X_1^- and X_2^+ where the linear branches k^{ℓ^-} and k^{ℓ^+} cross the k_r-axis they change over to the corresponding nonlinear branches $k^{n\ell^-}$ and $k^{n\ell^+}$. Thus the nonlinear region is delimited by X_1^- (where $k^{\ell^-} = k^{n\ell^-}$) and X_2^+ (where $k^{n\ell^+} = k^{\ell^+}$), and a continuous global mode solution must necessarily connect both these nonlinear branches.

A smooth crossover between the nonlinear branches $k^{n\ell^-}$ and $k^{n\ell^+}$ (fig.3-s2) can only be achieved for frequencies such that the line $\omega = $ const. meets the critical curve limiting the allowable domain in the X-ω plane. Furthermore, the line $\omega = $ const. has to be entirely contained within the allowable domain. Thus, *the leading order global frequency ω_s is obtained by requiring that the line $\omega = \omega_s$ be tangent to the allowable domain in the X-ω plane at a point X_s.* Since, to each point in the allowable domain of the X-ω plane, correspond two pairs $(k^{n\ell^+}, \mathcal{R}^{2^+})$ and $(k^{n\ell^-}, \mathcal{R}^{2^-})$, the allowable domain may be considered as the superposition of two sheets respectively labelled (+) and (−) which necessarily join along the critical curve where $(k^{n\ell^+}, \mathcal{R}^{2^+}) = (k^{n\ell^-}, \mathcal{R}^{2^-})$. A plane $\omega = $ const. cuts the surface made up of the two sheets along two lines, one on each sheet, which correspond to the (+) and (−) spatial branches respectively. Passing from one sheet to the other on such a line is possible only for $\omega = \omega_s$. The additional condition that the line $\omega = \omega_s$ be entirely contained in the allowable domain guarantees that the surface made up of the two sheets exhibits a saddle point when cut by the plane $\omega = \omega_s$. Thus, *at leading order, the global frequency ω_g is given by a saddle point of the nonlinear dispersion relation.* Moreover nonlinear global modes only exist if the saddle point is located in a region where the wavenumber $k_s \equiv k^{n\ell^+}(X_s,\omega_s) = k^{n\ell^-}(X_s,\omega_s)$ is linearly unstable, *i.e.*, $R_s^2 \equiv \mathcal{R}^{2^+}(X_s,\omega_s) = \mathcal{R}^{2^-}(X_s,\omega_s) > 0$.

An explicit condition for the existence of a saddle point may be derived from the local reduced nonlinear dispersion relation (24)

$$\omega = \Omega^{NL}(k, X).$$

This relation defines a surface in (ω, k, X) space which bears the same features as the complete nonlinear dispersion relation (23). For a given frequency ω, the spatial branches $k^{n\ell\pm}(X, \omega)$ are obtained as the intersection of this surface and the plane $\omega = \text{const}$. The condition that the branches $k^{n\ell\pm}(X)$ be connected, requires that the global frequency be given by a saddle point of the surface $\omega = \Omega^{NL}(k, X)$. Thus, the global frequency ω_g is obtained, at leading order in the WKBJ approximation, for a saddle point of the reduced nonlinear dispersion relation, *i.e.*,

$$\omega_g \sim \omega_s = \Omega^{NL}(k_s, X_s), \tag{30}$$

where the pair (k_s, X_s) satisfies

$$\frac{\partial \Omega^{NL}}{\partial k}(k_s, X_s) = \frac{\partial \Omega^{NL}}{\partial X}(k_s, X_s) = 0. \tag{31}$$

The additional condition [2]

$$\left(\Omega^{NL}_{kX,s}\right)^2 - \Omega^{NL}_{kk,s}\Omega^{NL}_{XX,s} > 0 \tag{32}$$

guarantees that (ω_s, k_s, X_s) is actually a saddle point and not a local extremum.

Criterion (30,31) may also be expressed in terms of the complete dispersion relation (23)

$$\omega = \Omega^{n\ell}(k, R^2, X).$$

Bearing in mind that

$$\Omega^{NL}(k, X) = \Omega^{n\ell}_r\left(k, R^2(k, X), X\right),$$

where $R^2(k, X)$ is implicitely defined by

$$\Omega^{n\ell}_i\left(k, R^2(k, X), X\right) = 0,$$

one may relate the derivatives of Ω^{NL} to those of $\Omega^{n\ell}$. After elementary calculations, one finds that criterion (31) takes the alternate form

$$\mathrm{Im}[(\Omega^{n\ell}_{R^2,s})^\star \Omega^{n\ell}_{k,s}] = \mathrm{Im}[(\Omega^{n\ell}_{R^2,s})^\star \Omega^{n\ell}_{X,s}] = 0,$$

[2] Throughout, subscript (s) denotes evaluation at the saddle point (k_s, R^2_s, X_s).

i.e., the derivatives of the complex function $\Omega^{n\ell}$ with respect to each of its arguments have the same phase. Thus the leading order global frequency ω_s and the associated quantities (k_s, R_s^2, X_s) are equivalently determined by

$$\omega_s = \Omega^{n\ell}(k_s, R_s^2, X_s) \quad \text{and} \quad \operatorname{Arg}\Omega^{n\ell}_{k,s} = \operatorname{Arg}\Omega^{n\ell}_{R^2,s} = \operatorname{Arg}\Omega^{n\ell}_{X,s}.$$

Additional condition (32) may also be expressed in terms of $\Omega^{n\ell}$ after cumbersome but straightforward calculations.

The essential result of the present section is summarized by the saddle point conditions (30,31) applicable to the reduced nonlinear dispersion relation $\omega = \Omega^{NL}(k, X)$: to leading order, the *nonlinear* global frequency ω_s satisfies a criterion that is formally identical to its *linear* counterpart (1,2). However it should be emphasized that the linear criterion involves *complex* values of the wavenumber, frequency and spatial coordinate, whereas the nonlinear criterion only involves purely real values for these quantities.

It is possible to compute higher order corrections to the global frequency ω_g by a detailed analysis of the saddle point region (SP). As in the case of linear global modes with a double turning point [13,39,51,59], it is found that its characteristic thickness is $O(\epsilon^{1/2})$. Matching between the SP layer and the surrounding CNL$^{\pm}$ regions leads to an expansion of the form

$$\omega_g \sim \omega_s + \epsilon\,\omega_{1,n}\,,$$

where the $O(\epsilon)$ frequency correction term $\omega_{1,n}$ is parametrized by a non-negative integer n. Detailed calculations of this quantified set of fully nonlinear global modes are postponed to a future publication.

6 Spatial Structure of Transition Layers TL^{1,2}

At the locations X_1^- and X_2^+ where the amplitude of nonlinear WKBJ approximations vanishes, nonlinearities become weak, and, in the semi-infinite regions (OL$^{\pm}$) extending towards $X = \pm\infty$, the solution is described by linear WKBJ approximations. The structure of the transition layer connecting the finite amplitude nonlinear solution in (CNL$^{\pm}$) to exponentially decaying linear solutions in (OL$^{\pm}$) is analyzed in this section.

It is essential to bear in mind that this transition layer plays no rôle in the global frequency selection mechanism which solely depends on the local nonlinear dispersion relation at the saddle point X_s, in the core of the nonlinear region. The locations of the transition layers indeed depend on the frequency ω_g but the linear and nonlinear solutions can be matched for any frequency. For this reason matching is carried out for an arbitrary fixed real frequency ω.

With the definitions of §5, the linear branch $k^{\ell^-}(X)$ meets the nonlinear branch $k^{n\ell^-}(X)$ at $X = X_1^-$. Let $k_1 \equiv k^{\ell^-}(X_1^-) = k^{n\ell^-}(X_1^-)$ be the local real wavenumber at[3] X_1. For $X < X_1$ the global mode is approximated by the linear WKBJ ψ^ℓ approximation (17) and for $X > X_1$ by the nonlinear WKBJ $\psi^{n\ell}$ approximation (26). None of these expressions are uniformly valid in a full neighborhood of X_1. An inner solution must then be constructed in an inner layer TL[1] around X_1 to allow a smooth transition between both outer WKBJ approximations.

The form of the inner solution is obtained from the behavior of the outer solutions as $X \to X_1$. Near X_1 the nonlinear solution (26) expands into

$$\psi^{n\ell}(X) \sim (X - X_1)^{1/2} \sqrt{\mathcal{R}^2_{X,1}} e^{i\theta_0(X)} e^{ik_1 x} \exp\left(\frac{i}{2\epsilon} k^{n\ell}_{X,1} (X - X_1)^2\right), \tag{33}$$

with[4]

$$\mathcal{R}^2_{X,1} = -\frac{\mathrm{Im}[(\Omega^{n\ell}_{k,1})^\star \Omega^{n\ell}_{X,1}]}{\mathrm{Im}[(\Omega^{n\ell}_{k,1})^\star \Omega^{n\ell}_{R^2,1}]} \quad \text{and} \quad k^{n\ell}_{X,1} = -\frac{\mathrm{Im}[(\Omega^{n\ell}_{R^2,1})^\star \Omega^{n\ell}_{X,1}]}{\mathrm{Im}[(\Omega^{n\ell}_{R^2,1})^\star \Omega^{n\ell}_{k,1}]}, \tag{34}$$

and eq.(29) shows that

$$\theta_0(X) \sim \frac{1}{2}\Theta_0 \ln(X - X_1) + \text{const.} \quad \text{with} \quad \Theta_0 = \frac{\mathrm{Re}[(\Omega^{n\ell}_{R^2,1})^\star \Omega^{n\ell}_{k,1}]}{\mathrm{Im}[(\Omega^{n\ell}_{R^2,1})^\star \Omega^{n\ell}_{k,1}]}; \tag{35}$$

while the linear solution displays the following asymptotic behavior

$$\psi^\ell(X) \sim A^\ell_0(X_1) e^{ik_1 x} \exp\left(\frac{i}{2\epsilon} k^\ell_{X,1} (X - X_1)^2\right), \tag{36}$$

with

$$k^\ell_{X,1} = -\frac{\Omega^\ell_{X,1}}{\Omega^\ell_{k,1}}.$$

The expansion of the outer solutions (33) and (36) shows that the inner solution proceeds in the form

$$\tilde{\psi}(\tilde{X}) \sim \epsilon^{1/4} \left(\tilde{A}_0(\tilde{X}) + \epsilon^{1/2} \tilde{A}_{1/2}(\tilde{X}) + \ldots\right) e^{ik_1 x}, \tag{37}$$

where $\tilde{X} = (X - X_1)/\epsilon^{1/2}$ is the inner local space variable in the TL[1] layer.

From the governing equation for the inner solution $\tilde{\psi}$ in the transition layer

[3] For simplicity we drop from now on the superscript $(-)$.

[4] Subscript (1) always denotes evaluation at $k = k_1$, $R^2_1 = 0$, $X = X_1$. Note that $\Omega^{n\ell}_1 = \Omega^\ell_1$ because $\mathcal{R}^2(X_1) = 0$.

$$\omega\left(\tilde{A}_0+\epsilon^{\frac{1}{2}}\tilde{A}_{\frac{1}{2}}+\ldots\right)=\Omega^{n\ell}\Big(k_1-i\epsilon^{\frac{1}{2}}\partial_{\tilde{X}},\epsilon^{\frac{1}{2}}|\tilde{A}_0+\epsilon^{\frac{1}{2}}\tilde{A}_{\frac{1}{2}}+\ldots|^2,X_1+\epsilon^{\frac{1}{2}}\tilde{X}\Big)\left(\tilde{A}_0+\epsilon^{\frac{1}{2}}\tilde{A}_{\frac{1}{2}}+\ldots\right) \quad (38)$$

we recover at lowest order

$$\omega=\Omega^{n\ell}(k_1,0,X_1)=\Omega^{\ell}(k_1,X_1). \quad (39)$$

At order $\epsilon^{1/2}$ equation (38) reduces to

$$\left(\omega-\Omega_1^{\ell}\right)\tilde{A}_{1/2}=-i\Omega_{k,1}^{n\ell}\frac{d\tilde{A}_0}{d\tilde{X}}+\Omega_{R^2,1}^{n\ell}|\tilde{A}_0|^2\tilde{A}_0+\Omega_{X,1}^{n\ell}\tilde{X}\tilde{A}_0.$$

Bearing in mind (39), this leads to a solvability condition for $\tilde{A}_0$

$$i\Omega_{k,1}^{n\ell}\frac{d\tilde{A}_0}{d\tilde{X}}=\left(\Omega_{X,1}^{n\ell}\tilde{X}+\Omega_{R^2,1}^{n\ell}|\tilde{A}_0|^2\right)\tilde{A}_0. \quad (40)$$

This equation is of the form

$$\frac{d\tilde{A}_0}{d\tilde{X}}=\left((a_r+ia_i)\tilde{X}+(b_r+ib_i)|\tilde{A}_0|^2\right)\tilde{A}_0, \quad (41)$$

and admits the solution

$$\tilde{A}_0(\tilde{X})=\frac{\tilde{A}_0(0)\exp\left[\frac{a_r+ia_i}{2}\tilde{X}^2-\frac{i}{2}\frac{b_i}{b_r}\ln\left(1-2b_r|\tilde{A}_0(0)|^2\int_0^{\tilde{X}}e^{a_ru^2}du\right)\right]}{\sqrt{1-2b_r|\tilde{A}_0(0)|^2\int_0^{\tilde{X}}e^{a_ru^2}du}}. \quad (42)$$

The inner solution $\tilde{\psi}$ in the TL^1 layer has to be matched for $\tilde{X}\to\pm\infty$ with the outer solutions $\psi^{n\ell}$ and ψ^{ℓ} in the CNL^- and OL^- regions respectively. The square root behavior of $\psi^{n\ell}$ in (33) requires that $\tilde{A}_0(\tilde{X})=O(\tilde{X}^{1/2})$ as $\tilde{X}\to+\infty$. This implies that

$$2b_r|\tilde{A}_0(0)|^2\int_0^{\infty}e^{a_ru^2}du=1;\quad\text{or}\quad|\tilde{A}_0(0)|^2=\frac{1}{b_r}\sqrt{\frac{-a_r}{\pi}}.$$

With this value for $|\tilde{A}_0(0)|$ the inner solution (42) admits for $\tilde{X}\to+\infty$ the asymptotic expansion

$$\tilde{A}_0(\tilde{X})\sim\sqrt{-\frac{a_r}{b_r}\tilde{X}}\exp\frac{i}{2}\left[\left(a_i-\frac{b_i}{b_r}a_r\right)\tilde{X}^2+\frac{b_i}{b_r}\left(\ln\tilde{X}+\text{const.}\right)\right]. \quad (43)$$

Comparison of the coefficients in (40) and (41), and use of (34,35) leads to

$$-\frac{a_r}{b_r}=\mathcal{R}_{X,1}^2,\quad a_i-\frac{b_i}{b_r}a_r=k_{X,1}^{n\ell}\quad\text{and}\quad\frac{b_i}{b_r}=\Theta_0.$$

Thus the choice of

$$\tilde{A}_0(0) = \left(\frac{-a_r}{\pi b_r^2}\right)^{1/4}$$

completely matches, at leading order, the inner solution $\tilde{\psi}$ given by (37) and (42) with the outer nonlinear solution $\psi^{n\ell}$ in the limit (33).

For this value of $\tilde{A}_0(0)$ the asymptotic behavior of the inner solution (42) as $\tilde{X} \to -\infty$ is

$$\tilde{A}_0(\tilde{X}) \sim \frac{\tilde{A}_0(0)}{\sqrt{2}} \exp\left(\frac{1}{2}(a_r + ia_i)\tilde{X}^2 + i\,\text{const.}\right).$$

As $a_r + ia_i = ik_{X,1}^{\ell}$, the inner solution $\tilde{\psi}$ matches the outer linear WKBJ approximation ψ^{ℓ} given by (36) as long as

$$|A_0^{\ell}(X_1)| = \epsilon^{1/4}\frac{|\tilde{A}_0(0)|}{\sqrt{2}}.$$

This completes the proof that, for a given frequency, the linear and nonlinear WKBJ approximations can be matched at leading order through a transition layer of width $\epsilon^{1/2}$ (in terms of X). A similar analysis holds for the transition layer at X_2^+.

7 Conclusions and Discussion

A fully nonlinear frequency selection criterion has been derived for global modes on a doubly infinite interval, governed by the complex Ginzburg-Landau equation with spatially varying coefficients.

Let $\omega = \Omega^{NL}(k, X)$ denote the local reduced nonlinear dispersion relation obtained by eliminating the amplitude R^2 from the complete local nonlinear dispersion relation $\omega = \Omega^{n\ell}(k, R^2, X)$ pertaining to finite amplitude travelling waves. The global frequency ω_g on the doubly infinite interval is then, at leading order, a *real saddle point* ω_s of Ω^{NL} associated with the *real* wavenumber k_s and station X_s such that

$$\omega_g \sim \omega_s = \Omega^{NL}(k_s, X_s) \quad \text{and} \quad \frac{\partial \Omega^{NL}}{\partial k}(k_s, X_s) = \frac{\partial \Omega^{NL}}{\partial X}(k_s, X_s) = 0. \quad (44)$$

This saddle point condition is selected so as to ensure a smooth crossover between the two nonlinear spatial branches $k^{n\ell^-}$ and $k^{n\ell^+}$ present on either side of X_s.

The nonlinear global mode spatial structure is illustrated in fig.1. A spatially evolving complex k^{ℓ^-} branch issuing from $X = -\infty$ and governed by the local linear dispersion relation $\omega = \Omega^\ell(k, X)$ in the OL^- region experiences a transition to the fully nonlinear régime within a layer TL^1 of thickness $O(\epsilon^{1/2})$ centered around a point X_1^- of local neutral stability. In a "downstream" CNL^- region of finite extent, the wave is fully nonlinear and its real wavenumber $k^{n\ell^-}$ and amplitude $\mathcal{R}^{2^-}$ are governed by the local nonlinear dispersion relation $\omega = \Omega^{n\ell}(k, R^2, X)$. As the wave enters the SP layer centered around X_s, it is smoothly converted into a $k^{n\ell^+}$ spatial branch since condition (44) is satisfied. The CNL^+ region mirrors, for the $k^{n\ell^+}$ wave, the CNL^- region for the $k^{n\ell^-}$ wave. A second transition layer TL^2 centered around the locally neutral station X_2^+ allows a return to a linear k^{ℓ^+} spatial wave in the OL^+ region, and a final exponential decay at $X = +\infty$.

These results should be compared with the corresponding double turning point *linear* frequency selection criterion derived in [13,51,59]. For infinitesimal waves governed by a local linear dispersion relation $\omega = \Omega^\ell(k, X)$ between *complex* wavenumber k and frequency ω, the complex global frequency ω_g is given by the saddle point condition (1,2), where the frequency ω_s, wavenumber k_s, and spatial coordinate X_s are all *complex*. The linear global mode spatial structure is thus made up of complex k^{ℓ^-} and k^{ℓ^+} spatially evolving waves governed by the local linear dispersion relation $\omega = \Omega^\ell(k, X)$ in corresponding OL^- and OL^+ regions near $X = \mp\infty$. The saddle point condition (2) ensures a smooth crossover from the k^{ℓ^-} to the k^{ℓ^+} branch in an inner region SP of thickness $O(\epsilon^{1/2})$ centered around the *complex* saddle point X_s. In the linear case, the $\mathrm{TL}^{1,2}$ and $\mathrm{CNL}^\pm$ regions are naturally absent, but an inner SP layer structure is necessary in both linear and nonlinear studies. Indeed, both frequency selection criteria are formally identical. Paradoxically the nonlinear criterion involves only real variables and therefore appears simpler to implement, without any of the complexities associated with analytic continuation in the complex X-plane.

According to [13,51], a necessary condition for the existence of a growing *linear* global mode is that the basic state be linearly absolutely unstable in a region of finite extent. According to the present study, a necessary condition for the existence of a self-sustained *nonlinear* gobal mode appears to be that the basic state only contain a linearly unstable region of finite extent corresponding to $\mathcal{R}^{2^\pm} > 0$. Fully nonlinear global modes of the type shown here may in principle occur even if the medium is only convectively unstable.

The latter result is entirely consistent with the studies of Chomaz [10] and Couairon & Chomaz [16]. In these recent investigations, nonlinear global modes on the semi-infinite interval $0 < X < \infty$ and governed by the real Ginzburg-Landau equation with constant coefficients and both cubic and quintic nonlinearities have been examined from the dynamical systems point of

view. In the supercritical case (stabilizing nonlinear terms), it is found that nonlinear global modes may exist even if the basic state is only linearly convectively unstable. Thus, there is clearly more and more evidence that the relation between local *linear* stability properties and global modes becomes somewhat tenous as the fully nonlinear régime is approached.

The recent numerical simulations of wakes in shallow layers performed by Schär & Smith [77] underscore the importance of nonlinearities in the frequency selection process. When nonlinearities were turned off, the wake was found to oscillate at a Strouhal frequency $\omega \sim 0.17$, to be compared with $\omega_s = 0.19$ resulting from the linear frequency selection criterion (1,2). Upon retaining nonlinear terms, the "observed" wake frequency increased substantially to $\omega \sim 0.27$. The criterion proposed in the present study could possibly account for this discrepancy.

Acknowledgements

We wish to thank Stéphane Le Dizès for many stimulating discussions and his careful reading of the manuscript. We are particularly indebted to the gentle people of LadHyX for providing and maintaining a friendly research atmosphere. LadHyX is jointly supported by the École polytechnique and by the Engineering Science Directorate of the French National Center for Scientific Research (CNRS).

Commentaires

Les modes de type chapeau obéissent à un critère de point-selle pour la relation de dispersion non linéaire, formellement analogue au critère linéaire de [13], mais il ne fait intervenir que des quantités réelles. Le passage de la branche linéaire $k^{\ell-}$ à la branche $k^{\ell+}$ se fait non pas directement en utilisant un prolongement analytique de $\omega_0(X)$ dans le plan des X complexes mais par l'intermédiaire d'une région non linéaire d'extension finie. Les non-linéarités permettent de continuer tout droit sur l'axe physique plutôt que de faire des détours dans le plan complexe. Le critère d'instabilité linéaire globale exige une région AI d'extension finie. Dans le cas des modes chapeaux, deux branches spatiales non linéaires se rencontrent ce qui n'est possible que si le milieu est également AI ; contrairement à ce qui a été supposé dans la conclusion de l'article (p. 46). À ce stade, la condition d'instabilité absolue reste une condition nécessaire, mais on ne sait pas si elle est suffisante. Cette question de l'existence des modes globaux non linéaires sera traitée en détail au chapitre $\mathfrak{F}$.

Au moment d'écrire cet article, je n'avais pas encore fait le calcul complet de la région du point selle et je croyais avoir montré que cela conduisait à une quantification des fréquences globales comme dans le cas linéaire. Ce résultat annoncé à la fin de la section 5 de l'article s'est révélé inexact. Le calcul complet de cette couche de point-selle figure au chapitre $\mathfrak{F}$.

La théorie exposée dans l'article précédent démontre l'existence de modes chapeaux mais ne dit rien sur leur stabilité. En effet, il se pourrait que de telles structures ne soient pas observables dans la pratique. Les simulations numériques réalisées en parallèle avec le développement de la théorie montrent qu'il n'en est rien et que des modes de type chapeau sont bien sélectionnés dans des simulations numériques directes initialisées avec du bruit. La figure 3.1 illustre la sélection d'un mode chapeau obtenu avec le jeu de coefficients suivant. Les valeurs de $k_0(X) = 1 - 0.1\mathrm{i}$, $\omega_{kk}(X) = 1 - 0.5\mathrm{i}$ et $\gamma(X) = 0.2 - \mathrm{i}$ sont maintenues constantes ; seul $\omega_0(X)$ dépend de l'espace : la variation de $\omega_{0,r}(X)$ est linéaire, celle de $\omega_{0,i}(X)$ parabolique de façon à ce que $\omega_0(0.2L) = 0.5$, $\omega_0(0.8L) = 0.6$, $\mathrm{Max}\omega_{0,i} = 0.5$, où L est la taille du domaine de la simulation comprenant 512 éléments de longueur $\delta x = 0.2$ ($L = 512\delta x$). Un algorithme de Runge–Kutta du quatrième ordre en temps est utilisé avec un pas $\delta t = 0.01$. En (*a*) l'évolution spatio-temporelle de ψ_r en niveaux de gris montre la naissance du mode global à partir du bruit initial jusqu'à synchronisation des trains d'onde sur tout le domaine. L'intervalle $0 < t < 110$ est représenté. La structure de l'amplitude et de la partie réelle de ce mode à la fin de la simulation ($t = 1000$) est donnée en (*b*). Le graphe (*c*) montre que le nombre d'onde local obtenu numériquement (courbe en pointillé) suit exactement les branches spatiales $k^{\ell\pm}$ et $k^{n\ell\pm}$ théoriques. On remarque l'arrondi au passage des points neutres, correspondant aux zones étroites de faible non-linéarité. La fréquence calculée en fin de simulation est en excellent accord avec sa prédiction théorique :

$$\omega_g^{\text{numérique}} = 0.742 \qquad \text{et} \qquad \omega_g^{\text{théorique}} = 0.746.$$

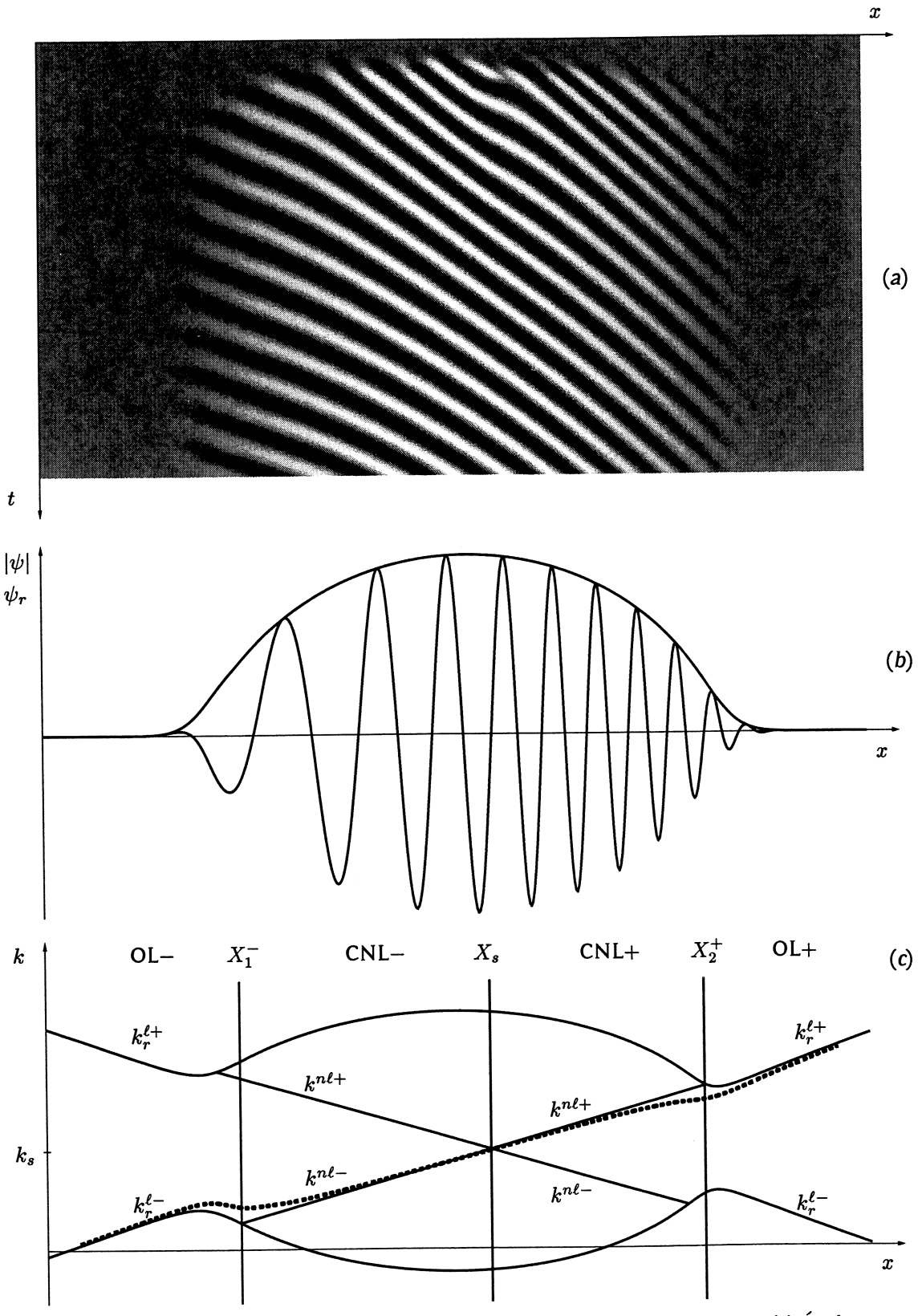
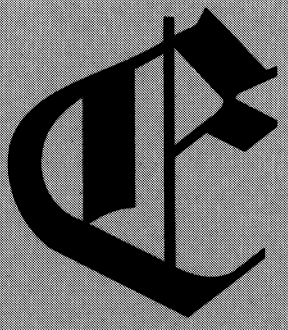


FIGURE 3.1. Simulation numérique du mode chapeau dans l'équation de GLC. (*a*) Évolution spatio-temporelle de ψ_r en niveaux de gris. (*b*) Formes de $|\psi|$ et ψ_r à la fin de la simulation. (*c*) Branches spatiales linéaires $k_r^{\ell\pm}(X,\omega_g)$ et non linéaires $k^{n\ell\pm}(X,\omega_g)$ (courbes continues) et nombre d'onde local de la simulation (courbe pointillée).



Éléphants avec un front raide

Le critère des modes de type chapeau du chapitre précédent a été démontré théoriquement et vérifié numériquement pour une variété de jeux de coefficients de l'équation GLC inhomogène. Après avoir démontré l'existence de ces structures non linéaires, j'ai voulu explorer plus en détail leur domaine d'existence dans l'espace des paramètres et vérifier en particulier si une région AI d'extension finie est bien nécessaire pour avoir un comportement globalement synchronisé.

En réduisant l'étendue de la région AI dans mes simulations, j'ai constaté que souvent j'obtenais des solutions parfaitement synchronisées mais dont la fréquence n'obéissait pas au critère du point-selle non linéaire. Après de nombreuses explorations numériques, j'ai compris qu'il s'agissait d'une autre espèce de solution synchronisée. Ce type de mode global, appelé ensuite mode "éléphant" ou mode raide, obéit à un critère différent. Contrairement aux modes doux, ses amplitude et nombre d'onde locaux ne sont pas continus partout : à l'amont, le passage de la région linéaire à la région non linéaire de la solution se fait de façon abrupte par un front associé à un saut d'amplitude et de nombre d'onde. En revanche, partout ailleurs, la structure d'un mode éléphant présente les mêmes caractéristiques que les modes chapeau.

Steep nonlinear global modes in spatially developing media

Benoît Pier, Patrick Huerre,
Jean-Marc Chomaz and Arnaud Couairon

Laboratoire d'hydrodynamique (LadHyX),
CNRS - École polytechnique, F-91128 Palaiseau cedex, France

Abstract

A new frequency selection criterion valid in the fully nonlinear régime is presented for extended oscillating states in spatially developing media. The spatial structure and frequency of these modes are dominated by the existence of a sharp front connecting linear to nonlinear regions. A new type of fully nonlinear time harmonic solutions called *steep global modes* is identified in the context of the supercritical complex Ginzburg–Landau equation with slowly spatially varying coefficients. A similar formulation is likely to be applicable to fully nonlinear synchronized global oscillations in spatially developing free shear flows.

Spatially developing free shear flows such as mixing layers [38], wakes [47,57], and jets [61] typically give rise to intrinsic self-sustained oscillations when they exhibit a sufficiently large region of absolute instability [5]. Fluctuations saturate at a finite amplitude in the locally unstable regions of the flow and become tuned at an overall frequency. The intrinsic frequency and the associated spatial distribution of fluctuations define a *global mode* living on the underlying unstable basic flow. In the present letter we show the existence of fully nonlinear global modes with a sharp stationary front separating linear and nonlinear regions. The complex Ginzburg–Landau (CGL) equation is chosen as a model of open flows since families of linear and nonlinear wave solutions are readily determined analytically. As summarized below, the study of CGL models has been found to lead to linear frequency selection criteria [13] that remain applicable for the Navier–Stokes equations [59]. The same approach is adopted here in the fully nonlinear context.

In the *linear* approximation, global frequency selection in *doubly infinite domains* is dictated by saddle point conditions [13,59] imposed on the local linear dispersion relation. Such a criterion predicts remarkably well the vortex shedding frequency behind blunt edged plates [34]. *Nonlinear* extensions of these

Article published in Physics of Fluids 10 (1998) 2433–2435

concepts have only recently been developed, mainly in the context of various one-dimensional evolution models in *semi-infinite* [10,16] or *finite* [56] *domains*. The results compare satisfactorily with numerical simulations and experiments for Taylor–Couette flow [7] and Rayleigh–Bénard convection with throughflow [62,16]. Surprisingly, fully nonlinear *soft global modes* of the CGL equation varying smoothly over a doubly infinite domain have been shown [65], by application of WKBJ theory, to satisfy a nonlinear saddle point criterion which is formally analogous to its linear counterpart. Here we show the existence of a second class of nonlinear spatially extended states in doubly infinite domains: *steep global modes* with a sharp front.

We assume that the fluctuating complex scalar field $\psi(x,t)$ is governed by the supercritical CGL equation written as

$$i\frac{\partial\psi}{\partial t}=\left(\omega_0(X)+\frac{1}{2}\omega_{kk}(X)k_0(X)^2\right)\psi+i\omega_{kk}(X)k_0(X)\frac{\partial\psi}{\partial x} -\frac{1}{2}\omega_{kk}(X)\frac{\partial^2\psi}{\partial x^2}+\gamma(X)|\psi|^2\psi, \tag{1}$$

where the complex functions $\omega_0(X)$, $\omega_{kk}(X)$, $k_0(X)$, and $\gamma(X)$ solely depend on the slow space variable $X=\epsilon x$, $\epsilon \ll 1$, to account for the weak inhomogeneity of the medium. The choice of these functions and their meaning will become clear when we discuss the resulting linear and nonlinear dispersion relations.

In regions where the amplitude of ψ is small, its behavior is governed by the linearized counterpart of (1). Under the assumption of weak inhomogeneity, linear solutions are approximated at leading order by waves of the form $\exp(\frac{i}{\epsilon}\int^X k(u)du-i\omega t)$. The corresponding *local linear dispersion relation* reads

$$\omega=\Omega^\ell(k,X)\equiv\omega_0(X)+\frac{1}{2}\omega_{kk}(X)(k-k_0(X))^2, \tag{2}$$

with associated complex local linear spatial branches

$$k^{\ell\pm}(X;\omega)\equiv k_0(X)\pm\sqrt{2\frac{\omega-\omega_0(X)}{\omega_{kk}(X)}}. \tag{3}$$

As defined in [5], the complex absolute frequency ω_0 necessarily coincides with the branch point of (3): at $\omega=\omega_0$ both wavenumber branches are equal to the local absolute wavenumber k_0. The following basic flow structure is assumed: a central absolutely unstable (AU) region of finite extent characterized by $\omega_{0,i}(X)\equiv\mathrm{Im}\,\omega_0(X)>0$, surrounded by convectively unstable (CU) regions with $\omega_{0,i}(X)<0$, which in turn become stable far downstream ($X\to+\infty$) and upstream ($X\to-\infty$). In order to enforce causality, sufficiently large wavenumbers are assumed to be damped, *i.e.*, $\omega_{kk,i}(X)<0$ for all X. We assume a basic flow advection towards increasing X which is readily shown to

correspond to $k_{0,i} < 0$. The + and − superscripts are unambiguously assigned to the spatial branches exponentially decaying towards $X = +\infty$ and $X = -\infty$ respectively.

In unstable regions the CGL equation admits local nonlinear traveling wave solutions of the form $\psi = R(X)\exp(\frac{i}{\epsilon}\int^X k(u)du - i\omega t)$, with *real* wavenumber k, *real* frequency ω and *real* amplitude R governed by the *local nonlinear dispersion relation*

$$\omega = \omega_0(X) + \frac{1}{2}\omega_{kk}(X)(k - k_0(X))^2 + \gamma(X)R^2. \tag{4}$$

This complex equation with three real unknowns can easily be cast in the form

$$\omega = \Omega^{n\ell}(k, X) \quad \text{and} \quad R^2 = \mathcal{R}_2(k, X), \tag{5ab}$$

where functions $\Omega^{n\ell}$ and $\mathcal{R}_2$ are quadratic polynomials in k with X-dependent *real* coefficients. The real nonlinear wavenumber branches $k^{n\ell\pm}(X;\omega)$ are derived from (5a); the allowed wavenumbers are those for which $\mathcal{R}_2(k, X) > 0$. We only consider CGL coefficients for which the finite amplitude traveling waves are stable.

Global mode solutions over the entire flow are obtained by asymptotically matching together local travelling wave solutions of the same frequency. By definition, a global mode is necessarily made up of the decaying $k^{\ell-}$ branch for $X \to -\infty$ and the decaying $k^{\ell+}$ branch for $X \to +\infty$. The frequency selection gives rise to a nonlinear eigenvalue problem: the matching of finite amplitude oscillations in a central region to exponentially decaying tails in both upstream and downstream directions can only be achieved for a specific frequency.

This problem has been solved for purely *linear global modes* in [13]. In the fully nonlinear régime, *soft global modes* with an overall slowly varying spatial envelope have been identified and described in [65]; their real global frequency ω_s is obtained at a saddle point (k_s, X_s) of the nonlinear dispersion relation $\Omega^{n\ell}(k, X)$. The objective of this letter is to report the existence of a second type of fully nonlinear solutions: in situations where *soft* modes fail to exist, they are replaced by a *steep* mode with a sharp front.

The spatial structure of a steep global mode of frequency ω_f is given in Fig. 1(a). Such a solution is characterized by a sharp front at the upstream boundary X_f of the AU region indicated in grey. Associated linear $k^{\ell\pm}$ and nonlinear $k^{n\ell\pm}$ wavenumber branches at the frequency ω_f vary along the streamwise direction X, as shown by solid and dashed lines in the X-k_r plane of Fig. 1(b). The local wavenumber making up the actual solution follows the path indicated by a thick line in Fig. 1(b). Except for the jump at the front (repeated arrows

in (b)) local wavenumber and amplitude vary slowly. The nonlinear solution prevails in the region $X_f < X < X_2$ which extends beyond the AU region.

The steep global frequency ω_f and the front location X_f are then solely determined by applying the following criterion to the local *linear* dispersion relation:

$$\omega_f = \Omega^\ell(k_f, X_f), \tag{6}$$

where the pair (k_f, X_f) satisfies

$$\frac{\partial \Omega^\ell}{\partial k}(k_f, X_f) = 0 \quad \text{and} \quad \Omega_i^\ell(k_f, X_f) = 0. \tag{7}$$

In terms of $\omega_0(X)$ these conditions read

$$\omega_f = \omega_0(X_f) \quad \text{and} \quad \omega_{0,i}(X_f) = 0. \tag{8}$$

The above equations are reminiscent of the Dee–Langer selection criterion [22] for a propagating front connecting an unstable state $\psi = 0$ to a fully nonlinear wave pattern in a homogenous medium undergoing a supercritical bifurcation. According to this criterion, a stationary front exists in homogenous media only when the control parameters are chosen to be exactly at the CU/AU transition. In the present inhomogenous, *i.e.*, spatially varying context, the CU/AU transition precisely occurs at the single location X_f. The front at this station has the overall frequency ω_f and the complex wavenumber at the decaying front edge coincides [Fig. 1(b)] with the local absolute wavenumber $k_f = k_0(X_f) = k^{\ell\pm}(X_f, \omega_f)$.

By definition of the absolute wavenumber, the linear $k^{\ell\pm}$ branches meet at k_f for $\omega = \omega_f$ and $X = X_f$. In a neighborhood of X_f, the upstream $k^{\ell-}$ branch decays towards $X = -\infty$ when $X < X_f$, whereas the downstream spatially amplified $k^{\ell+}$ branch is replaced by the nonlinear $k^{n\ell+}$ branch when $X > X_f$. The front at X_f exactly connects the linear $k^{\ell-}$ branch in the CU region $X < X_f$ with the nonlinear $k^{n\ell+}$ branch prevailing in the AU region $X > X_f$. Further downstream the nonlinear $k^{n\ell+}$ branch eventually returns to the linear $k^{\ell+}$ via a neutral stability station X_2 where the nonlinear amplitude vanishes, exactly as for soft global modes [65].

A front located at the upstream boundary of the AU region is a stable configuration due to the following argument. Consider a small displacement from the front equilibrium position at X_f towards $X > X_f$. The front now experiences a slightly AU medium and hence [22] propagates slowly towards its decaying edge, *i.e.*, upstream. When the front is displaced to $X < X_f$, it penetrates into a CU region and is thus pushed downstream. In any case the front is seem to return to its equilibrium position. The complete asymptotic representation

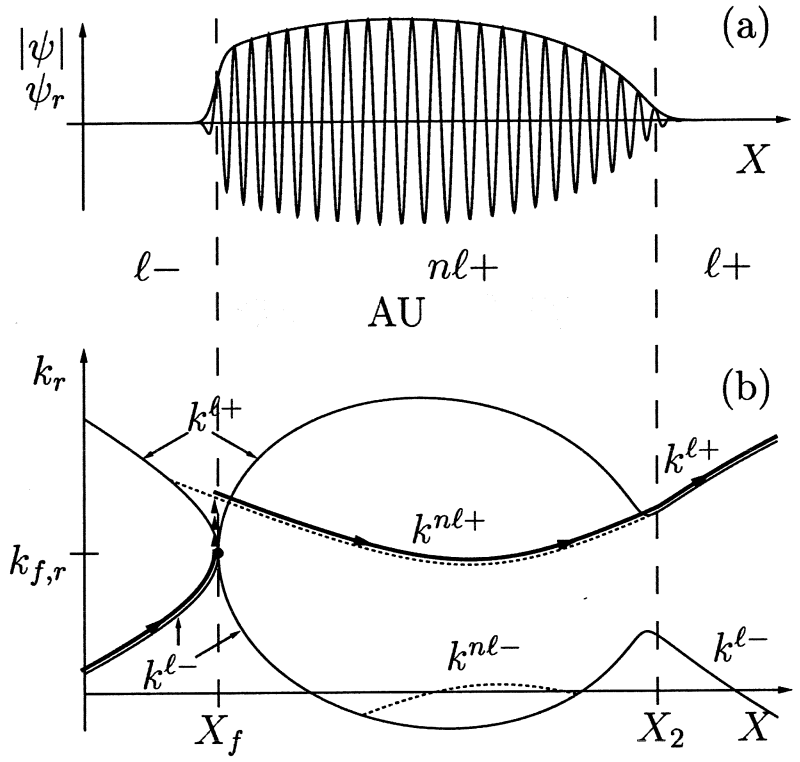


Fig. 1. (a) Envelope $|\psi|$ and real part ψ_r of steep global mode with sharp front at upstream boundary X_f of AU region (in grey). (b) Corresponding linear and nonlinear spatial branches in the X-k_r plane. Local wavenumber making up solution in (a) follows path indicated by a thick line. The wavenumber jump at the front is indicated by repeated arrows.

of steep global modes is obtained by linear and nonlinear WKBJ matching techniques as in [65].

According to the present theory the CGL equation with spatially varying coefficients has been shown to admit two types of time harmonic solutions. Soft global modes are characterized by a nonlinear saddle point condition [65], whereas steep global modes display a stationary front (6,7) at the upstream boundary of the AU domain. The nature of the selected global mode is determined by formally computing the respective characteristic frequencies ω_s and ω_f: in a future publication we will show that the mode of largest frequency is selected and that no other global mode type occurs. The validity of these theoretical criteria is confirmed by spatio-temporal numerical simulations of (1). Furthermore, according to the results of [50], one expects the nature of the bifurcation to a fully nonlinear global mode to be extremely sensitive to ϵ.

In both instances, frequency selection takes place at the downstream position where a $-$ branch is linked to a $+$ branch: $k^{n\ell-}$ and $k^{n\ell+}$ at X_s for a soft global mode, $k^{\ell-}$ and $k^{n\ell+}$ at X_f for a steep global mode. These stations ef-

fectively act as frequency generators for the entire flow. Such locations may be interpreted as local oscillators inducing the upstream − branch and the downstream + branch, regardless whether these branches are linear or nonlinear. It is noteworthy that the present steep frequency selection criterion (6,7) demonstrates in the CGL context, the validity of the initial resonance principle postulated by Monkewitz and Nguyen [60] to account for self-excited resonances in bluff body wakes.

An essential difference between steep and soft global modes is that steep global modes only involve one nonlinear spatial branch $k^{n\ell+}$. The sharp front allows an immediate crossover from the linear − to the nonlinear + branch. Generalization of the present theory to real flows is in progress: In the context of free shear flows governed by the Navier–Stokes equations, the local $k^{n\ell+}$ is represented by fully nonlinear saturated solutions on a streamwise periodic domain as obtained in direct numerical simulations for a given parallel basic flow. To our knowledge local $k^{n\ell-}$ branches for free shear flows have never been identified. It therefore seems likely that fully nonlinear global modes in wakes, jets or shear-layers may be described as steep rather than soft global modes.

Commentaires

Dans le cas des modes chapeaux, les simulations numériques de GLC sont venues confirmer *a posteriori* le bien-fondé du critère de point-selle non linéaire. Le contraire s'est produit pour les modes éléphants : ces structures synchronisées ont d'abord été identifiées numériquement avant de trouver leur explication théorique dans l'application du critère de stabilité marginale de Dee & Langer [22].

La figure 4.1 illustre la sélection d'un mode éléphant à partir d'une condition initiale aléatoire. Dans l'équation de GLC les coefficients $k_0(X) = 1 - 0.6\mathrm{i}$, $\omega_{kk}(X) = 1 - 0.5\mathrm{i}$, $\gamma(X) = 0.2 - \mathrm{i}$ sont maintenus constants, seul $\omega_0(X)$ dépend de l'espace : la variation de $\omega_{0,r}(X)$ est linéaire, celle de $\omega_{0,i}(X)$ parabolique de façon à ce que $\omega_0(0.1L) = 0.4$, $\omega_0(0.7L) = 0.3$, $\mathrm{Max}\omega_{0,i} = 0.5$. Les résolutions spatiale et temporelle sont identiques à celles de la figure 3.1. En (*a*) l'évolution spatio-temporelle de ψ_r en niveaux de gris montre comment le mode global émerge du bruit initial jusqu'à synchronisation des trains d'onde sur tout le domaine ($0 < t < 230$). La structure de ce mode à la fin de la simulation ($t = 1000$) est indiquée en (*b*) où l'amplitude et la partie réelle de ψ sont représentées. On distingue nettement le front raide en amont où la variation de l'enveloppe change de pente. Le graphe (*c*) montre que le nombre d'onde local obtenu numériquement (courbe en pointillé) suit précisément les branches spatiales $k^{\ell\pm}$ et $k^{n\ell+}$ théoriques. Le côté non linéaire du front est légèrement repoussé en aval de X_f. Ceci est tout à fait normal puisque le critère de stabilité marginale régit la partie décroissante du front ; la saturation non linéaire ne devient effective qu'un peu plus loin. Le même phénomène est observé au chapitre 6 à propos des structures synchronisées dans les sillages. Ici, l'accord entre fréquence globale numérique et la prédiction théorique est un peu moins bon que dans le cas des modes chapeaux :

$$\omega_g^{\text{numérique}} = 0.429 \qquad \text{et} \qquad \omega_g^{\text{théorique}} = 0.400.$$

Mais la validité du critère de sélection de fréquence est bien confirmée. Absent dans la structure uniforme des modes chapeaux, le front raide des éléphants exige une fine résolution numérique pour reproduire fidèlement le résultat théorique.

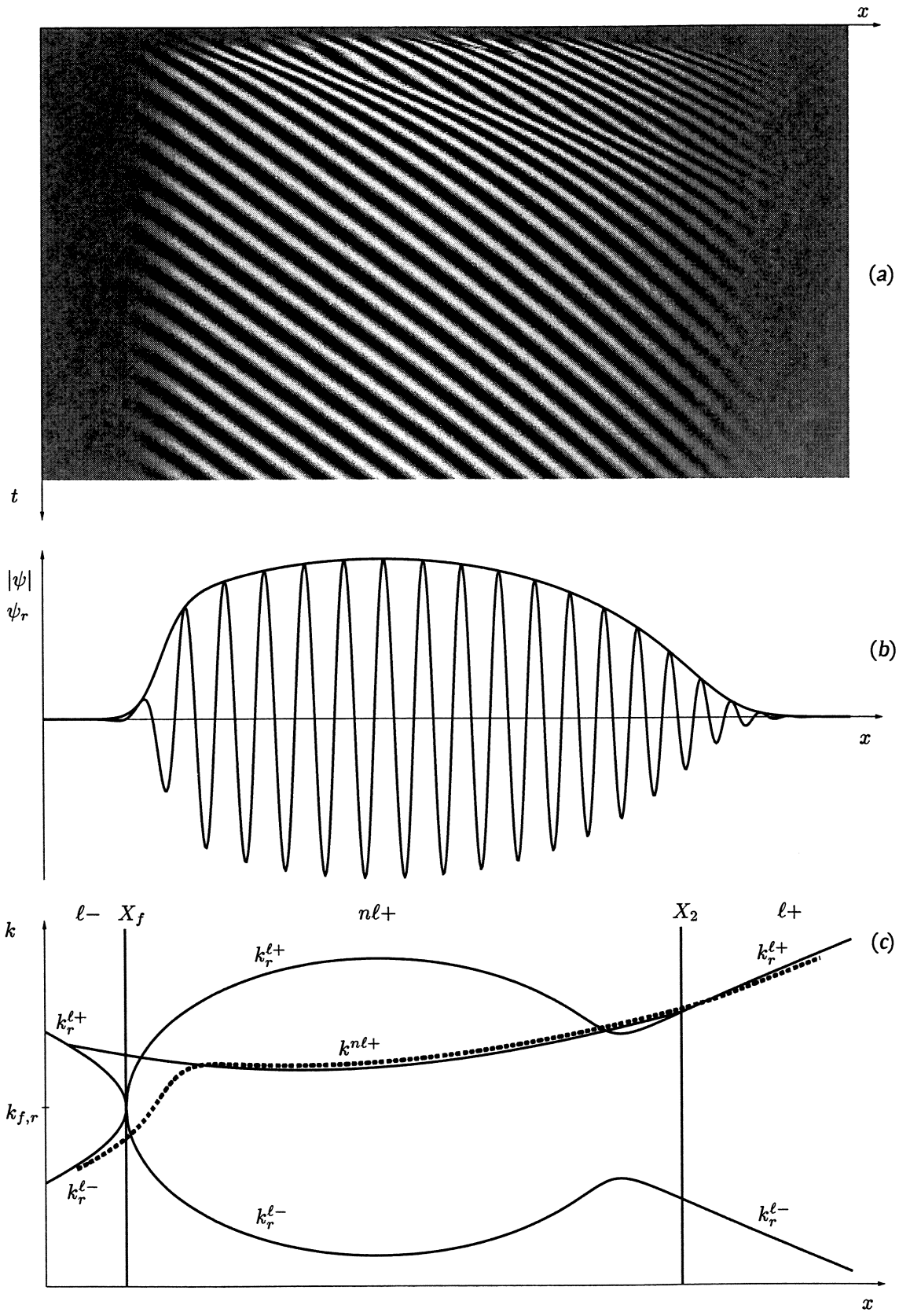
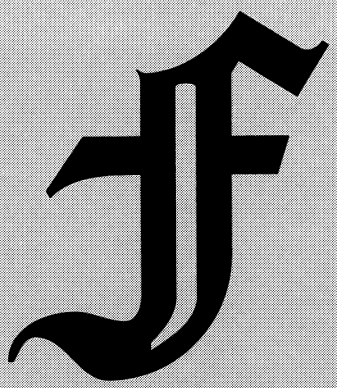


FIGURE 4.1. Simulation numérique de mode éléphant dans l'équation de GLC. (*a*) Évolution spatio-temporelle de ψ_r en niveaux de gris. (*b*) Formes de $|\psi|$ et ψ_r à la fin de la simulation. (*c*) Branches spatiales linéaires $k_r^{\ell\pm}(X,\omega_g)$ et non linéaire $k^{n\ell+}(X,\omega_g)$ (courbes continues) et nombre d'onde local de la simulation (courbe pointillée).



Formation et déformation des structures synchronisées

Comme cela a été dit dans la conclusion de l'article précédent, les modes éléphants ne font intervenir que la branche non linéaire $k^{n\ell+}$. Les conditions requises pour leur existence semblent donc plus faciles à remplir dans le cadre de la mécanique des fluides. Dès lors j'ai travaillé pour adapter la technique développée grâce à l'étude du modèle de GLC aux équations de Navier–Stokes. Pour tester si les méthodes WKBJ non linéaires développées précédemment s'adaptent à la mécanique des fluides où les trains d'ondes non linéaires ne sont pas connus analytiquement, une première étape consistait à d'abord traiter une équation aux dérivées partielles unidimensionnelle quelconque. Et effectivement, les méthodes qui ont fait leurs preuves dans le cas des ondes planes d'amplitude finie $R\mathrm{e}^{\mathrm{i}(kx-\omega t)}$ de GLC s'appliquent aussi dans des situations où les solutions d'amplitude finie ne sont plus sinusoïdales mais des fonctions périodiques quelconques d'une phase $\theta = kx - \omega t$.

En parallèle à ce travail de généralisation aux écoulements réels, j'ai voulu explorer les domaines d'existence des deux types de modes globaux non linéaires pour mieux comprendre les situations physiques qui leur donnent naissance et identifier les paramètres de contrôle caractéristiques. J'ai mentionné que les modes éléphants ont été découverts dans des situations où la région AI est relativement petite. Comment se passe la transition entre les deux modes ? Dans quelles situations n'existent-ils pas ? Y a-t-il d'autres structures synchronisées ?

De même que les critères de sélection des deux structures reposent sur les propriétés géométriques des branches spatiales à la fois linéaires $k^{\ell\pm}(X,\omega)$ et non linéaires $k^{n\ell\pm}(X,\omega)$, de même leur sélection mutuelle s'obtient par un suivi détaillé de l'évolution de ces mêmes courbes pour différentes valeurs de la fréquence. C'est ainsi qu'on démontre qu'il n'y a pas de compétition entre ces deux modes et que les deux critères s'excluent mutuellement : si l'un des critères est vérifié, le mode associé à l'autre n'existe pas. Par le même raisonnement sur les branches spatiales on déduit aussi que forcément un des deux modes existe. Ainsi on a montré que ce sont les deux seuls modes possibles, et, pour un jeu de coefficients donné, on a un critère qui donne le mode effectivement sélectionné.

Ceci dit, je ne prétends en aucun cas avoir été exhaustif. Vu le grand nombre de paramètres qui entrent en jeu (il faudrait considérer toutes les distributions spatiales de coefficients possibles), il se trouvera toujours des situations où le scénario général de l'article suivant sera mis en défaut. Mon but n'a pas été d'établir la carte complète des solutions de GLC, mais plutôt de comprendre les mécanismes qui sont à la base du comportement synchronisé des écoulements. C'est dans cette perspective que je n'ai considéré que des variations de paramètres ayant un sens physique, et ainsi j'ai pu identifier les ingrédients pertinents dans le cas des écoulements réels.

Bifurcation to fully nonlinear synchronized structures in slowly varying media

Benoît Pier, Patrick Huerre, Jean-Marc Chomaz

Laboratoire d'hydrodynamique (LadHyX)
CNRS - École polytechnique, F-91128 Palaiseau cedex, France

Abstract

The selection of fully nonlinear extended oscillating states is analysed in the context of one-dimensional nonlinear evolution equations with slowly spatially varying coefficients on a doubly-infinite domain. Two types of synchronized structures referred to as *steep* and *soft* global modes are shown to exist. Steep global modes are characterized by the presence of a sharp stationary front at the marginally absolutely unstable station and their frequency is determined by the corresponding linear absolute frequency, as in Dee–Langer propagating fronts. Soft global modes exhibit slowly varying amplitude and wavenumber over the entire domain and their frequency is determined by the application of a saddle point condition to the local nonlinear dispersion relation. The two selection criteria are compared and shown to be mutually exclusive. The onset of global instability first gives rise to a steep global mode via a saddle-node bifurcation as soon as local linear absolute instability is reached somewhere in the medium. As a result, such self-sustained structures may be observed while the medium is still linearly globally stable. Soft global modes only occur further above global onset and for sufficiently weak advection. The entire bifurcation scenario and state diagram are described in terms of three characteristic control parameters. The complete spatial structure of nonlinear global modes is analytically obtained in the framework of WKBJ approximations.

1 Introduction

It is now well established that spatially developing open shear flows may be divided into two classes: some flows are very sensitive to inflow conditions and essentially behave as *noise amplifiers*, others display intrinsic dynamics and may be interpreted as *global oscillators* [39,40,37]. The present paper is concerned with the latter class of systems and examines in detail the synchronized self-sustained structures which they can support. In previous studies we have demonstrated the existence of nonlinear *soft global modes* [65] and *steep*

global modes [68]. The objective of the present investigation is to analyse the bifurcation scenarii which lead from the basic state to either of these fully nonlinear structures as the global control parameters are varied. The analysis is carried out in the context of one dimensonal evolution models with spatially varying coefficients, in order to account for the streamwise development of the basic state.

A variety of physical systems give rise to intrinsic self-sustained oscillations: mixing layers with strong enough counterflow [83], low-density jets [80,58], cylinder wakes [55,71,81], wakes behind blunt-edged plates [35,34], thin aerofoilwakes [93], Taylor–Couette flow between concentric spheres [79], Taylor–Couette flow between circular cylinders with throughflow [7], Rayleigh–Bénard convection with throughflow [62], baroclinically unstable atmospheric flows [69,24], sunspot cycles [1,56]... Many of these flows display a spatially varying basic state, and hence a spatial dependence of the local instability characteristics. The goal of a global analysis is to obtain in a self-consistent manner a spatially extended structure made up of wave trains governed by the local properties of the medium and tuned at an overall global frequency ω_g. The unknown global frequency ω_g is to be derived from a nonlinear eigenvalue problem consisting of the evolution equation and associated boundary conditions. The associated eigenfunction yields the spatial structure of the corresponding self-sustained oscillations. The resolution of the eigenvalue problem is typically undertaken in the context of a slowly varying approximation whereby the underlying basic state evolves slowly over a typical instability length scale. In this framework, the main objective of the global mode analysis is to derive *global* frequency selection criteria from the *local* dispersion relation prevailing at each streamwise station.

Linear global mode analyses are now fairly complete. Chomaz *et al.* [13] demonstrated that the complex global frequency is determined by a saddle point (equivalently a double turning point) condition applied to the local linear dispersion relation for the linear complex Ginzburg–Landau equation with spatially varying coefficients. This criterion had previously been discovered and implemented by Soward and Jones [79] to describe oscillating states in Taylor–Couette flow between concentric spheres. According to Monkewitz *et al.* [59], the same criterion also holds for the Navier–Stokes equations linearized about an arbitrary slowly varying basic flow. More recently, Le Dizès *et al.* [51] reexamined the case of the spatially varying linear complex Ginzburg–Landau equation and demonstrated the existence of another family of linear global modes with two simple turning points. The causal nature of these linear global modes has been established for the same model by Hunt and Crighton [41]: the exact linear impulse response does converge, for large time, to the most unstable linear global mode. The validity of the linear saddle point criterion has been fully confirmed in the direct numerical simulations of the Kármán vortex street behind a blunt-edged plate by Hammond and Redekopp [34].

Paradoxically, the weakly nonlinear extension of these concepts is fraught with difficulties, as emphasized by Chomaz *et al.* [12] and Le Dizès *et al.* [50]: the Landau constant pertaining to the Hopf bifurcation near global mode onset does not display a well-defined sign as the WKBJ spatial inhomogeneity parameter is decreased. Furthermore, the weakly nonlinear formulation is only valid in an exponentially small vicinity of threshold.

To obviate such weakly nonlinear studies, it appears natural to resort to a fully nonlinear approach where fluctuations are of order unity. Such a line of thought has been consistently pursued since the early nineties in the framework of nonlinear Ginzburg–Landau type models. The classical absolute/convective instability concepts introduced in a linear context by Briggs [6] and Bers [5] have been generalized to the fully nonlinear régime by Chomaz [10]. The absolute/convective nature of the nonlinear dynamics is then directly related to the propagation direction of the front separating the basic state from the bifurcated state [22,72–74]. The properties of fully nonlinear global modes on a semi-infinite domain governed by Ginzburg–Landau type equations with constant coefficients have been thoroughly studied by Couairon and Chomaz [15–17]. In this case, a nonlinear global mode is obtained when an upstream travelling front is halted in its motion by the upstream boundary point. This event occurs whenever the medium is nonlinearly absolutely unstable in the sense of Chomaz [10]. The reader is referred to Tobias, Proctor and Knobloch [86] and Chomaz and Couairon [11] for a corresponding analysis of the finite-interval problem.

Corresponding fully nonlinear analyses have been performed for the complex Ginzburg–Landau equation with spatially varying coefficients in doubly infinite media. Two varieties of nonlinear global modes have been identified. *Soft* global modes, obtained by Pier and Huerre [65], obey a saddle point frequency selection criterion applied to the *local nonlinear dispersion relation*. This criterion is formally analogous to its linear counterpart. The associated spatial eigenfunction structure displays smoothly varying amplitude and wave number over the entire domain. By contrast, according to the preliminary results reported by Pier *et al.* [68], *steep* global modes are governed by a marginal *linear* instability criterion: the steep global frequency is imposed by the real absolute frequency [5] prevailing at the transition station between linear convective and absolute instability. This criterion is akin to the linear front velocity selection principle put forward by Dee and Langer [22]: for a wide class of systems, the speed of the front separating the basic state from the bifurcated state is such that in the co-moving frame the medium is marginally linearly absolutely unstable. The steep global spatial structure displays a stationary sharp front at the transition station with a sudden jump in wave number. In all other regions, the amplitude and wave number are slowly varying. Similar steep self-sustained structures have been numerically identified and analytically determined in amplitude evolution models pertaining to solar and stellar

magnetic activity cycles by Meunier *et al.* [56] and Bassom *et al.* [1]. The properties of nonlinear global modes governed by the real Ginzburg–Landau equation in a semi-infinite domain with combined distributed spatial inhomogeneity have been obtained by Couairon [14] and Couairon and Chomaz [18]. Predicted scaling laws for amplitude and position of the maximum very favorably compare with experimental and numerical observations of bluff-body wakes.

The purpose of the present study is two-fold: first we wish to map out the domains of existence of soft or steep global modes in an appropriate control parameter space and to characterize the associated bifurcations. Secondly we present the detailed asymptotic structure of the various layers and regions which make up their spatial distribution.

Consider a system governed by a one-dimensional nonlinear partial differential equation that is first order in time of the form

$$\frac{\partial \psi}{\partial t} = \mathcal{F}(\partial_x; X)[\psi], \tag{1}$$

where x and t represent space and time coordinates respectively, and X is a slow space variable to be defined shortly. The basic state is assumed to be $\psi = 0$, and the function $\psi(x,t)$ represents the fluctuations riding on the basic state. In regions of finite amplitude, ψ is governed by the full nonlinear operator $\mathcal{F}$. In small amplitude regions, ψ is a perturbation governed by equation (1) linearized around the basic state, *i.e.*,

$$\frac{\partial \psi}{\partial t} = \mathcal{L}(\partial_x; X)[\psi]. \tag{2}$$

A crucial assumption of the present investigation is the *slow spatial development* of the medium as exemplified by the introduction of the slow spatial variable X in the operators $\mathcal{F}$ and $\mathcal{L}$. The weak non-uniformity hypothesis is fulfilled if the ratio $\epsilon = \lambda/L$ between the typical instability length scale λ and the inhomogeneity length scale L is small. As a result of this scale separation, the weak variations of the medium instability properties may be described through the slow variable

$$X = \epsilon x \quad \text{with} \quad \epsilon \ll 1. \tag{3}$$

If the slow space variable X is frozen, system (1) becomes a p.d.e. in x and t with constant coefficients which captures the *local* instability properties prevailing at that station X. In order to construct a global mode it is necessary to "piece together" local wave trains at different X by explicitly accounting for the weak coupling between local and global properties via relation (3).

The outline of the paper is as follows. The bulk of the study (Sections 2–4) is concerned with the determination of the leading order approximation

for fully nonlinear synchronized structures governed by (1). Local instability properties where X is frozen are summarized in Section 2. Emphasis is given to the relationship between causality and the spatial response to a localized harmonic forcing (Section 2.3). In this framework, stationary fronts are shown to naturally arise as the limiting spatial response of the system in the absence of forcing when the medium is marginally absolutely unstable (Section 2.4). Variations of the local instability properties over the entire X-domain are analysed in Section 3. More specifically, the distribution over X of linear spatial branches (Section 3.2) and nonlinear spatial branches (Section 3.3) is investigated as the global frequency is varied. Section 4 contains the essential results concerning the structure of steep global modes (Section 4.2), the nature of their bifurcation from the basic state (Sections 4.3–4.5), the structure of soft global modes (Section 4.6), and finally the respective domains of existence of steep and soft global modes (Sections 4.7,4.8) in control parameter space. The results of Sections 2–4, in principle, apply to any nonlinear system governed by an equation of the form (1). In order to obtain explicit results, we repeatedly use as an illustrative example the complex Ginzburg Landau (CGL) equation

$$i\frac{\partial\psi}{\partial t} = \left(\omega_0(X) + \frac{1}{2}\omega_{kk}(X)k_0(X)^2\right)\psi + i\omega_{kk}(X)k_0(X)\frac{\partial\psi}{\partial x} - \frac{1}{2}\omega_{kk}(X)\frac{\partial^2\psi}{\partial x^2} + \gamma(X)|\psi|^2\psi \tag{4}$$

for a complex function $\psi(x,t)$. For convenience, the CGL equation is written here as derived from the Taylor expansion of the dispersion relation around $k_0(X)$ in the same manner as [39]. The precise meaning of all these quantities is discussed in detail in Section 2. The complex X-dependent coefficients $\omega_0(X)$ and $k_0(X)$ denote the usual local absolute frequency and wave number respectively, while $\omega_{kk}(X)$ is the second derivative of the linear dispersion relation with respect to the wave number k. The complex Landau "constant" $\gamma(X)$ is chosen so that nonlinearities are stabilizing everywhere (supercritical bifurcation), *i.e.*, $\gamma_i(X) \equiv \mathrm{Im}\,\gamma(X) < 0$ for all X. In the entire paper, the field $\psi(x,t)$ is assumed to be advected in the positive x-direction everywhere to mimic the dynamics of open flows. As demonstrated in Section 4.8, this assumption is equivalent to $k_{0,i}(X) < 0$ for all X. Thus the increasing and decreasing x-directions will be referred to as "downstream" and "upstream" respectively.

Model (4) has been shown to successfully describe a large range of pattern formation phenomena [54,20,63]. Here it is used as an idealized representation of spatially developing flows, Similar conclusions are expected to hold for a general system governed by (1). The analytical results obtained in Sections 2–4 are further supported by numerical simulations of the CGL equation (4), as depicted in the accompanying figures. The remaining part of the paper (Section 5) is devoted to the complete higher-order asymptotic analyses of the

various regions and layers appearing as ingredients in the spatial structure of global modes. The results are derived in the general context of system (1) by following a methodology analogous to that previously used by Pier and Huerre [65] and Bassom *et al.* [1]. This complete asymptotic analysis is rather technical and may be skipped in a first reading. The main conclusions are discussed in a final Section 6.

2 Local instability properties

Under the assumption that the governing equation only depends on space through the slow variable X, local characteristics of the medium are recovered by freezing X in (1) and studying the corresponding strictly uniform medium. In the sequel, "local" always refers to properties of uniform systems obtained by extending the medium of a specific downstream station X towards $x = \pm\infty$. At this local level of analysis, X and x are then considered to be independent: the fast component x is involved in spatial differentiation whereas X plays the part of an independent control parameter. The rigorous asymptotic analysis reestablishing the link between x and X via (3) in terms of WKBJ approximations [3] is postponed to Section 5.

In the present section the properties of infinite spatially uniform media governed by an equation of the form

$$\frac{\partial \psi}{\partial t} = \mathcal{F}(\partial_x)[\psi] \tag{5}$$

are reviewed. The results are applicable to any nonlinear operator $\mathcal{F}(\partial_x) = \mathcal{F}(\partial_x; X_0)$ derived from (1) for some fixed location $X = X_0$. Explicit forms are obtained for the uniform CGL equation

$$i\frac{\partial \psi}{\partial t} = \Big(\omega_0 + \frac{1}{2}\omega_{kk}k_0^2\Big)\psi + i\omega_{kk}k_0\frac{\partial \psi}{\partial x} - \frac{1}{2}\omega_{kk}\frac{\partial^2 \psi}{\partial x^2} + \gamma|\psi|^2\psi. \tag{6}$$

The linear properties dictating the dynamics of small amplitude perturbations are routinely obtained. The main assumption used throughout the present study is that (5) admits a continuous family of nonlinear travelling waves. This is guaranteed as long as the nonlinearities are supercritically stabilizing, as demonstrated below.

Small amplitude perturbations are governed by the counterpart of (5) linearized around $\psi = 0$,

$$\frac{\partial \psi}{\partial t} = \mathcal{L}(\partial_x)[\psi]. \tag{7}$$

Any perturbation is a superposition of elementary waves $e^{i(kx-\omega t)}$ where the complex wave number k and frequency ω satisfy the linear dispersion relation

$$\omega = \Omega^{\ell}(k) \equiv i\mathcal{L}(ik). \tag{8}$$

For eq.(6), it takes the simple form

$$\omega = \omega_0 + \frac{1}{2}\omega_{kk}(k-k_0)^2, \tag{9}$$

where it is assumed that $\omega_{kk,i} \equiv \mathrm{Im}\,\omega_{kk} < 0$ in order to enforce causality (see Section 2.3).

The dispersion relation (8) governs all linear properties of the system. Three situations are of particular interest: the temporal evolution problem, the impulse response, and the spatial response problem.

2.1 Temporal evolution and nonlinear dispersion relation

Consider the evolution of an initial spatially harmonic perturbation

$$\psi(x, t=0) = Ae^{ikx} + \text{c.c.}$$

of real wave number k and small amplitude $A \ll 1$. Its linear temporal growth rate is $\Omega_i^{\ell}(k) \equiv \mathrm{Im}\,\Omega^{\ell}(k)$. Two typical variations of Ω_r^{ℓ} and Ω_i^{ℓ} with k are sketched by solid lines in Fig.1. When $\Omega_i^{\ell}(k) < 0$, the wave exponentially decays in time. When $\Omega_i^{\ell}(k) > 0$, the wave is temporally amplified and eventually governed by the full nonlinear equation (5). Assume that stabilizing nonlinearities lead to a fully nonlinear travelling wave of the form

$$\psi(x,t) = \Psi(kx - \omega t; k), \tag{10}$$

where ω is a *real* frequency and the function $\Psi(\theta; k)$ is 2π-periodic in θ. This one-parameter family of nonlinear solutions parametrized by k is characterized by the *nonlinear dispersion relation*

$$\omega = \Omega^{n\ell}(k), \tag{11}$$

represented by the dashed curves in Fig.1-a,c. The travelling waves (10) and dispersion relation (11) are the nonlinear counterparts of the linear normal modes $e^{i(kx-\omega t)}$ and dispersion relation (8). Since the medium is assumed to be supercritical, nonlinear solutions $\Psi(\theta; k)$ only exist in the *unstable wave number range* $k_1 < k < k_2$ defined by $\Omega_i^{\ell}(k) > 0$. Towards the boundaries of this range, the linear growth rate vanishes as well as the nonlinear saturation amplitude of $\Psi(\theta; k)$. A weakly nonlinear calculation then shows that the

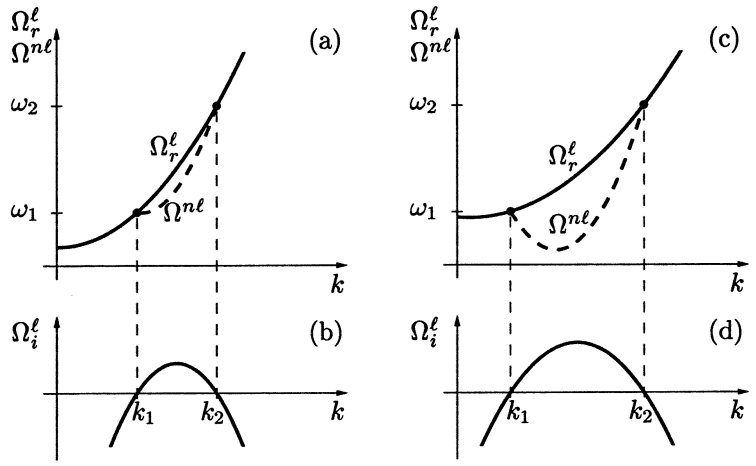


Fig. 1. Linear and nonlinear temporal branches of the CGL equation. (b,d) Temporal growth rate $\Omega_i^\ell(k)$ as a function of the real wave number. Unstable wave numbers lie in the range $k_1 < k < k_2$. (a,c) The nonlinear temporal branch $\Omega^{n\ell}(k)$ (dashed curves) is defined in the unstable wave number range and is connected to the $\Omega_r^\ell(k)$ curve (solid lines) at the neutrally stable boundaries where $\omega_1 = \Omega^\ell(k_1) = \Omega^{n\ell}(k_1)$ and $\omega_2 = \Omega^\ell(k_2) = \Omega^{n\ell}(k_2)$. The nonlinear branch may be either monotonous (a) or exhibit an extremum (c).

higher harmonics of $\Psi(\theta)$ are slaved to the fundamental, and, in the neutrally stable limit, the nonlinear frequency equals the linear real frequency

$$\Omega^{n\ell}(k) = \Omega^\ell(k) \quad \text{when} \quad \Omega_i^\ell(k) = 0. \tag{12}$$

In Fig.1-a,c, the nonlinear temporal branches are seen to be connected to their linear counterparts at $\omega_1 = \Omega^{n\ell}(k_1) = \Omega^\ell(k_1)$ and $\omega_2 = \Omega^{n\ell}(k_2) = \Omega^\ell(k_2)$ respectively. In weakly unstable media, the unstable wave number range is small and in general the nonlinear frequency is a monotonous function of the wave number (Fig.1-a). Further above threshold, the unstable wave number range increases and the nonlinear temporal branch $\Omega^{n\ell}(k)$ may exhibit an extremum (Fig.1-c). As a result, one value of ω may be associated to two distinct wave numbers as further discussed in Section 2.5.

In general the functions Ψ as well as $\Omega^{n\ell}$ cannot be calculated analytically, but they are easily obtained by performing a numerical simulation in a spatially periodic interval of wave length $2\pi/k$. In the particular case of the CGL equation (6), nonlinear solutions are explicitly obtained as finite amplitude harmonic waves

$$\psi(x,t) = R(k) \exp i[kx - \Omega^{n\ell}(k)t],$$

with

$$\Omega^{n\ell}(k) = \frac{\operatorname{Im}\left(\gamma^\star \Omega^\ell(k)\right)}{\operatorname{Im}\gamma^\star} \quad \text{and} \quad R^2(k) = \frac{\operatorname{Im}\left(\Omega^\ell(k)\right)}{\operatorname{Im}\gamma^\star},$$

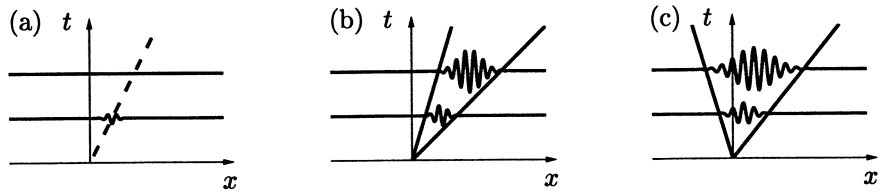


Fig. 2. Typical impulse response of (a) stable (b) convectively unstable (c) absolutely unstable medium.

where the superscript $\star$ denotes the complex conjugate. Recall that the condition of stabilizing nonlinearities implies $\gamma_i < 0$.

2.2 Impulse response and absolute instability

The impulse response as defined by many authors [6,5,39,40,37] is given by

$$\frac{\partial \psi}{\partial t} = \mathcal{L}(\partial_x)[\psi] + \delta(x)\delta(t), \tag{13}$$

where δ denotes the Dirac delta function. Different behaviors arise as illustrated in the (x,t)-plane in Fig.2.

The medium is said to be *linearly stable* (Fig.2-a) if the response $\psi(x,t)$ decays on all rays $x/t = \mathrm{C}^{\mathrm{st}}$. This is fulfilled when

$$\Omega_i^\ell(k) < 0 \quad \text{for all real } k.$$

In an unstable medium, at least one growing wavepacket develops from $(x,t) = (0,0)$. If the growing wavepacket moves away from the source at $x = 0$ and eventually leaves the medium unperturbed, the instability is said to be *convective* (Fig.2-b). If, by contrast, the instability grows in place and invades the system both upstream and downstream, the instability is said to be *absolute* (Fig.2-c). The convective or absolute nature of the instability depends on the *absolute frequency* ω_0 associated with the *absolute wave number* k_0 observed along the ray $x = 0$ defined as

$$\omega_0 = \Omega^\ell(k_0) \quad \text{where} \quad \frac{d\Omega^\ell}{dk}(k_0) = 0. \tag{14}$$

The medium is absolutely unstable (AU) if $\omega_{0,i} > 0$, convectively unstable (CU) if $\omega_{0,i} < 0$. The form (6) in which the CGL equation has been cast explicitly puts forward its dependence on ω_0 and k_0.

2.3 Spatial response and causality

Consider the response of the medium to a localized time harmonic forcing. The response to a forcing of *real* frequency ω_f and amplitude A_f, switched on at $t = 0$, is governed by the signalling problem

$$\frac{\partial \psi}{\partial t} = \mathcal{F}(\partial_x)[\psi] + \left[A_f \delta(x) H(t) e^{-i\omega_f t} + \text{c.c.}\right], \tag{15}$$

with H denoting the Heaviside unit step function.

For small amplitude forcing ($A_f \ll 1$), the response in the neighborhood of the forcing location is governed by the linear spatial problem with $\mathcal{F}$ replaced by $\mathcal{L}$ in (15). Switching on the forcing at $t = 0$ produces a transient wave packet together with the steady state response at the forcing frequency. Whenever the medium is stable or convectively unstable, transients decay or move away out of the system, and the long time response is established at the forcing frequency. When the medium is absolutely unstable, switch-on transients overwhelm the response at the forcing frequency and the signalling problem (15) is ill-posed [6,5]. Hence *we only consider the spatial problem (15) for at most CU systems.* The steady state response is made up of normal modes $e^{i(kx-\omega_f t)}$ satisfying $\omega_f = \Omega^\ell(k)$. This equation in general admits several solutions $k_m^\ell(\omega_f)$ indexed by m, the number of which very much depends on the particular form of $\Omega^\ell(k)$.

Causality requires that $\psi = 0$ for all $t < 0$. Using a residue calculation in the complex ω-plane to solve (15) with $\mathcal{F}$ replaced by $\mathcal{L}$, and assuming that temporal growth rates are bounded ($\max\{\Omega_i^\ell(k), k \text{ real}\}$ finite), it is readily shown [6,5,39] that the spatial branches k_m^ℓ either pertain to the downstream ($x > 0$) or to the upstream ($x < 0$) response to forcing. The downstream (upstream) branches are denoted by $k_m^{\ell+}$ ($k_m^{\ell-}$). For a given *real* forcing frequency the distribution of the spatial branches $k_m^\ell(\omega)$ into + or − branches is derived, according to classical arguments [6,5], from an examination of the complete linear dispersion relation $\Omega^\ell(k)$ in the entire complex k-plane. In the sequel spatial branches are said to be causal + branches or causal − branches according to whether they prevail downstream ($x > 0$) or upstream ($x < 0$) of the forcing location. Hence causality always refers to the spatial response to a localized harmonic forcing.

For simplicity assume that $\Omega^\ell(k)$ exhibits a single second-order branch point ω_0 with only two spatial branches $k^{\ell+}$ and $k^{\ell-}$, as in the case of the CGL dispersion relation (9) where

$$k^{\ell\pm}(\omega) = k_0 \pm \sqrt{2\frac{\omega - \omega_0}{\omega_{kk}}}. \tag{16}$$

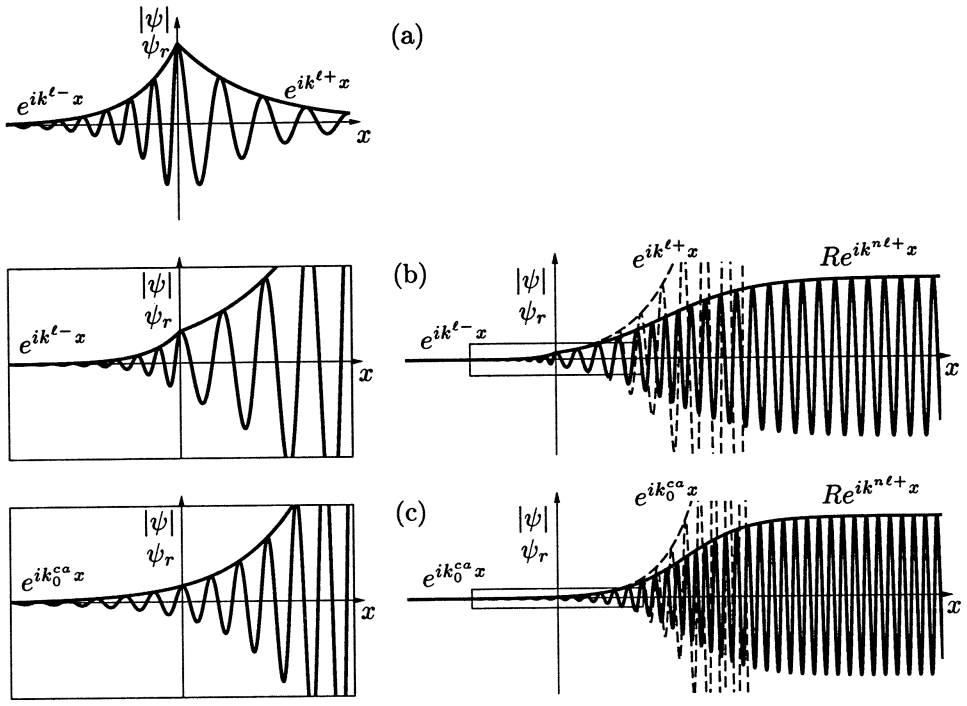


Fig. 3. Response to time-harmonic forcing applied at $x = 0$. (a) Upstream and downstream decaying response in a stable or CU medium. (b) Linearly amplified downstream response and nonlinearly saturated solution in a CU medium. (c) Stationary front in a marginally absolutely unstable medium. Note that slope discontinuity at the forcing location has vanished. Dashed lines indicate exponentially growing branches in the linear approximation.

The spatial growth rate of the response depends on $k_i^\ell \equiv \mathrm{Im}\, k^\ell$. The downstream response decays for frequencies such that $k_i^{\ell+}(\omega) > 0$; upstream decay occurs when $k_i^{\ell-}(\omega) < 0$. This is always the case for stable media (Fig.3-a). Whenever a linear spatial $k^{\ell+}(\omega)$ branch is amplified, nonlinear terms have to be taken into account at some distance from the source, however small the forcing amplitude. When the response reaches finite amplitude, nonlinear saturation prevents further amplification and leads to a nonlinear travelling wave at the excitation frequency for some *real* wave number $k^{n\ell}$ (Fig.3-b). Since the nonlinear wave train is asymptotically reached far downstream of the source, it is denoted as $k^{n\ell+}(\omega)$. This nonlinear solution would also be obtained in a temporal evolution problem at the same wave number. Thus, the forcing frequency ω_f and the nonlinear response wave number $k^{n\ell+}$ again satisfy the nonlinear dispersion relation (11). Note that due to the choice of a basic advection towards $x = +\infty$, only the downstream response may be spatially amplified, and only the $k^{n\ell+}(\omega)$ branch is accessible via a forcing problem.

The precise discussion of the relationship between linear and nonlinear spatial branches is postponed to Section 2.5.

2.4 Stationary fronts as spatial response without forcing

Many studies [22,72–75] have been devoted to the derivation of selection criteria for propagating fronts connecting an unstable $\psi = 0$ state to a fully nonlinear saturated state in a uniform medium. In situations where the front velocity is linearly selected [22,73], the front moves towards its decaying edge in AU media, towards its finite amplitude edge in CU media. A stationary front is then precisely obtained when the medium is exactly at the CU/AU transition. The same stationary front solution may be recovered in the context of the spatial response to time-harmonic forcing as discussed below.

Consider the signalling problem (15) in a uniform medium

$$\frac{\partial \psi}{\partial t} = \mathcal{F}(\partial_x; X)[\psi] + \left[A_f \delta(x) H(t) e^{-i\omega_f t} + \text{c.c.}\right], \tag{17}$$

where the frozen slow scale X has been explicitly introduced as an external control parameter. Let us examine how the response to a localized forcing of frequency ω_f varies with the parameter X which controls the instability properties of the medium. Assume that the medium is CU for $X < X^{ca}$ and marginally AU at $X = X^{ca}$, *i.e.*, $\omega_{0,i}(X) < 0$ for $X < X^{ca}$, and $\omega_0^{ca} \equiv \omega_0(X^{ca})$ real. Let $k_0^{ca} \equiv k_0(X^{ca})$ denote the complex absolute wave number at the CU/AU transition. Since basic advection is assumed to be in the positive x-direction, $k_{0,i}^{ca} < 0$, as shown in Section 4.8.

Upon making use of the associated linear dispersion relation Ω^ℓ and invoking continuity of the response at $x = 0$, the exact long time *linear* response associated with the CGL equation (17) is obtained as

$$\psi(x,t) = \frac{2A_f}{\omega_{kk}(X)} \frac{\exp i[k^{\ell\pm}(\omega_f)x - \omega_f t]}{k^{\ell+}(X,\omega_f) - k^{\ell-}(X,\omega_f)} + \text{c.c.} \tag{18}$$

The $e^{ik^{\ell+}x}$ and $e^{ik^{\ell-}x}$ branches naturally pertain to the regions $x > 0$ and $x < 0$ respectively. In order to obtain a normalized response such that $\max|\psi(0,t)| = \alpha$, the forcing amplitude is adjusted to the level

$$A_f(X,\omega_f) = \frac{\alpha}{4}\omega_{kk}(X)\left[k^{\ell+}(X,\omega_f) - k^{\ell-}(X,\omega_f)\right] \tag{19}$$

If $\alpha \ll 1$, the linear response is guaranteed to remain valid in a neighborhood of $x = 0$ even though the response may reach a finite amplitude further downstream.

If the medium is stable for large $X < 0$, both upstream and downstream parts of the response decay, *i.e.*, $k_i^{\ell+}(\omega_f; X) > 0$ and $k_i^{\ell-}(\omega_f; X) < 0$ for large $X < 0$ (cf. Fig.3-a). As the control parameter X and forcing frequency ω_f are varied continuously to approach the limit X^{ca}, ω_0^{ca}, the downstream response $k^{\ell+}$ is

eventually amplified, whereas the upstream branch $k^{\ell-}$ still decays (Fig.3-b). Indeed, by definition of ω_0^{ca} [see also (16)] both spatial branches meet at $X = X^{ca}$ and $\omega_f = \omega_0^{ca}$, *i.e.*,

$$k^{\ell+}(X^{ca}, \omega_0^{ca}) = k^{\ell-}(X^{ca}, \omega_0^{ca}) = k_0^{ca}.$$

Since $k_{0,i}^{ca} < 0$, it is therefore guaranteed that $k_i^{\ell+}(X, \omega_f)$ changes sign and becomes negative as (X, ω_f) approach (X^{ca}, ω_0^{ca}), while $k_i^{\ell-}(X, \omega_f)$ does not. In such a régime, the downstream growing response $\alpha \exp[ik^{\ell+}(X, \omega_f)x]$ reaches a finite amplitude at $x \sim (\ln \alpha)/k_i^{\ell+} > 0$. At this station, the linearly growing wave $k^{\ell+}(X, \omega_f)$ is replaced by its nonlinear counterpart $k^{n\ell+}(X, \omega_f)$.

In the convectively unstable régime ($X < X^{ca}$), both the spatial growth rate and wave number are discontinuous at $x = 0$, *i.e.*, $k^{\ell+} \neq k^{\ell-}$. The forcing location is then a singular point of the total response (Fig.3-a,b).

When $(X, \omega_f) \to (X^{ca}, \omega_0^{ca})$, the medium approaches absolute instability and both branches $k^{\ell+}(X, \omega_f)$ and $k^{\ell-}(X, \omega_f)$ tend towards k_0^{ca}. Thus, in this process, the slope discontinuity in the response at $x = 0$ smoothes out. Moreover, according to (19), the forcing amplitude $A_f(X)$ required to maintain the normalization condition $\max|\psi(0,t)| = \alpha$ vanishes. Thus in the marginally AU régime $X = X^{ca}$, a smooth stationary front of frequency $\omega_f = \omega_0^{ca}$ prevails without any forcing (Fig.3-c). This front directly connects the upstream linear $k^{\ell-}$ branch to the downstream nonlinear $k^{n\ell+}$ branch. As mentioned in Section 2.3, the + and − notations have causal meaning only in CU systems. The previous argument indicates that, in a marginally AU system, the two branches on both sides of a front are still determined by causal considerations through a continuation procedure from the CU side. From the above discussion, a stationary front in a spatially uniform system is obtained for zero-amplitude forcing whenever *the medium becomes marginally AU and the forcing frequency equals the corresponding real absolute frequency* ω_0^{ca}.

2.5 Nature of nonlinear spatial branches: Cautionary remarks

In Section 2.3 it has been demonstrated that, in the framework of a signalling problem, nonlinear wave trains are generated downstream of the forcing location in a CU system. Such a formulation naturally leads to a causal definition of spatial $k^{n\ell+}(\omega)$ branches. These fully nonlinear wave trains satisfy the nonlinear dispersion relation (11). Thus the nonlinear wave number $k^{n\ell}(\omega)$ may formally be obtained by solving (21) for a given frequency. In this subsection we discuss the precise relationship between linear and nonlinear spatial branches as illustrated in Fig.4, and introduce definitions of $k^{n\ell+}$ or $k^{n\ell-}$ branches which apply to all formal solutions of the nonlinear dispersion relation. In this process it will be seen that only the + superscript in CU systems may be assigned

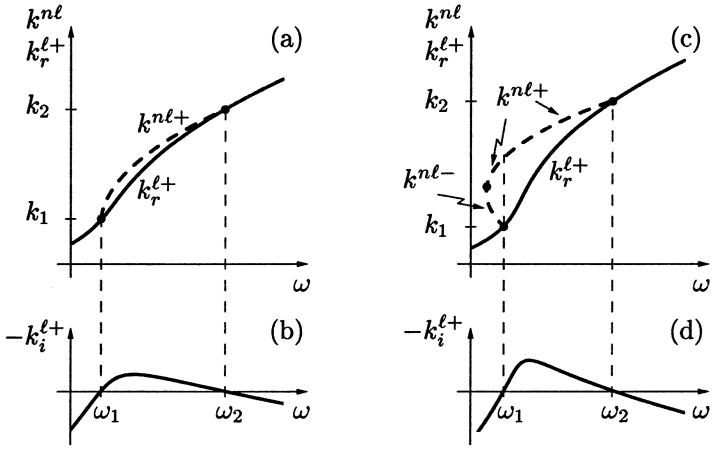


Fig. 4. Linear and nonlinear spatial branches of the CGL equation. (b,d) Spatial growth rate $-k_i^{\ell+}(\omega)$ of downstream spatial branch as a function of the real frequency. Unstable frequencies lie in the range $\omega_1 < \omega < \omega_2$. The nonlinear spatial wave number $k^{n\ell}(\omega)$ may be either single-valued as in (a) or double-valued as in (c). (a) The unique nonlinear spatial branch $k^{n\ell+}(\omega)$ (dashed curve) is defined in the unstable frequency range and is connected to the $k_r^{\ell+}(\omega)$ curve (solid line) at the neutrally stable boundaries where $k_1 = k^{\ell+}(\omega_1) = k^{n\ell+}(\omega_1)$ and $k_2 = k^{\ell+}(\omega_2) = k^{n\ell+}(\omega_2)$. (c) Two nonlinear spatial branches $k^{n\ell+}(\omega)$ and $k^{n\ell-}(\omega)$ (dashed curve) coexist, which issue from the neutrally stable boundaries at k_1 and k_2 respectively and merge at a turning point (solid dot). Note that $k^{n\ell-}$ is now connected to $k^{\ell+}$ at k_1.

to nonlinear branches *according to causality considerations.*

Whereas the temporal problem yields the real nonlinear frequency as a function of real wave number as represented by the dashed lines in Fig.1, conversely the spatial problem yields the real nonlinear wave number as a function of real frequency. This inversion process is straightforward in situations where $\Omega^{n\ell}(k)$ is monotonous as in Fig.1-a. But it is more delicate in situations where $\Omega^{n\ell}(k)$ exhibits an extremum as in Fig.1-c.

In the first case (Fig.1-a), the behavior of the linear and nonlinear spatial branches is illustrated in Fig.4-a,b. The linear downstream response is specified by the spatial growth rate $-k_i^{\ell+}$ displayed in Fig.4-b. For forcing frequencies in the range $\omega_1 < \omega < \omega_2$, the response is amplified and gives way to a nonlinear spatial solution of wave number $k^{n\ell+}$ as indicated by the dashed line in Fig.4-a. Note that, as in the temporal case (Fig.1-a), the nonlinear branch $k^{n\ell+}$ is connected to its linear counterpart $k^{\ell+}$ at the neutrally stable frequencies ω_1 and ω_2.

In the second case (Fig.1-c), the behavior of the linear and nonlinear spatial branches is as illustrated in Fig.4-c,d. The presence of an extremum in $\Omega^{n\ell}(k)$ (dashed line in Fig.1-c) is responsible for the double-valuedness of $k^{n\ell}(\omega)$ (dashed line in Fig.4-c). In the linearly unstable range $\omega_1 < \omega < \omega_2$

there is still a single nonlinear wave number $k^{n\ell+}(\omega)$ which governs the far downstream nonlinear response to forcing, and it is legitimately assigned the superscript + with a causal meaning. As in the first case, it is connected to a linear $k^{\ell+}$ branch at the neutral frequency ω_2. Note however that for $\omega < \omega_1$, two nonlinear $k^{n\ell}$ branches coexist. Following the definition adopted by the front community [75] let us introduce the "nonlinear group velocity" $d\Omega^{n\ell}(k)/dk$. The + (−) superscript is then given to the spatial $k^{n\ell}$ branch with positive (negative) nonlinear group velocity. With this convention, the + superscript is assigned to the extension of the $k^{n\ell+}$ branch down to the turning point (solid dot in Fig.4-c), whereas the − superscript is assigned to the remaining part of the $k^{n\ell}$ curve. It is now this $k^{n\ell-}$ curve that is connected to the linear $k^{\ell+}$ branch at the neutral frequency ω_1. It is essential to note that the nonlinear branches $k^{n\ell+}$ and $k^{n\ell-}$ may not be accessible via forcing at frequencies $\omega < \omega_1$. They are therefore not necessarily causal and the + and − superscripts are purely chosen for notational convenience in this frequency range.

For infinitesimally small forcing level, the wave number observed far downstream as the forcing frequency ω is varied follows the decaying complex $k^{\ell+}(\omega)$ for $\omega < \omega_1$ or $\omega > \omega_2$, and the real $k^{n\ell+}(\omega)$ in the range $\omega_1 < \omega < \omega_2$. Hence the transition between a linear and a nonlinear wave train is continuous at ω_2 where $k^{n\ell+}$ and $k^{\ell+}$ merge, but discontinuous at ω_1 with a consequent jump in wave number.

This spatial analysis only holds for CU media. In AU media, switch-on transients spread and grow *in situ*. Long time evolution is thus completely contaminated by transients and no steady state response at the forcing frequency may be identified. However solving the linear and nonlinear dispersion relations (8) and (11) for a given frequency still yields $k^{\ell}(\omega)$ and $k^{n\ell}(\omega)$ solutions. These linear and nonlinear branches then loose their causal meaning. But the corresponding nonlinear wave trains may still be generated from a temporal problem and the superscripts + and − may be assigned to the nonlinear branches $k^{n\ell}(\omega)$ via the sign of $d\Omega^{n\ell}/dk$.

3 Spatial variations of local instability properties

The previous results derived for spatially uniform media also yield the local linear and nonlinear instability characteristics of weakly nonuniform media, provided that the control parameter X now be interpreted as the slow streamwise coordinate. The respective dispersion relations at each station X read

$$\omega = \Omega^{\ell}(k, X), \quad \omega \text{ and } k \text{ complex}, \tag{20}$$

$$\omega = \Omega^{n\ell}(k, X), \quad \omega \text{ and } k \text{ real}. \tag{21}$$

The local *linear* dispersion relation pertains to any *complex* wave number whereas the local *nonlinear* dispersion relation is defined only for *real* wave numbers associated with a positive temporal growth rate $\Omega_i^\ell(k,X) > 0$. In strictly uniform media, linear normal modes are sought in the form $\psi = A\exp i[k^\ell(\omega)x - \omega t] + \text{c.c.}$ In weakly nonuniform media, such modes are replaced by

$$\psi = A(X)\exp\left(\frac{i}{\epsilon}\int^X k^\ell(u,\omega)du - i\omega t\right) + \text{c.c.} \tag{22}$$

As demonstrated in the classical WKBJ procedure outlined in Section 5, the local linear wave number $k^\ell(X,\omega)$ necessarily satisfies the local linear dispersion relation (20). In strictly uniform media, nonlinear travelling waves are sought in the form $\Psi[k^{n\ell}(\omega)x - \omega t]$. In weakly nonuniform media, such travelling waves are replaced by slowly modulated wave packets of the form

$$\psi \sim \Psi\left(\frac{1}{\epsilon}\int^X k^{n\ell}(u,\omega)du - \omega t + \Theta(X); k^{n\ell}(X,\omega), X\right), \tag{23}$$

where the local nonlinear wave number $k^{n\ell}(X,\omega)$ satisfies the nonlinear local dispersion relation (21). The slowly varying functions $A(X)$ and $\Theta(X)$ appearing in (22) and (23) respectively are obtained in the complete asymptotic analysis (Section 5).

The objective of this section is then to study the changing topology of linear complex k^ℓ and nonlinear real $k^{n\ell}$ spatial branches as the global real frequency is varied.

3.1 Instability domains

Let us first introduce the regions of local convective or absolute instability in physical X-space and determine the domain of existence of nonlinear wave trains in (X,k)-space. The local absolute frequency $\omega_0(X)$ and wave number $k_0(X)$ are derived from the local linear dispersion relation (20) as in (14). The local convective or absolute nature of the medium is determined by the sign of $\omega_{0,i}(X)$. In a typical situation of interest, absolute instability occurs in a central finite domain. Consider $\omega_0(X)$ to be of the form sketched in the complex ω-plane in Fig.5-a: $\omega_{0,i}(X)$ is an increasing-decreasing function of X with a single maximum $\omega_{0,i}^{max}$ reached at $X = X^{max}$.

Whenever $\omega_{0,i}^{max} > 0$, there exists a finite *AU domain*, $X^{ca} < X < X^{ac}$, defined as the region where $\omega_{0,i}(X) > 0$. Its boundaries X^{ca} and X^{ac} are the stations where the local absolute frequency is real, $\omega_0^{ca} \equiv \omega_0(X^{ca})$ and $\omega_0^{ac} \equiv \omega_0(X^{ac})$

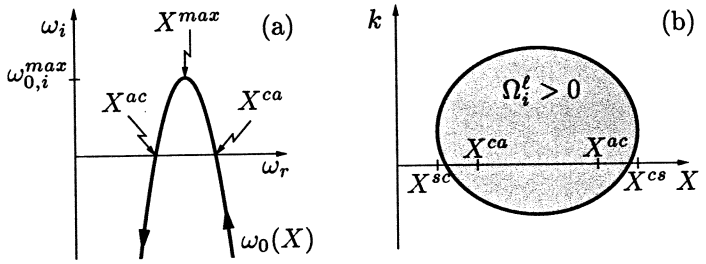


Fig. 5. (a) Locus of the local absolute frequency $\omega_0(X)$ in the complex frequency plane for $-\infty < X < +\infty$. The AU interval $X^{ca} < X < X^{ac}$ is associated with $\omega_{0,i}(X) > 0$. (b) Nonlinear balloon in the (X,k)-plane defined by $\Omega_i^\ell(k,X) > 0$ and bounded by the curve of neutral stability $\Omega_i^\ell(k,X) = 0$. In the X-direction the balloon spans the domain of local linear instability $X^{sc} < X < X^{cs}$ and extends beyond the AU interval.

respectively.

The domain of local instability, characterized by unstable real wave numbers, $\Omega_i^\ell(k,X) > 0$, defines the *nonlinear balloon* in the (X,k)-plane (Fig.5-b). In the X-direction the balloon extends beyond the AU domain to the stations of linear neutral stability, denoted X^{sc} and X^{cs}. At each unstable location, the nonlinear balloon extends in the k-direction over the local unstable wave number range. Note that, due to causality, large wave numbers are always temporally decaying; thus the nonlinear balloon is necessarily bounded in the k-direction.

A typical system therefore displays the following structure: a central AU domain $X^{ca} < X < X^{ac}$ of finite extent, surrounded by two CU regions $X^{sc} < X < X^{ca}$ and $X^{ac} < X < X^{cs}$, which in turn are embedded in two semi-infinite stable regions extending to $X = \pm\infty$. As mentioned in Section 4.1, one may relax the stability requirement at $X = \pm\infty$ and the medium may remain CU to $X = \pm\infty$.

3.2 Linear spatial branches

The loci of linear spatial branches $k^\ell(X,\omega)$ as functions of X is now qualitatively discussed in the complex k-plane for different values of the complex frequency ω. Such an analysis will illustrate the relationship between the behavior of linear spatial branches and the local CU/AU properties of the medium. Linear spatial branches $k^\ell(X,\omega)$ are obtained by solving the local linear dispersion relation (20) for a given frequency ω. In the case of the CGL equation (4) they read

$$k^{\ell\pm}(X,\omega) = k_0(X) \pm \sqrt{2\frac{\omega - \omega_0(X)}{\omega_{kk}(X)}}. \tag{24}$$

In Section 2.3 the choice of the + and − branches was shown to be dictated by causality for real frequencies in stable or CU media. Thus the $k^{\ell+}$ and $k^{\ell-}$ branches are unambiguously defined in the distinct regions $X < X^{ca}$ and $X > X^{ac}$ for real frequencies. The fate of spatial branches in the AU range $X^{ca} < X < X^{ac}$ is now examined for different frequencies in the complex ω-plane as illustrated in Fig.6.

As a result of causality [6,5], the spatial branches $k^{\ell\pm}(X,\omega)$ do not cross the k_r-axis in the complex k-plane for large enough $\omega_i > 0$. For such frequencies far above the absolute frequency curve $\{\omega_0(X)\}$ (cf. Fig.6-a), the $k^{\ell+}$ ($k^{\ell-}$) branch is globally defined as the one located in the upper (lower) half k-plane for all real X. The $k^{\ell\pm}(X,\omega)$ branches continuously deform as ω is varied. They may cross the k_r-axis for finite values of X (Fig.6-b,c,d), but remain in the same half k-plane for $X \to \pm\infty$. As ω is kept above the curve $\{\omega_0(X)\}$ (denoted by $\omega \succ \{\omega_0(X)\}$), no branch switching may occur as readily seen by inspection of eq.(24). This property yields definitions of the $k^{\ell\pm}$ branches that remain uniformly valid in X, for all complex frequencies $\omega \succ \{\omega_0(X)\}$, even though the medium may be locally AU.

When $\omega \in \{\omega_0(X)\}$, say $\omega = \omega_0(X_0)$, the two $k^{\ell\pm}$ branches pinch at $k_0(X_0)$ for $X = X_0$ (Fig.6-e illustrates the case of particular interest where $X_0 = X^{ca}$). For frequencies $\omega \prec \{\omega_0(X)\}$ below the absolute frequency curve (Fig.6-f), the continuous k^{ℓ} curves connect the upper and lower half k-planes as X is varied from $-\infty$ to $+\infty$. Global $k^{\ell\pm}$ branches can no longer be defined, but the + and − superscripts may still be assigned according to causality in the distinct $X < X^{ca}$ and $X > X^{ac}$ regions represented by thick lines in Fig.6. For $\omega \prec \{\omega_0(X)\}$ (Fig.6-f), the $k^{\ell-}$ branch for $X < X^{ca}$ is connected to the $k^{\ell+}$ branch in the region $X > X^{ac}$, across the AU domain (part of the curve being represented by a thin line).

These considerations apply in particular to real ω. For frequencies outside the ω_0^{ca}-ω_0^{ac} interval, *i.e.*, $\omega \succ \{\omega_0(X)\}$, the $k^{\ell+}$ and $k^{\ell-}$ branches are globally defined, although causality considerations do not apply in the central AU domain. For frequencies in the ω_0^{ca}-ω_0^{ac} interval, *i.e.*, $\omega \prec \{\omega_0(X)\}$, the $k^{\ell+}$ and $k^{\ell-}$ branches turn one into the other across the AU domain.

3.3 Nonlinear spatial branches

The goal of this section is to describe synthetically the qualitative properties of the nonlinear spatial branches $k^{n\ell}(X,\omega)$ as functions of X for different values of the real frequency ω. Finite amplitude waves are governed by the nonlinear dispersion relation (21). Figure 7-a,b illustrates its properties by projecting the surface defined as $\omega = \Omega^{n\ell}(k,X)$ in the (X,k,ω)-space onto the (X,k) and

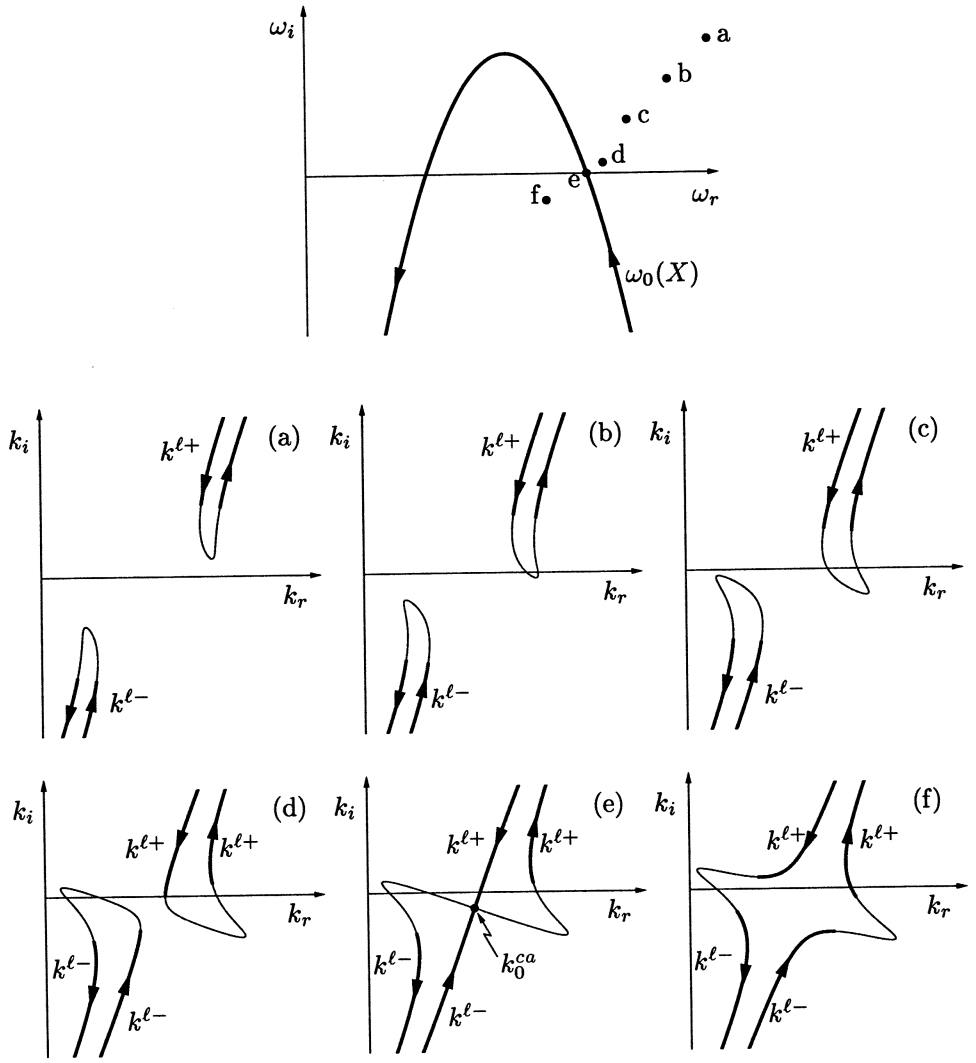


Fig. 6. (a-f) Loci of linear spatial branches $k^{\ell}(X,\omega)$ of CGL equation in the complex k-plane for frequencies ω indicated in the complex frequency plane on top sketch. Arrows on the curves indicate direction of increasing X. Thick lines pertain to the stable or CU regions $X < X^{ca}$ and $X > X^{ac}$, thin lines to the central AU region $X^{ca} < X < X^{ac}$. (a-d) For frequencies $\omega \succ \{\omega_0(X)\}$, the spatial branches $k^{\ell\pm}(X)$ remain distinct and are located in the same half k-plane for $X \to \pm\infty$, but they may cross the k_r-axis for finite values of X. As the frequency approaches the $\omega_0(X)$ curve, the spatial branches move closer to each other. (e) For a frequency located on the $\omega_0(X)$ curve, here $\omega = \omega_0(X^{ca})$, pinching occurs at the corresponding absolute wave number, here at $k = k_0^{ca}$, when $X = X^{ca}$. (f) When $\omega \prec \{\omega_0(X)\}$, the continuous curves connect the upper and lower half k-planes as $X \to \pm\infty$. Definition as $k^{\ell\pm}$ branches still holds in the distinct CU domains $X < X^{ca}$ and $X > X^{ac}$, but not in the central AU region.

(X,ω) planes respectively. Nonlinear spatial branches $k^{n\ell}(X,\omega)$ for a given frequency ω are obtained as the intersections of this surface with planes of constant frequency.

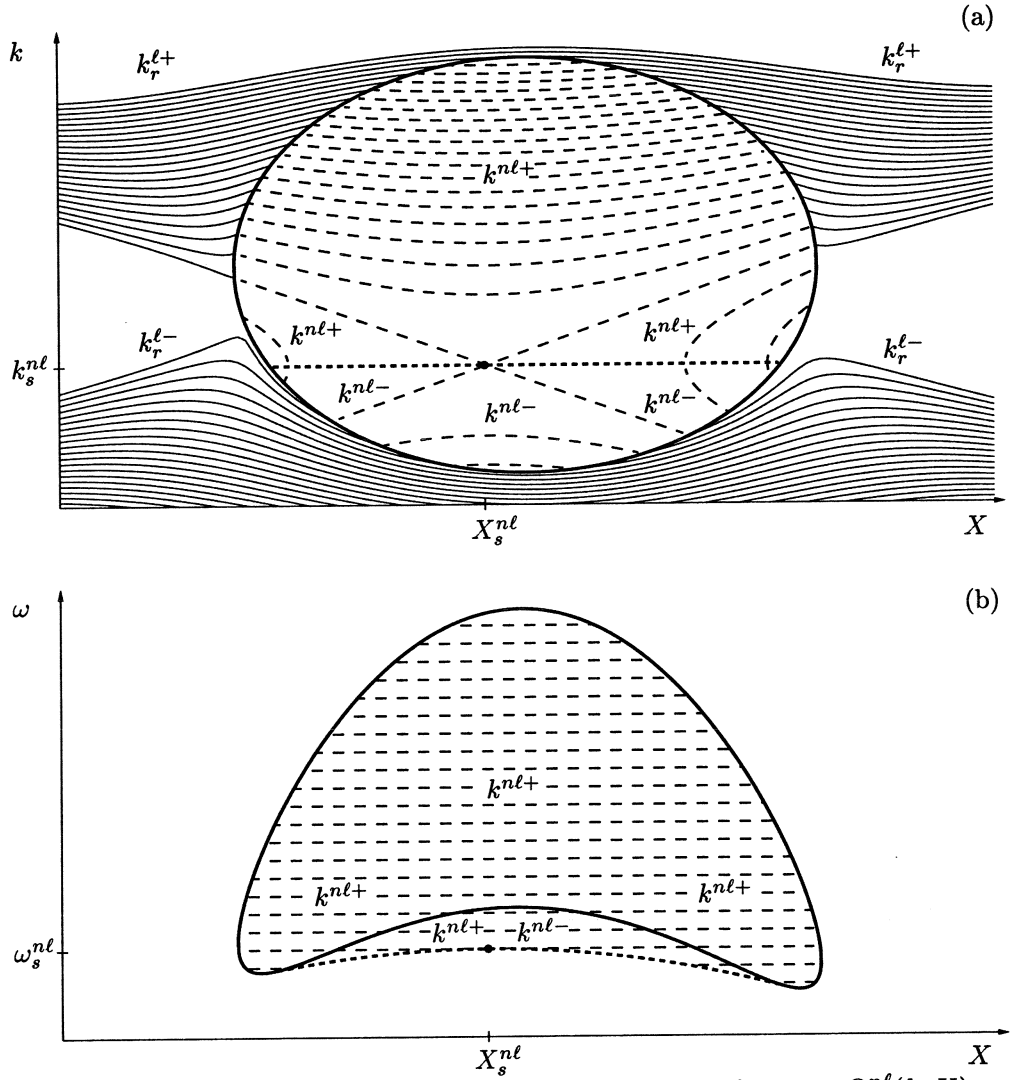


Fig. 7. Projections of the nonlinear dispersion relation surface $\omega = \Omega^{n\ell}(k, X)$ on the (X, k)- and (X, ω)-planes. Nonlinear spatial branches $k^{n\ell+}(X, \omega)$ and $k^{n\ell-}(X, \omega)$ represented by constant frequency level curves (dashed lines) live within the neutral stability boundary (thick solid line). Similarly marked curves in (a) and (b) map one into the other. (a) Nonlinear spatial branches display a saddle structure and, by convention, $k^{n\ell+}$ and $k^{n\ell-}$ refer to the upper and lower regions on either side of the steepest descent curve (thick dotted line) emerging from the saddle point $X_s^{n\ell}, k_s^{n\ell}$ (solid dot). The real parts $k_r^{\ell\pm}$ of the linear spatial branches (thin solid lines) are also shown outside the nonlinear balloon for the same frequencies as the nonlinear branches. Note their continuous connection at the neutral stability boundary. (b) In the (X, ω)-plane, the $k^{n\ell+}$ and $k^{n\ell-}$ branches give rise to two overlapping sheets joining along a fold curve (thick dotted line). Within the neutral stability boundary (solid curve), only the $k^{n\ell+}$ sheet exists. Between the fold line and the neutral curve, both $k^{n\ell+}$ and $k^{n\ell-}$ sheets coexist. The saddle point located at $X_s^{n\ell}$ corresponds to the frequency $\omega_s^{n\ell}$.

Nonlinear wave trains only exist inside the nonlinear balloon of the (X,k)-plane, defined by $\Omega_i^\ell(k,X) > 0$ (see Fig.5-b). Its neutrally stable boundary characterized by $\Omega_i^\ell(k,X) = 0$ is represented by the thick closed curve in Fig.7-a. Since the nonlinear dispersion relation $\omega = \Omega^{n\ell}(k,X)$ is always a single-valued function of k, the mapping in the (X,k)-plane (Fig.7-a) is one-to-one and all the nonlinear solutions are contained inside the neutral stability boundary.

By contrast, $k^{n\ell}(X,\omega)$ is not ensured to be a single-valued function of ω, the projection of the same surface in the (X,ω)-plane (Fig.7-b) may therefore display an overlap region represented by two sheets that are connected at a fold, as indicated by the thick dotted line. In this view, the region inside the neutral curve (thick line) corresponds to a unique wave number $k^{n\ell+}(X,\omega)$ of the nonlinear dispersion relation, whereas the domain between the neutral curve and the fold corresponds to two distinct sheets associated with two wave numbers $k^{n\ell\pm}$. The image of the fold line in the (X,k)-plane is also represented by a thick dotted line in Fig.7-a.

The nonlinear spatial branches $k^{n\ell}(X,\omega)$ of real frequency ω are obtained as the level contours $\Omega^{n\ell}(k,X) = \mathrm{C}^{\mathrm{st}}$ indicated by thin dashed lines in both figures. In Fig.7-b they are just straight lines. Depending on the frequency, these straight lines may intersect either only the single-valued domain, or both domains. The double-valued nature of the nonlinear spatial branches merely reflects features already encountered in the uniform case in Section 2.5 (Fig.4-c). We have deliberately chosen a configuration displaying this double-valuedness, which is made manifest here by the saddle point structure in the contour levels $\Omega^{n\ell}(k,X) = \mathrm{C}^{\mathrm{st}}$ of Fig.7-a. Following the definition adopted in Section 2.5, the nonlinear spatial branches are labelled $k^{n\ell+}$ and $k^{n\ell-}$ according to the sign of the "nonlinear group velocity" $\partial\Omega^{n\ell}/\partial k$. Accordingly, the $k^{n\ell+}$ and $k^{n\ell-}$ domains of Fig.7-a precisely correspond to the two sheets of Fig.7-b connected via the thick dashed fold line.

In order to emphasize the relationship between linear and nonlinear branches, the linear spatial branches $k^{\ell\pm}(X,\omega)$ have also been displayed by thin solid lines in Fig.7-a through their real part $k_r^{\ell\pm}(X,\omega)$ at the same frequencies. Note that linear branches continuously connect to nonlinear branches at the neutral stability boundary. This property is not surprising: At the neutral stability boundary in the (X,k)-plane, the linear branch $k^\ell(X,\omega)$ is purely real and equals its nonlinear counterpart $k^{n\ell}(X,\omega)$ so that

$$k^{n\ell}(X,\omega) = k_r^\ell(X,\omega) \quad \text{and} \quad k_i^\ell(X,\omega) = 0.$$

Equivalently,

$$\Omega^{n\ell}(k,X) = \Omega_r^\ell(k,X) \quad \text{and} \quad \Omega_i^\ell(k,X) = 0.$$

As discussed in Section 3.2 (Fig.6), the linear spatial branches are globally defined as $k^{\ell+}$ or $k^{\ell-}$ for $\omega \succ \{\omega_0(X)\}$. While lowering the frequency, starting from large positive values, the $k^{\ell+}$ and/or $k^{\ell-}$ branch may cross the k_r-axis in the complex k-plane (Fig.6-b,c,d). As this linear wave number branch moves into the opposite half k-plane, it becomes spatially amplified and gives birth to a nonlinear branch. This corresponds in the (X,k)-plane to the emergence of a $k^{n\ell}$ branch connected at the boundary of the nonlinear balloon to a k_r^{ℓ}-branch (Fig.7-a).

By further lowering the frequency, switching between the nonlinear branches may take place, as implied by the saddle structure of the dashed curves in Fig.7-a. When the frequency decreases, pinching between $k^{n\ell-}$ and $k^{n\ell+}$ will take place for $\omega = \omega_s^{n\ell}$ at the saddle point $(X_s^{n\ell}, k_s^{n\ell})$ of the nonlinear dispersion relation (21) in the (X,k)-plane. Below this saddle-point frequency, the nonlinear spatial branches move into the left- and right-hand sectors bounded by the saddle-point asymptotes (Fig.7-a). For a given frequency in this range, nonlinear spatial branches are indeed generated at the boundary of the nonlinear balloon but they fail to exist in the heart of the nonlinear region surrounding the saddle-point. This behavior is provoked by the merging of $k^{n\ell+}$ and $k^{n\ell-}$ on the fold line (thick dotted line of Fig.7-a) and their subsequent disappearance. The implications of such a nonlinear saddle point structure on global mode selection is discussed in Section 4.6.

4 Globally synchronized structures

Having investigated local instability properties of the spatially developing medium, we now turn to the study of globally synchronized solutions of system (1) and associated bifurcations. Such *global modes* are defined as stationary time-periodic solutions satisfying

$$\psi(x, t + 2\pi/\omega_g) = \psi(x,t)$$

where ω_g is the global real frequency. Frequency selection criteria for self-sustained global oscillations are derived below and their spatial structure is obtained. The properties of the medium which dictate the selected global mode type are identified and the ensuing bifurcations are analyzed as global control parameters are varied.

4.1 Boundary conditions

To completely determine the global mode problem, proper boundary conditions in connection with eq.(1) have to be specified. Global modes are defined

as intrinsic oscillations which are due to the dynamics of the central region and not to perturbations invading the system from $X = \pm\infty$. Consequently the boundary conditions must be *causal*: The solution close to the boundaries is necessarily dictated by the intrinsic oscillations occurring in the central region. Thus, far downstream near $X = +\infty$ the solution is necessarily made up of a + branch caused by the dynamics governing the central region upstream of it. Similarly the solution necessarily involves a − branch towards $X = -\infty$. Such boundary conditions at $X = \pm\infty$ will be referred to as causal.

When the medium is assumed to be stable in the far downstream and upstream regions, causal boundary conditions are equivalent with decaying ones. Indeed, in the stable regions no nonlinear solutions exist. Causality then requires a linear $k^{\ell+}$ ($k^{\ell-}$) branch towards $X = +\infty(-\infty)$. Due to stability, $k_i^{\ell+} > 0$ and $k_i^{\ell-} < 0$, thus the solution necessarily decays towards $X = \pm\infty$.

However the medium may remain CU up to $X = \pm\infty$. In such instances, decaying boundary conditions are not necessarily fulfilled. However causality still holds: if the solution remains fully nonlinear down to $X = +\infty$, it is there necessarily made up of the $k^{n\ell+}$ branch only. Thus proper boundary conditions for the global mode problem do not necessarily require exponential decay: they should however satisfy causality.

Since a global mode is a solution over the entire X-axis, it necessarily connects a − branch at $X = -\infty$ to a + branch at $X = +\infty$. This crossover from − to + branches may only be achieved for certain frequencies. The search for global modes is thus a nonlinear eigenvalue problem for the global frequency ω_g. The manner in which this crossover takes place in the central region gives rise to different types of global modes as described below.

4.2 Steep global modes

According to [68], the spatial structure of *steep global modes* is characterized by the presence of a sharp front at the upstream boundary X^{ca} of the AU region, as sketched in Fig.8-a.

This front at the location of marginal absolute instability $[\omega_{0,i}(X^{ca}) = 0]$ is precisely of the type obtained in Section 2.4: It oscillates at the *real* absolute frequency $\omega_g = \omega_0^{ca} \equiv \omega_0(X^{ca})$ and allows a crossover between the upstream $k^{\ell-}$ and the downstream $k^{n\ell+}$ branches. The exponential decay of the upstream tail of the front is determined by the imaginary part of the corresponding absolute wave number $k_0^{ca} \equiv k_0(X^{ca})$. The upstream $k^{\ell-}(X, \omega_g)$ branch extending towards $X = -\infty$ is precisely generated at the pinch point $X = X^{ca}$ in the complex k-plane (Fig.8-b). The downstream nonlinear wake of the front is made up of the $k^{n\ell+}(X, \omega_g)$ branch. As depicted in the (X, k)-plane

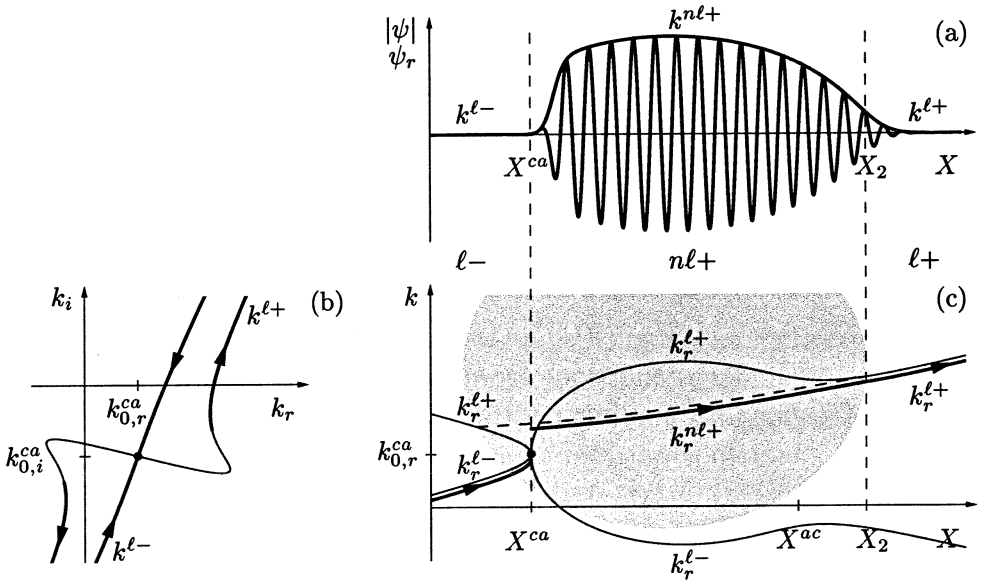


Fig. 8. Structure of steep global mode in CGL equation. (a) Envelope $|\psi|$ and real part ψ_r as functions of downstream distance X. The sharp front located at the upstream boundary X^{ca} of AU region initiates the fully nonlinear development extending down to the neutral station X_2. (b) Linear spatial branches $k^{\ell\pm}(X)$ of steep global frequency ω_0^{ca} in the complex k-plane. Pinching occurs for the absolute wave number k_0^{ca} at $X = X^{ca}$. Thick lines pertain to the stable or CU regions $X < X^{ca}$ and $X > X^{ac}$, thin lines to the central AU region $X^{ca} < X < X^{ac}$. (c) Corresponding linear $k_r^{\ell\pm}$ (solid) and nonlinear $k^{n\ell+}$ (dashed) spatial branches in the (X,k)-plane. Local wave number of steep global mode in (a) follows path indicated by thick line. Three domains are identified: the $k^{\ell-}$ branch prevails in the upstream linear $\ell-$ region $X < X^{ca}$; the front at X^{ca} is associated with a jump in wave number and in its wake the $k^{n\ell+}$ branch develops in the fully nonlinear $n\ell+$ domain $X^{ca} < X < X_2$ extending towards the boundary of the nonlinear balloon (shaded); the $k^{\ell+}$ branch continuously takes over in the linear $\ell+$ region downstream of the neutral station X_2.

of Fig.8-c, nonlinear travelling waves prevail in the region $X^{ca} < X < X_2$ extending down to the location X_2 where the $k^{n\ell+}$ branch meets the boundary of the nonlinear balloon in the (X,k)-plane. At the neutrally stable station X_2 the amplitude of the nonlinear travelling wave vanishes and the linear branch $k^{\ell+}(X,\omega_g)$ continuously takes over in the downstream linear region $X > X_2$.

The following frequency selection criterion then holds: the steep global frequency ω_g is given by the real absolute frequency ω_0^{ca} prevailing at the front location X^{ca} separating the CU and AU regions. In other words

$$\omega_g = \omega_0(X^{ca}) \quad \text{and} \quad \omega_{0,i}(X^{ca}) = 0. \tag{25}$$

The front at X^{ca} effectively acts as a wave maker for the entire flow. It may be interpreted as a local oscillator inducing the linear upstream $-$ branch and the nonlinear downstream $+$ branch.

4.3 Saddle node bifurcation to steep global modes

It should be noted that the steep global mode criterion (25) is also fulfilled by the absolute frequency ω_0^{ac} prevailing at the downstream boundary X^{ac} of the AU region. Thus, whenever $\omega_{0,i}^{max} > 0$, two steep global modes exist: one of frequency ω_0^{ca} with a front at the upstream boundary X^{ca} of the AU region and one of frequency ω_0^{ac} with a front at its downstream boundary X^{ac} (see Fig.5-a). When $\omega_{0,i}^{max} < 0$, no AU region is present and no steep global mode exists. Thus $\omega_{0,i}^{max}$ constitutes the global control parameter governing the existence of steep global modes. When $\omega_{0,i}^{max}$ is varied, transition to steep global modes occurs via a saddle-node bifurcation at $\omega_{0,i}^{max} = 0$ as demonstrated below.

The spatial structure of a solution with a front at X^{ca} has been detailed in the previous subsection. The structure of a solution with a front at X^{ac} is similar. Indeed, both linear $k^{\ell\pm}(X, \omega_0^{ac})$ branches equal $k_0^{ac} \equiv k_0(X^{ac})$ at $X = X^{ac}$. Due to the assumption $k_{0,i} < 0$, the $k^{\ell-}$ branch is again exponentially damped while the $k^{\ell+}$ branch is amplified. As a result, nonlinear travelling waves $k^{n\ell+}$ are only present downstream of the front ($X > X^{ac}$) and linear damped waves $k^{\ell-}$ upstream of the front ($X < X^{ac}$). Thus the nonlinear part of such a global mode extends in the downstream CU region, whereas the central AU domain is covered by an exponentially decaying upstream tail.

Let us now show that an upstream front is a stable configuration whereas a downstream front is unstable. Consider a small displacement of the upstream front from its equilibrium location X^{ca} towards $X > X^{ca}$. The front now experiences a slightly AU medium, hence, according to Dee and Langer [22], the nonlinear part grows and the front propagates towards its decaying edge, *i.e.*, upstream. When this front is displaced towards $X < X^{ca}$, it penetrates into a CU region and is thus pushed downstream. In any case the front is seen to return to its equilibrium position X^{ca}.

On the contrary, a downstream front displaced from its equilibrium position X^{ac} towards the AU region $X < X^{ac}$ continues to propagate upstream and completely invades the AU domain. When the front is displaced towards the CU region $X > X^{ac}$, it is swept away downstream towards $X = +\infty$. A downstream front is therefore unstable.

Thus when $\omega_{0,i}^{max} > 0$, a pair of steep global modes exists: the mode with a front at the upstream (resp. downstream) boundary of the AU region is stable (resp. unstable). In the limit $\omega_{0,i}^{max} \downarrow 0$, the AU domain shrinks and the front locations move in closer to each other, $X^{ca} \uparrow X^{max}$ and $X^{ac} \downarrow X^{max}$. When $\omega_{0,i}^{max} = 0$ both front frequencies ω_0^{ca} and ω_0^{ac} equal $\omega_0(X^{max})$, and both steep global modes coincide. When $\omega_{0,i}^{max} < 0$, the domain is nowhere AU and no steep global mode exists.

This behavior is typical of a saddle node bifurcation: while decreasing the bifurcation parameter $\omega_{0,i}^{max}$, a stable and an unstable solution meet and disappear at the critical value $\omega_{0,i}^{max} = 0$.

Note that in general the steep global mode remains fully nonlinear for all $\omega_{0,i}^{max} > 0$. Indeed, for $0 < \omega_{0,i}^{max} \ll 1$ the extent of the convectively unstable domain remains $\mathcal{O}(1)$ (in terms of X) and so does the nonlinear region where the global mode lives.

4.4 Linear global modes

The linear global instability of the unperturbed $\psi = 0$ state has been studied by Chomaz *et al.* [13] and Le Dizès *et al.* [51]. The instability properties were derived from an analytic continuation of the local absolute frequency $\omega_0(X)$ in the complex X-plane, as summarized below.

Linear global modes are assumed to be of the form $\psi(x,t) = \phi(X)e^{-i\omega_g t}$ of complex global frequency ω_g. The spatial function ϕ is defined over the complex X-plane and the local complex wave number satisfies the linear dispersion relation (20) with *complex* X. A linear global mode is entirely made up of linear spatial branches $k^{\ell\pm}$. Due to causal boundary conditions, the $k^{\ell-}$ branch prevailing near $X = -\infty$ must necessarily connect to the $k^{\ell+}$ branch near $X = +\infty$. This can be achieved at a saddle point X_s^ℓ of the absolute frequency in the complex X-plane[1]. The frequency of the linear global mode is then equal to the saddle point frequency ω_s^ℓ, defined by

$$\omega_s^\ell = \omega_0(X_s^\ell) \quad \text{where} \quad \frac{d\omega_0}{dX}(X_s^\ell) = 0, \tag{26}$$

or equivalently by

$$\omega_s^\ell = \Omega^\ell(k_s^\ell, X_s^\ell) \quad \text{where} \quad \frac{\partial\Omega^\ell}{\partial k}(k_s^\ell, X_s^\ell) = \frac{\partial\Omega^\ell}{\partial X}(k_s^\ell, X_s^\ell) = 0. \tag{27}$$

Linear instability is determined by the sign of $\omega_{s,i}^\ell \equiv \mathrm{Im}\,\omega_s^\ell$; when $\omega_{s,i}^\ell < 0$ (resp. $\omega_{s,i}^\ell > 0$) the state $\psi = 0$ is linearly stable (resp. unstable).

[1] Only linear global modes with a double turning point are considered here. The reader is referred to Le Dizès *et al.* [51] for a detailed analysis of linear global modes with two simple turning points.

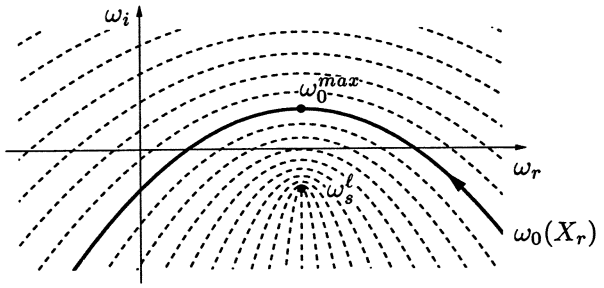


Fig. 9. Curves $\omega_0(X_r+iX_i)$ in the complex frequency plane for different values of X_i when X_r varies along the entire real axis. Bold curve pertains to $X_i = 0$. The linear saddle point frequency ω_s^ℓ is obtained at a cusp of this set of curves and is seen to lie below ω_0^{max}, towards the center of curvature of the $\omega_0(X_r)$ curve.

4.5 Hysteresis

The existence of nonlinear steep global modes is determined by the sign of $\omega_{0,i}^{max}$, while the linear global instability of the unperturbed state $\psi = 0$ is dictated by the sign of $\omega_{s,i}^\ell$. It is now shown qualitatively that always $\omega_{0,i}^{max} \geq \omega_{s,i}^\ell$, and in general $\omega_{0,i}^{max} > \omega_{s,i}^\ell$. Thus steep global modes may exist in globally linearly stable media (situations where $\omega_{s,i}^\ell < 0 < \omega_{0,i}^{max}$), and the saddle node bifurcation implies hysteretic behavior as $\omega_{0,i}^{max}$ is varied.

The relative position of $\omega_{0,i}^{max}$ and $\omega_{s,i}^\ell$ is most conveniently illustrated in the complex frequency plane as sketched in Fig.9. The solid curve represents $\omega_0(X)$ for real X. The AU region corresponds to the X-interval over which $\omega_0(X)$ lies in the $\omega_i > 0$ half-plane. The maximum $\omega_{0,i}^{max}$ is reached at $X = X^{max}$. Thus steep global modes exist whenever the curve $\omega_0(X)$ crosses the real ω-axis. The complex frequency ω_s^ℓ is obtained at a saddle point of the analytically continued function $\omega_0(X)$. For most situations of physical interest, $\omega_{0,i}(X)$ is an increasing-decreasing function on the real X-axis, while $\omega_{0,r}(X)$ is simply a smooth function. The dashed curves of Fig.9 represent the loci of $\omega_0(X_r+iX_i)$ for different values of X_i when X_r varies along the entire real axis. The saddle point frequency ω_s^ℓ is obtained at a cusp of this set of curves and lies below the $\omega_0(X_r)$ curve, towards its center of curvature. Thus it follows clearly that $\omega_{0,i}^{max} > \omega_{s,i}^\ell$ and one recovers the well known result that global linear instability requires an AU region of finite extent [13,51].

In the neighborhood of ω_0^{max}, the absolute frequency $\omega_0(X)$ may be approximated by the Taylor expansion

$$\omega_0(X) \sim \omega_0^{max} + \omega_{0X}(X - X^{max}) + \frac{1}{2}\omega_{0XX}(X - X^{max})^2, \tag{28}$$

with $\omega_{0X,i} = 0$ and $\omega_{0XX,i} < 0$. The linear saddle point, solution of (26), is

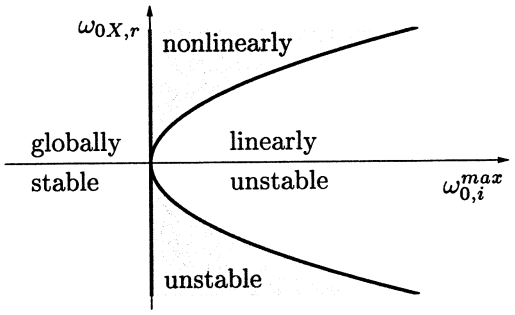


Fig. 10. Global linear and nonlinear stability in the $(\omega_{0,i}^{max}, \omega_{0X,r})$-plane. Global stability is governed by the sign of $\omega_{0,i}^{max}$. When $\omega_{0,i}^{max} > 0$ the medium is globally nonlinearly unstable although linearly stable in the gray region.

then explicitly given by

$$X_s^\ell = X^{max} - \frac{\omega_{0X,r}}{\omega_{0XX}} \quad \text{and} \quad \omega_s^\ell = \omega_0^{max} - \frac{1}{2}\frac{(\omega_{0X,r})^2}{\omega_{0XX}}, \tag{29}$$

thus

$$\mathrm{Im}\,\omega_s^\ell = \omega_{0,i}^{max} + \frac{1}{2}\frac{(\omega_{0X,r})^2}{|\omega_{0XX}|^2}\omega_{0XX,i}.$$

Only if $d\omega_{0,r}(X^{max})/dX = 0$, does the saddle point X_s^ℓ coincide with X^{max} on the real X-axis and, under such a condition, $\omega_s^\ell = \omega_0(X^{max})$. The difference between $\omega_{0,i}^{max}$ and $\omega_{s,i}^\ell$ is seen to depend on the magnitude of $\omega_{0X,r} \equiv d\omega_{0,r}(X^{max})/dX$ and to scale as $(\omega_{0X,r})^2$. The influence of the two parameters $\omega_{0,i}^{max}$ and $\omega_{0X,r}$ on global linear and nonlinear instability is illustrated in Fig.10.

The following scenario holds as the global control parameter $\omega_{0,i}^{max}$ is varied at a fixed $\omega_{0X,r}$ setting. When $\omega_{0,i}^{max} < 0$ (left-hand half-plane of Fig.10), the unperturbed state is stable, no nonlinear global mode exists. When $\omega_{0,i}^{max} > 0$ while $\omega_{s,i}^\ell < 0$ (shaded region of Fig.10), a pair of steep global modes exist, one of which is stable, the other unstable. However the unperturbed state is still linearly globally stable[2], but nonlinearly unstable. Only for $\omega_{0,i}^{max}$ large enough such that $\omega_{s,i}^\ell > 0$ (clear region inside parabola of Fig.10), does the basic state become linearly unstable. Whereas the global saddle node bifurcation is controlled by $\omega_{0,i}^{max}$, the extent of the hysteresis range in $\omega_{0,i}^{max}$ is governed by a second control parameter, namely $\omega_{0X,r}$.

[2] The unperturbed state is however *locally* unstable.

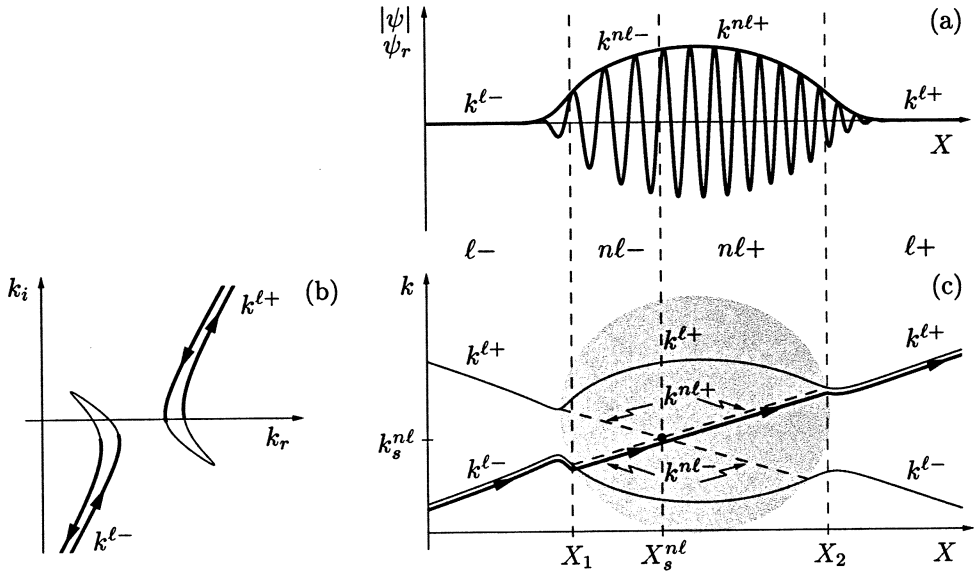


Fig. 11. Structure of soft global mode in CGL equation. (a) Overall smoothly varying envelope $|\psi|$ and real part ψ_r as functions of downstream distance X. (b) Linear spatial branches $k^{\ell\pm}(X)$ of nonlinear saddle point frequency $\omega_s^{n\ell}$ in the complex k-plane. Both linear branches cross the k_r-axis and give birth to their nonlinear counterparts at the respective neutral stations. Thick lines pertain to the stable or CU regions $X < X^{ca}$ and $X > X^{ac}$, thin lines to the central AU region $X^{ca} < X < X^{ac}$. (c) Corresponding linear $k_r^{\ell\pm}$ (solid) and nonlinear $k^{n\ell\pm}$ (dashed) spatial branches in the (X,k)-plane. Pinching of nonlinear branches occurs for $k_s^{n\ell}$ at $X = X_s^{n\ell}$ in the core of the nonlinear region. Local wave number of soft global mode in (a) follows path indicated by thick line. Four domains are identified: the central nonlinear $n\ell-$ and $n\ell+$ regions prevail upstream and downstream of $X_s^{n\ell}$ where the nonlinear spatial branches $k^{n\ell-}$ and $k^{n\ell+}$ meet; at the upstream X_1 and downstream X_2 boundaries of the nonlinear balloon (shaded) the nonlinear spatial branches are continuously connected to their respective linear counterparts $k^{\ell\pm}$ prevailing in the semi-infinte linear regions $\ell-$ and $\ell+$ respectively.

4.6 Soft global modes

The existence of *soft global modes* has been analyzed in an earlier study [65]. Their structure is now briefly summarized, as well as their relationship to steep global modes.

An example is illustrated in Fig.11-a. In contrast to steep modes, no front is present and soft modes display an overall smoothly varying envelope and wave number. The connection between the upstream − branch and the downstream + branch occurs here in the core of the nonlinear region, at a saddle point of the nonlinear dispersion relation (21).

As already discussed in Section 3.3, the nonlinear branches $k^{n\ell\pm}(X,\omega)$, formally defined as the level contours $\Omega^{n\ell}(k,X) = \mathrm{C}^{\mathrm{st}}$, may display a saddle

point point $(X_s^{n\ell}, k_s^{n\ell})$ in the (X,k)-plane (solid dot in Fig.7-a). More precisely, pinching of the nonlinear branches, defined by the condition

$$k^{n\ell+}(X_s^{n\ell}, \omega_s^{n\ell}) = k^{n\ell-}(X_s^{n\ell}, \omega_s^{n\ell}) = k_s^{n\ell},$$

then occurs at the real station $X_s^{n\ell}$ for the real saddle point frequency $\omega_s^{n\ell}$ of $\Omega^{n\ell}$ such that

$$\omega_s^{n\ell} = \Omega^{n\ell}(k_s^{n\ell}, X_s^{n\ell}) \quad \text{and} \quad \frac{\partial \Omega^{n\ell}}{\partial k}(k_s^{n\ell}, X_s^{n\ell}) = \frac{\partial \Omega^{n\ell}}{\partial X}(k_s^{n\ell}, X_s^{n\ell}) = 0, \tag{30}$$

with the saddle condition

$$\left(\frac{\partial^2 \Omega^{n\ell}}{\partial k \partial X}(k_s^{n\ell}, X_s^{n\ell})\right)^2 - \frac{\partial^2 \Omega^{n\ell}}{\partial k^2}(k_s^{n\ell}, X_s^{n\ell}) \frac{\partial^2 \Omega^{n\ell}}{\partial X^2}(k_s^{n\ell}, X_s^{n\ell}) > 0. \tag{31}$$

Note the formal analogy of this nonlinear saddle point criterion (30) with its linear counterpart (27) which involves in general complex values of k_s^{ℓ} and X_s^{ℓ}. The upstream $k^{n\ell-}(X, \omega_s^{n\ell})$ branch and downstream $k^{n\ell+}(X, \omega_s^{n\ell})$ branch are precisely initiated at the nonlinear saddle point $X_s^{n\ell}$, as depicted in Fig.11-c. These nonlinear travelling waves prevail in the range $X_1 < X < X_2$, where X_1 and X_2 denote neutral stability stations of frequency $\omega_s^{n\ell}$, at the boundary of the nonlinear balloon in the (X,k)-plane. At X_1 and X_2, the amplitudes of the nonlinear travelling waves $k^{n\ell-}$ and $k^{n\ell+}$ respectively vanish and give way to their linear counterparts $k^{\ell-}$ and $k^{\ell+}$ respectively.

For the CGL equation (4) with $\omega_0(X)$ of the form (28), all other coefficients being kept uniform in X, the nonlinear saddle point location is explicitly obtained as

$$X_s^{n\ell} = X^{max} + \frac{\gamma_i \omega_{0X,r}}{\operatorname{Im}(\gamma^\star \omega_{0XX})}, \tag{32}$$

$$k_s^{n\ell} = k_{0,r} + \frac{\operatorname{Re} \gamma^\star \omega_{kk}}{\operatorname{Im} \gamma^\star \omega_{kk}} k_{0,i}. \tag{33}$$

and the soft global mode frequency reads

$$\omega_s^{n\ell} = \omega_{0,r}^{max} - \frac{\gamma_r}{\gamma_i} \omega_{0,i}^{max} + \frac{\gamma_i (\omega_{0X,r})^2}{2 \operatorname{Im}(\gamma^\star \omega_{0XX})} + \frac{|\gamma^\star \omega_{kk}|^2}{2\gamma_i \operatorname{Im}(\gamma^\star \omega_{kk})} k_{0,i}^2. \tag{34}$$

Condition (31) requires that $(\operatorname{Im} \gamma^\star \omega_{kk})(\operatorname{Im} \gamma^\star \omega_{0XX}) < 0$.

It was shown in [65] that in situations where

$$\operatorname{Im}(\gamma^\star \omega_{kk}) > 0, \tag{35}$$

the nonlinear branches $k^{n\ell\pm}$ exist in the neighborhood of $X_s^{n\ell}$ for frequencies such that $\omega > \omega_s^{n\ell}$. When $\omega \downarrow \omega_s^{n\ell}$, the branches pinch at $k_s^{n\ell}$ for $X = X_s^{n\ell}$; and

for $\omega < \omega_s^{n\ell}$, they fail to be defined around $X_s^{n\ell}$. In the following it is always assumed that the possible frequencies for the nonlinear spatial branches lie in the range $\omega > \omega_s^{n\ell}$. The opposite situation is exactly analogous and applies when $\mathrm{Im}\,(\gamma^\star \omega_{kk}) < 0$. From (31) and (35), the following inequality is then derived

$$\mathrm{Im}\,(\gamma^\star \omega_{0XX}) < 0. \tag{36}$$

4.7 Transition between soft and steep global modes

The selection mechanisms governing steep and soft global modes are now compared.

The steep criterion (25) only involves the boundary of the AU domain on the physical X-axis, regardless of the characteristics of the regions $X \neq X^{ca}$. Nevertheless a steep global mode only exists if the nonlinear $k^{n\ell+}(X, \omega_0^{ca})$ branch can be followed from X^{ca} down to the boundary of the nonlinear balloon and if it can there be continuously connected to the linear branch $k^{\ell+}(X, \omega_0^{ca})$. In contrast, the soft criterion (30), involves a saddle point of the nonlinear dispersion relation. Again, a soft global mode only exists if the nonlinear spatial branches issuing from this nonlinear pinch point may effectively be continued via corresponding linear $k^{\ell\pm}$ branches in the respective downstream and upstream linear domains.

The selection of either steep or soft global modes depends not only on the local criteria (25,30) but also on the necessity to enforce the boundary conditions. The key argument in the following derivation is based on a careful monitoring of the linear wave number branches in the complex k-plane and of their nonlinear counterparts in the (X, k)-plane as the global frequency is varied. The connection between linear and nonlinear spatial branches is shown to crucially depend on the relative magnitude of the characteristic frequencies $\omega_s^{n\ell}$ and ω_0^{ca}. In all instances, only one global mode, steep or soft, is capable of continuously converting $k^{\ell-}$ at $X = -\infty$ to $k^{\ell+}$ at $X = +\infty$, as X is varied. The two main scenarii of interest are illustrated in Fig.12 and 13 respectively, as discussed below.

Since nonlinear global modes necessarily involve real frequencies, let us focus on frequencies on the real ω-axis. As shown in Section 3.2, for large positive or negative ω the linear spatial branches do not cross the k_r-axis in the complex k-plane. Since nonlinear spatial branches are assumed to exist for $\omega > \omega_s^{n\ell}$, we start with large positive values of the frequency.

As ω is decreased, the $k^{\ell\pm}(X, \omega)$ branches move in closer to each other and one or both cross the k_r-axis for finite values of X. A change in sign of k_i^ℓ sig-

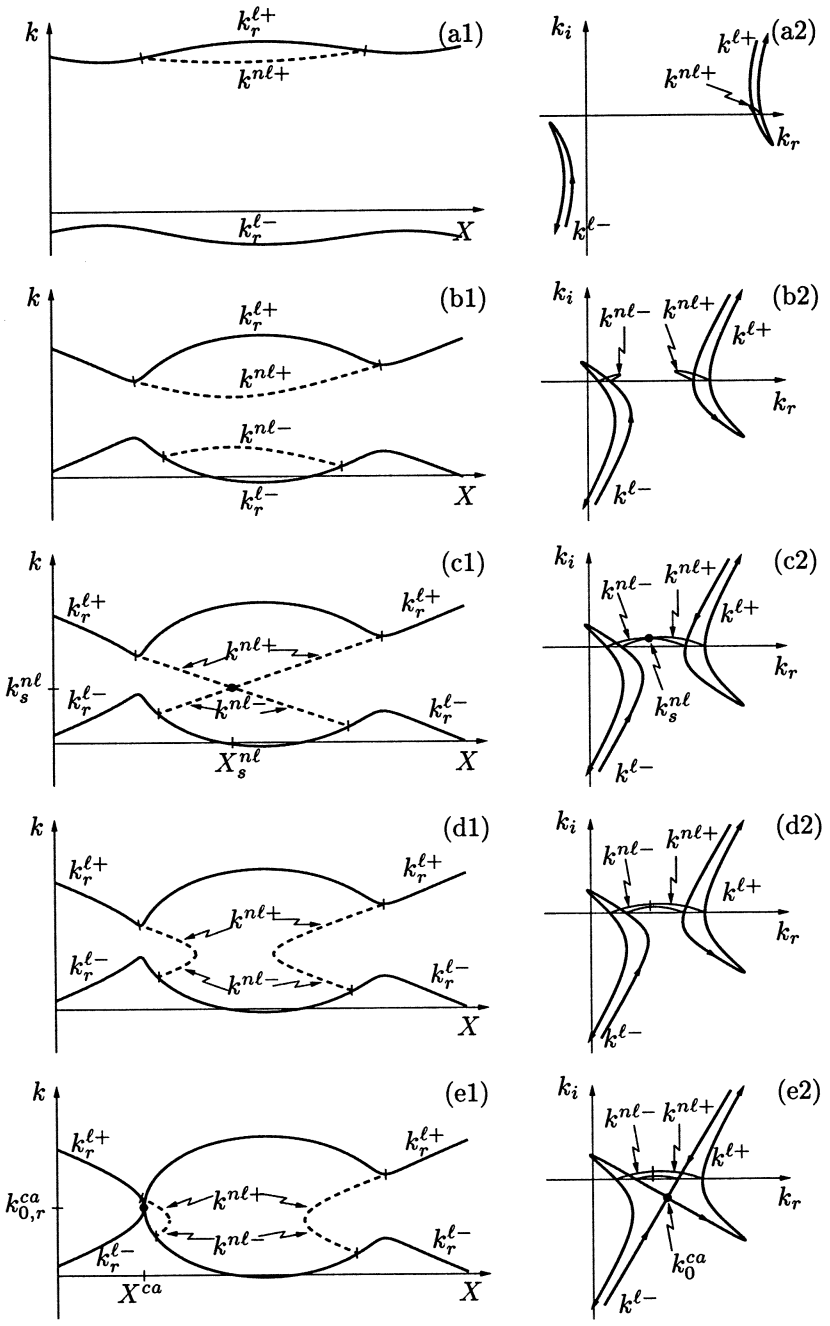
Fig. 12. (facing page) Evolution of CGL spatial branches with decreasing real frequency in a situation where the soft global mode is selected. The left sequence illustrates the evolution of the real part of linear branches $k_r^{\ell\pm}(X,\omega)$ (solid lines) and of nonlinear branches $k^{n\ell\pm}(X,\omega)$ (dashed lines) in the (X,k)-plane. Connecting points between linear and nonlinear branches are indicated with tick marks. In the right sequence, corresponding complex linear $k^{\ell\pm}(X,\omega)$ branches are sketched in the complex (k_r,k_i)-plane; superimposed on the same graphs are the curves $(k^{n\ell\pm},R^2)$ of the nonlinear spatial branches. (a,b) For frequencies $\omega > \omega_s^{n\ell}$ linear $k^{\ell\pm}$ spatial branches successively cross the k_r-axis in the complex k-plane and give birth to the nonlinear $k^{n\ell\pm}$ branches between the corresponding neutral stations. (c) For the nonlinear saddle point frequency $\omega_s^{n\ell}$, nonlinear spatial branches pinch at $k_s^{n\ell}$ when $X = X_s^{n\ell}$. This pinch point joining $k^{n\ell-}$ and $k^{n\ell+}$ branches gives rise to a soft global mode connecting the $k^{\ell-}$ branch near $X = -\infty$ to the $k^{\ell+}$ branch prevailing near $X = +\infty$. (d,e) For frequencies $\omega < \omega_s^{n\ell}$, the nonlinear spatial branches fail to exist in the neighborhood of $X_s^{n\ell}$, but linear $k^{\ell\pm}$ branches are still defined. (e) When $\omega = \omega_0^{ca}$, the linear branches in turn pinch at $k = k_0^{ca}$ at the upstream boundary X^{ca} of AU region. However, this pinch point is not associated with a steep global mode since the $k^{n\ell+}$ branch prevailing for $X > X^{ca}$ is not connected to the $k^{\ell+}$ branch extending to $X = +\infty$.

nifies that the corresponding branch is spatially growing: downstream spatial growth for $k_i^{\ell+} < 0$ and upstream spatial growth for $k_i^{\ell-} > 0$. As already mentioned (Section 2.3) a spatially growing branch $k^{\ell\pm}$ gives way to its nonlinear counterpart $k^{n\ell\pm}$ as a neutrally stable station is crossed in the (X,k)-plane.

Nonlinear $k^{n\ell}$ branches are by construction always real-valued. However, to illustrate their relationship with the linear k^{ℓ} branches they are also represented in the complex k-planes of Fig.12 and 13. For clarity their missing imaginary part is replaced by the square of the amplitude of the corresponding nonlinear solution. This avoids the collapse of the $k^{n\ell}$ branches onto the k_r-axis, and brings to the fore the continuity between linear and nonlinear branches at the neutral stations where k_i^{ℓ} as well as the square of the nonlinear amplitude vanish.

In the following discussion representations in the (X,k_r)- and the (k_r,k_i)-planes are always shown in parallel. Although the + and − superscripts may not be derived from causality considerations in the AU domain, linear as well as the nonlinear + and − branches may be defined without ambiguity as long as the linear and nonlinear branches remain distinct (Sections 3.2 and 3.3).

The branch switching scenario as ω decreases depends on the relative values of the characteristic frequencies $\omega_s^{n\ell}$ and ω_0^{ca}. The frequency ω_0^{ac} which corresponds to an unstable steep global mode with a front at the *downstream* boundary of the AU domain does not play an essential part. For clarity assume that $\omega_0^{ca} > \omega_0^{ac}$ and $\omega_s^{n\ell} > \omega_0^{ac}$. If these assumptions are not satisfied, the same selection mechanisms as discussed below prevail, although the detailed



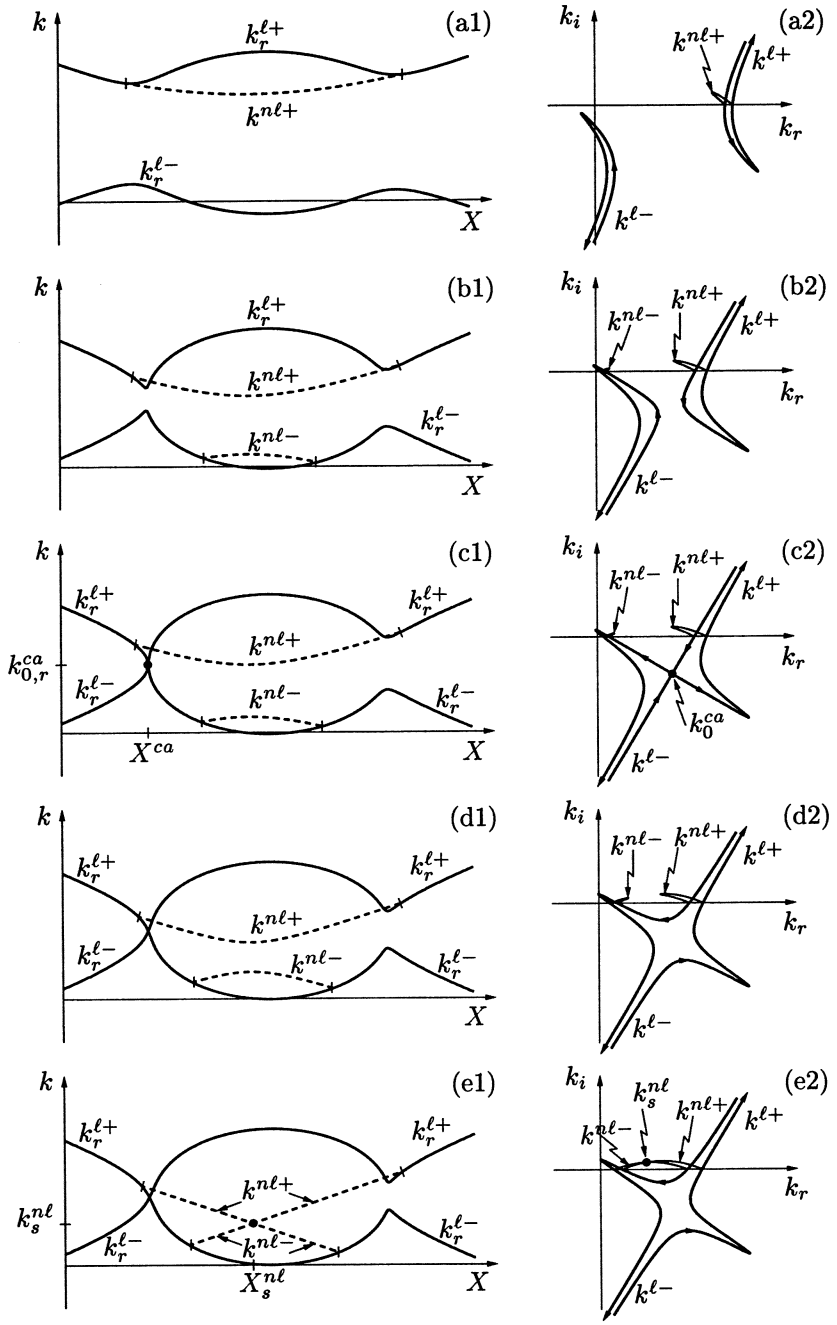
topology of spatial branches may be different. Two possibilities now arise: $\omega_s^{n\ell} > \omega_0^{ca}$ or $\omega_s^{n\ell} < \omega_0^{ca}$.

The scenario for $\omega_s^{n\ell} > \omega_0^{ca}$ is illustrated in the sequence of Fig.12. As ω is decreased, the two linear spatial branches successively cross the k_r-axis while remaining separated as depicted in Fig.12-a,b. Each crossing gives birth to a corresponding nonlinear branch, connected to its linear counterpart at the

Fig. 13. (facing page) Evolution of CGL spatial branches with decreasing real frequency in a situation where the steep global mode is selected. The left sequence illustrates the evolution of the real part of linear branches $k_r^{\ell\pm}(X,\omega)$ (solid lines) and of nonlinear branches $k^{n\ell\pm}(X,\omega)$ (dashed lines) in the (X,k)-plane. Connecting points between linear and nonlinear branches are indicated with tick marks. In the right sequence, corresponding complex linear $k^{\ell\pm}(X,\omega)$ branches are sketched in the complex (k_r,k_i)-plane; superimposed on the same graphs are the curves $(k^{n\ell\pm},R^2)$ of the nonlinear spatial branches. (a,b) For frequencies $\omega > \omega_0^{ca}$ linear spatial branches remain separated, nonlinear branches exist between the corresponding neutral stations. (c) For the front frequency ω_0^{ca}, linear spatial branches pinch at k_0^{ca} when $X = X^{ca}$. A sharp front associated with a wave number jump then gives rise to a global mode connecting the $k^{\ell-}$ branch near $X = -\infty$ to the $k^{\ell+}$ branch prevailing near $X = +\infty$. (d,e) For frequencies $\omega < \omega_0^{ca}$, branch switching between $k^{\ell+}$ and $k^{\ell-}$ occurs. (e) When $\omega = \omega_s^{n\ell}$, the nonlinear branches meet at the nonlinear saddle point location $X_s^{n\ell}$. However, this saddle point is not associated with a global mode since no continuous connection to the $k^{\ell-}$ branch prevailing near $X = -\infty$ exists.

neutrally stable locations where k^ℓ is real. Both linear and nonlinear + and − branches are well identified and separated. When $\omega \downarrow \omega_s^{n\ell}$, the nonlinear branches gradually approach each other. For $\omega = \omega_s^{n\ell}$ (Fig.12-c), the $k^{n\ell+}$ branch meets the $k^{n\ell-}$ branch at $k_s^{n\ell}$ for $X = X_s^{n\ell}$ as determined by (30). This is the soft global mode configuration, where the nonlinear saddle point at $X_s^{n\ell}$ connects the nonlinear $k^{n\ell-}(X,\omega_s^{n\ell})$ in the region $X < X_s^{n\ell}$ to the nonlinear $k^{n\ell+}(X,\omega_s^{n\ell})$ in the region $X > X_s^{n\ell}$. Further outward, the nonlinear $k^{n\ell\pm}$ branches give way to their respective linear counterparts $k^{\ell\pm}$ at the locations of their respective neutral growth. When decreasing the global frequency to values $\omega < \omega_s^{n\ell}$, the nonlinear branches fail to exist in the neighborhood of $X_s^{n\ell}$ (Fig.12-d). As ω reaches ω_0^{ca} (Fig.12-e), linear spatial branches do pinch at $X = X^{ca}$, but the nonlinear spatial branch $k^{n\ell+}$ prevailing around X^{ca} cannot be continued far downstream towards the $k^{\ell+}$ branch extending down to $X = +\infty$: There is no global mode of frequency ω_0^{ca}.

The scenario for $\omega_0^{ca} > \omega_s^{n\ell}$ is sketched in the sequence of Fig.13. As ω decreases, the first characteristic frequency encountered is now ω_0^{ca}. When $\omega \downarrow \omega_0^{ca}$ (Fig.13-a,b,c), the linear branches approach and pinch at k_0^{ca} for $X = X^{ca}$ determined by (25). Since $k_{0,i}^{ca} < 0$, the relevant branches in a neighborhood of X^{ca} are $k^{\ell-}$ and $k^{n\ell+}$. A front of frequency ω_0^{ca} at X^{ca} allows a discontinuous jump in wave number from $k^{\ell-}(X^{ca},\omega_0^{ca}) = k_0^{ca}$ to $k^{n\ell+}(X^{ca},\omega_0^{ca})$. This front performs the connection between − and + branches necessary to obtain a steep global mode: further downstream, the amplitude of the nonlinear $k^{n\ell+}$ branch vanishes at a neutrally stable station and there the linear $k^{\ell+}$ branch takes over to $X = +\infty$. Note that the $k^{\ell+}(X,\omega_0^{ca})$ branch necessarily crosses the k_r-axis; the $k^{\ell-}(X,\omega_0^{ca})$ branch however may or may not cross. For $\omega = \omega_0^{ca}$, the nonlinear branches, if they both exist, do not meet. Decreasing further ω towards $\omega_s^{n\ell}$ (Fig.13-d,e), the nonlinear branches in turn approach and pinch for $\omega = \omega_s^{n\ell}$. However, since $\omega_s^{n\ell} < \omega_0^{ca}$, the linear $k^{\ell\pm}$ branches



have undergone branch switching for $\omega = \omega_0^{ca}$. As can be seen in Fig.13-e, the nonlinear branches issuing at $k_s^{n\ell}, X_s^{n\ell}$ cannot be continued towards the $k^{\ell-}$ branch near $X = -\infty$. In this situation, due to global considerations, no soft mode exists, although the local criterion (30) may be satisfied.

This completes the discussion of the global mode selection mechanism: the type of selected global mode depends on the relative values of the linear pinch-

point frequency ω_0^{ca} and nonlinear pinchpoint frequency $\omega_s^{n\ell}$. If

$$\omega_s^{n\ell} < \omega_0^{ca},$$

linear spatial branches meet first as the overall frequency is lowered: the steep criterion (25) yields a global solution on the entire X-axis with a sharp front located at X^{ca}. However if

$$\omega_0^{ca} < \omega_s^{n\ell},$$

the nonlinear saddle point is encountered first and a soft global mode with overall smoothly varying envelope and wave number prevails. There exists of course situations where the nonlinear dispersion relation displays no saddle point in the nonlinear balloon. Then a steep mode is necessarily obtained.

The preceding close inspection of spatial linear and nonlinear branches guarantees that the selection criteria for steep and soft global modes are mutually exclusive, and that all situations are accounted for.

According to this discussion, when a global control parameter is continuously varied, the transition mechanism between soft and steep global modes is the following. Starting with a system where a soft mode is selected, *i.e.*, where $\omega_s^{n\ell} > \omega_0^{ca}$, two possibilities arise if the control parameter is changed:

- The saddle point frequency $\omega_s^{n\ell}$ may equal the front frequency ω_0^{ca} for a critical value of the control parameter. Beyond this value, $\omega_s^{n\ell} < \omega_0^{ca}$, and a steep mode prevails. The transition to a steep mode of the same frequency takes place when $\omega_s^{n\ell} = \omega_0^{ca}$.
- The nonlinear saddle point may reach the boundary of the nonlinear balloon and disappear while still $\omega_s^{n\ell} > \omega_0^{ca}$. Then, transition to a steep mode again occurs, but in this situation the global frequency is discontinuous at transition.

This will be fully justified in Section 4.9, where we map out the domains of existence of soft and steep global modes in an appropriate control parameter space. To identify the relevant control parameters, a discussion of the rôle of the absolute wave number is first required.

4.8 Rôle of the absolute wave number

The local instability properties are seen to be essentially controlled by the streamwise evolution of the absolute frequency $\omega_0(X)$ and wave number $k_0(X)$ which in principle can be varied independently. The criterion for steep global modes (25) only depends on the local absolute frequency $\omega_0(X)$ regardless of the local absolute wave number $k_0(X)$. The soft global mode criterion (30),

however, depends on $k_0(X)$ through the complete nonlinear dispersion relation. In this subsection, the rôle of the absolute wave number is discussed by varying $k_0(X)$ in the CGL equation, all other coefficients remaining fixed.

From expressions (24) for the linear spatial $k^{\ell\pm}$ branches it is readily seen that a change in $k_0(X)$ by some constant value, say κ, results in a displacement of the $k^{\ell\pm}$ curves in the complex k-plane. Under this process, the linear pinchpoint properties are not affected. Nonlinear characteristics, however, are closely related to the crossing of the k_r-axis by the $k^{\ell\pm}$ branches; it follows that changes in $k_{0,i}$ strongly influence the nonlinear properties of the medium, unlike changes of $k_{0,r}$. This calls for two distinct physical interpretations of $k_{0,r}$ and $k_{0,i}$ respectively.

Consider the uniform CGL equation (6) with k_0 replaced by $k_0 - \kappa_r$. Then, under the change of unknown function

$$\psi(x,t) = \phi(x,t)e^{i\kappa_r x},$$

the original CGL equation (6) is recovered for ϕ. This shows that the only effect of a change in $k_{0,r}$ is a change in wave length; linear spatial growth or decay rates, frequencies as well as nonlinear amplitudes remain the same. A variation of $k_{0,r}$ results in a change of carrier wave but does not alter the linear nor the nonlinear stability properties of the system. In the spatially dependent CGL equation (4), the following change of unknown function

$$\psi(x,t) = \phi(x,t)\exp\frac{i}{\epsilon}\int^{X}\kappa_r(u)du$$

results in modifying the absolute wave number to $k_0(X) - \kappa_r(X)$. Any slowly modulated carrier wave defined by the *real* function $\kappa_r(X)$ may thus be used to transform the real part of the absolute local wave number. Under such a transformation, the global mode selection criteria as well as the characteristic frequencies remain unaltered: *The function $k_{0,r}(X)$ may be chosen arbitrarily since it does not affect the local and global dynamics.*

In order to bring to the fore the rôle of $k_{0,i}(X)$, it is convenient, in the remainder of this section, to select $k_{0,r}(X)$ so that the function $\omega_{kk}(X)k_0(X)$ appearing in front of the advection term $\partial\psi/\partial x$ in (4) is real [16]. Under such a condition,

$$k_{0,r}(X) = -\frac{\omega_{kk,r}(X)}{\omega_{kk,i}(X)}k_{0,i}(X),$$

and the CGL equation reads

$$\frac{\partial\psi}{\partial t} + \frac{|\omega_{kk}|^2}{\omega_{kk,i}}k_{0,i}\frac{\partial\psi}{\partial x} = -i\Big(\omega_0 + \frac{1}{2}\omega_{kk}k_0^2\Big)\psi + \frac{i}{2}\omega_{kk}\frac{\partial^2\psi}{\partial x^2} - i\gamma|\psi|^2\psi. \qquad (37)$$

The form (37) clearly indicates that the *real* factor

$$U(X) = \frac{|\omega_{kk}(X)|^2}{\omega_{kk,i}(X)} k_{0,i}(X)$$

may be interpreted as an advection velocity. Since causality requires that $\omega_{kk,i} < 0$, a negative (positive) $k_{0,i}$ is readily seen to correspond to advection towards $X = +\infty$ ($X = -\infty$). Thus the sign of $k_{0,i}$ controls the advection direction whereas its magnitude is directly related to the advection velocity. As stated in the introduction, it is assumed that $U(X) > 0$, *i.e.*, $k_{0,i}(X) < 0$ in the entire domain: the basic advection is then directed towards $X = +\infty$.

In order to further discuss the rôle of $k_{0,i}$ in the selection of global modes, consider, for definiteness, that $k_{0,i}$ is constant over the entire domain. A change in $k_{0,i}$ is seen to be associated with a displacement of the $k^{\ell\pm}$ curves along the k_i-axis in the complex k-plane. Its effect on the nonlinear balloon and nonlinear spatial branches in the (X,k)-plane is outlined in Fig.14. Since the function $\omega_0(X)$ is kept fixed, a change of $k_{0,i}$ leaves the extent of the AU range $X^{ca} < X < X^{ac}$ unaltered, as indicated by vertical dashed lines $X = X^{ca}$ and $X = X^{ac}$ in Fig.14. Without mean advection, $k_{0,i} = 0$ (Fig.14-a), the nonlinear balloon exactly spans the AU region. In this situation, local linear instability coincides with local absolute instability: $X^{sc} = X^{ca}$ and $X^{ac} = X^{cs}$. Nonlinear spatial branches cover the nonlinear balloon symmetrically with respect to $k = k_s^{n\ell}$. Figures 14-b,c,d are obtained for increasing negative values of $k_{0,i}$, *i.e.*, increasing advection towards $X = +\infty$. Increasing $|k_{0,i}|$ then shifts the $k^{\ell\pm}$ branches (24) towards negative k_i in the complex k-plane, thereby enhancing the instability of the downstream $k^{\ell+}$ branches and reducing the instability of the upstream $k^{\ell-}$ branches. Under such circumstances, the onset of linear instability no longer coincides with transition to absolute instability: The nonlinear balloon inflates and extends beyond the AU range into the CU regions $X^{sc} < X < X^{ca}$ and $X^{ac} < X < X^{cs}$. The basic flow advection breaks the $k^{n\ell+}/k^{n\ell-}$ symmetry, and the part of the nonlinear balloon spanned by the $k^{n\ell+}$ branches increases to the detriment of the $k^{n\ell-}$ branches. During this process, the nonlinear saddle point moves towards the neutral stability boundary and eventually leaves the nonlinear balloon. The advection velocity, measured by $k_{0,i}$, thus strongly affects the existence of the nonlinear saddle point and hence the existence of smooth global modes.

In the remainder of this subsection we temporarily allow advection in the positive or negative direction so that $k_{0,i}$ may change sign. It has been shown in Section 4.2 that among the two stationary fronts at X^{ca} and X^{ac}, only the one located at the *upstream* boundary of the AU region is stable. Since flow direction is directly related to the sign of $k_{0,i}$, the stable steep global mode frequency is ω_0^{ca} for $k_{0,i} < 0$ and ω_0^{ac} for $k_{0,i} > 0$. These are indeed the fronts at the stations of local marginal absolute instability with their nonlinear wave train covering the AU domain and their exponentially decaying tail extending

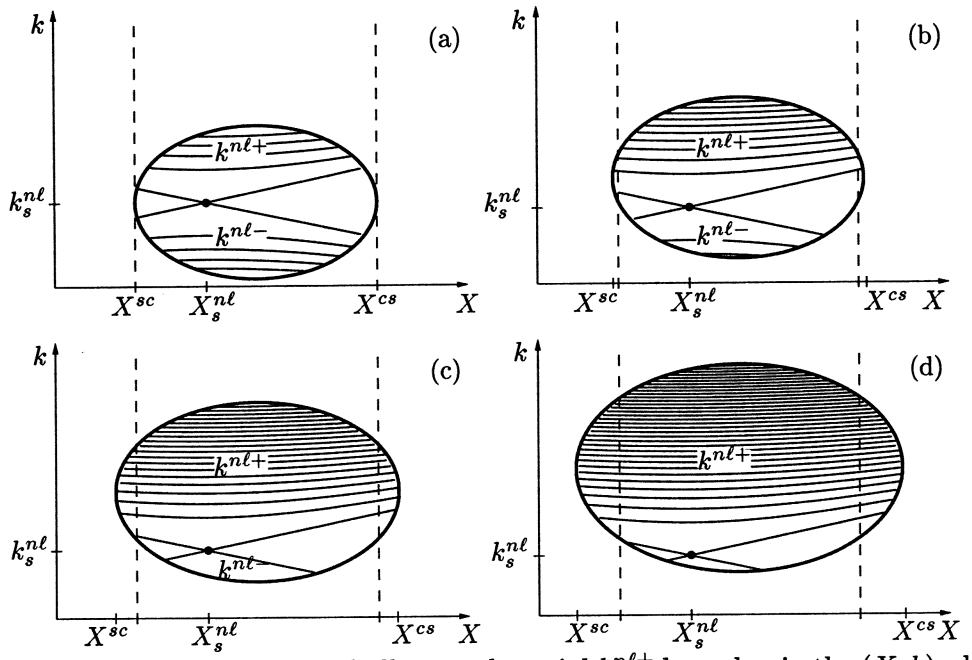


Fig. 14. Evolution of nonlinear balloon and spatial $k^{nl\pm}$ branches in the (X,k)-plane as the advection towards $X=+\infty$ is increased. Vertical dashed lines indicate AU domain extending over $X^{ca} < X < X^{ac}$. (a) Without mean advection ($k_{0,i}=0$), spatial branches display symmetry with respect to the nonlinear saddle point wave number k_s^{nl} and the nonlinear domain exactly spans the AU region, $X^{sc}=X^{ca}$ and $X^{ac}=X^{cs}$. (b,c,d) With increasing downstream advection $k_{0,i}<0$, the nonlinear balloon inflates and extends beyond the AU region, $X^{sc}<X^{ca}$ and $X^{ac}<X^{cs}$. During this process the fraction of the nonlinear balloon covered by the downstream k^{nl+} branches increases with respect to the k^{nl-} branches. Simultaneously, the nonlinear saddle point (X_s^{nl}, k_s^{nl}) is seen to descend to eventually leave the nonlinear balloon.

into the CU region (see also Fig.15-a). The soft global mode frequency ω_s^{nl} has been obtained in (34), and, in contrast to the steep global mode frequencies ω_0^{ca} and ω_0^{ac}, it is seen to depend on $k_{0,i}$.

In the previous subsection it has been demonstrated that the global mode of largest frequency is selected; thus the transition scenario between steep and soft global modes as a function of $k_{0,i}$ is derived from the relative values of ω_0^{ca}, ω_0^{ac} and $\omega_s^{nl}(k_{0,i})$, as displayed in Fig.15. According to (34), the soft frequency ω_s^{nl} is largest for $k_{0,i}=0$, all other coefficients being kept fixed. Thus soft modes prevail when advection is small enough, $\omega_s^{nl}>\omega_0^{ca}$ and $\omega_s^{nl}>\omega_0^{ac}$. With increasing downstream advection ($k_{0,i}<0$), the nonlinear saddle point frequency ω_s^{nl} decreases. When $\omega_s^{nl}<\omega_0^{ca}$, the soft mode is replaced by a steep mode with a sharp front at X^{ca} (left-hand side of Fig.15). Similarly, if $k_{0,i}$ increases from 0 ($k_{0,i}>0$), which corresponds to advection towards $X=-\infty$, the nonlinear saddle point frequency ω_s^{nl} again decreases. When $\omega_s^{nl}<\omega_0^{ac}$, the soft mode is now replaced by a steep mode with a front at $X=X^{ac}$ (right-hand side of Fig.15). Since $k_{0,i}>0$, the front at X^{ac} is now the stable one:

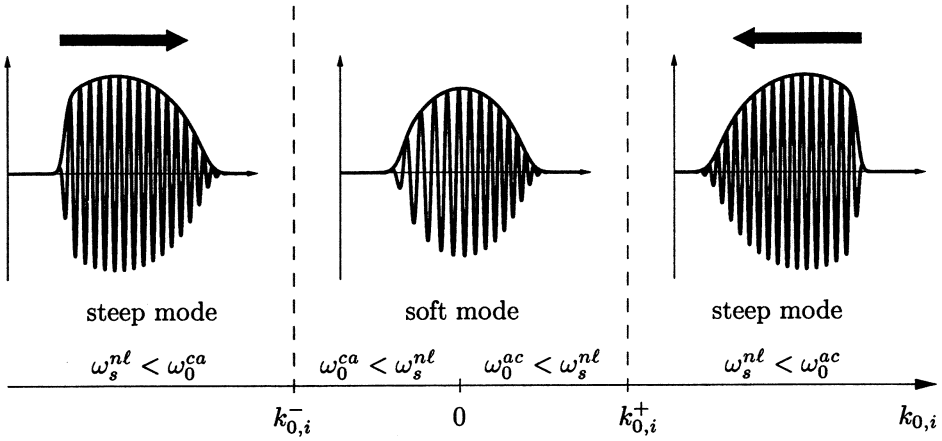


Fig. 15. Transition between steep and soft global modes as a function of $k_{0,i}$. Black arrows indicate advection direction. For small advection velocities ($k_{0,i}$ small), the saddle point frequency ω_s^{nl} is larger than the front frequencies ω_0^{ca} and ω_0^{ac}, and thus a soft global mode is selected. With increasing advection towards $X = +\infty$ ($k_{0,i} < 0$), the saddle point frequency ω_s^{nl} decreases, and, when $k_{0,i} < k_{0,i}^-$ the soft mode is replaced by a steep global mode with a front at the left boundary of the AU region. Similarly, with increasing advection towards $X = -\infty$ ($k_{0,i} > 0$), the saddle point frequency ω_s^{nl} again decreases, and at $k_{0,i} = k_{0,i}^+$ transition takes place to a steep global mode with a front at the right boundary of the AU region.

upstream and downstream directions have been interchanged. In any case, the front location corresponds to the upstream boundary of the AU region. The critical transition values $k_{0,i}^- < 0$ and $k_{0,i}^+ > 0$ between soft and steep global modes are defined by $\omega_0^{ca} = \omega_s^{nl}$ and $\omega_0^{ac} = \omega_s^{nl}$ respectively.

4.9 Domains of existence in control parameter space

Now that the rôles of $\omega_{0,i}^{max}$, $\omega_{0X,r}$ and $k_{0,i}$ have been separately discussed, the domains of existence of steep and soft global modes may be obtained in the three-dimensional space of these control parameters (Fig.16). Consider the CGL equation (4) with $\omega_0(X)$ of the form (28), all other coefficients being assumed uniform in X for simplicity. The front frequencies ω_0^{ca} and ω_0^{ac} then read

$$\omega_0^{ca}, \omega_0^{ac} = \omega_{0,r}^{max} - \frac{\omega_{0XX,r}}{\omega_{0XX,i}}\omega_{0,i}^{max} \mp \omega_{0X,r}\sqrt{\frac{2\omega_{0,i}^{max}}{-\omega_{0XX,i}}}. \tag{38}$$

They exist whenever $\omega_{0,i}^{max} > 0$ and their values are seen to be effectively independent of $k_{0,i}$.

The selected gobal mode type depends on the relative values of the front frequencies (38) and the nonlinear saddle point frequency ω_s^{nl} obtained in eq.(34). However note that the nonlinear saddle point formally defined by (32,33) only

exists if $(k_s^{n\ell}, X_s^{n\ell})$ lies in the nonlinear balloon, *i.e.*, if

$$\Omega_i^\ell(k_s^{n\ell}, X_s^{n\ell}) > 0. \tag{39}$$

For the CGL equation under study, one readily obtains

$$\Omega_i^\ell(k_s^{n\ell}, X_s^{n\ell}) = \omega_{0,i}^{max} + \frac{1}{2}\omega_{0XX,i}\left(\frac{\gamma_i}{\mathrm{Im}\,\gamma^\star\omega_{0XX}}\right)^2(\omega_{0X,r})^2 + \frac{|\omega_{kk}|^2\mathrm{Im}\,\gamma^2\omega_{kk}^\star}{2(\mathrm{Im}\,\gamma^\star\omega_{kk})^2}(k_{0,i})^2. \tag{40}$$

Whenever $\Omega_i^\ell(k_s^{n\ell}, X_s^{n\ell}) < 0$, the nonlinear saddle point does not exist, and only a steep global mode is obtained. In the control parameter space of Fig.16, the domain where condition (39) is satisfied is located above the surface labelled $\Omega_i^\ell(k_s^{n\ell}, X_s^{n\ell}) = 0$. According to (40), this surface is a paraboloid entirely contained in the half-space $\omega_{0,i}^{max} \geq 0$ and tangent to the plane $\omega_{0,i}^{max} = 0$ at $\omega_{0X,r} = k_{0,i} = 0$. Below this surface no soft mode may exist and only steep modes are obtained. Above this surface, the soft global frequency $\omega_s^{n\ell}$ must be compared to ω_0^{ca} and ω_0^{ac}. For simplicity consider only situations with advection towards $X = +\infty$, *i.e.*, the half-space $k_{0,i} < 0$, so that only ω_0^{ca} comes into consideration for steep modes. Within the region where a nonlinear saddle point exists, transition between soft and steep modes occurs when $\omega_s^{n\ell} = \omega_0^{ca}$. This transition surface is derived from (34) and (38) and it is sketched in Fig.16. It is seen to meet the surface $\Omega_i^\ell(k_s^{n\ell}, X_s^{n\ell}) = 0$ along a curve in the plane $k_{0,i} = 0$. As may be inferred from these critical surfaces, the parameter space is divided into four regions (Fig.16):

- (a) Below the global threshold, $\omega_{0,i}^{max} < 0$, no front and no saddle point exists, the unperturbed state $\psi = 0$ remains stable.
- (b) When $\omega_{0,i}^{max} > 0$ and $\Omega_i^\ell(k_s^{n\ell}, X_s^{n\ell}) < 0$, no saddle point exists and a steep global mode prevails.
- (c) When $\Omega_i^\ell(k_s^{n\ell}, X_s^{n\ell}) > 0$ and $\omega_s^{n\ell} < \omega_0^{ca}$, a saddle point exists but the steep mode is selected.
- (d) When $\Omega_i^\ell(k_s^{n\ell}, X_s^{n\ell}) > 0$ and $\omega_s^{n\ell} > \omega_0^{ca}$, the soft mode is selected.

Thus at global mode onset $\omega_{0,i}^{max} = 0$, transition occurs always via a steep global mode except for the triply degenerate case $\omega_{0,i}^{max} = k_{0,i} = \omega_{0X,r} = 0$. With increasing $\omega_{0,i}^{max}$, transition from a steep to a soft mode occurs for finite values of $\omega_{0,i}^{max}$ either as soon as the nonlinear saddle point comes into existence (on the surface $\Omega_i^\ell(k_s^{n\ell}, X_s^{n\ell}) = 0$) or when its frequency reaches the steep frequency (on the surface $\omega_s^{n\ell} = \omega_0^{ca}$).

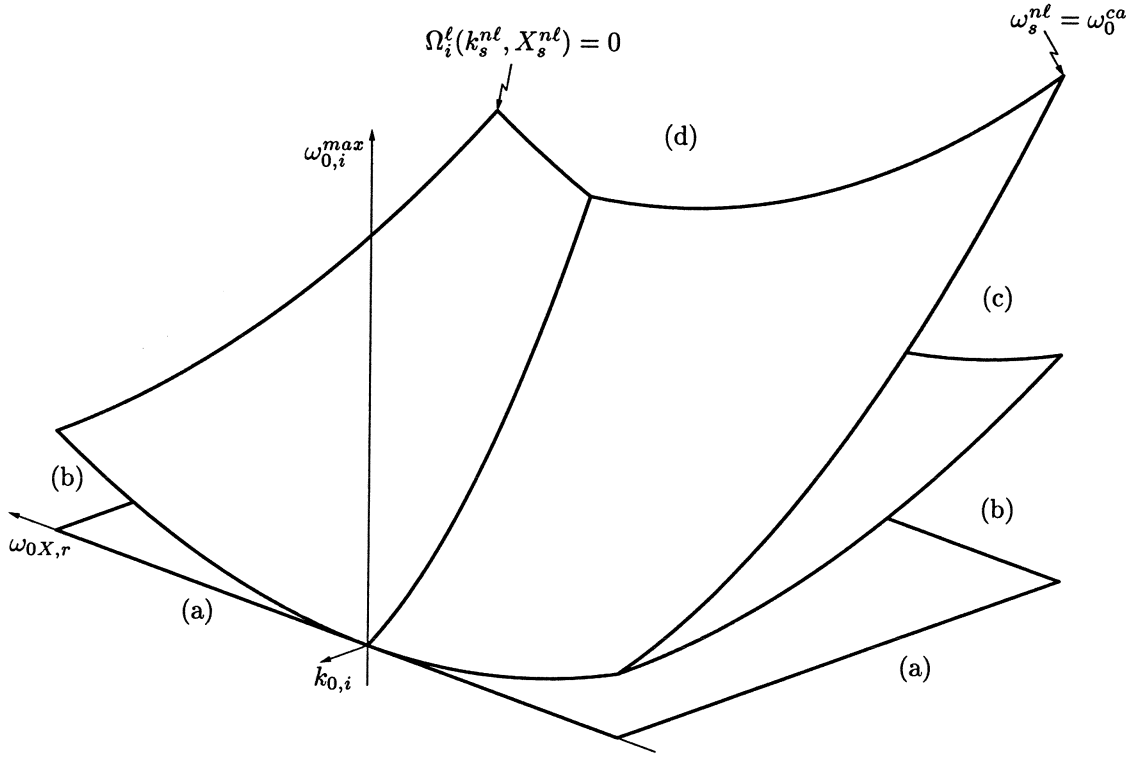


Fig. 16. Domains of existence of steep and soft global modes in the three-dimensional control parameter space $(\omega_{0X,r}, k_{0,i}, \omega_{0,i}^{max})$. A nonlinear saddle point exists above the surface $\Omega_i^\ell(k_s^{n\ell}, X_s^{n\ell}) = 0$. The associated frequency $\omega_s^{n\ell}$ is larger than the front frequency ω_0^{ca} above the surface labelled $\omega_s^{n\ell} = \omega_0^{ca}$. Hence soft global modes prevail in region (d). In region (c), steep modes are selected according to $\omega_s^{n\ell} < \omega_0^{ca}$. In region (b), no nonlinear saddle point exists and only steep modes are obtained. In region (a), below global threshold $\omega_{0,i}^{max} < 0$, the unperturbed state is stable.

4.10 Summary of transition mechanisms

To conclude the first part of this paper, let us summarize the main transition mechanisms. Three distinct control parameters governing global mode selection have been identified.

The global bifurcation parameter is the maximum absolute growth rate over the entire medium $\omega_{0,i}^{max}$. Nonlinear global modes exist whenever a region of absolute instability is present ($\omega_{0,i}^{max} > 0$). The transition to a steep global mode occurs discontinuously at $\omega_{0,i}^{max} = 0$ through a saddle-node bifurcation. In the absence of absolute instability ($\omega_{0,i}^{max} < 0$), no self-sustained global modes exist and the basic state is globally stable.

The basic state remains globally linearly stable up to a finite positive value of $\omega_{0,i}^{max}$. The hysteresis width in $\omega_{0,i}^{max}$ is governed by $\omega_{0X,r}$ and scales as $(\omega_{0X,r})^2$.

The advection parameter $k_{0,i}$ strongly influences transition from steep to soft

nonlinear global modes. Soft modes exist for small values of $k_{0,i}$, wheras for increasing upstream or downstream advection, steep modes prevail.

The main global mode properties may be inferred from the three above mentioned control parameters.

5 Asymptotic spatial structure of global modes

The preceding results have been derived under the assumption that the global mode is, at each station close to the local wave train at the global frequency. This local wave train is governed by the local linear dispersion relation (20) in regions where the amplitude is small, whereas it follows the local nonlinear dispersion relation (21) in finite amplitude domains. These considerations, which only involve the local characteristics of the medium, yield the leading order WKBJ approximation to the spatial structure. Within this framework, the selection criteria for steep and soft global modes have been identified and the leading order global frequencies have been derived.

The objective of this section is to incorporate the previous results into a consistent WKBJ approximation scheme [3], in order to obtain higher order correction terms, and to establish that the global mode structures outlined in the preceding sections may effectively be constructed by matching together extended wavepackets prevailing in different regions.

The organization of the following sections is motivated by the spatial structure of both steep and soft global modes illustrated in Fig.17. As already discussed, global modes display *nonlinear regions* of finite amplitude as well as *linear regions* of infinitesimal amplitude. In the outer semi-infinite linear regions ($\ell\pm$) extending towards $X = \pm\infty$ (Section 5.1) the respective complex linear spatial branch $k^{\ell\pm}$ prevails. The central nonlinear regions ($n\ell\pm$) are of finite extent, *i.e.*, order unity measured in terms of X, and they are dominated by the respective nonlinear spatial branch $k^{n\ell\pm}$ as discussed in Section 5.2. These extended regions are connected via three types of narrow *transition layers*:

- The *front layer* (fl) of size $\mathcal{O}(\epsilon^{2/3})$ located at the upstream boundary of the steep global mode nonlinear region connects $k^{\ell-}$ and $k^{n\ell+}$ branches (Section 5.3).
- The *nonlinear saddle point layer* (sp) of size $\mathcal{O}(\epsilon^{1/2})$ allows crossover between the $k^{n\ell\pm}$ branches within the nonlinear soft global mode region (Section 5.4).
- *Weakly nonlinear transition layers* (tl$\pm$) of size $\mathcal{O}(\epsilon^{1/2})$ at the downstream end of the steep global mode nonlinear region and at both ends of the soft global mode nonlinear region connect the fully developed nonlinear branches with their linear counterparts (Section 5.5).

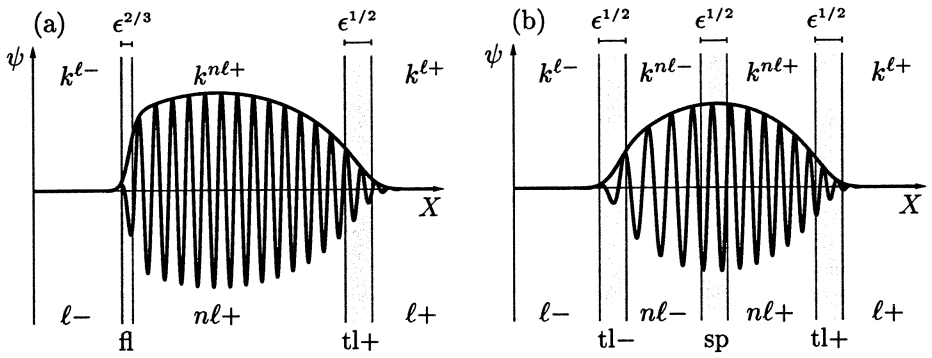


Fig. 17. Spatial structure of (a) steep and (b) soft global modes: ($\ell\pm$), outer semi-infinite linear regions near $X = \pm\infty$ with respective linear spatial $k^{\ell\pm}$ branch; ($n\ell\pm$), central nonlinear regions of size $\mathcal{O}(1)$ with respective nonlinear spatial $k^{n\ell\pm}$ branch; (tl$\pm$), weakly nonlinear transition layers of width $\mathcal{O}(\epsilon^{1/2})$ connecting linear and nonlinear branches of same superscript; (fl), front layer of size $\mathcal{O}(\epsilon^{2/3})$ connecting the $k^{\ell-}$ and $k^{n\ell+}$ branches and selecting the steep global mode; (sp), saddle point layer of size $\mathcal{O}(\epsilon^{1/2})$ connecting the $k^{n\ell\pm}$ branches and selecting the soft global mode.

Each of these regions is analysed in turn to obtain a uniformly valid asymptotic approximation over the entire range $-\infty < X < +\infty$. Since the width of the narrow layers is $\mathcal{O}(\epsilon^{1/2})$ or $\mathcal{O}(\epsilon^{2/3})$ measured in units of X, their characteristic scale is intermediate between the inhomogeneity length scale $\mathcal{O}(1)$ and the instability length scale $\mathcal{O}(\epsilon)$. Thus, although the medium may be considered uniform in the transition layers, they still display many wave lengths, typically $\mathcal{O}(\epsilon^{-1/2})$ or $\mathcal{O}(\epsilon^{-1/3})$.

In the preceding sections, the bifurcation study was largely based on the CGL equation (4) and a complete understanding of the global selection mechanisms was achieved in this context. In the present section, the WKBJ approximation scheme is presented in the more general framework of p.d.e. (1).

5.1 Linear WKBJ *instability waves*

In the semi-infinite linear regions extending towards $X = \pm\infty$ ($\ell\pm$ in Fig.17-a,b), the global mode amplitude exponentially decays on the fast x-scale. These regions are thus governed by the linear equation (2). Under the slowly varying medium hypothesis (3) a solution of (2) with global frequency ω_g may be obtained in terms of WKBJ approximations [3]. The spatial structure is described by a rapidly varying complex phase, accounting for the local wave length and spatial decay rate, and a slowly varying envelope. For a given value of the

frequency ω_g, the solution reads

$$\psi(x,t) = A^\ell(X) \exp\left(\frac{i}{\epsilon}\int^X k^\ell(u)du - i\omega_g t\right) + \text{c.c.}, \tag{41}$$

where $k^\ell(X)$ is one of the linear spatial branches associated with the frequency ω_g. The functions $A^\ell(X)$ and $k^\ell(X)$ implicitly depend on ω_g; for simplicity their frequency dependence is omitted.

In classical WKBJ fashion, the slowly varying envelope $A^\ell(X)$ is expanded in powers of ϵ as

$$A^\ell(X) \sim A_0^\ell(X) + \epsilon A_1^\ell(X) + \epsilon^2 A_2^\ell(X) + \ldots \tag{42}$$

Thus, spatial differentiation takes the form

$$\frac{\partial\psi}{\partial x} = \left[(ik^\ell(X) + \epsilon\partial_X)A^\ell(X)\right] \exp\left(\frac{i}{\epsilon}\int^X k^\ell(u)du - i\omega_g t\right) + \text{c.c.} \tag{43}$$

Upon substituting (41,42,43) into the governing equation (2) and bearing in mind that $\Omega^\ell(-i\partial_x) = i\mathcal{L}(\partial_x)$, see (8), one obtains

$$\omega_g(A_0^\ell + \epsilon A_1^\ell + \ldots) = \Omega^\ell(k^\ell(X) - i\epsilon\partial_X, X)\left(A_0^\ell + \epsilon A_1^\ell + \ldots\right). \tag{44}$$

Note that differentiation with respect to the fast variable, *i.e.*, multiplication by $ik^\ell(X)$, does not commute with the slow derivative operator ∂_X. The linear operator appearing in (44) admits the expansion

$$\begin{aligned}\Omega^\ell(k^\ell(X) - i\epsilon\partial_X, X) = {} & \Omega^\ell(X) \\ & - i\epsilon\left(\Omega_k^\ell(X)\partial_X + \frac{1}{2}k_X^\ell(X)\Omega_{kk}^\ell(X)\right) + \mathcal{O}(\epsilon^2),\end{aligned} \tag{45}$$

with the notations

$$\Omega^\ell(X) \equiv \Omega^\ell(k^\ell(X), X), \qquad \Omega_k^\ell(X) \equiv \frac{\partial\Omega^\ell}{\partial k}(k^\ell(X), X), \quad \text{etc.}$$

At lowest order, eq.(44) reduces to the linear dispersion relation (20), *i.e.*,

$$\omega_g = \Omega^\ell(k^\ell(X), X), \tag{46}$$

which yields the local wave number $k^\ell(X)$ for a given frequency ω_g.

The order ϵ terms read

$$\left[\omega_g - \Omega^\ell(k^\ell(X), X)\right] A_1^\ell(X) = -i\Omega_k^\ell(X)\frac{dA_0^\ell}{dX} - \frac{i}{2}\Omega_{kk}^\ell(X)k_X^\ell(X)A_0^\ell(X).$$

By invoking (46), one obtains the obvious solvability condition for $A_0^\ell(X)$, namely

$$\frac{dA_0^\ell}{dX} = -\frac{1}{2}k_X^\ell(X)\frac{\Omega_{kk}^\ell(X)}{\Omega_k^\ell(X)}A_0^\ell(X). \tag{47}$$

Thus, the first order asymptotic approximation to the solution of the linearized equation reads

$$\psi \sim A_0^\ell(X_1)\exp\left(-\frac{1}{2}\int_{X_1}^{X} k_X^\ell(u)\frac{\Omega_{kk}^\ell(u)}{\Omega_k^\ell(u)}du\right)\exp\left(\frac{i}{\epsilon}\int_{X_1}^{X} k^\ell(u)du - i\omega_g t\right) + \text{c.c.}, \tag{48}$$

where X_1 is some arbitrarily specified reference point. In each of the semi-infinite linear regions the respective causal k^ℓ branch has to be chosen: $k^{\ell-}$ for $X \to -\infty$ and $k^{\ell+}$ for $X \to +\infty$.

In the linear region, the nonlinear terms of (1) are seen to be exponentially smaller than the linear ones. The nonlinear operator then produces higher harmonics that are exponentially slaved to the fundamental (48). A complete expansion of ψ reveals that the exponential envelope of the n-th harmonic reads

$$\exp\left(-\frac{|n|}{\epsilon}\int^{X} k_i^\ell(u)du\right).$$

Their exact expressions are therefore irrelevant to this work and will not be computed here.

5.2 Nonlinear WKBJ *wave trains*

In the central nonlinear regions ($n\ell\pm$ in Fig.17-a,b), the solution of (1) is obtained in terms of local nonlinear wavetrains (10). An asymptotic approximation scheme for nonlinear wavetrains is derived in this section, which is formally analogous to linear WKBJ theory.

The fast oscillations of the propagating wave and its slowly varying local wave number and amplitude suggest the following change of variables,

$$\psi(x,t) = \psi(\theta; X),$$

where the real phase function $\theta(x,t)$ is 2π-periodic and accounts for propagation on the fast space and time scales, whereas $X = \epsilon x$ allows for slow spatial

modulation. Local frequency and wave number are defined as

$$\omega = -\partial_t \theta \quad \text{and} \quad k = \partial_x \theta.$$

For a synchronized global solution, the frequency $\omega = \omega_g$ is constant, whereas the local wave number $k = k^{n\ell}(X)$ depends on the slow space variable.

Upon expanding the derivative operators according to

$$\begin{aligned} \partial_x &= k^{n\ell}(X)\partial_\theta + \epsilon \partial_X, \\ \partial_t &= -\omega_g \partial_\theta, \end{aligned}$$

the governing equation (1) is recast in the form

$$\omega_g \partial_\theta \psi + \mathcal{F}(k^{n\ell}(X)\partial_\theta + \epsilon \partial_X; X)[\psi] = 0. \tag{49}$$

Again note that differentiation of $\psi(\theta; X)$ with respect to the fast variable does *not* commute with ∂_X since $k^{n\ell}(X)$ depends on X. Next ψ is expanded according to

$$\psi \sim \psi_0 + \epsilon \psi_1 + \epsilon^2 \psi_2 + \dots,$$

and substituted into (49).

The lowest order in ϵ yields the local equation

$$\omega \partial_\theta \psi + \mathcal{F}(k\partial_\theta; X)[\psi] = 0, \tag{50}$$

where X acts as an external parameter. When X is considered frozen, the family of local nonlinear wavetrains $\Psi(\theta; k, X)$ is recovered. This equation admits solutions only if $\omega = \Omega^{n\ell}(k, X)$. In other words, for a global frequency ω_g, the nonlinear spatial branch $k^{n\ell}(X)$ is derived from the local nonlinear dispersion relation (21) as

$$\omega_g = \Omega^{n\ell}(k^{n\ell}(X), X), \tag{51}$$

and the leading order solution ψ_0 then reads

$$\psi_0 = \Psi(\theta; k^{n\ell}(X), X). \tag{52}$$

The function Ψ is 2π-periodic in the phase variable θ which accounts for the fast propagation through

$$\theta = \frac{1}{\epsilon} \int^X k^{n\ell}(u) du - \omega_g t + \theta_0(X). \tag{53}$$

The so far undetermined slowly drifting phase function $\theta_0(X)$ obeys a solvability condition to be obtained at next order.

The $\mathcal{O}(\epsilon)$ terms in (49) require some care. For clarity of presentation assume that spatial differentiation only occurs in the linear operator,

$$\mathcal{F}(\partial_x; X)[\psi] = \mathcal{L}(\partial_x; X)[\psi] + \mathcal{N}(X)[\psi].$$

The linear terms are expanded as

$$\mathcal{L}(k^{n\ell}(X)\partial_\theta + \epsilon\partial_X; X)[\psi_0(\theta; X) + \epsilon\psi_1(\theta; X) + \ldots] \sim$$

$$\mathcal{L}(X)[\psi_0] + \epsilon\left(\mathcal{L}(X)[\psi_1] + \mathcal{L}'(X)[\partial_X\psi_0] + \frac{1}{2}\frac{dk^{n\ell}}{dX}\mathcal{L}''(X)[\partial_\theta\psi_0]\right) + \mathcal{O}(\epsilon^2),$$

where the notation $\mathcal{L}(X)$ is shorthand for $\mathcal{L}(k^{n\ell}(X)\partial_\theta; X)$ and the primes denote differentiation of $\mathcal{L}(\partial_x; X)$ with respect to its first argument. The nonlinear terms are expanded as

$$\mathcal{N}(X)[\psi_0 + \epsilon\psi_1 + \ldots] = \mathcal{N}(X)[\psi_0] + \epsilon\frac{\partial\mathcal{N}(X)[\psi_0]}{\partial\psi}\psi_1 + \mathcal{O}(\epsilon^2).$$

Thus (49) yields at $\mathcal{O}(\epsilon)$,

$$L[\psi_1] = -\mathcal{L}'(X)[\partial_X\psi_0] - \frac{1}{2}\frac{dk^{n\ell}}{dX}\mathcal{L}''(X)[\partial_\theta\psi_0], \tag{54}$$

where the linear differential operator L on the l.h.s. is defined as

$$L \equiv \omega_g\partial_\theta + \mathcal{L}(X) + \frac{\partial\mathcal{N}(X)[\psi_0]}{\partial\psi}. \tag{55}$$

Thus ψ_1 satisfies a linear differential equation with respect to θ with X-dependent coefficients. The operator L is singular since one may readily verify that

$$L[\Psi_\theta] = 0 \quad \text{with} \quad \Psi_\theta \equiv \partial_\theta\Psi(\theta; k^{n\ell}(X), X).$$

Thus (54) admits solutions for ψ_1 only if its r.h.s. satisfies a solvability condition.

Let us introduce an inner product for 2π-periodic functions of θ defined by

$$\langle\phi, \psi\rangle = \frac{1}{2\pi}\int_0^{2\pi}\phi(\theta)\psi(\theta)d\theta. \tag{56}$$

The adjoint operator $L^\dagger$ of L is then obtained via successive integration by parts through the relation

$$\langle\phi, L\psi\rangle = \langle L^\dagger\phi, \psi\rangle,$$

and it reads

$$L^\dagger = -\omega_g \partial_\theta + \mathcal{L}(-k^{n\ell}(X)\partial_\theta; X) + \frac{\partial \mathcal{N}(X)[\psi_0]}{\partial \psi}. \tag{57}$$

Let $\Psi_\theta^\dagger$ be the adjoint eigenfunction of Ψ_θ. Taking the inner product of (54) with $\Psi_\theta^\dagger$ and substituting

$$\partial_X \psi_0 = \frac{d\theta_0}{dX}\Psi_\theta + \frac{dk^{n\ell}}{dX}\Psi_k + \Psi_X,$$

yields the following solvability condition for $\theta_0(X)$,

$$\frac{d\theta_0}{dX}\langle \Psi_\theta^\dagger, \mathcal{L}'\Psi_\theta\rangle + \frac{1}{2}\frac{dk^{n\ell}}{dX}\langle \Psi_\theta^\dagger, 2\mathcal{L}'\Psi_k + \mathcal{L}''\Psi_\theta\rangle + \langle \Psi_\theta^\dagger, \mathcal{L}'\Psi_X\rangle = 0. \tag{58}$$

This entirely specifies the leading order approximation to the global nonlinear solution

$$\psi(x,t) \sim \Psi\left(\frac{1}{\epsilon}\int^X k^{n\ell}(u)du - \omega_g t + \theta_0(X); k^{n\ell}(X), X\right), \tag{59}$$

where the parametric dependence of $k^{n\ell}(X)$ on the global frequency ω_g is entirely determined by (51).

5.3 Front layer

According to Section 4.2, the front of steep global modes is located at the station of local marginal absolute instability X^{ca} and it is associated with a wave number jump from the $k^{\ell-}$ to the $k^{n\ell+}$ branch. On the slow scale X, the front discontinuously connects the linear solution (48) of wave number $k^{\ell-}$ prevailing in the upstream domain $X < X^{ca}$ to the nonlinear solution (59) of wave number $k^{n\ell+}$ on the downstream side of the front $X > X^{ca}$. In this subsection, the linear solution is shown to match to the nonlinear solution through a narrow front layer (fl) as depicted in Fig.17-a. The formulation essentially follows the same approach as in the asymptotic description of the front boundary layer arising in nonlinear dynamo waves developed by Bassom *et al.* [1] and is based on linear turning point theory [90].

The envelope of the outer linear solution is governed by the amplitude equation (47) which is singular at a *turning point* X_0 of the dispersion relation (46) defined by

$$\omega_0(X_0) = \omega_g. \tag{60}$$

For $\omega_g = \omega_0^{ca}$, the turning point is at $X_0 = X^{ca}$. However it is to be anticipated that the global frequency does not exactly equal ω_0^{ca}. As outlined below, it is convenient to implement a matching procedure in the turning point region for an arbitrary complex global frequency ω_g. Thus consider the linear governing equation (2) for complex X. The results of Section 5.1 pertaining to linear instability waves remain valid in the complex X-plane, provided that $\Omega^\ell(k, X)$ and hence $\omega_0(X)$ are analytically continued for complex values of X. Then (60) associates to a frequency ω_g the turning point $X_0(\omega_g)$ in the complex X-plane.

Expansion of the dispersion relation (46) in the neighborhood of the turning point X_0 yields

$$0 = \frac{1}{2}\Omega^\ell_{kk,0}(k^\ell(X) - k_0)^2 + \Omega^\ell_{X,0}(X - X_0) + \text{h.o.t.}, \tag{61}$$

where k_0 is the associated absolute wavenumber $k_0 \equiv k_0(X_0)$ and the subscript 0 denotes evaluation at (k_0, X_0). By definition of the turning point, $\Omega^\ell_{k,0} = 0$, and under the assumption that the turning point is simple, $\Omega^\ell_{X,0} \neq 0$. Thus

$$k^\ell(X) \sim k_0 \pm \sqrt{\frac{-2\Omega^\ell_{X,0}}{\Omega^\ell_{kk,0}}}(X - X_0)^{1/2}.$$

The linear amplitude equation (47) then reduces to

$$\frac{dA_0}{dX} \sim -\frac{A_0(X)}{4(X - X_0)}.$$

Hence $A_0(X) \sim \mathrm{C}^{\mathrm{st}}(X - X_0)^{-1/4}$ as $X \to X_0$, and the complete behavior of the outer linear solution (48) as $X \to X_0$ reads

$$\psi \sim \mathrm{C}^{\mathrm{st}}(X - X_0)^{-1/4} \exp\left[\frac{2i}{3\epsilon}\sqrt{\frac{-2\Omega^\ell_{X,0}}{\Omega^\ell_{kk,0}}(X - X_0)^3}\right] e^{i(k_0 x - \omega_g t)} + \text{c.c.} \tag{62}$$

Here it is assumed that the square root branch cut is chosen so that the wave number $k^{\ell-}$ prevailing in the domain $X \to -\infty$ is recovered.

It is seen that in the neighborhood of the turning point X_0, the amplitude A_0 becomes singular. Balance of dominant terms, as shown below, yields an inner turning point region of size $\mathcal{O}(\epsilon^{2/3})$. Thus define an inner variable $\tilde{X}$ by

$$X = X_0 + \epsilon^{2/3}\tilde{X}, \tag{63}$$

and expand ψ as

$$\psi = \tilde{A}(\tilde{X})e^{i(k_0 x - \omega_g t)} + \text{c.c.}, \tag{64}$$

with

$$\tilde{A}(\tilde{X}) = \tilde{C}^{st}[\tilde{A}_0(\tilde{X}) + \epsilon^{2/3}\tilde{A}_{2/3}(\tilde{X}) + \dots], \tag{65}$$

where $\tilde{A}_0(\tilde{X})$ is $\mathcal{O}(\epsilon^0)$. Spatial differentiation now becomes

$$\frac{\partial \psi}{\partial x} = \left[(ik_0 + \epsilon^{1/3}\partial_{\tilde{X}})\tilde{A}(\tilde{X})\right] e^{i(k_0 x - \omega_g t)} + \text{c.c.} \tag{66}$$

Note that in this inner transition layer, the leading order wave number is constant and equal to k_0, thus $\partial_{\tilde{X}}$ and ik_0 now commute. Replacing (63,64,66) into the governing equation (2) yields

$$\begin{aligned}\omega_g \tilde{A}(\tilde{X}) &= \Omega^\ell(k_0 - i\epsilon^{1/3}\partial_{\tilde{X}}, X_0 + \epsilon^{2/3}\tilde{X})\tilde{A}(\tilde{X}) \\ &\sim \left[\Omega^\ell(k_0, X_0) + \epsilon^{2/3}\left(\tilde{X}\Omega^\ell_{X,0} - \frac{1}{2}\Omega^\ell_{kk,0}\partial_{\tilde{X}\tilde{X}}\right)\right]\tilde{A}(\tilde{X}),\end{aligned}$$

where $\omega_g = \Omega^\ell(k_0, X_0)$. The scaling $X - X_0 \sim \epsilon^{2/3}\tilde{X}$ and $x \sim \epsilon^{-1/3}\tilde{X}$ guarantees the balance of dominant terms at order $\mathcal{O}(\epsilon^{2/3})$ in the previous equation and leads to the following Airy equation for the leading order amplitude

$$\frac{1}{2}\Omega^\ell_{kk,0}\frac{d^2\tilde{A}_0}{d\tilde{X}^2} = \tilde{X}\Omega^\ell_{X,0}\tilde{A}_0(\tilde{X}). \tag{67}$$

Thus $\tilde{A}_0(\tilde{X})$ is a linear superposition of the Airy functions $\mathrm{Ai}(-\lambda\tilde{X})$ and $\mathrm{Bi}(-\lambda\tilde{X})$ with

$$\lambda^3 = -\frac{2\Omega^\ell_{X,0}}{\Omega^\ell_{kk,0}}.$$

Upon choosing for λ the solution with $|\mathrm{Arg}\,\lambda| < \pi/3$, the Bi component exponentially grows whereas the Ai component decays according to

$$\mathrm{Ai}(-\lambda\tilde{X}) \sim \frac{1}{2\sqrt{\pi}}(-\lambda\tilde{X})^{-1/4}\exp\left[\frac{2i}{3}\sqrt{\frac{-2\Omega^\ell_{X,0}}{\Omega^\ell_{kk,0}}\tilde{X}^3}\right], \tag{68}$$

as $\tilde{X} \to -\infty$ [3]. Expressing the outer solution (62) in terms of the inner variable $\tilde{X}$, shows that it matches with the inner solution (64) provided that

$$\tilde{A}(\tilde{X}) = \tilde{C}^{st}[\mathrm{Ai}(-\lambda\tilde{X}) + \mathcal{O}(\epsilon^{2/3})], \tag{69}$$

with $C^{st} = \epsilon^{1/6}\frac{(-\lambda)^{-1/4}}{2\sqrt{\pi}}\tilde{C}^{st}$.

Thus, for any frequency ω_g, linear instability waves are governed by the Airy equation (67) in a region of size $\mathcal{O}(\epsilon^{2/3})$ located at the turning point of the linear local dispersion relation. The location of the turning point in the complex

X-plane depends on ω_g. For frequencies $\omega_g = \omega_0^{ca} + \delta\omega$, close to the marginal absolute frequency, the turning point is located at

$$X_0 \sim X^{ca} + \frac{\delta\omega}{\omega_{0,X}(X^{ca})}.$$

For $\mathcal{O}(\epsilon^{2/3})$ frequency corrections, $\delta\omega = \epsilon^{2/3}\omega_{2/3}$, the inner Airy region in the complex X-plane contains in its neighborhood the point X^{ca} on the real X-axis.

Before analysing in more detail the properties of the Airy solutions on the $\tilde{X}$-scale, let us turn to the front structure. As discussed in Section 5.3, a uniform medium at the transition between convective and absolute instability admits stationary front solutions oscillating at its real absolute frequency. Thus the original nonlinear governing equation (1) rewritten at $X = X^{ca}$ as

$$\omega_0^{ca}\frac{\partial\psi}{\partial\theta} + \mathcal{F}(\partial_x; X^{ca})[\psi] = 0, \tag{70}$$

admits the front solution $\Psi_f(x,\theta)$, which is 2π-periodic in the phase function $\theta = \omega_0^{ca}t$. Towards $x = +\infty$ this solution approaches a fully nonlinear wavetrain of the form (52). Thus

$$\Psi_f(x,\omega_0^{ca}t) \sim \Psi[k^{n\ell+}(X^{ca},\omega_0^{ca})x - \omega_0^{ca}t; k^{n\ell+}(X^{ca},\omega_0^{ca}), X^{ca}]$$

as $x \to +\infty$. Towards $x = -\infty$ the exponential decay rate is dictated by the absolute wave number $k_0^{ca} = k_0(X^{ca})$ and the front solution reads

$$\Psi_f(x,\omega_0^{ca}t) \sim (\mathrm{c}_0^{\mathrm{st}} + \mathrm{c}_1^{\mathrm{st}}x)e^{i(k_0^{ca}x - \omega_0^{ca}t)} + \text{c.c.}, \tag{71}$$

where the secular term is due to the double root $k^{\ell+} = k^{\ell-} = k_0^{ca}$ of the linear dispersion relation. In the uniform medium, the front has no preferred location. A translation of Δx only changes the phase by $k^{n\ell+}(\omega_0^{ca})\Delta x$ in the asymptotic behavior towards the nonlinear side $x = +\infty$ and leads to an additional factor $e^{ik_0^{ca}\Delta x}$ in the upstream exponentially decaying tail.

The exponentially decaying tail (71) has to be matched with (64) in the Airy region. Due to the secular term in (71), matching with (64) is only possible at the zeroes of the Airy function.

The Airy function Ai appearing in (69) admits real negative zeros a_i. Thus the zeros of $\tilde{A}_0$ are located at $\tilde{X}_i = -a_i/\lambda$. In terms of the outer variable X these occur at

$$X_i \equiv X_0(\omega_g) + \epsilon^{2/3}\tilde{X}_i = X^{ca} + \epsilon^{2/3}\left(\frac{\omega_{2/3}}{\omega_{0,X}} - \frac{a_i}{\lambda}\right) + \mathcal{O}(\epsilon^{4/3}). \tag{72}$$

Whereas the linear WKBJ approximations as well as the turning point region may be investigated in the complex X-plane, the front involves a nonlinear

wavetrain and is thus necessarily restricted to the *real* X-axis. Requiring that the i-th zero (72) of the Airy function is on the real X-axis yields the frequency correction term

$$\omega_{2/3} = a_i \frac{|\omega_{0,X}|^2}{|\lambda|^2} \frac{\mathrm{Im}\,\lambda}{\mathrm{Im}\,\omega_{0,X}},$$

for a zero located at

$$X_i \sim X^{ca} + \epsilon^{2/3} \frac{a_i}{|\lambda|^2} \frac{\mathrm{Im}\,(\omega_{0,X}^{\star}\lambda)}{\mathrm{Im}\,\omega_{0,X}}.$$

Since X^{ca} is the transition location from convective to absolute instability, $\mathrm{Im}\,\omega_{0,X}$ is positive. Under the slightly more restrictive assumption that $\pi/3 < \mathrm{Arg}\,\omega_{0,X} < 2\pi/3$, we are guaranteed that $\mathrm{Im}\,(\omega_{0,X}^{\star}\lambda) < 0$. In most situations of physical interest, variations of $\omega_{0,r}$ are small compared to those of $\omega_{0,i}$ and thus the condition on $\mathrm{Arg}\,\omega_{0,X}$ is readily fulfilled.

So far the matching conditions yield a countable set of frequencies

$$\omega_g \sim \omega_0^{ca} + \epsilon^{2/3} a_i \Omega_{2/3} \quad \text{with} \quad \Omega_{2/3} = \frac{|\omega_{0,X}|^2}{|\lambda|^2} \frac{\mathrm{Im}\,\lambda}{\mathrm{Im}\,\omega_{0,X}}, \tag{73}$$

each being associated with the i-th zero $a_i < 0$ of the Airy function. The corresponding fronts are located at

$$X \sim X^{ca} - \epsilon^{2/3} a_i X_{2/3} \quad \text{with} \quad X_{2/3} = \frac{-\mathrm{Im}\,(\omega_{0,X}^{\star}\lambda)}{|\lambda|^2 \mathrm{Im}\,\omega_{0,X}} > 0. \tag{74}$$

Since $X_{2/3} > 0$, higher order global modes display a front located further downstream in the AU domain. These situations are likely to be unstable since the exponentially decaying tail of the front partly penetrates into the AU domain. Such a higher order front prevailing in a slightly AU medium tends to move upstream, until it reaches the most upstream possible station associated with a_0. Thus we argue, although we have not proven the result, that the only stable global mode solution is obtained for the first zero indexed by a_0. Up to $\mathcal{O}(\epsilon^{2/3})$, the global frequency and the front location therefore respectively read

$$\omega_g \sim \omega_0^{ca} + \epsilon^{2/3} a_0 \Omega_{2/3} \quad \text{and} \quad X \sim X^{ca} - \epsilon^{2/3} a_0 X_{2/3},$$

with

$$a_0 = -2.3381\ldots$$

This completes the investigation of the detailed structure of the front region.

5.4 Fully nonlinear saddle point layer

The nonlinear saddle point is defined as the location $X_s^{n\ell}$ where the two nonlinear wave number branches meet. The saddle point frequency $\omega_s^{n\ell}$ is given by the criterion (30). In the nonlinear regions surrounding the saddle location $X_s^{n\ell}$ the asymptotic approximation of the global solution is of the form (59) and the slowly drifting phase function $\theta_0(X)$ is governed by the solvability condition (58).

At the saddle point, the first order differential equation (58) for θ_0 becomes singular since $\langle \Psi_\theta^\dagger, \mathcal{L}'\Psi_\theta \rangle = 0$ at $X_s^{n\ell}$ [cf. equation (93) below]. Thus the nonlinear WKBJ approximation worked out in Section 5.2 is no longer valid in the neighborhood of $X_s^{n\ell}$, because θ_0 varies there on a spatial scale which is faster than X. In this section, a nonlinear transition layer at $X_s^{n\ell}$ is introduced, (sp) in Fig.17-b, and a *second order* differential equation for the phase θ_0 is derived after rescaling the spatial variable in the neighborhood of $X_s^{n\ell}$. This inner solution in the saddle point region allows a smooth crossover between the WKBJ wave trains in both nonlinear regions.

Let us introduce an inner local space variable $\tilde{X}$ in the saddle point region defined as

$$X = X_s^{n\ell} + \epsilon^{1/2}\tilde{X},$$

and expand ψ according to

$$\psi \sim \tilde{\psi}_0 + \epsilon^{1/2}\tilde{\psi}_{1/2} + \epsilon\tilde{\psi}_1 + \dots \tag{75}$$

The subsequent analysis yields the higher order corrections to the global frequency as

$$\omega_g \sim \omega_s^{n\ell} + \epsilon^{1/2}\omega_{1/2} + \epsilon\omega_1 + \dots \tag{76}$$

Replacing the spatial derivative ∂_x in the inner region by $k_s^{n\ell}\partial_\theta + \epsilon^{1/2}\partial_{\tilde{X}}$, the linear operator expands as[3]

$$\begin{aligned} &\mathcal{L}(k_s^{n\ell}\partial_\theta + \epsilon^{1/2}\partial_{\tilde{X}}, X_s^{n\ell} + \epsilon^{1/2}\tilde{X}) \\ &= \mathcal{L}_s + \epsilon^{1/2}(\mathcal{L}'_s\partial_{\tilde{X}} + \tilde{X}\mathcal{L}_{X,s}) + \frac{\epsilon}{2}(\mathcal{L}''_s\partial_{\tilde{X}\tilde{X}} + 2\tilde{X}\mathcal{L}'_{X,s}\partial_{\tilde{X}} + \tilde{X}^2\mathcal{L}_{XX,s}) \\ &\quad + \mathcal{O}(\epsilon^{3/2}). \end{aligned} \tag{77}$$

Substituting the expansions (75,76,77) into the governing equation (1), one recovers at leading order

$$\omega_s^{n\ell}\partial_\theta\tilde{\psi}_0 + \mathcal{L}(k_s^{n\ell}\partial_\theta, X_s^{n\ell})\tilde{\psi}_0 + \mathcal{N}(X_s^{n\ell})[\tilde{\psi}_0] = 0.$$

[3] Subscript (s) always denotes evaluation at $\partial_x = k_s^{n\ell}\partial_\theta$, $X = X_s^{n\ell}$, $k = k_s^{n\ell}$.

Thus

$$\tilde{\psi}_0 = \Psi_s \equiv \Psi(\theta + \tilde{\theta}_0(\tilde{X}); k_s^{n\ell}, X_s^{n\ell}), \tag{78}$$

where the fast phase function in the saddle point layer reads $\theta = k_s^{n\ell}x - \omega_s^{n\ell}t$ and the slow phase $\tilde{\theta}_0(\tilde{X})$ is a so far an undetermined function varying on the intermediate length scale $\tilde{X}$.

The nonlinear term is expanded as

$$\begin{aligned}
&\mathcal{N}(X_s^{n\ell} + \epsilon^{1/2}\tilde{X})[\Psi_s + \epsilon^{1/2}\tilde{\psi}_{1/2} + \epsilon\tilde{\psi}_1 + \mathcal{O}(\epsilon^{3/2})] \\
&= \mathcal{N}_s + \epsilon^{1/2}(\tilde{X}\mathcal{N}_{X,s} + \mathcal{N}_{\psi,s}\tilde{\psi}_{1/2}) \\
&+ \epsilon\left(\frac{1}{2}\tilde{X}^2\mathcal{N}_{XX,s} + \tilde{X}\mathcal{N}_{X\psi,s}\tilde{\psi}_{1/2} + \frac{1}{2}\mathcal{N}_{\psi\psi,s}\tilde{\psi}_{1/2}^2 + \mathcal{N}_{\psi,s}\tilde{\psi}_1\right) + \mathcal{O}(\epsilon^{3/2}),
\end{aligned} \tag{79}$$

where

$$\mathcal{N}_s \equiv \mathcal{N}(X_s^{n\ell})[\Psi_s], \quad \mathcal{N}_{\psi,s} \equiv \partial_\psi \mathcal{N}(X_s^{n\ell})[\Psi_s],$$

$$\mathcal{N}_{X,s} \equiv \partial_X \mathcal{N}(X_s^{n\ell})[\Psi_s], \quad \text{etc.}$$

The order $\epsilon^{1/2}$ problem reads

$$L_s\tilde{\psi}_{1/2} + \omega_{1/2}\Psi_{\theta,s} + \frac{d\tilde{\theta}_0}{d\tilde{X}}\mathcal{L}_s'\Psi_{\theta,s} + \tilde{X}(\mathcal{L}_{X,s}\Psi_s + \mathcal{N}_{X,s}) = 0, \tag{80}$$

where

$$L_s \equiv \omega_s^{n\ell}\partial_\theta + \mathcal{L}_s + \mathcal{N}_{\psi,s}.$$

Let $\Psi_{\theta,s}^\dagger$ be the adjoint eigenfunction of $\Psi_{\theta,s}$. Eq.(80) admits solutions for $\tilde{\psi}_{1/2}$ if the following solvability condition is met

$$\omega_{1/2}\langle\Psi_{\theta,s}^\dagger, \Psi_{\theta,s}\rangle + \frac{d\tilde{\theta}_0}{d\tilde{X}}\langle\Psi_{\theta,s}^\dagger, \mathcal{L}_s'\Psi_{\theta,s}\rangle + \tilde{X}\langle\Psi_{\theta,s}^\dagger, \mathcal{L}_{X,s}\Psi_s + \mathcal{N}_{X,s}\rangle = 0.$$

In Section 5.4.1 below, the two last terms of this equation are shown to vanish (93,94). Thus the solvability condition requires that

$$\omega_{1/2} = 0.$$

There is no correction to the global frequency at order $\epsilon^{1/2}$ and no equation for $\tilde{\theta}_0$ is obtained at this order.

With $\omega_{1/2} = 0$ and using (95,96), the general solution of the linear inhomogenous equation (80) is obtained as

$$\tilde{\psi}_{1/2} = \tilde{X}\Psi_{X,s} + \frac{d\tilde{\theta}_0}{d\tilde{X}}\Psi_{k,s} + A(\tilde{X})\Psi_{\theta,s}, \tag{81}$$

where $A(\tilde{X})$ is an arbitrary real amplitude function.

At order ϵ, the following inhomogenous equation for $\tilde{\psi}_1$ is obtained

$$L_s\tilde{\psi}_1 + \mathcal{L}'_s\partial_{\tilde{X}}\tilde{\psi}_{1/2} + \tilde{X}\left(\mathcal{L}_{X,s} + \mathcal{N}_{X\psi,s}\right)\tilde{\psi}_{1/2} + \frac{1}{2}\mathcal{N}_{\psi\psi,s}\tilde{\psi}^2_{1/2} + \omega_1\Psi_s + \left(\frac{1}{2}\mathcal{L}''_s\partial_{\tilde{X}\tilde{X}} + \tilde{X}\mathcal{L}'_{\tilde{X},s}\partial_{\tilde{X}} + \frac{1}{2}\tilde{X}^2\mathcal{L}_{XX,s}\right)\Psi_s + \frac{1}{2}\tilde{X}^2\mathcal{N}_{XX,s} = 0.$$

Replacing $\tilde{\psi}_{1/2}$ according to (81) leads to

$$\begin{aligned}
&L_s\tilde{\psi}_1 + \frac{1}{2}\frac{d^2\tilde{\theta}_0}{d\tilde{X}^2}\left(2\mathcal{L}'_s\Psi_{k,s} + \mathcal{L}''_s\Psi_{\theta,s}\right)\\
&\quad + \frac{1}{2}\left(\frac{d\tilde{\theta}_0}{d\tilde{X}}\right)^2\left(2\mathcal{L}'_s\Psi_{\theta k,s} + \mathcal{L}''_s\Psi_{\theta\theta,s} + \mathcal{N}_{\psi\psi,s}(\Psi_{k,s})^2\right)\\
&\quad + \tilde{X}\frac{d\tilde{\theta}_0}{d\tilde{X}}\left((\mathcal{L}_{X,s} + \mathcal{N}_{X\psi,s})\Psi_{k,s} + \mathcal{L}'_{X,s}\Psi_{\theta,s} + \mathcal{L}'_s\Psi_{\theta X,s} + \mathcal{N}_{\psi\psi,s}\Psi_{k,s}\Psi_{X,s}\right)\\
&\quad + \frac{1}{2}\tilde{X}^2\left(2(\mathcal{L}_{X,s} + \mathcal{N}_{X\psi,s})\Psi_{X,s} + \mathcal{L}_{XX,s}\Psi_s + \mathcal{N}_{XX,s} + \mathcal{N}_{\psi\psi,s}(\Psi_{X,s})^2\right)\\
&\quad + \frac{d\tilde{\theta}_0}{d\tilde{X}}A(\tilde{X})\left(\mathcal{L}'_s\Psi_{\theta\theta,s} + \mathcal{N}_{\psi\psi,s}\Psi_{\theta,s}\Psi_{k,s}\right)\\
&\quad + \tilde{X}A(\tilde{X})\left((\mathcal{L}_{X,s} + \mathcal{N}_{\psi X,s})\Psi_{\theta,s} + \mathcal{N}_{\psi\psi,s}\Psi_{\theta,s}\Psi_{X,s}\right)\\
&\quad + \frac{dA}{d\tilde{X}}\mathcal{L}'_s\Psi_{\theta,s} + \frac{1}{2}A(\tilde{X})^2\mathcal{N}_{\psi\psi,s}(\Psi_{\theta,s})^2\\
&\quad + \mathcal{L}'_s\Psi_{X,s} + \omega_1\Psi_{\theta,s}\\
&\quad = 0.
\end{aligned} \tag{82}$$

This equation admits solutions for $\tilde{\psi}_1$ if the inner product of the forcing terms (everything except $L_s\tilde{\psi}_1$) with $\Psi^\dagger_{\theta,s}$ vanishes. The different inner products are computed in Section 5.4.1. From (97,98,99) it follows that all the terms involving the function $A(\tilde{X})$ vanish: this function remains undetermined at this order. Using (100,101,102) the solvability condition for $\tilde{\theta}_0$ reads

$$A\frac{d^2\tilde{\theta}_0}{d\tilde{X}^2} = B\left(\frac{d\tilde{\theta}_0}{d\tilde{X}}\right)^2 + 2C\tilde{X}\frac{d\tilde{\theta}_0}{d\tilde{X}} + D\tilde{X}^2 - E - 2\omega_1, \tag{83}$$

where

$$\begin{aligned}
A &= \langle\Psi^\dagger_{\theta,s}, 2\mathcal{L}'_s\Psi_{k,s} + \mathcal{L}''_s\Psi_{\theta,s}\rangle\big/\langle\Psi^\dagger_{\theta,s}, \Psi_{\theta,s}\rangle,\\
B &= \Omega^{n\ell}_{kk,s},\\
C &= \Omega^{n\ell}_{kX,s},\\
D &= \Omega^{n\ell}_{XX,s},
\end{aligned}$$

$$E = \langle \Psi^{\dagger}_{\theta,s}, \mathcal{L}'_s \Psi_{X,s} \rangle \Big/ \langle \Psi^{\dagger}_{\theta,s}, \Psi_{\theta,s} \rangle.$$

Let

$$\Theta(\tilde{X}) = \exp\left[-\frac{B}{A}\tilde{\theta}_0(\alpha \tilde{X}) - \frac{C\alpha^2}{2A}\tilde{X}^2 \right] \tag{84}$$

with

$$\alpha^4 = \frac{A^2}{4(C^2 - BD)}. \tag{85}$$

Note that $C^2 - BD > 0$ since $(k_s^{n\ell}, X_s^{n\ell})$ is a saddle point of $\Omega^{n\ell}(k, X)$. Rewriting the solvability condition (83) in terms of Θ yields the parabolic cylinder equation [3]

$$\frac{d^2\Theta}{d\tilde{X}^2} = \left(\frac{1}{4}\tilde{X}^2 - \nu - \frac{1}{2} \right) \Theta, \tag{86}$$

where

$$\nu + \frac{1}{2} = \frac{1}{2} \frac{AC - B(E + 2\omega_1)}{\sqrt{A^2(C^2 - BD)}}.$$

This solution in the inner saddle point layer needs to be matched with the wave trains (59) in the outer nonlinear regions. In terms of the inner variable $\tilde{X}$, the phase of the outer nonlinear solutions (59) expands as

$$\begin{aligned} \frac{1}{\epsilon} \int_{X_s^{n\ell}}^{X_s^{n\ell} + \epsilon^{1/2}\tilde{X}} & k^{n\ell}(u)du - \omega_g t + \theta_0(X) \\ & = (k_s^{n\ell} x - \omega_s^{n\ell} t) + \frac{1}{2} k_{X,s}^{n\ell} \tilde{X}^2 + \mathcal{O}(\epsilon^{1/2}). \end{aligned} \tag{87}$$

Matching to the phase $k_s^{n\ell} x - \omega_s^{n\ell} t + \tilde{\theta}_0(\tilde{X})$ of the inner solution (78) when $\tilde{X} \to \pm\infty$, requires that

$$\tilde{\theta}_0(\tilde{X}) \sim \frac{1}{2} k_{X,s}^{n\ell} \tilde{X}^2 \quad \text{when} \quad \tilde{X} \to \pm\infty. \tag{88}$$

At the saddle point, the derivative of the wave number reads

$$k_{X,s}^{n\ell} = \frac{-\Omega_{kX,s}^{n\ell} + \sqrt{(\Omega_{kX,s}^{n\ell})^2 - \Omega_{XX,s}^{n\ell}\Omega_{kk,s}^{n\ell}}}{\Omega_{kk,s}^{n\ell}} = \frac{-C + \sqrt{C^2 - BD}}{B}. \tag{89}$$

Using (88) with (89) in (84) shows that the function $\Theta(\tilde{X})$ behaves asymptotically as

$$\ln \Theta(\tilde{X}) \sim -\frac{1}{4}\tilde{X}^2,$$

when $\tilde{X} \to \pm\infty$. The only solution of (86) satisfying this asymptotic behavior and taking only nonnegative values is obtained for $\nu = 0$ and simply reads

$$\Theta(\tilde{X}) = \exp(-\tilde{X}^2/4).$$

Thus the asymptotic expansion (88) is exact for all $\tilde{X}$. Then the soft global mode frequency reads to $\mathcal{O}(\epsilon)$

$$\omega_g \sim \omega_s^{n\ell} + \epsilon\omega_1$$

with

$$\omega_1 = \frac{1}{2B}\left(AC - BE - \sqrt{A^2(C^2 - BD)}\right).$$

5.4.1 Computation of inner products

The values of the inner products used in the previous analysis are obtained from

$$\Omega^{n\ell}(k, X)\partial_\theta\Psi + \mathcal{L}(k\partial_\theta, X)\Psi + \mathcal{N}(X)[\Psi] = 0. \tag{90}$$

Differentiation of (90) with respect to θ, k or X yields

$$\begin{aligned} L\Psi_\theta &\equiv (\Omega^{n\ell}\partial_\theta + \mathcal{L} + \mathcal{N}_\psi)\Psi_\theta = 0, \\ L\Psi_k + \Omega_k^{n\ell}\Psi_\theta + \mathcal{L}'\Psi_\theta &= 0, \qquad (91) \\ L\Psi_X + \Omega_X^{n\ell}\Psi_\theta + \mathcal{L}_X\Psi + \mathcal{N}_X &= 0. \qquad (92) \end{aligned}$$

Taking the inner product of (91,92) with $\Psi_\theta^\dagger$ yields

$$\begin{aligned} \Omega_k^{n\ell}\langle\Psi_\theta^\dagger, \Psi_\theta\rangle + \langle\Psi_\theta^\dagger, \mathcal{L}'\Psi_\theta\rangle &= 0, \\ \Omega_X^{n\ell}\langle\Psi_\theta^\dagger, \Psi_\theta\rangle + \langle\Psi_\theta^\dagger, \mathcal{L}_X\Psi\rangle + \langle\Psi_\theta^\dagger, \mathcal{N}_X\rangle &= 0. \end{aligned}$$

At the saddle point $(k_s^{n\ell}, X_s^{n\ell})$ the derivatives $\Omega_k^{n\ell}$ and $\Omega_X^{n\ell}$ vanish by definition, thus

$$\langle\Psi_{\theta,s}^\dagger, \mathcal{L}_s'\Psi_{\theta,s}\rangle = 0, \tag{93}$$

$$\langle\Psi_{\theta,s}^\dagger, \mathcal{L}_{X,s}\Psi_s + \mathcal{N}_{X,s}\rangle = 0. \tag{94}$$

From (91) and (92) we deduce

$$L_s\Psi_{k,s} = -\mathcal{L}_s'\Psi_{\theta,s}, \tag{95}$$

$$L_s\Psi_{X,s} = -\mathcal{L}_{X,s}\Psi_{\theta,s} - \mathcal{N}_{X,s}. \tag{96}$$

From these identities, the particular solution (81) to eq.(80) follows.

The order ϵ problem in the saddle point region specified by (82) requires to compute inner products by double differentiation. Differentiating (90) with respect to $\theta\theta$, θk or θX yields

$$\begin{aligned} L\Psi_{\theta\theta} + \mathcal{N}_{\psi\psi}(\Psi_\theta)^2 &= 0, \\ L\Psi_{\theta k} + \Omega_k^{n\ell}\Psi_{\theta\theta} + \mathcal{L}'\Psi_{\theta\theta} + \mathcal{N}_{\psi\psi}\Psi_\theta\Psi_k &= 0, \\ L\Psi_{\theta X} + \Omega_X^{n\ell}\Psi_{\theta\theta} + \mathcal{L}_X\Psi_\theta + \mathcal{N}_{X\psi}\Psi_\theta + \mathcal{N}_{\psi\psi}\Psi_\theta\Psi_X &= 0, \end{aligned}$$

and, after taking the inner product with $\Psi_\theta^\dagger$ at the saddle point, one obtains

$$\langle \Psi_{\theta,s}^\dagger, \mathcal{N}_{\psi\psi,s}(\Psi_{\theta,s})^2\rangle = 0, \tag{97}$$

$$\langle \Psi_{\theta,s}^\dagger, \mathcal{L}'_s\Psi_{\theta\theta,s} + \mathcal{N}_{\psi\psi,s}\Psi_{\theta,s}\Psi_{k,s}\rangle = 0, \tag{98}$$

$$\langle \Psi_{\theta,s}^\dagger, (\mathcal{L}_{X,s} + \mathcal{N}_{X\psi,s})\Psi_{\theta,s} + \mathcal{N}_{\psi\psi,s}\Psi_{\theta,s}\Psi_{X,s}\rangle = 0. \tag{99}$$

Differentiation of (90) with respect to kk, kX or XX yields

$$\begin{aligned} &L\Psi_{kk} + \Omega_{kk}^{n\ell}\Psi_\theta + 2(\Omega_k^{n\ell} + \mathcal{L}')\Psi_{\theta k} + \mathcal{L}''\Psi_{\theta\theta} + \mathcal{N}_{\psi\psi}(\Psi_k)^2 = 0, \\ &L\Psi_{kX} + (\Omega_{kX}^{n\ell} + \mathcal{L}'_X)\Psi_\theta + (\Omega_k^{n\ell} + \mathcal{L}')\Psi_{\theta X} \\ &\qquad + \Omega_X^{n\ell}\Psi_{\theta k} + (\mathcal{L}_X + \mathcal{N}_{X\psi})\Psi_k + \mathcal{N}_{\psi\psi}\Psi_k\Psi_X = 0, \\ &L\Psi_{XX} + \Omega_{XX}^{n\ell}\Psi_\theta + 2\Omega_X^{n\ell}\Psi_{\theta X} + 2(\mathcal{L}_X + \mathcal{N}_{X\psi})\Psi_X \\ &\qquad + \mathcal{L}_{XX}\Psi + \mathcal{N}_{\psi\psi}(\Psi_X)^2 + \mathcal{N}_{XX} = 0, \end{aligned}$$

and thus

$$\begin{aligned} &\langle \Psi_{\theta,s}^\dagger, 2\mathcal{L}'_s\Psi_{\theta k,s} + \mathcal{L}''_s\Psi_{\theta\theta,s} + \mathcal{N}_{\psi\psi,s}(\Psi_{k,s})^2\rangle \\ &\qquad = -\Omega_{kk,s}^{n\ell}\langle \Psi_{\theta,s}^\dagger, \Psi_{\theta,s}\rangle, \end{aligned} \tag{100}$$

$$\begin{aligned} &\langle \Psi_{\theta,s}^\dagger, (\mathcal{L}_{X,s} + \mathcal{N}_{X\psi,s})\Psi_{k,s} + \mathcal{L}'_{X,s}\Psi_{\theta,s} + \mathcal{L}'_s\Psi_{\theta X,s} + \mathcal{N}_{\psi\psi,s}\Psi_{k,s}\Psi_{X,s}\rangle \\ &\qquad = -\Omega_{kX,s}^{n\ell}\langle \Psi_{\theta,s}^\dagger, \Psi_{\theta,s}\rangle, \end{aligned} \tag{101}$$

$$\begin{aligned} &\langle \Psi_{\theta,s}^\dagger, 2(\mathcal{L}_{X,s} + \mathcal{N}_{X\psi,s})\Psi_{X,s} + \mathcal{L}_{XX,s}\Psi_s + \mathcal{N}_{XX,s} + \mathcal{N}_{\psi\psi,s}(\Psi_{X,s})^2\rangle \\ &\qquad = -\Omega_{XX,s}^{n\ell}\langle \Psi_{\theta,s}^\dagger, \Psi_{\theta,s}\rangle. \end{aligned} \tag{102}$$

Results (97–102) are invoked to cast the phase evolution equation in its final form (83).

5.5 *Weakly nonlinear transition layers*

Frequency corrections for steep and soft global modes have been derived by performing a detailed asymptotic analysis of the corresponding narrow transition layers where their respective frequency selection mechanism takes place: the *front layer* for steep modes and the *nonlinear saddle point layer* for soft modes. The only type of layer that remains to be investigated in order to

obtain uniformly valid asymptotic approximations for global modes is the *weakly nonlinear transition layer*. This layer applies to the downstream end of the steep mode nonlinear region (tl+ in Fig.17-a) and to both ends of the soft mode nonlinear region (tl± in Fig.17-b). It should be emphasized that these layers are slaved to the dynamics imposed by the front or the nonlinear saddle point frequency.

A smooth transition between nonlinear and linear solutions occurs at the boundary of the nonlinear balloon (Fig.5 and 7) in the (X,k)-plane. Consider a global solution of frequency ω_g. Its local linear and nonlinear wave number branches $k^{\ell}(X,\omega_g)$ and $k^{n\ell}(X,\omega_g)$ are derived respectively from the curves $\Omega^{\ell}(k,X)=\omega_g$ and $\Omega^{n\ell}(k,X)=\omega_g$. A $k^{n\ell}(X,\omega_g)$ branch is connected at the border of the nonlinear balloon to the corresponding linear $k^{\ell}(X,\omega_g)$ branch at the particular station $X=X_t(\omega_g)$ for $k=k_t(\omega_g)$ where the pair (k_t,X_t) is defined by

$$\omega_g=\Omega^{\ell}(k_t,X_t)=\Omega^{n\ell}(k_t,X_t). \tag{103}$$

As demonstrated in Sections 4.2 and 4.6, a continuous transition between linear and nonlinear wave number branches occurs at the downstream boundary of the nonlinear region of a steep global mode and at both downstream and upstream boundaries of the nonlinear region of a soft global mode. At a downstream boundary, the $k^{n\ell+}$ branch prevailing in the region $X<X_t$ is continuously connected to the $k^{\ell+}$ branch for $X>X_t$. At an upstream boundary, transition from $k^{\ell-}$ for $X<X_t$ to $k^{n\ell-}$ for $X>X_t$ occurs.

When $X\to X_t$ from within the nonlinear region, the amplitude of the nonlinear wave train decays, nonlinearities weaken, higher harmonics become slaved to the fundamental, and eventually a linear instability wave takes over. In the present section we show how the connection between linear and nonlinear solutions is achieved across a narrow transition layer located at X_t.

Let us focus on an upstream transition layer (tl−), *i.e.*, the solution is fully nonlinear for $X>X_t$ and decays exponentially for $X<X_t$. The same analysis applies in the downstream transition layer (tl+). The asymptotic behavior of the nonlinear wave trains $\Psi(\theta;k,X)$ is first derived as (k,X) approaches the neutral stability boundary of the nonlinear balloon (Section 5.5.1). This result is then used along the particular path $(k^{n\ell}(X),X)$ to derive expansions for the modulus (Section 5.5.2) and phase (Section 5.5.3) of the global mode as $X\downarrow X_t$. This outer expansion is shown in Section 5.5.4 to match with the inner solution prevailing in the transition layer. Finally the inner solution is matched in Section 5.5.5 to the outer linear WKBJ approximation prevailing in the region $X<X_t$.

5.5.1 Weakly nonlinear behavior

In the nonlinear balloon of the (X,k)-plane characterized by $\Omega_i^\ell(k,X) > 0$, the governing equation (1) admits local solutions of the form (52). A global mode of frequency ω_g follows the line $\omega_g = \Omega^{n\ell}(k,X)$ in the (k,X)-plane. The boundary of the nonlinear balloon is reached at (k_t, X_t) defined in (103). Let us first study the behavior of the periodic functions $\Psi(\theta;k,X)$ in the (k,X)-plane as (k,X) approaches the boundary of the nonlinear balloon, *i.e.*, $\Omega_i^\ell(k,X) \downarrow 0$.

The nonlinear operator $\mathcal{F}[\psi]$ in (1) is expanded in powers of ψ and (1) is rewritten as

$$\frac{\partial\psi}{\partial t} = \mathcal{L}(\partial_x, X)[\psi] + \sum_{r=2}^{\infty} \mathcal{N}_r(\partial_x, X)[\psi], \tag{104}$$

where the operators $\mathcal{N}_r$ are of r-th order in ψ. In all generality, each $\mathcal{N}_r$ depends on ∂_x, but to simplify the subsequent computations, it is assumed that the $\mathcal{N}_r$'s do not involve spatial derivation, *i.e.*,

$$\mathcal{N}_r(\partial_x, X)[\psi] = N_r(X)\psi^r. \tag{105}$$

The results would remain valid for any nonlinear operator with spatial derivatives, but the notation and results becom unwieldy in more general cases. The method is easily extended to specific examples.

The 2π-periodic function Ψ is expanded as the Fourier series

$$\Psi(\theta;k,X) = \sum_n \Psi^{(n)}(k,X)e^{in\theta}, \tag{106}$$

where $\Psi^{(-n)} = (\Psi^{(n)})^\star$. Due to the invariance of the governing equation under the transformation $\theta \to \theta + \mathrm{C^{st}}$., $\Psi^{(1)}(k,X)$ may be chosen to be real for each (k,X).

Substituting (105,106) into (104) yields the equations for the harmonic components of Ψ,

$$\begin{aligned} n\Omega^{n\ell}(k,X)\Psi^{(n)}(k,X) = {} & \Omega^\ell(nk,X)\Psi^{(n)}(k,X) \\ & + i\sum_{r=2}^{\infty} N_r(X) \sum_{n_1+\ldots+n_r=n} \Psi^{(n_1)}(k,X)\cdots\Psi^{(n_r)}(k,X). \end{aligned} \tag{107}$$

With the definition

$$\Delta^{(n)}(k,X) = n\Omega^{n\ell}(k,X) - \Omega^\ell(nk,X),$$

equations (107) read,

$$\Delta^{(n)}(k,X)\Psi^{(n)}(k,X)$$
$$= i\sum_{r=2}^{\infty} N_r(X) \sum_{n_1+\ldots+n_r=n} \Psi^{(n_1)}(k,X)\cdots\Psi^{(n_r)}(k,X). \tag{108}$$

When $\Omega_i^\ell(k,X) \downarrow 0$, the term $\Delta^{(1)}(k,X)$ vanishes, whereas the $\Delta^{(n)}(k,X)$ remain finite for $|n| \neq 1$. Thus, in this limit, the components with $|n| \neq 1$ are slaved to the fundamental $n = \pm 1$ and scale as

$$\Psi^{(n)}(k,X) = \begin{cases} \mathcal{O}[(\Psi^{(1)}(k,X))^{|n|}] \text{ if } n \neq 0 \\ \mathcal{O}[(\Psi^{(1)}(k,X))^2] \text{ if } n = 0 \end{cases} \quad \text{when} \quad \Omega_i^\ell(k,X) \downarrow 0. \tag{109}$$

The dominant terms of (108) for $n = 2$ read

$$\Delta^{(2)}(k,X)\Psi^{(2)}(k,X) = iN_2(X)[\Psi^{(1)}(k,X)]^2 + \mathcal{O}[(\Psi^{(1)})^4], \tag{110}$$

and for $n = 0$,

$$\Delta^{(0)}(k,X)\Psi^{(0)}(k,X) = 2iN_2(X)\Psi^{(1)}(k,X)\Psi^{(-1)}(k,X) + \mathcal{O}[(\Psi^{(1)})^4]. \tag{111}$$

For $n = 1$, equation (108) yields

$$\Delta^{(1)}(k,X)\Psi^{(1)}(k,X)$$
$$= 2iN_2(X)[\Psi^{(2)}(k,X)\Psi^{(-1)}(k,X) + \Psi^{(1)}(k,X)\Psi^{(0)}(k,X)]$$
$$+3iN_3(X)|\Psi^{(1)}(k,X)|^2\Psi^{(1)}(k,X) + \mathcal{O}[(\Psi^{(1)})^5]. \tag{112}$$

Substituting (110,111) into (112) yields the leading order expression for $\Psi^{(1)}$

$$|\Psi^{(1)}(k,X)|^2 \sim \frac{\Delta^{(1)}(k,X)}{3iN_3(X) - 2N_2(X)^2\left(\frac{1}{\Delta^{(2)}(k,X)} + \frac{2}{\Delta^{(0)}(k,X)}\right)}. \tag{113}$$

Thus

$$|\Psi^{(1)}(k,X)|^2 = \mathcal{O}[\Delta^{(1)}(k,X)],$$

and

$$\Psi^{(1)}(k,X) = \mathcal{O}\left[\sqrt{\Omega_i^\ell(k,X)}\right]. \tag{114}$$

5.5.2 Asymptotic decay of outer nonlinear wave trains

The preceding results, valid for any (k,X) when $\Omega_i^\ell(k,X) \downarrow 0$, yield the asymptotic behavior of the nonlinear part (59) of a global mode as $X \downarrow X_t$.

Let us expand the nonlinear solution (59) into harmonic components as follows

$$\Psi(\theta; k^{n\ell}(X), X) =$$

$$\sum_n \left(\psi_0^{(n)}(X) + \epsilon\psi_1^{(n)}(X) + \ldots\right) \exp\left\{in\left(\frac{1}{\epsilon}\int^X k^{n\ell}(u)du - \omega_g t\right)\right\}. \quad (115)$$

Then, according to (106),

$$\psi_0^{(n)}(X) = \Psi^{(n)}(k^{n\ell}(X), X)e^{in\theta_0(X)}.$$

From (109,114) with $\Omega_i^\ell(k^{n\ell}(X), X) = \mathcal{O}(X - X_t)$, it follows that, for each $n \neq 0$,

$$\psi_0^{(n)}(X) = \mathcal{O}[(X - X_t)^{|n|/2}] \quad \text{as} \quad X \downarrow X_t. \quad (116)$$

The asymptotic behavior of $\psi_0^{(1)}(X)$ for $X \downarrow X_t$ is derived from (113) as

$$\psi_0^{(1)}(X) \sim \hat{\Psi}_0^{(1)} e^{i\theta_0(X)}(X - X_t)^{1/2}, \quad (117)$$

with

$$|\hat{\Psi}_0^{(1)}|^2 = \frac{\Delta_{X,t}^{(1)}}{3iN_{3,t} - 2(N_{2,t})^2\left(\frac{1}{\Delta_t^{(2)}} + \frac{2}{\Delta_t^{(0)}}\right)}, \quad (118)$$

where subscript t means evaluation at $X = X_t$ and $k = k_t = k^{n\ell}(X_t)$, and

$$\Delta_{X,t}^{(1)} = \frac{d}{dX}\Delta^{(1)}(k^{n\ell}(X), X)\bigg|_{X=X_t}.$$

In the same fashion one obtains for the second harmonic

$$\psi_0^{(2)}(X) \sim \hat{\Psi}_0^{(2)} e^{i2\theta_0(X)}(X - X_t), \quad (119)$$

with, according to (110),

$$\hat{\Psi}_0^{(2)} = \frac{N_{2,t}}{\Delta_t^{(2)}}(\hat{\Psi}_0^{(1)})^2. \quad (120)$$

In the bulk of the nonlinear region the harmonic spectrum is fully developed but towards the neutral stability boundary the higher order harmonics become slaved to the fundamental. Since the higher order harmonics decay faster than $\Psi^{(1)}$ as the neutral stability boundary is approached, the nonlinear solution is approximated by a purely sinusoidal wave of vanishing amplitude. Matching to a linear solution in the region $X < X_t$ therefore becomes possible.

5.5.3 Diverging slow phase

So far only the behavior of the amplitude as $X \downarrow X_t$ has been obtained. In this subsection the asymptotic behavior of the slow phase $\theta_0(X)$ at the neutral

stability boundary of the nonlinear region is computed.

Let us write the solvability condition (58) as

$$0 = \frac{d\theta_0}{dX}\langle \Psi_\theta^\dagger, \mathcal{L}'\Psi_\theta\rangle + \frac{1}{2}\frac{dk^{n\ell}}{dX}\langle \Psi_\theta^\dagger, \mathcal{L}''\Psi_\theta\rangle + \langle \Psi_\theta^\dagger, \mathcal{L}'\left(\frac{dk^{n\ell}}{dX}\Psi_k + \Psi_X\right)\rangle \quad (121)$$

According to (106) the nonlinear solution Ψ admits the expansion

$$\Psi(\theta + \theta_0(X); k^{n\ell}(X), X) = \sum_n \Psi^{(n)}(k^{n\ell}(X), X) e^{in\theta_0(X)} e^{in\theta}.$$

Thus

$$\mathcal{L}'\left(\frac{dk^{n\ell}}{dX}\Psi_k + \Psi_X\right) = \sum_n \mathcal{L}'(ink^{n\ell}(X); X)\frac{d}{dX}\left[\Psi^{(n)}(X)\right] e^{in\theta_0(X)} e^{in\theta},$$

$$\mathcal{L}''\Psi_\theta = \sum_n in\mathcal{L}''(ink^{n\ell}(X); X)\Psi^{(n)}(X) e^{in\theta_0(X)} e^{in\theta},$$

$$\mathcal{L}'\Psi_\theta = \sum_n in\mathcal{L}'(ink^{n\ell}(X); X)\Psi^{(n)}(X) e^{in\theta_0(X)} e^{in\theta},$$

with

$$\Psi^{(n)}(X) \equiv \Psi^{(n)}(k^{n\ell}(X), X).$$

According to (109,114) the harmonic components exhibit the following behavior

$$\Psi^{(n)}(X) \sim \begin{cases} (X - X_t)^{|n|/2}\hat{\Psi}^{(n)} & \text{if } n \neq 0 \\ (X - X_t)^2\hat{\Psi}^{(0)} & \text{if } n = 0 \end{cases} \quad \text{as} \quad X \downarrow X_t,$$

where $\hat{\Psi}^{(1)}$ and $\hat{\Psi}^{(2)}$ have explicitly been obtained in (118,120). Thus the term $\mathcal{L}'\left(k_X^{n\ell}\Psi_k + \Psi_X\right)$ diverges as $(X - X_t)^{-1/2}$ whereas the other terms scale as $(X - X_t)^{1/2}$. In order to evaluate the inner products involved in (121), the adjoint $\Psi_\theta^\dagger$ has to be explicitly determined. The term in $L^\dagger$ (57) associated with the nonlinear operator $\mathcal{N}$ reads

$$\frac{\partial \mathcal{N}(X)[\Psi]}{\partial \psi} = 2(X - X_t)^{1/2} N_{2,t}(\hat{\Psi}^{(1)} e^{i\theta_0(X)} e^{i\theta} + \text{c.c.}) + \mathcal{O}[X - X_t];$$

whereas

$$\mathcal{L}(-k^{n\ell}(X)\partial_\theta; X) = \mathcal{L}(-k_t\partial_\theta; X_t) + (X - X_t)(-k_{X,t}^{n\ell}\mathcal{L}'(-k_t\partial_\theta; X_t)\partial_\theta + \mathcal{L}_X(-k_t\partial_\theta; X_t)) + \mathcal{O}[(X - X_t)^2].$$

Thus the adjoint operator (57) reads

$$L^\dagger = -\omega_g \partial_\theta + \mathcal{L}(-k_t \partial_\theta; X_t) + 2(X - X_t)^{1/2} N_{2,t} (\hat{\Psi}^{(1)} e^{i\theta_0(X)} e^{i\theta} + \text{c.c.}) + \mathcal{O}[X - X_t].$$

A solution of $L^\dagger \phi = 0$ sought under the form

$$\phi = \sum_n in(X - X_t)^{|n|/2} \Phi^{(n)}(X) e^{in\theta},$$

leads to

$$\begin{aligned} 0 = {} & (X - X_t)^{1/2} [(-i\omega_g + \mathcal{L}(-ik_t; X_t)) i\Phi^{(1)}(X) e^{i\theta} + \text{c.c.}] \\ & + (X - X_t)[(-2i\omega_g + \mathcal{L}(-2ik_t; X_t)) 2i\Phi^{(2)}(X) e^{i2\theta} + \text{c.c.}] \\ & + (X - X_t) 2N_{2,t} [\hat{\Psi}^{(1)} e^{i\theta_0(X)} e^{i\theta} + \text{c.c.}][i\Phi^{(1)}(X) e^{i\theta} + \text{c.c.}] \\ & + \mathcal{O}[(X - X_t)^{3/2}]. \end{aligned}$$

Due to (103) the $\mathcal{O}[(X - X_t)^{1/2}]$ term identically vanishes. At order $(X - X_t)$, the equations

$$\begin{aligned} 0 &= 2iN_{2,t} \hat{\Psi}^{(1)} e^{i\theta_0(X)} \Phi^{(-1)}(X) + \text{c.c.}, \\ 0 &= (2\omega_g + i\mathcal{L}(-2ik_t, X_t)) 2\Phi^{(2)}(X) + 2N_2(X_t) \hat{\Psi}^{(1)} e^{i\theta_0(X)} i\Phi^{(1)}(X), \end{aligned}$$

yield

$$\begin{aligned} \Phi^{(1)}(X) &\propto \hat{\Psi}^{(1)} e^{i\theta_0(X)} \\ \Phi^{(2)}(X) &\propto \frac{iN_2(X_t)}{2\omega_g + i\mathcal{L}(-2ik_t, X_t)} (\hat{\Psi}^{(1)} e^{i\theta_0(X)})^2, \end{aligned}$$

with a *real* constant of proportionality. A simple calculation then leads to

$$\begin{aligned} \langle \Psi_\theta^\dagger, \mathcal{L}' \Psi_\theta \rangle &= (X - X_t)[\mathcal{L}'(ik_t; X_t) + \text{c.c.}] |\hat{\Psi}^{(1)}|^2 + \mathcal{O}[(X - X_t)^2], \\ \langle \Psi_\theta^\dagger, \mathcal{L}'' \Psi_\theta \rangle &= (X - X_t)[\mathcal{L}''(ik_t; X_t) + \text{c.c.}] |\hat{\Psi}^{(1)}|^2 + \mathcal{O}[(X - X_t)^2], \\ \langle \Psi_\theta^\dagger, \mathcal{L}' \left(k_X^{n\ell} \Psi_k + \Psi_X \right) \rangle &= -\frac{1}{2} [i\mathcal{L}'(ik_t; X_t) + \text{c.c.}] |\hat{\Psi}^{(1)}|^2 + \mathcal{O}[X - X_t]. \end{aligned}$$

Upon substituting the preceding results into (121) the governing equation for the slow phase at the boundary of the nonlinear region becomes

$$\frac{d\theta_0}{dX} = -\frac{1}{2} \frac{1}{X - X_t} \frac{\text{Im } \mathcal{L}'(ik_t; X_t)}{\text{Re } \mathcal{L}'(ik_t; X_t)} + \mathcal{O}[(X - X_t)^0].$$

Hence, θ_0 diverges logarithmically as

$$\theta_0(X) = -\frac{1}{2} \frac{\text{Im } \mathcal{L}'(ik_t; X_t)}{\text{Re } \mathcal{L}'(ik_t; X_t)} \ln(X - X_t) + \text{C}^{\text{st}} + \mathcal{O}[X - X_t], \tag{122}$$

when $X \downarrow X_t$.

5.5.4 Inner transition layer solution

The asymptotic matching of a finite amplitude nonlinear wave train to an exponentially decaying linear solution takes place *via* an inner solution valid in a narrow transition layer at X_t between the nonlinear and linear regions.

Define an inner variable $\tilde{X}$ in the neighborhood of X_t by $X = X_t + \epsilon^{1/2}\tilde{X}$. The outer solution obtained in the previous section is rewritten in terms of this inner variable. The fast phase θ reads

$$\theta \equiv \frac{1}{\epsilon}\int^{X_t+\epsilon^{1/2}\tilde{X}} k^{n\ell}(u)du - \omega_g t = (k_t x - \omega_g t) + \frac{1}{2}k^{n\ell}_{X,t}\tilde{X}^2 + \mathcal{O}(\epsilon^{1/2}), \quad (123)$$

whereas the slow phase θ_0 of eq.(122) is expanded as

$$\theta_0 \sim -\frac{1}{2}\frac{\operatorname{Im}\mathcal{L}'(ik_t;X_t)}{\operatorname{Re}\mathcal{L}'(ik_t;X_t)}\ln\tilde{X} + \mathrm{C}^{\mathrm{st}} \quad (124)$$

Thus, as $X \downarrow X_t$, keeping only the leading order terms in the harmonics $|n| \leq 2$ of the outer solution given by (115) yields the following expansion

$$\begin{aligned}\psi \sim{}& \epsilon^{1/4}\tilde{X}^{1/2}\left[\hat{\Psi}_0^{(1)}e^{i(\theta+\theta_0)} + \text{c.c.}\right] \\ &+ \epsilon^{1/2}\tilde{X}\left(\frac{iN_{2,t}}{\Delta_t^{(2)}}\left[(\hat{\Psi}_0^{(1)})^2 e^{2i(\theta+\theta_0)} + \text{c.c.}\right] + \frac{iN_{2,t}}{\Delta_t^{(0)}}2|\hat{\Psi}_0^{(1)}|^2\right) + \mathcal{O}(\epsilon^{3/4}). \quad (125)\end{aligned}$$

This behavior of the outer solution in terms of the inner variable $\tilde{X}$ suggests to expand the harmonic components of the inner solution as

$$\psi \sim \sum_n \epsilon^{n/4}\left(\tilde{\psi}_0^{(n)}(x,\tilde{X}) + \epsilon^{1/2}\tilde{\psi}_{1/2}^{(n)}(x,\tilde{X}) + \ldots\right)e^{-in\omega_g t}, \quad (126)$$

with $\tilde{\psi}_0^{(0)} = 0$ since $\psi^{(0)} = \mathcal{O}(|\psi^{(1)}|^2)$. Each component of the inner expansion has to be matched for $\tilde{X} \to +\infty$ with the corresponding component of the outer expansion. Due to the presence of slow and fast spatial scales $\tilde{X}$ and x, the spatial derivative in the governing equation (1) now reads $\partial_x + \epsilon^{1/2}\partial_{\tilde{X}}$. Thus the following equations are obtained for each harmonic component

$$\begin{aligned}0 = {}& \left(in\omega_g + \mathcal{L}(\partial_x + \epsilon^{1/2}\partial_{\tilde{X}}; X_t + \epsilon^{1/2}\tilde{X})\right)\left[\tilde{\psi}_0^{(n)} + \epsilon^{1/2}\tilde{\psi}_{1/2}^{(n)} + \ldots\right] \\ &+ \sum_{r=2}^{\infty} N_r(X_t + \epsilon^{1/2}\tilde{X}) \sum_{n_1+\ldots+n_r=n}\left(\tilde{\psi}_0^{(n_1)} + \ldots\right)\cdots\left(\tilde{\psi}_0^{(n_r)} + \ldots\right). \quad (127)\end{aligned}$$

For $n = 1$ the leading order problem in ϵ reads

$$\omega_g\tilde{\psi}_0^{(1)} = i\mathcal{L}(\partial_x; X_t)[\tilde{\psi}_0^{(1)}].$$

This linear differential equation in x admits solutions of the form $A(\tilde{X})e^{ikx}$ where the *a priori* possible complex wave numbers k satisfy the linear dispersion relation (20): $\omega_g = \Omega^\ell(k, X_t)$. However, the slowly (algebraically) decaying outer nonlinear solution is oscillating on the fast scale as $e^{ik_t x}$ with k_t defined by (103). Hence matching of outer and inner solutions ensures that $\tilde{\psi}_0^{(1)}$ contains the single Fourier mode

$$\tilde{\psi}_0^{(1)} = \tilde{A}_0^{(1)}(\tilde{X})e^{ik_t x}, \tag{128}$$

with a slowly varying amplitude $\tilde{A}_0^{(1)}(\tilde{X})$.

For $n = 2$ the leading order problem in ϵ of (127) reads

$$2\omega_g \tilde{\psi}_0^{(2)} - i\mathcal{L}(\partial_x; X_t)[\tilde{\psi}_0^{(2)}] = iN_{2,t}\tilde{\psi}_0^{(1)}\tilde{\psi}_0^{(1)}. \tag{129}$$

Using (128) yields the particular solution

$$\tilde{\psi}_0^{(2)} = \frac{iN_{2,t}}{\Delta_t^{(2)}}[\tilde{A}_0^{(1)}(\tilde{X})]^2 e^{2ik_t x}. \tag{130}$$

The homogenous differential equation associated with (129) admits solutions of the form $e^{ik_2 x}$ for wave numbers k_2 satisfying $2\omega_g = \Omega^\ell(k_2, X_t)$. Again none of these complex wave numbers k_2 satisfy the matching conditions, thus only the particular solution (130) needs to be retained.

For $n = 0$, the equation

$$0 = \mathcal{L}(\partial_x; X_t)[\tilde{\psi}_{1/2}^{(0)}] + 2N_{2,t}|\tilde{\psi}_0^{(1)}|^2$$

yields

$$\tilde{\psi}_{1/2}^{(0)} = \frac{2iN_{2,t}}{\Delta_t^{(0)}}|\tilde{A}_0^{(1)}(\tilde{X})|^2. \tag{131}$$

In eq.(127), the linear operator expands as

$$\mathcal{L}(\partial_x + \epsilon^{1/2}\partial_{\tilde{X}}; X_t + \epsilon^{1/2}\tilde{X}) = \mathcal{L}(\partial_x; X_t) + \epsilon^{1/2}\left[\mathcal{L}'(\partial_x; X_t)\partial_{\tilde{X}} + \tilde{X}\mathcal{L}_X(\partial_x; X_t)\right] + \mathcal{O}(\epsilon).$$

Thus for $n = 1$ the order $\epsilon^{1/2}$ terms of (127) read

$$\begin{aligned} 0 = {} & i\omega_g \tilde{\psi}_{1/2}^{(1)} + \mathcal{L}(\partial_x; X_t)[\tilde{\psi}_{1/2}^{(1)}] + \left[\mathcal{L}'(\partial_x; X_t)\partial_{\tilde{X}} + \tilde{X}\mathcal{L}_X(\partial_x; X_t)\right]\tilde{\psi}_0^{(1)} \\ & + 3N_{3,t}|\tilde{\psi}_0^{(1)}|^2\tilde{\psi}_0^{(1)} + 2N_{2,t}[\tilde{\psi}_0^{(2)}\tilde{\psi}_0^{(-1)} + \tilde{\psi}_{1/2}^{(0)}\tilde{\psi}_0^{(1)}], \end{aligned} \tag{132}$$

and at this order there are no derivatives of the nonlinear term with respect to X. This inhomogenous differential equation in x admits solutions for $\tilde{\psi}_{1/2}^{(1)}$

only if the resonant terms in $e^{ik_t x}$ of the forcing terms vanish. Upon using (128,130,131) in (132), this leads to the solvability condition

$$0 = \mathcal{L}'(ik_t; X_t)\frac{d\tilde{A}_0^{(1)}}{d\tilde{X}} + \mathcal{L}_X(ik_t; X_t)\tilde{X}\tilde{A}_0^{(1)}(\tilde{X}) \qquad (133)$$
$$+ \left(3N_{3,t} + 2i(N_{2,t})^2\left(\frac{1}{\Delta_t^{(2)}} + \frac{2}{\Delta_t^{(0)}}\right)\right)|\tilde{A}_0^{(1)}(\tilde{X})|^2\tilde{A}_0^{(1)}(\tilde{X}).$$

This amplitude equation for $\tilde{A}_0^{(1)}(\tilde{X})$ is of the form

$$\frac{d\tilde{A}_0^{(1)}}{d\tilde{X}} + \left((a_r + ia_i)\tilde{X} + (b_r + ib_i)|\tilde{A}_0^{(1)}(\tilde{X})|^2\right)\tilde{A}_0^{(1)}(\tilde{X}) = 0, \qquad (134)$$

and its solutions are

$$\frac{\tilde{A}_0^{(1)}(\tilde{X})}{\tilde{A}_0^{(1)}(0)} = \frac{\exp\left[-\frac{a_r+ia_i}{2}\tilde{X}^2 - \frac{i}{2}\frac{b_i}{b_r}\ln\left(1 + 2b_r|\tilde{A}_0^{(1)}(0)|^2\int_0^{\tilde{X}} e^{-a_r u^2}du\right)\right]}{\sqrt{1 + 2b_r|\tilde{A}_0^{(1)}(0)|^2\int_0^{\tilde{X}} e^{-a_r u^2}du}}, \qquad (135)$$

where $\tilde{A}_0^{(1)}(0)$ is the integration constant. Matching of the inner solution $\tilde{\psi}_0^{(1)}$ to the outer solution $\psi_0^{(1)}$ of (117) requires that $|\tilde{A}_0^{(1)}(\tilde{X})| \sim \sqrt{\tilde{X}}$ as $\tilde{X} \to +\infty$. This implies that

$$1 + 2b_r|\tilde{A}_0^{(1)}(0)|^2\int_0^{+\infty} e^{-a_r u^2}du = 0, \quad i.e., \quad |\tilde{A}_0^{(1)}(0)|^2 = \frac{-1}{b_r}\sqrt{\frac{a_r}{\pi}}.$$

With this value for $|\tilde{A}_0^{(1)}(0)|$ the inner solution (135) admits for $\tilde{X} \to +\infty$ the asymptotic expansion

$$\tilde{A}_0^{(1)}(\tilde{X}) \sim \sqrt{-\frac{a_r}{b_r}\tilde{X}}\exp\frac{i}{2}\left[\left(\frac{b_i}{b_r}a_r - a_i\right)\tilde{X}^2 + \frac{b_i}{b_r}\ln\tilde{X} + \mathrm{C}^{\mathrm{st}}\right]. \qquad (136)$$

Comparison of (133) and (134) yields

$$a_r + ia_i = \frac{\mathcal{L}_X(ik_t; X_t)}{\mathcal{L}'(ik_t; X_t)} = -ik_{X,t}^{\ell},$$
$$b_r + ib_i = |\hat{\Psi}_0^{(1)}|^{-2}\frac{\Delta_{X,t}^{(1)}}{i\mathcal{L}'(ik_t; X_t)} = -|\hat{\Psi}_0^{(1)}|^{-2}\left(ik_{X,t}^{n\ell} + \frac{\mathcal{L}_X(ik_t; X_t)}{\mathcal{L}'(ik_t; X_t)}\right),$$

with $|\hat{\Psi}_0^{(1)}|^2$ obtained in (118). Thus

$$-\frac{a_r}{b_r} = |\hat{\Psi}_0^{(1)}|^2,$$
$$\frac{b_i}{b_r}a_r - a_i = k_{X,t}^{n\ell},$$

$$-\frac{b_i}{b_r} = \frac{\operatorname{Im} \mathcal{L}'(ik_t, X_t)}{\operatorname{Re} \mathcal{L}'(ik_t, X_t)}.$$

This completes the proof that the first harmonic of the outer nonlinear solution given by eq.(125) completely matches the first harmonic of the inner weakly nonlinear solution $\epsilon^{1/4}\tilde{A}_0^{(1)}(\tilde{X})e^{i(k_t x - \omega_g t)}$, where $\tilde{A}_0^{(1)}(\tilde{X})$ is given by (135).

5.5.5 *Matching to the outer linear solution*

As $X \uparrow X_t$, the outer linear WKBJ approximation (41) reads, at leading order,

$$\psi \sim A_0^{\ell}(X_t)e^{i(k_t x - \omega_g t)} \exp\left(\frac{i}{2}k_{X,t}^{\ell}\tilde{X}^2\right) + \text{c.c.}, \tag{137}$$

when expressed in terms of the inner variable $\tilde{X}$. Using (135), the asymptotic behavior of the inner solution as $\tilde{X} \to -\infty$ yields

$$\begin{aligned}\psi &\sim \epsilon^{1/4}\tilde{A}_0^{(1)}(\tilde{X})e^{i(k_t x - \omega_g t)} + \text{c.c.} \\ &\sim \epsilon^{1/4}\frac{\tilde{A}_0^{(1)}(0)}{\sqrt{2}}e^{i(k_t x - \omega_g t)} \exp\left(-\frac{a_r + ia_i}{2}\tilde{X}^2 - \frac{i}{2}\frac{b_i}{b_r}\ln 2\right) + \text{c.c.}\end{aligned} \tag{138}$$

Since $a_r + ia_i = -ik_{X,t}^{\ell}$, both expansions (137) and (138) asymptotically match with

$$A_0^{\ell}(X_t) = \epsilon^{1/4}\frac{\tilde{A}_0^{(1)}(0)}{\sqrt{2}}e^{-i\frac{b_i}{2b_r}\ln 2}.$$

Thus, at leading order, the weakly nonlinear inner expansion (138) exactly matches the outer linear WKBJ approximation (41). In the inner transition layer the slaved higher order harmonics scale as $\epsilon^{|n|/4}$. In the outer linear region, each harmonic component matches the corresponding exponentially slaved harmonic and decays as

$$\epsilon^{|n|/4} \exp -\frac{|n|}{\epsilon}\int^{X} k_i^{\ell}(u)du.$$

The width of the transition layer at X_t is of order $\epsilon^{1/2}$ measured in terms of X. The intermediate scaling between the fast length scale x and the slow spatial variation $X = \epsilon x$ allows the asymptotic analysis of the crossover between linear and nonlinear regions. Even in the narrow transition layer the solution exhibits slowly modulated fast oscillations; the transition layer contains $\mathcal{O}(\epsilon^{-1/2})$ wave lengths.

6 Conclusions

It has been demonstrated that a wide class of one-dimensional nonlinear evolution equations with spatially varying coefficients may support two types of fully nonlinear self-sustained global modes in a doubly infinite domain: Steep global modes are triggered by the presence of a sharp stationary front located at the upstream transition point between local convective and absolute instability. This front acts as a source and imposes its real absolute frequency to the entire medium. Soft global modes are due to the presence of a saddle point of the local nonlinear dispersion relation which again acts as a source and imposes its frequency to the entire medium, as given by saddle point conditions.

A necessary condition for the occurrence of either of these modes is the existence of a region of local absolute instability. Recall that linearly unstable global modes given by a complex saddle point of the local linear dispersion relation [13,51,59] also require a range of local absolute instability. But, this range must in general be of finite extent whereas nonlinear global modes exist, however small the AU domain. The relationship between linear global instability and the existence of fully nonlinear global modes is non-trivial: In the generic case, nonlinear global instability does not coincide with linear global instability. The nature of the various global bifurcation scenarii constitute the major result of the present investigation. Steep global modes occur *right at local absolute instability onset below the linear global instability threshold*, via a saddle node bifurcation, while the medium is still linearly globally stable.

Soft global modes generically do not appear at local absolute instability onset but only for a sufficiently large domain of local absolute instability. Furthermore, they are more likely to be observed in systems with weak advection. It is essential to note that steep and soft global modes are mutually exclusive, as dictated by the relative magnitude of their respective frequencies. The existence and selection of either kind of global modes has been confirmed by direct numerical simulations of the CGL equation with varying coefficients for small but finite values of ϵ. As a word of caution, it should be stated that soft global modes are likely to be more fragile than their steep counterparts. They may become unstable whenever the region of local absolute instability protrudes beyond the central nonlinear regions, in the tails of the extended wavepacket. This lack of robustness is all the more acute as the WKBJ limit $\epsilon = 0$ is approached.

In several physical systems [69,1] linear and nonlinear global instability have been found to occur at the same value of the global control parameter. This peculiar feature takes place in situations where the entire spatial dependence is accounted for in a single real spatially varying parameter, say $R(X)$, which

displays an extremum at a real position X^{max} such that $dR(X^{max})/dX = 0$. Under these circumstances, the local linear dispersion relation is necessarily of the form $\Omega^{\ell}(k, X) = \Omega^{\ell}_{\star}[k, R(X)]$ and the local absolute frequency is readily obtained as $\omega_0(X) = \omega_{0\star}[R(X)]$. The real station X^{max} is then simultaneously associated with a maximum of $\omega_{0,i}(X)$ and with a saddle point X^{ℓ}_s of $\omega_0(X)$.

The analytical structure underlying the spatial distribution of steep and soft global modes has been systematically derived in the WKBJ approximation $\epsilon \ll 1$. It has been shown that for a wide class of one-dimensional evolution equations the various inner layers and outer regions may be matched together to arrive at a consistent description valid over the entire spatial domain. In particular, higher-order frequency corrections have been obtained.

It should be emphasized that the different transition scenarii depend on the precise form of the linear and nonlinear dispersion relations. Due to the number of parameters required to specify the spatial variations of the medium, a comprehensive survey of all possible configurations has not been attempted.

This study has been undertaken in order to understand the nature of synchronized structures in real slowly varying open shear flows. In the latter framework, the local linear dispersion relation is obtained from the Rayleigh or the Orr–Sommerfeld equation, whereas the local nonlinear dispersion relation requires the computation of finite amplitude structures in a streamwise periodic interval. In this context, steep global modes may be constructed as reported elsewhere [67].

Ackowledgements

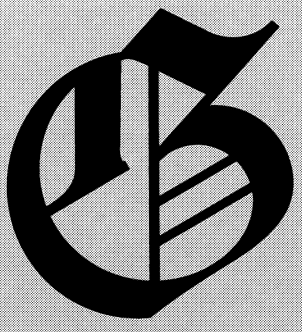
The authors have benefitted from many enlightening and fruitful discussions with Arnaud Couairon.

Commentaires

Avec cette étude des bifurcations s'achève ma contribution à l'équation de GLC à coefficients variables. Il reste beaucoup de portes ouvertes. Je n'ai jamais examiné l'instabilité secondaire des ondes planes d'amplitude finie : on pourrait imaginer des modes globaux secondaires vivant sur un train d'ondes lui-même lentement variable. L'analyse détaillée de la structure globale près de la situation dégénérée où à la fois l'advection est faible et la région AI de petite étendue est également envisageable. On peut aussi essayer de créer des modes plus exotiques avec un choix de coefficients *ad hoc*.

Plus intéressante est la question de la stabilité des modes chapeaux et l'influence du paramètre ϵ du développement WKBJ. En effet, la partie non linéaire de ces modes ne couvre pas entièrement la région AI, mais est légèrement décalée vers l'aval de telle sorte à laisser apparaître le bord AI amont sous la région $\ell-$. On s'attend à ce que dans une région AI d'autres perturbations croissent sur place ; ce n'est pas le cas des modes chapeaux. Le figure 3.1 démontre qu'un mode chapeau peut être sélectionné même en présence d'advection ($k_{0,i} = -0.1$ partout) qui repousse la région non linéaire vers l'aval. Des simulations sur un domaine beaucoup plus grand et une variation spatiale de $\omega_0(X)$ plus lente indiquent une possible instabilité du mode chapeau, mais je n'ai pas voulu entreprendre une étude systématique.

Les développements asymptotiques détaillés dans la dernière partie de l'article montrent la cohérence des structures spatiales obtenues et permettent d'obtenir les corrections de fréquence. Cependant la théorie asymptotique ne dégage aucun résultat nouveau. Les mécanismes fondamentaux sont établis au niveau des relations de dispersion locales et de la forme des branches spatiales correspondantes. C'est donc vers ces relations de dispersion qu'il faut nous tourner maintenant pour résoudre le problème du comportement synchronisé des sillages.



Généralisation aux écoulements réels

Les trois chapitres précédents sont entièrement consacrés à l'étude de systèmes lentement variables en espace à l'aide de l'équation de Ginzburg–Landau complexe. Ce modèle n'a jamais été considéré comme un but en soi, mais comme un outil pour tester certaines hypothèses et pour mettre en avant les principes fondamentaux de sélection de fréquence. Le but initial de ces recherches étant de comprendre les oscillations intrinsèques de certains écoulements ouverts, il est temps de vérifier que les principes généraux dégagés dans le cadre de ce modèle restent valables.

Deux critères de sélection ont été obtenus avec le modèle. Qu'en est-il des écoulements réels ? Les modes chapeaux sont tributaires d'un point-selle de la relation de dispersion non linéaire. Un tel point-selle exige une relation de dispersion non linéaire très dispersive, et il faut absolument des branches amplifiées vers l'aval et vers l'amont. Or, le peu de choses qu'on connaît des trains d'ondes non linéaires dans les écoulements cisaillés est qu'ils obéissent grossièrement à une relation du type $\omega = kc$, où c est la vitesse moyenne de l'écoulement. Ceci signifie que les structures non linéaires se propagent à peu près toutes à la vitesse du fluide quel que soit leur nombre d'onde. Un point-selle dans $\Omega^{n\ell}(k, X)$ est donc peu probable. En revanche, les modes éléphants ne requièrent qu'une seule branche spatiale non linéaire. Ce sont donc les éléphants qui ont le plus de chance de surmonter les difficultés posées par les écoulements réels.

La généralisation des critères de sélection aux équations de Navier–Stokes ne coule pas de source. Le premier problème est le choix de l'écoulement de base. D'une part il faut une région centrale AI, et d'autre part il faut vérifier l'hypothèse de faible inhomogénéité spatiale. La plupart des écoulements expérimentaux autour d'obstacles ne satisfont pas la dernière condition : dans la zone de recirculation du sillage proche, les profils de vitesse varient rapidement, et la présence de l'obstacle constitue une inhomogénéité forte. En revanche, ces sillages comportent bien une région AI qui s'étend depuis l'obstacle jusqu'à une certaine distance en aval.

Comme cela se fait couramment, on aurait pu prendre un écoulement fictif qui lui-même ne vérifie pas les équations de la mécanique des fluides, mais qui a les bonnes propriétés. Une solution plus satisfaisante a été de créer sur mesure un sillage "synthétique" : on enlève l'obstacle qui bouche la vue du théoricien et on enlève aussi la région de recirculation. Mais ce sillage est un écoulement bien réel qui vérifie les équations de Navier–Stokes. L'hypothèse de lente variation spatiale est associée à des nombres de Reynolds élevés ; et, à l'ordre dominant, ce sont alors les équations de la couche limite qui déterminent la forme de l'écoulement. Dans ce cas, l'évolution du profil de vitesse le long du courant est contrôlée par la pression appliquée de l'extérieur. Un gradient de pression adverse ralentit globalement le fluide et creuse le fond du profil de sillage. Un choix astucieux de champ de pression permet alors de créer une zone AI sans qu'il y ait recirculation. Un tel sillage présente donc tous les avantages (région AI, lente variation spatiale) et aucun des inconvénients (recirculation, parois solides) tout en obéissant aux équations de la mécanique des fluides.

Après avoir choisi comme écoulement de base un bon candidat pour donner lieu à des oscillations intrinsèques, il faut vérifier que les autres éléments constitutifs identifiés précédemment ont leur équivalent.

La relation de dispersion linéaire locale d'un tel écoulement s'obtient classiquement dans le cadre de la théorie des écoulements parallèles. La résolution du problème aux valeurs propres associé se fait sans surprises. Ainsi on trouve les valeurs concrètes des branches spatiales $k^{\ell\pm}(X,\omega)$ et de la fréquence absolue $\omega_0(X)$ pour un écoulement donné. Plus difficile à établir est l'existence des trains d'ondes non linéaires et d'une structure de front pour les sillages. Alors que pour GLC tous les calculs se font explicitement, l'analyse du sillage nécessite l'emploi systématique de simulations numériques pour établir le catalogue de tous les éléments qui entrent dans la composition d'un mode global. Une fois que tous ces ingrédients sont obtenus, il faut confronter les prédictions théoriques avec le comportement global également issu d'une simulation numérique directe. L'ensemble de ces résultats fait l'objet du dernier chapitre.

N.B. Les codes utilisés ne font appel à aucun programme préexistant (sauf les routines d'algèbre linéaire de la librairie Lapack). Je les ai développés de A à Z en C++.

Nonlinear self-sustained structures and fronts in spatially developing wake flows

By BENOÎT PIER AND PATRICK HUERRE

Laboratoire d'hydrodynamique (LadHyX), CNRS – École polytechnique,
F-91128 Palaiseau cedex, France.

A family of slowly spatially developing wakes with variable pressure gradient is numerically demonstrated to sustain a synchronized finite-amplitude vortex street tuned at a well defined frequency. This oscillating state is shown to be described by a *steep global mode* exhibiting a sharp Dee–Langer type front at the streamwise station of marginal absolute instability. The front acts as a wavemaker which sends out nonlinear travelling waves in the downstream direction, the global frequency being imposed by the real absolute frequency prevailing at the front station. The nonlinear travelling waves are determined to be governed by the local nonlinear dispersion relation resulting from a temporal evolution problem on a local wake profile considered as parallel. Although the vortex street is fully nonlinear, its frequency is dictated by a purely linear marginal absolute instability criterion applied to the local linear dispersion relation.

1. Introduction

The qualitative behaviour of spatially developing free shear flows such as wakes, jets, and mixing layers may be reasonably well understood within the framework of *linear* instability theory. In this context, one may distinguish between *amplifiers*, the dynamics of which are sensitive to inflow perturbations, and *oscillators*, which sustain intrinsic global modes tuned at a well defined frequency. Co-flow mixing layers, constant density jets, wakes below the onset of Kármán vortex shedding belong to the former class, while mixing layers with a sufficiently strong countercurrent (Strykowski & Niccum 1991), wakes in the Kármán vortex shedding régime (Provansal *et al.* 1987; Triantafyllou *et al.* 1986), inhomogenous jets (Monkewitz *et al.* 1990) belong to the latter class. The amplifier or oscillator behaviour is intimately related to the convective or absolute nature of the linear instability (Huerre & Rossi 1998). Note however that absolute instability may also induce a rapid transition to turbulence as strikingly demonstrated by Lingwood (1995, 1996) for rotating disk boundary layers.

One of the central problems regarding the dynamics of *flow oscillators* is concerned with the prediction of the overall frequency and associated spatial structure, hereafter referred to as *global mode*. For real flows, governed by the Navier–Stokes equations, this question has until now solely been studied in the framework of *linear theory* (Monkewitz, Huerre & Chomaz 1993). The objective of the present analysis is to address the same issue in the *fully nonlinear* régime.

Koch (1985) appears to be the first to have related the onset of global oscillations in wakes to the existence of an absolutely unstable region immediately downstream of the obstacle. Further progress in our understanding of frequency selection mechanisms has

Under consideration for publication in J. Fluid Mech.

typically proceeded in two distinct steps: The theoretical formulation is first established for relatively simple one-dimensional evolution models such as the celebrated complex Ginzburg–Landau (CGL) equation (Cross & Hohenberg 1993). It is then adapted and generalized to real flows governed by the Navier–Stokes equations. This line of thought has been fully implemented in the linear approximation. Linear global modes pertaining to the CGL equation with varying coefficients on an infinite interval have been analysed by Chomaz, Huerre & Redekopp (1991), and Le Dizès *et al.* (1996). The formulation essentially relies on the assumption of slow spatial variations characterized by the slow space variable $X = \epsilon x$, where $\epsilon \ll 1$ is a small non-uniformity parameter. A complex local absolute frequency $\omega_0(X)$ may then be defined in classical fashion (Briggs 1964; Bers 1983; Huerre & Monkewitz 1990) by imposing a zero group velocity condition on the local linear dispersion relation. Under these conditions, the complex global frequency ω_s of self-sustained linear structures is given by the saddle point criterion

$$\omega_s = \omega_0(X_s) \quad \text{with} \quad \frac{d\omega_0}{dX}(X_s) = 0, \tag{1.1}$$

where it is understood that $\omega_0(X)$ has been analytically continued in the complex X-plane. Whenever $\omega_{s,i} \equiv \mathrm{Im}\,\omega_s > 0$, the medium is globally unstable. Global instability then requires a finite region of local absolute instability where $\omega_{0,i}(X) > 0$ for real X, as demonstrated by Chomaz *et al.* (1991) and Le Dizès *et al.* (1996). The same criterion (1.1) was previously derived by Soward & Jones (1983) for oscillating states in Taylor–Couette flow between concentric spheres. As shown by Monkewitz *et al.* (1993) it also holds for the two-dimensional Navier–Stokes equations linearized about an arbitrary slowly streamwise developing shear flow. It should be emphasized that other frequency selection criteria have been proposed. In spatially developing flows of semi-infinite streamwise extent, say $x > 0$, the global frequency is given by the absolute frequency $\omega_0(0)$ at the upstream boundary (Monkewitz *et al.* 1993; Woodley & Peake 1997; Taylor & Peake 1999). The initial resonance principle conjectured by Monkewitz & Nguyen (1987) is of particular interest in the present context: according to these authors, in spatially developing flows with an absolutely unstable region, the first streamwise station of non-negative absolute growth rate imposes its absolute frequency to the global oscillations.

The theoretical prediction (1.1) has been tested in direct numerical simulations. Schär & Smith (1993) have numerically investigated the flow behind a vertical cylinder in the shallow-water wave régime. At a critical value of the Froude number, the wake is observed to undergo a transition to large-scale Kármán vortex shedding. When all nonlinear terms in the numerical code are turned off, the wake beats at a global frequency $\omega_g \sim 0.17 + 0.045i$. Application of criterion (1.1) leads to the prediction $\omega_g \sim 0.19 + 0.040i$, which compares very favourably with the computed value. However, when all nonlinearities are restored, the observed global frequency becomes $\omega_g \sim 0.27$, which is noticeably different from the predicted linear value. Such a comparison clearly calls for a fully nonlinear formulation of the global mode problem. A similar comparative study has recently been undertaken by Hammond & Redekopp (1997) in the case of the wake behind a blunt-edged plate. At a Reynolds number 25% above global onset, the numerically determined non-dimensional global frequency is found to be $\omega_g/2\pi \sim 0.1000$, whereas the saddle-point criterion (1.1) yields $\omega_{s,r}/2\pi \equiv \mathrm{Re}\,\omega_s/2\pi \sim 0.1006$. In view of the linear nature of the criterion, such a close agreement is somewhat surprising. It is worth noting, however, that the complex absolute frequency $\omega_0(X)$ has been computed on the mean velocity profile in the presence of finite-amplitude oscillations and not on the undisturbed basic flow, as in the case of Schär & Smith (1993). Nonlinear effects are thereby partially accounted for through the Reynolds stresses which produce the mean flow.

The next step in the theoretical analysis of spatially developing flows would naturally involve a weakly nonlinear formulation in the vicinity of global mode onset. As emphasized by Le Dizès, Huerre, Chomaz & Monkewitz (1992), this approach is fraught with difficulties. For slowly spatially developing flows the Landau constant governing the nature of the bifurcation has neither a well defined limit nor a constant sign as ϵ goes to zero. As a result, the bifurcation keeps switching between subcritical and supercritical. In order to circumvent these technical difficulties, it seems appropriate to directly proceed to a fully nonlinear approach.

Most nonlinear studies have so far been restricted to amplitude evolution equations in one space dimension. Linear absolute/convective instability concepts have been generalized to finite-amplitude disturbances by Chomaz (1992): the propagation direction of fronts separating the basic state from the bifurcated state, as originally defined by Dee & Langer (1983), van Saarloos (1988, 1989) and van Saarloos & Hohenberg (1992), is found to essentially determine the absolute/convective nature of the instability in the nonlinear régime. Fully nonlinear global modes on a semi-infinite domain ($x > 0$) governed by Ginzburg–Landau type model equations *with constant coefficients* have been thoroughly analysed by Couairon & Chomaz (1996, 1997*a*,*b*). Whenever the medium is nonlinearly absolutely unstable, an upstream travelling front is pinned at the upstream boundary point and a nonlinear global mode is sustained. The corresponding analysis of the finite interval problem has been addressed by Tobias, Proctor & Knobloch (1998) and Chomaz & Couairon (1999). Couairon & Chomaz (1999) have further investigated the existence of nonlinear global modes of the real Ginzburg–Landau equation with varying coefficients on the semi-infinite domain $x > 0$. In this case, spatial inhomogeneities due to both a boundary point and varying bulk properties are combined. Although this model constitutes only a crude approximation of real flows, predicted scaling laws for the global mode amplitude and the position of its maximum agree surprisingly well with experimental and numerical results pertaining to the wake structure behind bluff bodies.

Fully nonlinear global modes on an infinite interval, have also been investigated for the CGL equation with *varying coefficients* in order to mimic the streamwise non-uniformity of spatially developing shear flows. Two distinct varieties of nonlinear objects are then possible. *Soft global modes* obtained by Pier & Huerre (1996) satisfy a saddle-point frequency selection criterion applied to the local *nonlinear* dispersion relation governing finite-amplitude states. The corresponding extended spatial structure displays smoothly varying amplitude and wave number everywhere. By contrast, *steep global modes*, as described by Pier *et al.* (1998), obey a marginal stability criterion: the steep global frequency coincides with the real absolute frequency at the transition station between linear convective and absolute instability. More specifically, the steep global mode is triggered at the upstream boundary X^{ca} of the absolutely unstable domain and is tuned at the associated real absolute frequency

$$\omega_0^{ca} = \omega_0(X^{ca}) \quad \text{where} \quad \omega_{0,i}(X^{ca}) = 0. \tag{1.2}$$

This condition is merely the linear frequency criterion put forward by Dee & Langer (1983), according to which the front velocity is such that, in the co-moving frame, the medium is marginally absolutely unstable. The associated spatial structure consists of a stationary sharp front located at the transition station and separating an upstream decaying tail from a finite-amplitude downstream wavetrain. The front acts as a wave maker and imposes its frequency to the entire flow. In contrast with soft global modes, the wave number exhibits a sharp jump across the front. Similar nonlinear states with sharp Dee–Langer type fronts have concurrently been identified in amplitude evolution models of solar and stellar magnetic activity cycles by Bassom, Kuzanyan & Soward

(1999). The reader is referred to Soward (2000) for a review of related WKBJ asymptotic studies in the astrophysical context.

The transition scenarii governing soft and steep global modes have been analysed by Pier & Huerre (1999a) for the CGL evolution model in an infinite domain. The main results of the investigation are as follows. Soft and steep global modes are mutually exclusive so that only one variety prevails for given parameter settings. The onset of steep global modes takes place via a saddle node bifurcation as soon as a point of local linear absolute instability appears within the medium. Since linear global modes in general become unstable only for a *finite* region of local linear absolute instability, the transition to a steep mode occurs *while the medium is still globally linearly stable.* Paradoxically, the onset of local linear absolute instability is seen to provide an accurate criterion for the bifurcation to fully nonlinear steep global modes while it is only a necessary condition for linear global instability. Local linear absolute instability in a sense prevails over global linear instability and dictates the nature of the observed finite-amplitude state. By contrast, soft global modes are only obtained further above the onset of steep global modes, provided that basic advection is sufficiently small.

The objective of the present study is to demonstrate that nonlinear self-sustained structures in real shear flows may be described in terms of steep global modes triggered by a stationary front located at the streamwise station of marginal absolute instability. Strong supporting evidence for this line of thought has recently been given by Delbende & Chomaz (1998) in a direct numerical simulation of the nonlinear impulse response in a parallel wake. The nonlinear wavepacket is observed to be confined between the same leading and trailing edges as its linear counterpart. The sharp fronts delineating the saturated wavepacket then travel according to the linear Dee & Langer (1983) velocity selection criterion.

In order to strictly enforce the weak streamwise nonuniformity condition underlying all the above notions, the basic flow must be carefully chosen. Bluff body wakes present a recirculation bubble near the obstacle which violates this assumption. To bypass this difficulty, we consider a "synthetic" wake with no solid obstacle! and no reverse flow region, which still displays the essential features of wake flows, namely a region of local absolute instability. The basic *ansatz* is the same as in the numerical simulations of wakes "without obstacles" performed by Triantafyllou & Karniadakis (1990): vortex streets are produced by a wave maker within the wake flow itself and the obstacle is only necessary in real laboratory experiments to generate the basic flow!

The outline of the study is as follows. The general formulation is presented in Section 2 together with the spatially developing basic wake flow derived as a solution of the Prandtl boundary layer equations. The ensuing local properties of linear instability waves are described in Section 3 in terms of a local *linear* dispersion relation at each downstream station. Corresponding local properties of fully nonlinear travelling waves are presented in Section 4 as solutions of a local *nonlinear* dispersion relation. These linear and nonlinear waves constitute the elementary building blocks of the globally synchronized structures in the upstream and downstream regions of the wake. Attention is then given in Section 5 to the missing link, namely the front structure supported by the wake profile at the marginally absolutely unstable station. Following the procedure proposed by Pier & Huerre (1999a), the front is obtained as the limit state of the spatial response to time-harmonic forcing in a parallel wake, when the convective/absolute transition is reached. The self-sustained structures supported by the spatially developing basic flow are documented in Section 6, as computed by direct numerical simulation of the Navier–Stokes equations. Section 7 is concerned with the interpretation of these results in terms of the constitutive elements identified in the previous sections.

2. General formulation and basic flow

Two-dimensional incompressible flows are conveniently studied in terms of the streamfunction $\Psi(x,y,t)$ governed by the vorticity equation

$$\left(\frac{\partial}{\partial t}+\frac{\partial\Psi}{\partial y}\frac{\partial}{\partial x}-\frac{\partial\Psi}{\partial x}\frac{\partial}{\partial y}\right)\Delta\Psi=\frac{1}{\mathrm{Re}}\Delta^2\Psi. \tag{2.1}$$

From the start nondimensional variables based on the characteristic length and velocity scales $\ell^\star$ and $U^\star$ have been introduced. The Reynolds number is then defined as $\mathrm{Re}=\ell^\star U^\star/\nu$, where ν is the kinematic viscosity. If x and y denote the streamwise and cross-stream coordinates, the corresponding x and y velocity components are obtained as $\partial\Psi/\partial y$ and $-\partial\Psi/\partial x$, and the vorticity as $-\Delta\Psi$.

The basic flow is steady and assumed to slowly develop in the streamwise direction. This is the case at large Reynolds numbers, where viscous spreading takes place on a slow streamwise scale. The order of magnitude of the weak streamwise nonuniformity is then effectively defined as

$$\epsilon=\frac{1}{\mathrm{Re}}\ll 1, \tag{2.2}$$

which is the *only small parameter* of the present investigation. Under this quasiparallel flow approximation, the basic flow stream function Ψ_b only depends on y and the slow streamwise coordinate

$$X=\epsilon x,$$

and it is expanded as

$$\Psi_b(y;X)\sim\Psi_0(y;X)+\epsilon\Psi_1(y;X)+\epsilon^2\Psi_2(y;X)+\ldots \tag{2.3}$$

The leading-order basic flow approximation Ψ_0 is then readily shown to obey the Prandtl boundary layer equation

$$\left(\frac{\partial\Psi_0}{\partial y}\frac{\partial}{\partial X}-\frac{\partial\Psi_0}{\partial X}\frac{\partial}{\partial y}\right)\frac{\partial\Psi_0}{\partial y}=-\frac{dP}{dX}+\frac{\partial^3\Psi_0}{\partial y^3}, \tag{2.4}$$

where the given streamwise pressure gradient dP/dX is the integration "constant" arising in the integration of the leading-order vorticity equation. Corresponding basic velocity components are then $U_0(y;X)=\partial\Psi_0/\partial y$ and $\epsilon V_1(y;X)=-\epsilon\partial\Psi_0/\partial X$.

The basic flow is affected by viscous diffusion and by the externally applied pressure field $P(X)$ which allows to precisely control its streamwise evolution. The parabolic boundary layer equation (2.4) is numerically integrated from $X=0$, with the sech^2 inlet velocity profile

$$U_0(y;0)=1-\frac{\Delta U}{\cosh^2(y\sinh^{-1}1)}. \tag{2.5}$$

Such a nondimensional representation holds when the previously introduced velocity scale $U^\star$ is specified to be the streamwise basic flow inlet velocity at $y=\pm\infty$. The length scale $\ell^\star$ is chosen to be the half width of the wake so that, in nondimensional variables, $U_0(1;0)=\frac{1}{2}[U(\infty;0)+U(0;0)]$. The nondimensional parameter ΔU measures the depth of the wake at the inlet and, in the present paper, we choose $\Delta U=0.8$.

In the upstream part of the flow, an adverse pressure gradient is carefully tailored in order to generate a central region of absolute instability, while avoiding reverse flow. The characteristics of the resulting basic flow are displayed in figure 1. For the adverse pressure gradient sketched in figure 1(*c*), the centreline velocity (figure 1*b*) decreases from $1-\Delta U=0.2$ at the inlet to reach a minimum 0.01 at the streamwise station $X=0.4$.

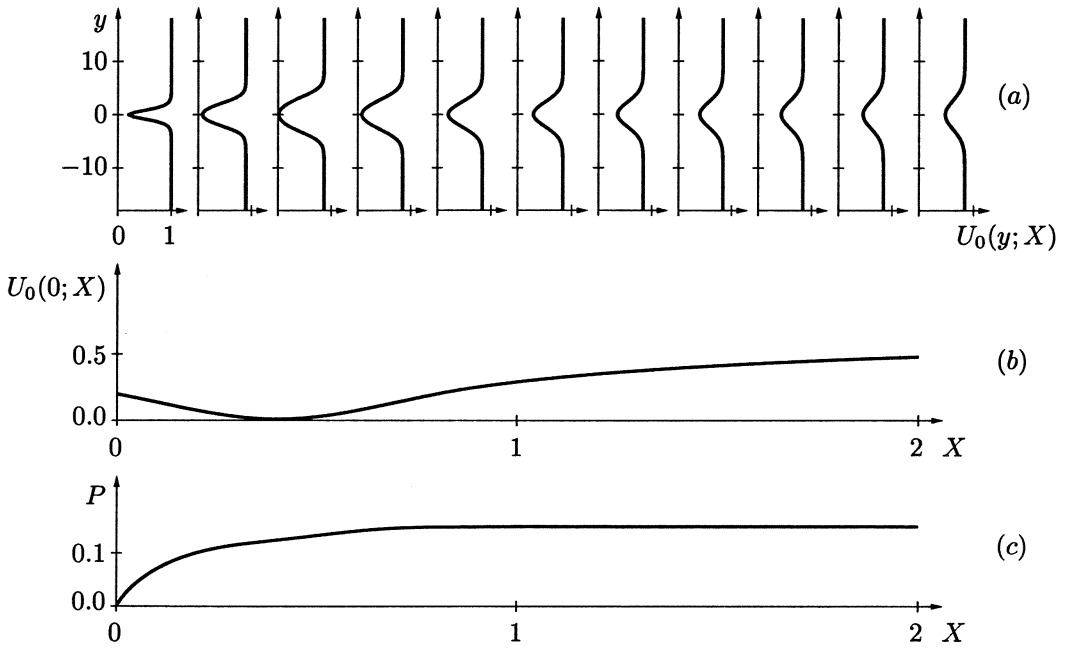


FIGURE 1. Streamwise development of the basic flow. (*a*) Velocity profiles $U_0(y;X)$ at different streamwise X locations. (*b*) Evolution of centreline velocity $U_0(0;X)$. The smallest value $U_0(0;X) = 0.01$ is reached at $X = 0.4$. (*c*) Basic pressure field $P(X)$.

The relatively strong adverse pressure gradient close to the inlet slows down the basic flow while increasing the wake depth and rounding off the dip of the profile (figure 1*a*). Further downstream a uniform pressure is reached and thus the flow evolves solely under the action of viscosity: the wake depth decreases and slow diffusive spreading takes place.

Note that the Reynolds number in the boundary layer equation (2.4) has been scaled out and incorporated in the slow streamwise variable $X = \epsilon x$. As a result, the above basic flow applies to all large Reynolds numbers: changes in Re are simply handled by a dilatation of the streamwise coordinate according to $x/X = \mathrm{Re}$, the velocity profile shapes remaining unaltered.

The total streamfunction is then decomposed into steady basic and unsteady perturbation contributions according to

$$\Psi(x,y,t) = \Psi_b(y;X) + \psi(x,y,t). \tag{2.6}$$

Substitution of (2.6) with (2.3) into the governing equation (2.1), yields

$$\begin{aligned}\Delta\psi_t + \ \Psi_{0,y}\,\Delta\psi_x \qquad\qquad - \Psi_{0,yyy}\psi_x + (\psi_y\partial_x - \psi_x\partial_y)\Delta\psi \\ + \epsilon\big[\Psi_{1,y}\,\Delta\psi_x - \Psi_{0,X}\,\Delta\psi_y - \Psi_{1,yyy}\psi_x + \Psi_{0,Xyy}\psi_y - \Delta^2\psi\big] \\ = \mathcal{O}(\epsilon^2),\end{aligned} \tag{2.7}$$

where the subscripts t, x, y and X denote differentiation with respect to these variables.

The slow streamwise variations of the basic flow call for an analysis of the perturbation field in terms of both linear and nonlinear WKBJ approximations (Bender & Orszag 1978). The properties of local linear and nonlinear wavetrain solutions sustained by the basic flow are derived in the following two sections.

3. Local linear instability waves

Following *e.g.* Crighton & Gaster (1976) and Monkewitz *et al.* (1993), in the linear approximation ψ is sought in the form of a slowly varying wave train of frequency ω

$$\psi(x,y,t) = \phi(y;X)\exp\left(\frac{i}{\epsilon}\int^X k(u)du - i\omega t\right) + \text{c.c.}, \tag{3.1}$$

where $k(X)$ denotes the local complex wave number and

$$\phi(y;X) \sim \phi_0(y;X) + \epsilon\phi_1(y;X) + \dots \tag{3.2}$$

accounts for the local cross-stream structure. Substitution of expressions (3.1,3.2) into the linearized version of (2.7) shows that the leading-order approximation ϕ_0 is governed by the local Rayleigh equation

$$\left(kU_0(y;X) - \omega\right)\left(\frac{\partial^2\phi_0}{\partial y^2} - k^2\phi_0\right) - kU_{0,yy}(y;X)\phi_0 = 0. \tag{3.3}$$

Linear eigenmodes $\Psi^\ell(y;k,X)$ solutions of (3.3) and exponentially decaying at $y = \pm\infty$ are obtained when the complex frequency ω and complex wave number k are bound by the *local linear dispersion relation*

$$\omega = \Omega^\ell(k,X), \tag{3.4}$$

at each station X. For a given wave number and a given wake velocity profile there exists a set of eigenfunctions to the Rayleigh equation. We only consider the *sinuous mode* (ϕ even) since it is the most amplified (Drazin & Reid 1981). In the sequel, the functions Ψ^ℓ and Ω^ℓ always refer to this particular eigenfunction and eigenvalue respectively. For definiteness, the linear Ψ^ℓ eigenfunctions are normalized by $\Psi^\ell(0;k,X) = 1$.

The Rayleigh equation (3.3) has been solved via a Chebyshev spectral method (Canuto *et al.* 1988). The Chebyshev collocation points $-1 \le \xi_i = -\cos[i\pi/(n_y+1)] \le +1$ for $i = 0,\dots,n_y+1$ are mapped onto $-\infty \le y_i \le +\infty$ through the transformation

$$\frac{\sqrt{2}}{l_y}y = \frac{\xi}{1-\xi^2}. \tag{3.5}$$

The parameter l_y dictates the distribution of collocation points on the y-axis: half are located in the interval $-l_y < y < l_y$ and are approximately equispaced, the remaining points extend towards $y = \pm\infty$ and their density decreases algebraically. For a given k, the differential Rayleigh equation is thus recast into a linear eigenvalue problem: the frequency ω and cross-stream distribution Ψ^ℓ are obtained as eigenvalues and eigenfunctions respectively. As many eigenfunctions as collocation points are obtained. The relevant sinuous eigenfrequency is then identified by inspection of its eigenfunction. The complete linear dispersion relation $\Omega^\ell(k,X)$ is generated by continuation in k and X. Note that, since the eigenfunctions Ψ^ℓ exponentially decay towards $y = \pm\infty$ as $e^{-|k_r y|}$, the transformation (3.5) is appropriate for this problem. In general $n_y = 50$ collocation points with $l_y = 5$ are found to be sufficient to accurately resolve the eigenfunction and precisely obtain the frequency; however for small values of k_r a larger n_y is necessary. As a validation, the mode shape is required not to vary when doubling the number of collocation points.

The dispersion relation (3.4) yields the local wave number $k^\ell(X,\omega)$ as a function of

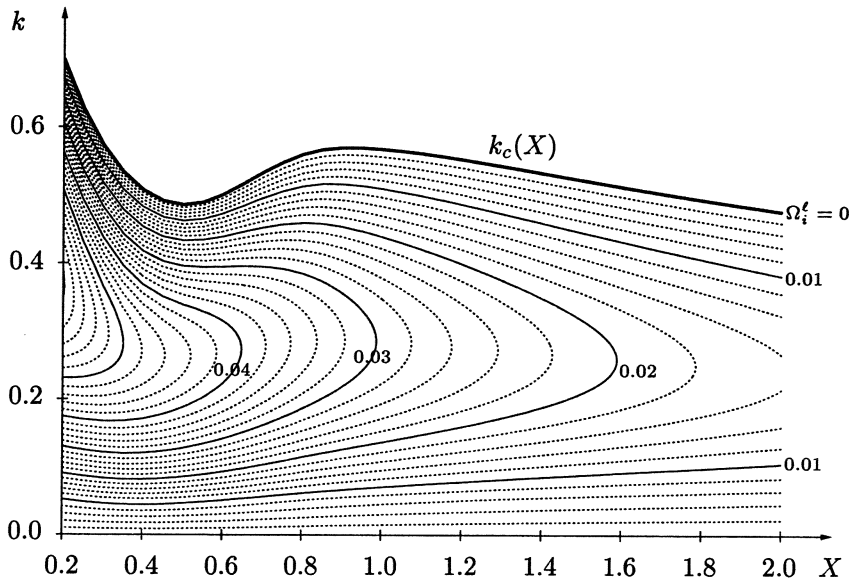


FIGURE 2. Isocontours of sinuous mode temporal growth rates Ω_i^ℓ in the (X,k)-plane in the interval $0.2 < X < 2.0$ of figure 1. Solid contours are separated by $\delta\Omega_i^\ell = 0.01$, dashed contours by $\delta\Omega_i^\ell = 0.002$. Larger growth rates occur in the upstream region whereas instability weakens further donwnstream. The unstable domain is bounded by the neutral curve $k_c(X)$ (thick line).

the global frequency. Thus at leading order in the WKBJ expansion

$$\psi(x,y,t) \sim A_0(X)\Psi^\ell\big(y;k^\ell(X,\omega),X\big)\exp\left(\frac{i}{\epsilon}\int^X k^\ell(u,\omega)du - i\omega t\right) + \text{c.c.}, \qquad (3.6)$$

where the slowly varying complex amplitude function $A_0(X)$ could be determined at next order by a secularity condition.

Local linear instability is characterized by the temporal growth of *real* wave numbers. Figure 2 illustrates the streamwise evolution of sinuous temporal growth rates $\Omega_i^\ell(k,X) \equiv \mathrm{Im}\,\Omega^\ell(k,X)$ in the (X,k)-plane for the basic flow of figure 1. All wake profiles exhibit long wavelength instability and the wake flow remains linearly unstable far downstream. However, the maximum temporal growth rate $\mathrm{Max}\{\Omega_i^\ell(k,X), k \text{ real}\}$ decreases with X. The *unstable domain* in the (X,k)-plane is defined by the condition $\Omega_i^\ell(k,X) > 0$. Its boundary yields the neutral curve $k_c(X)$ (thick line in figure 2) associated through (3.4) with a *real* frequency. Linear growth of unstable waves is limited by nonlinear saturation effects: the corresponding nonlinear wavetrains are then obtained as discussed in the next section.

The local complex absolute frequency $\omega_0(X)$ and absolute wavenumber $k_0(X)$ are defined via dispersion relation (3.4) as

$$\omega_0(X) = \Omega^\ell\big(k_0(X),X\big) \quad \text{with} \quad \frac{\partial\Omega^\ell}{\partial k}\big(k_0(X),X\big) = 0. \qquad (3.7)$$

The locus of $\omega_0(X)$ pertaining to the basic wake flow is represented in the complex ω-plane in figure 3(a) and the corresponding streamwise variation of absolute growth rate $\omega_{0,i}(X)$ is sketched in figure 3(b). According to these sketches, the properties of the flow under consideration present the following desirable features. The upstream region extending from the inlet at $X = 0$ to $X^{ca} = 0.24$ is convectively unstable (CU). The

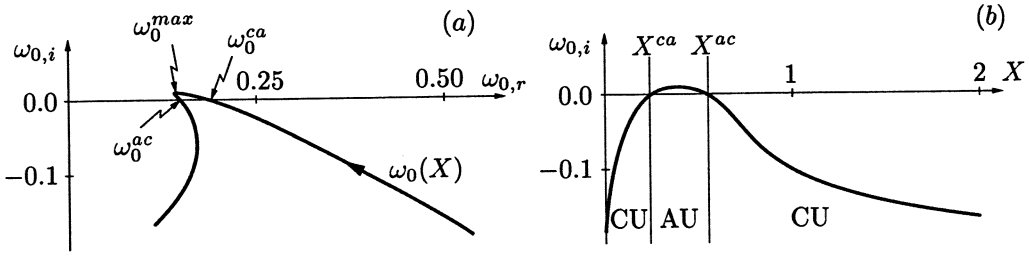


FIGURE 3. (*a*) Locus of local absolute frequency $\omega_0(X)$ in the complex frequency plane. (*b*) Local absolute growth rates $\omega_{0,i}(X)$ as a function of streamwise station.

adverse pressure gradient prevailing in this domain induces an increase of $\omega_{0,i}$ which leads to absolute instability at X^{ca}. Beyond this station of marginal absolute instability, the flow displays a central absolutely unstable (AU) region extending over the interval $X^{ca} < X < X^{ac}$, with $X^{ac} = 0.55$. In the absence of further adverse pressure gradient, the flow then returns to convective instability far downstream $X > X^{ac}$.

According to Pier *et al.* (1998), the boundaries of the AU region are of particular interest. These specific locations are defined by *real* absolute growth rates, $\omega_0^{ca} \equiv \omega_0(X^{ca}) = 0.190$ and $\omega_0^{ac} \equiv \omega_0(X^{ac}) = 0.150$ respectively. Note that $\omega_0^{ca} > \omega_0^{ac}$, a feature which has been observed for all wake flows of the present study. Although not essential to the observation of steep global modes, this inequality was taken as a working assumption in Pier & Huerre (1999a). The largest absolute growth rate occurs at $X^{max} = 0.38$ where $\omega_0^{max} \equiv \omega_0(X^{max}) = 0.144 + 0.010i$.

Following Chomaz *et al.* (1991) and Monkewitz *et al.* (1993), we may analyse the *linear* global instability of the present flow by applying the saddle point criterion (1.1). The analytic continuation of $\omega_0(X)$ in the complex X-plane yields a saddle point at $X_s = 0.43 + 0.03i$, associated with a linear global mode of frequency $\omega_s = 0.143 + 0.008i$. Since $\omega_{s,i} > 0$, the wake flow is linearly globally unstable.

4. Local fully nonlinear travelling waves

In regions where perturbations reach finite amplitude levels, the flow is governed by the complete nonlinear equation (2.7). The experiments of Provansal *et al.* (1987) as well as the numerical simulations of Hammond & Redekopp (1997) reveal that nonlinear structures in wakes are propagating in the streamwise direction: they are locally periodic and their (x,t)-dependence solely occurs via a phase function with only slow streamwise deformations. Guided by these observations and following the WKBJ formalism, we seek nonlinear slowly varying wavetrains to equation (2.7) of the form

$$\psi(x,y,t) = \phi(\theta,y;X) \quad \text{with} \quad \theta = \frac{1}{\epsilon}\int^X k(u)du - \omega t, \tag{4.1}$$

where ϕ is a 2π-periodic function of θ, and $k(X)$ is the *real* local wave number. Following the nonlinear WKBJ approximation scheme of Pier & Huerre (1996) and Pier & Huerre (1999a), the nonlinear wave train is again expanded as

$$\phi(\theta,y;X) \sim \phi_0(\theta,y;X) + \epsilon\phi_1(\theta,y;X) + \ldots \tag{4.2}$$

At leading order, one obtains

$$(kU_0(y;X)-\omega)\frac{\partial}{\partial\theta}\left(\frac{\partial^2\phi_0}{\partial y^2}+k^2\frac{\partial^2\phi_0}{\partial\theta^2}\right)-kU_{0,yy}(y;X)\frac{\partial\phi_0}{\partial\theta}$$
$$+k\left(\frac{\partial\psi_0}{\partial y}\frac{\partial}{\partial\theta}-\frac{\partial\psi_0}{\partial\theta}\frac{\partial}{\partial y}\right)\left(\frac{\partial^2\phi_0}{\partial y^2}+k^2\frac{\partial^2\phi_0}{\partial\theta^2}\right)=0. \tag{4.3}$$

As shown below, this partial differential equation in θ and y admits periodic solutions $\Psi^{n\ell}(\theta,y;k,X)$ when the real frequency ω and the real wave number k are bound by the *local nonlinear dispersion relation*

$$\omega=\Omega^{n\ell}(k,X), \tag{4.4}$$

at each station X. The dispersion relation (4.4) yields the local nonlinear wave number $k^{n\ell}(X,\omega)$ as a function of the global frequency. Thus at leading order in the nonlinear WKBJ expansion

$$\psi(x,y,t)\sim\Psi^{n\ell}\left(\frac{1}{\epsilon}\int^X k^{n\ell}(X,\omega)-\omega t+\theta_0(X),y;k^{n\ell}(X,\omega),X\right), \tag{4.5}$$

where the slowly varying phase function $\theta_0(X)$ could be determined at next order by a solvability condition.

Due to the separation of scales, the phase function θ governs the fast oscillations on a typical instability length scale, whereas X accounts for the slow development of the basic velocity profile and is not involved in spatial differentiation. Hence local properties at a given streamwise station X are recovered by freezing the X-dependence of the velocity profile and studying the corresponding strictly parallel flow. Thus the term "local" always refers to properties of strictly parallel flows obtained by extending towards $x=\pm\infty$ the velocity profile prevailing at a specific downstream station X.

The local nonlinear travelling waves $\Psi^{n\ell}(\theta,y;k,X)$ are now shown to naturally arise from a purely temporal analysis of the strictly parallel flow $U_0(y;X)$ obtained by freezing X. To this extent, the slow coordinate X is regarded as an external control parameter, frozen at a constant value although x varies on the entire real axis. The initial value problem of interest is the study of the development of a spatially periodic perturbation of given *real* wavenumber k. The initial evolution of such a small-amplitude perturbation is dictated by the linear temporal growth rate $\Omega_i^\ell(k,X)$. Whenever $\Omega_i^\ell>0$, its amplitude exponentially grows until nonlinearity sets in. Stabilizing nonlinearities lead to saturation at finite amplitude and, at large time, a fully nonlinear solution is obtained with streamwise periodicity imposed by the initial wavenumber k. In the absence of secondary instabilities, a propagating nonlinear wave solution is reached, and its frequency yields the nonlinear dispersion relation (4.4). The same thought experiment may be carried out at each streamwise station X. It should be emphasized that, without viscous dissipation, the above procedure does not single out a unique attracting wavetrain solution onto which the system converges for large time. In order to circumvent this difficulty, we have chosen to regard the pertinent finite-amplitude states as long-time saturated solutions of the full *viscous* vorticity equation

$$\left(\frac{\partial}{\partial t}+U_0(y)\frac{\partial}{\partial x}\right)\Delta\psi_0-U_{0,yy}(y)\frac{\partial\psi_0}{\partial x}+\left(\frac{\partial\psi_0}{\partial y}\frac{\partial}{\partial x}-\frac{\partial\psi_0}{\partial x}\frac{\partial}{\partial y}\right)\Delta\psi_0=\frac{1}{\mathrm{Re}}\Delta^2\psi_0, \tag{4.6}$$

for the perturbation stream function ψ_0. In the above expression, the basic flow is strictly parallel and its parametric dependence on X has been omitted. Note that the viscous term $\Delta^2\psi_0/\mathrm{Re}$ would only appear at higher order if the WKBJ asymptotic scheme were strictly applied. The use of a large but finite Re is brought in to select a unique periodic nonlinear wavetrain. The precise value of Re will later be proven unimportant.

One should also note that such a solution can only be preserved at large time if the basic wake shear is maintained steady and parallel. In the calculation, this is achieved by separating basic and perturbation fields. In effect, as in the direct numerical simulations of shear flows, *e.g.* Ehrenstein & Koch (1995), it is implicitly assumed that a body force is present to counteract viscous diffusion of the basic flow. Note that the extra terms introduced in the equations for the basic flow and perturbations are higher-order corrections: they are introduced for computational convenience, and in the limit $\epsilon = 1/\mathrm{Re} \to 0$ the original equation is recovered.

The temporal evolution of an initial spatially periodic perturbation $\psi_0(x, y, t)$ of real wave number k is treated by solving (4.6) on a streamwise periodic interval of given wavelength $2\pi/k$. The temporal linear sinuous eigenmode of real wavenumber k is chosen as initial perturbation, and, in the linear régime, it evolves according to $\Omega^\ell(k, X)$. Whenever $\Omega_i^\ell(k, X) > 0$, it is amplified, and nonlinear terms come into play to promote higher harmonics as well as a non fluctuating mean flow correction. The long-time finite-amplitude state is precisely the nonlinear travelling wave $\psi_0(x, y, t) = \Psi^{n\ell}(kx - \omega t, y)$ of frequency ω solution of the nonlinear dispersion relation (4.4) for the basic flow at the station X under consideration. In order to complete the specification of the temporal evolution problem, we assume that the flow rate is unaltered by the presence of the finite-amplitude perturbations.

An example of a nonlinear travelling wave state of wave number $k = 0.30$ is illustrated in figure 4 for the basic velocity field (thick line in figure 4*a*) at $X = 1.0$. This wave number is linearly amplified according to $\Omega^\ell = 0.183 + 0.029i$. Beyond a transient régime, a periodic state is reached, at the numerically determined nonlinear frequency $\Omega^{n\ell}(k, X) = 0.205$. In figure 4(*a*), the basic velocity profile $U_0(y)$ (thick line) is compared with the nonlinear mean flow correction $u_{(0)}(y)$ (thin line) and the total mean flow $U_0 + u_{(0)}$ (dashed line). The non-fluctuating component of the perturbation field is seen to essentially reduce the depth of the wake and to increase its width. Contour levels of the perturbation vorticity field $-\Delta\psi_0$ are displayed in figure 4(*b*). The periodic spatial structure is seen to consist of a double row of counterrotating vortices as one would expect in a Kármán vortex street. The main vortex street is surrounded by two vortex rows of smaller amplitude and opposite sign. The whole nonlinear structure propagates in the downstream direction at the celerity $\Omega^{n\ell}/k = 0.68$, slower than the far field basic velocity $U_0(\pm\infty) = 0.84$. Since the basic flow is maintained, such a periodic state persists at large time and the nonlinear frequency is well defined. Note however that the mean flow correction $u_{(0)}(y)$ (thin line in figure 4*a*) is observed to slowly diffuse in the y-direction over a slow viscous time scale.

Such nonlinear states naturally only exist in the unstable domain of the (X, k)-plane, defined by a positive linear growth rate (figure 2). Isocontours of $\Omega^{n\ell}$ in this region are represented in figure 5(*a*) and they should be compared to the corresponding isocontours of Ω_r^ℓ displayed in figure 5(*b*). At the neutral stability boundary (thick curves in figure 5), the linear temporal growth rate vanishes and the finite-amplitude wavetrains smoothly turn into the linear neutral eigenmodes. As a result, on the neutral curve

$$\Omega^{n\ell}(k, X) = \Omega_r^\ell(k, X) \quad \text{and} \quad \Omega_i^\ell(k, X) = 0.$$

Note that linear and nonlinear frequencies identically vanish for $k = 0$.

A careful comparison of figures 5(*a*, *b*) reveals that the nonlinear frequencies are always larger than the linear ones. Thus nonlinear interactions tend to increase the celerity ω/k of the wavetrains. It should be emphasized that the nonlinear iso-frequency curves in the (X, k)-plane displayed in figure 5(*a*) precisely coincide with the nonlinear spatial branches $k^{n\ell}(X, \omega)$ at the corresponding frequency, as introduced in the nonlinear wavetrain (4.5).

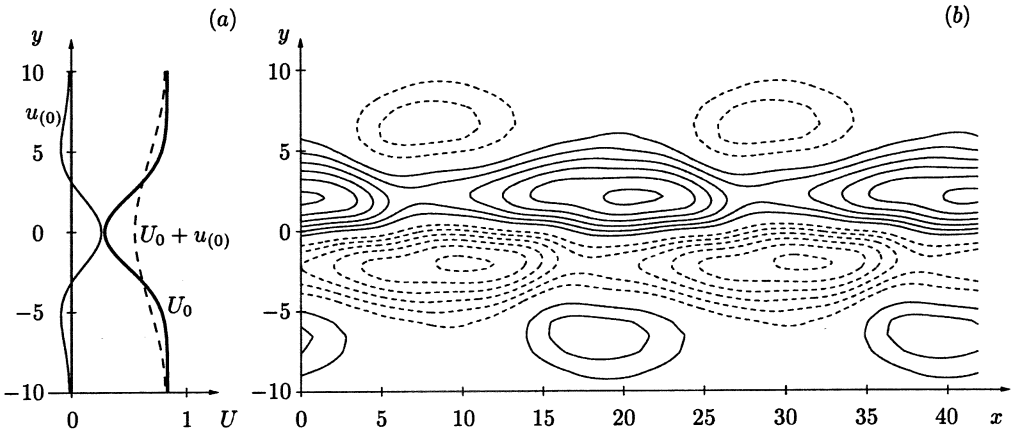


FIGURE 4. Local nonlinear travelling wave of wave number $k = 0.30$ at the downstream station $X = 1.0$ with $\mathrm{Re} = 100$ at time $t = 6000$. (*a*) Basic velocity profile $U_0(y)$ (thick line), mean-flow correction $u_{(0)}(y)$ (thin line) and total mean flow $U_0(y) + u_{(0)}(y)$ (dashed line). (*b*) Isolines of the perturbation vorticity field over two wavelengths. Positive isolines 0.025, 0.050, ..., 0.150 and negative isolines −0.025, −0.050, ..., −0.150 are represented by solid and dashed curves respectively.

The numerical technique used to solve (4.6) is based on the spectral method of Ehrenstein & Koch (1989) suitably adapted to wake flows. The streamfunction is decomposed into harmonic components as

$$\psi_0(x,y,t) = \sum_{-\infty<n<\infty} \phi_{(n)}(y,t)e^{inkx}, \tag{4.7}$$

with $\phi_{(-n)}(y,t) = \phi^\star_{(n)}(y,t)$, where $\star$ denotes the complex conjugate. Substitution of (4.7) into the governing equation (4.6) and identification of corresponding exponentials leads to the modal equations

$$\left[\partial_t D_n + ink\left[U_0(y)D_n - U_{0,yy}(y)\right] - \frac{1}{\mathrm{Re}}D_n^2\right]\phi_{(n)} + ik\sum_{-\infty<m<\infty} N_{n-m,m} = 0, \tag{4.8}$$

where $D_n = \partial_{yy} - (nk)^2$ and

$$N_{n,m} = m\left(\partial_y\phi_{(n)}\right)\left(D_m\phi_{(m)}\right) - n\phi_{(n)}\left(D_m\partial_y\phi_{(m)}\right). \tag{4.9}$$

Assuming that the nonlinear perturbation does not change the pressure gradient at $y = \pm\infty$ and leaves the flow rate unaltered, equation (4.8) may be integrated twice for $n = 0$ to obtain the mean flow distortion equation

$$\frac{\partial\phi_{(0)}}{\partial t} - \frac{1}{\mathrm{Re}}\frac{\partial^2\phi_{(0)}}{\partial y^2} = 2k\mathrm{Im}\sum_{m>0} m\phi^\star_{(m)}\frac{\partial\phi_{(m)}}{\partial y}. \tag{4.10}$$

The unknown functions $\phi_{(n)}(y,t)$ all vanish at $y = \pm\infty$, and the mean flow correction reads $u_{(0)} = \partial\phi_{(0)}/\partial y$.

The set of modal equations (4.8,4.10) is truncated at a finite number of harmonics $|n| \leq n_h$ and again a Chebyshev collocation method with n_y collocation points is implemented in the y-direction together with the mapping (3.5). Thus the governing equation (4.6) has been recast in a system of $n_y(2n_h + 1)$ real algebraic ordinary differential equations of the first order in time. These are solved via a fourth order Runge–Kutta scheme of time step δt. In the particular example of figure 4 at $\mathrm{Re} = 100$ and $t = 6000$, $n_h = 5$,

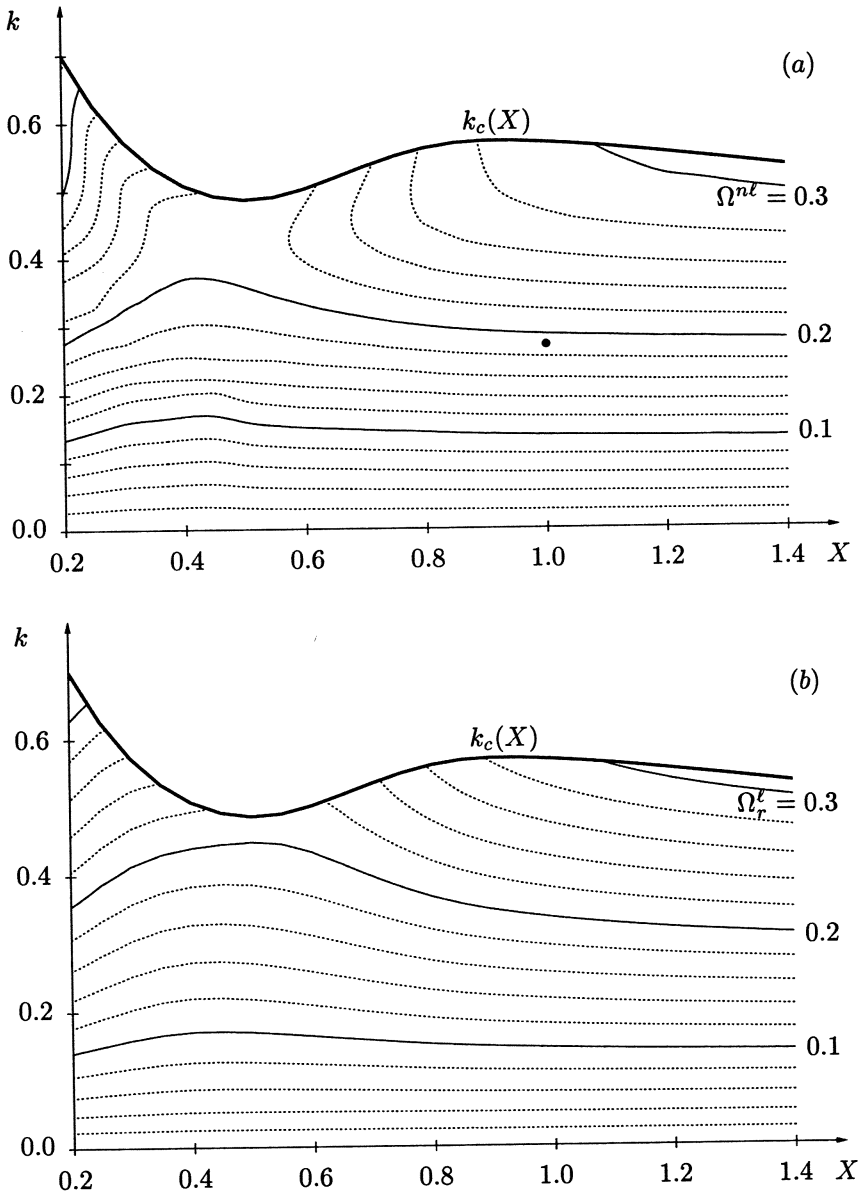


FIGURE 5. Isofrequency contours in the linearly unstable domain of the (X, k)-plane. Solid contours are separated by $\delta\Omega = 0.1$, dashed contours by $\delta\Omega = 0.02$. (*a*) Isocontours of $\Omega^{n\ell}$. (*b*) Isocontours of Ω_r^ℓ.

$n_y = 71$, $l_y = 5$ and $\delta t = 0.05$. It has been checked that higher resolutions leave the results unchanged.

The temporal evolution of the wave number spectrum is illustrated in figure 6. The kinetic energy $E_n(t)$ of each harmonic is sketched as a function of time on both logarithmic and linear scales. If $u_{(n)} = \partial_y \psi_{(n)} e^{inkx} + \text{c.c.}$ and $v_{(n)} = -ink\psi_{(n)} e^{inkx} + \text{c.c.}$ denote

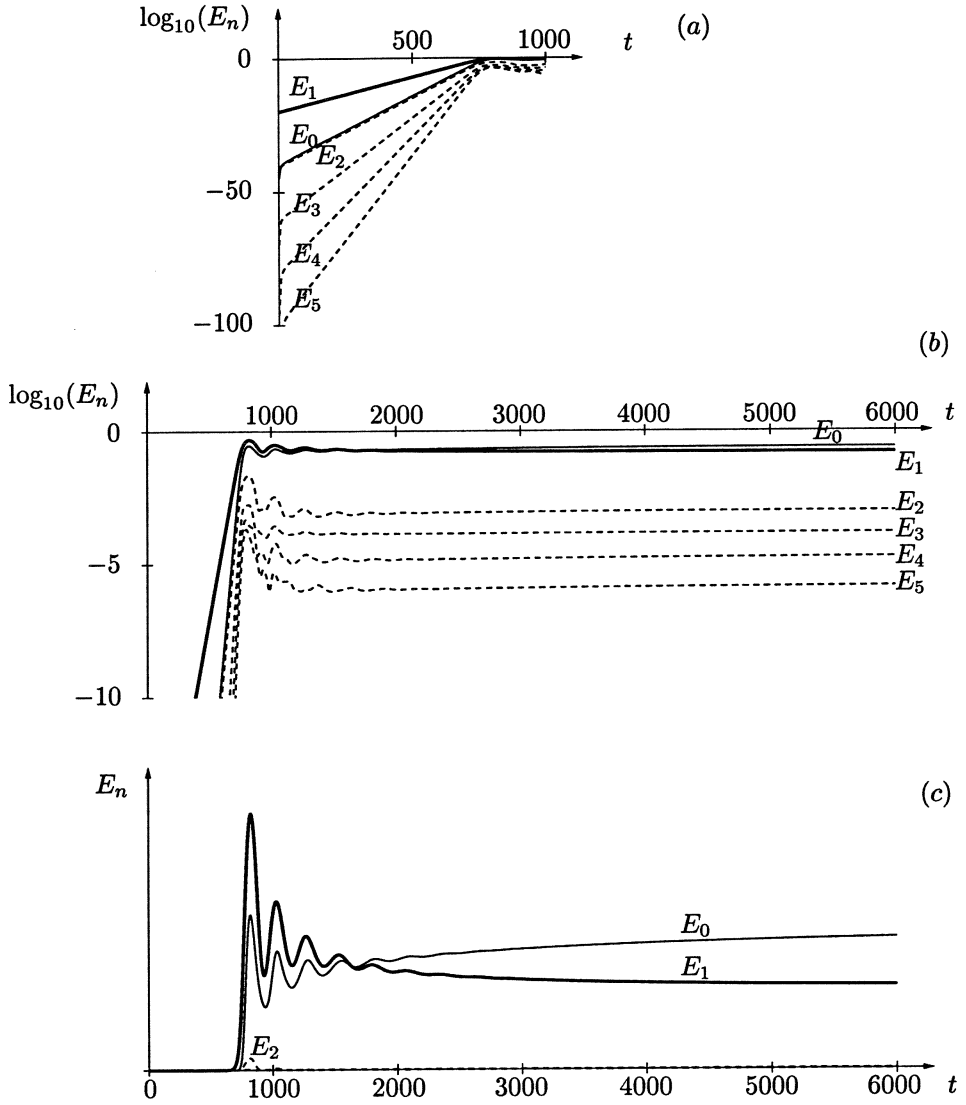


FIGURE 6. Temporal evolution of the energy contained in each harmonic component (nonlinear travelling wave of figure 4) for $0 < t < 6000$. (*a*) Semi-log plot of the initial linear growth phase ($t < 800$). The fundamental E_1 (thick solid line) grows acccording to $\exp 2\Omega_i^{\ell} t$, higher harmonics E_n ($n > 1$, dashed lines) are slaved as the n-th power of E_1, the mean flow correction E_0 as E_1^2. (*b*,*c*) Semi-log and linear plots of the long time evolution display a nonlinear transient régime ($800 < t < 2000$) with damped oscillations towards a quasi-stationary state. Note that the harmonics ($n > 2$) reach much lower saturation levels.

the velocity field associated with the n-th harmonic ($n > 0$), its energy is defined as

$$E_n(t) = \int_{-\infty}^{+\infty} \int_0^{2\pi/k} \frac{1}{2} \left(u_n^2 + v_n^2\right) dx\, dy.$$

During the linear growth phase ($t < 800$, figure 6*a*), all harmonics are exponentially amplified. The measured slope of the fundamental E_1 (thick line) in the semi-log plot is 0.0255, and precisely coincides with its theoretical value given by $2\Omega_i^{\ell}/\ln 10$. Higher

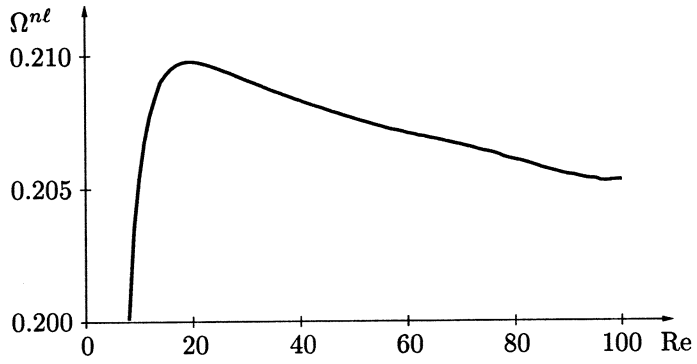


FIGURE 7. Variation of the nonlinear frequency Ω^{nl} associated with $k = 0.30$ and $X = 1.0$ as a function of the Reynolds number Re. Note the magnified vertical scale.

harmonics $E_n(t)$ ($n > 1$, dashed lines) are naturally slaved to the fundamental and grow as $[E_1(t)]^n$ whereas the mean flow correction $E_0(t)$ (thin solid line) scales as $[E_1(t)]^2$.

Beyond the nonlinear transient régime ($800 < t < 2000$), the system relaxes towards a quasi-stationary travelling wave state. The duration of the transients depends on the dissipation time scale as dictated by the magnitude of the selected Reynolds number. The choice Re = 100 appears to be a good compromise between reasonably long transients and inviscid-like dynamics. Although the motion is fully nonlinear, only a few harmonic components partake in the dynamics. Even for the most unstable wave number, only three harmonics are necessary to accurately capture the saturated wave state.

The final nonlinear propagating wave and its frequency hardly depend on the particular value of the Reynolds number as illustrated in figure 7. For $\mathrm{Re} > 50$, the frequency changes by less than 0.005. It is only for $\mathrm{Re} < 10$ that drastic changes in the frequency occur! This insensitivity to Reynolds number fully justifies the approach adopted in the present study. The addition of the viscous term in (4.6) does not significantly affect the properties of the nonlinear wavetrain. In the present calculation, the value Re = 100 has been deemed sufficient.

5. Nonlinear spatial response and fronts in parallel wakes

At each downstream location we have now at our disposal a complete family of linear as well as nonlinear local wavetrains which constitute the elementary building blocks of a globally synchronized flow. Whereas the upstream region extending to the inlet is expected to sustain small perturbation levels, correctly handled within a linear approximation, the downstream wake should be made up of fully nonlinear travelling wavetrains. In the framework of one-dimensional evolution models, it has been demonstrated Pier & Huerre (1999a) that, for steep global modes, a stationary front constitutes the missing link converting the upstream linear waves into the downstream nonlinear waves at a station of marginal local absolute instability. In the present section it is shown that an analogous front structure exists in wake flows. According to Dee & Langer (1983) and van Saarloos (1987, 1988), a propagating front moves towards its decaying edge if the basic state is AU, towards its finite-amplitude edge if the basic state is CU, and a stationary front is obtained when the medium is exactly at the CU/AU transition.

Here a slightly different point of view is adopted: instead of studying front propagation, we focus on the spatial response of a CU profile to a localized time harmonic forcing and argue that the stationary front is recovered at the CU/AU transition. This approach is motivated by the difficulty to directly compute the propagation of a front connecting a

fully nonlinear wavetrain to an unperturbed wake profile: in the co-moving frame the flow is marginally AU and thus very sensitive to various uncontrolled perturbations. In contrast, the signalling problem in a CU flow is not affected since the response to noise is swept away, and the stationary régime is easily identified.

Consider again a strictly parallel wake profile at a given streamwise station X. The forced perturbation vorticity and streamfunction fields ϖ and ψ are then governed by

$$\left(\frac{\partial}{\partial t}+U_0(y)\frac{\partial}{\partial x}\right)\varpi+U_{0,yy}(y)\frac{\partial\psi}{\partial x}+\left(\frac{\partial\psi}{\partial y}\frac{\partial}{\partial x}-\frac{\partial\psi}{\partial x}\frac{\partial}{\partial y}\right)\varpi=\frac{\Delta\varpi}{\mathrm{Re}}+S(x,y,t), \quad (5.1a)$$

$$\Delta\psi=-\varpi, \quad (5.1b)$$

where the temporally harmonic forcing function is taken to be of the form

$$S(x,y,t)=H(t)A_f\,e^{-\frac{x^2+(y-y_f)^2}{\ell_f^2}}\cos\omega_f t, \quad (5.2)$$

with $H(t)$ denoting the Heaviside unit step function, ω_f and A_f the forcing frequency and amplitude. The forcing is applied in a region of size ℓ_f centred at $(0,y_f)$. Switching on the forcing at $t=0$, produces a transient wavepacket together with the steady-state response at the forcing frequency. Whenever the basic flow is CU, transients move away from the source and a steady-state signal is left at the forcing frequency. When the medium is AU, switch-on transients overwhelm the response at the forcing frequency and the signalling problem is ill-posed. Hence only the spatial problem for CU velocity profiles is considered in the following discussion.

The linear signalling problem in shear flows has been investigated by Huerre & Monkewitz (1985). Here, the linear dispersion relation (3.4) gives rise to two linear spatial branches $k^{\ell+}(X,\omega)$ and $k^{\ell-}(X,\omega)$. The response streamfunction then reads

$$\psi(x,y,t)\propto A_f\frac{\Psi^\ell\left(y;k^{\ell\pm}(X,\omega_f),X\right)}{\Omega_k^\ell\left(k^{\ell\pm}(X,\omega_f),X\right)}\exp i\left[k^{\ell\pm}(X,\omega_f)x-\omega_f t\right]+\text{c.c.}, \quad (5.3)$$

where labels $(+)$ and $(-)$ pertain to the downstream ($x>0$) and upstream ($x<0$) response respectively. Note again that for convenience the viscous dissipation term $\Delta\varpi/\mathrm{Re}$ has been added to (5.1a). Thus the linear dispersion relation Ω^ℓ and corresponding eigenfunctions Ψ^ℓ are derived from the Orr–Sommerfeld equation rather than the Rayleigh equation (3.3), the streamwise decay or growth rates being dictated by $k_i^{\ell\pm}\equiv\mathrm{Im}\,k^{\ell\pm}$. An extensive survey of all the CU velocity profiles encountered in the present study reveals that the linear $k^{\ell-}(X,\omega)$ branches always remain in the $k_i<0$ half plane and thus never give rise to upstream amplification. Only downstream spatial branches $k^{\ell+}$ grow in a certain frequency range.

Whenever a linear spatial branch is amplified, nonlinear terms have to be taken into account at some distance from the source, however small the forcing amplitude. As the response reaches finite amplitude, nonlinear saturation prevents further amplification and leads to a nonlinear travelling wave at the excitation frequency for some *real* wave number $k^{n\ell}$. Since this nonlinear propagating wave train is reached downstream of the source, it is denoted as $k^{n\ell+}(X,\omega)$. The forcing frequency ω_f and the nonlinear response wave number $k^{n\ell+}$ satisfy the nonlinear dispersion relation (4.4). For a more complete discussion of the relationship between linear and nonlinear spatial branches, see Pier & Huerre (1999a).

Figure 8 illustrates the spatial response of the parallel CU wake velocity profile (a) prevailing at $X=1$, at a Reynolds number $\mathrm{Re}=100$. Forcing is applied at the origin $y_f=0$ with a frequency $\omega_f=0.19$, amplitude $A_f=10^{-3}$ and $\ell_f=1$. Total isovor-

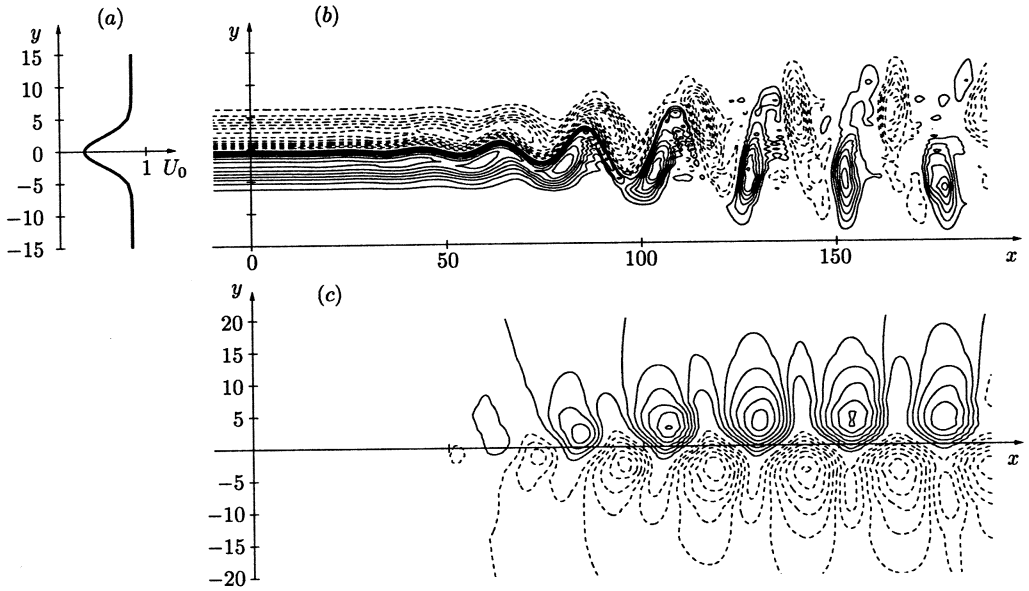


FIGURE 8. Spatial response of a CU parallel wake to harmonic forcing of frequency $\omega_f = 0.19$, amplitude $A_f = 10^{-3}$ and width $\ell_f = 1$ applied at the origin and given by (5.2). Re = 100. (*a*) Basic velocity profile at $X = 1$. (*b*) Total vorticity levels at $t = 500$. Positive contours 0.02, 0.04, ..., 0.14 and negative contours −0.02, −0.04, ..., −0.14 are represented by solid and dashed lines respectively. (*c*) Corresponding perturbation streamlines. Solid (dashed) isocontours pertain to the levels 0.2, 0.4, ..., 1.4 (−0.2, −0.4, ..., −1.4). Close to the forcing location the downstream response grows exponentially to reach a finite amplitude around $x = 70$. Further downstream, a nonlinear travelling wave is generated. The entire streamwise extent $-10 < x < 190$ of the computational domain is shown.

ticity contours and perturbation streamlines are displayed in (*b*) and (*c*) respectively. Close to the forcing location, the downstream response grows exponentially to reach a finite amplitude around $x \sim 70$. The measured nonlinear saturation wave number is $k^{n\ell+}(X, \omega_f) = 0.27$. The solid dot at $(k, X) = (0.27, 1)$ in figure 5(*a*) lies close to the contour level $\Omega^{n\ell} = \omega_f = 0.19$, which confirms that $k^{n\ell+} = 0.27$ is indeed a solution of the nonlinear dispersion relation (4.4).

The signalling problem (5.1) is numerically integrated via a finite difference scheme with n_x mesh points of size δx in the x-direction and n_y Chebyshev collocation points in the y-direction. According to the Poisson equation (5.1*b*), the perturbation streamfunction ψ is generated by the vorticiy field ϖ which is confined within the shear region. Thus, in general, ψ decays algebraically far away from the vortical region. As a result, the algebraic transformation (3.5) is still well adapted to this problem. The perturbation vorticity and streamfunction are both assumed to vanish at the upstream boundary and at infinity in the cross-stream direction. The nonreflecting boundary conditions introduced by Jin & Braza (1993)

$$\frac{\partial \varpi}{\partial t} = -\left(U_0 + \frac{\partial \psi}{\partial y}\right)\varpi + \frac{1}{\mathrm{Re}}\frac{\partial^2 \varpi}{\partial y^2}, \tag{5.4a}$$

$$\frac{\partial \psi_x}{\partial t} = -\left(U_0 + \frac{\partial \psi}{\partial y}\right)\psi_x + \frac{1}{\mathrm{Re}}\frac{\partial^2 \psi_x}{\partial y^2}, \tag{5.4b}$$

are implemented at the outlet. The Poisson equation (5.1*b*) is solved by a generalized

Thomas algorithm with given boundary values of ψ at the inlet and ψ_x at the outlet. Integration in time is performed with a second-order Runge–Kutta scheme of time step δt.

The parameters chosen in the computation of figure 8 are $n_x = 400$, $\delta x = 0.5$, $n_y = 31$, $l_y = 5$, $\delta t = 0.05$. The entire streamwise extent of the computational domain $-10 < x < 190$ is displayed to demonstrate that the outflow boundary is truly non-reflecting.

In order to analyse the spatio-temporal structure of the nonlinear response, harmonic components have been computed over one period in the stationary régime according to the Fourier expansion

$$\psi(x,y,t) = \sum_{-\infty<n<+\infty} \phi_{(n)}(x,y)e^{-in\omega_f t}. \tag{5.5}$$

Figure 9(a) displays a snapshot of the fundamental streamwise velocity $u_{(1)}(x,y) = \partial_y\phi_{(1)}(x,y) + \text{c.c.}$ It is seen that at the onset of nonlinearity, the fluctuation amplitude is higher than in the periodic nonlinear wavetrain reached further downstream. The associated envelope $|v_{(1)}|(x,y) = 2|\partial_x\phi_{(1)}(x,y)|$ plotted in figure 9(b) effectively represents the amplitude of the fundamental cross-stream velocity fluctuations. The non-fluctuating component of the streamfunction at $n = 0$ is associated with the nonlinear mean flow correction induced by Reynolds stresses. Figure 9(c) shows the isocontours of the mean streamwise perturbation velocity $u_{(0)}(x,y) = \partial_y\phi_{(0)}(x,y)$. In the finite-amplitude region, the mean flow distortion is seen to fill up the dip of the wake, thereby effectively reducing the shear experienced by the nonlinear travelling waves.

The Fourier expansion (5.5) allows to monitor the streamwise evolution of the kinetic energy $E_n(x)$ contained in each harmonic component, defined as

$$E_n(x) = \int_{-\infty}^{+\infty} \left(\left|\partial_y\phi_{(n)}\right|^2 + \left|\partial_x\phi_{(n)}\right|^2\right) dy \qquad (n > 0), \tag{5.6a}$$

$$E_0(x) = \int_{-\infty}^{+\infty} \frac{1}{2}\left(\left(\partial_y\phi_{(0)}\right)^2 + \left(\partial_x\phi_{(0)}\right)^2\right) dy. \tag{5.6b}$$

Semi-log plots of the streamwise evolution of $E_n(x)$ are given in figure 10. In the linear region, the fundamental component (thick line) grows exponentially according to $\exp(-k_i^{\ell+}x)$ until a finite amplitude level is reached. The mean slope over the interval $20 < x < 60$ is 0.054, close to its theoretical linear value $-2k_i^{\ell+}/\ln 10 = 0.055$ as predicted by the spatial branch $k^{\ell+} = 0.316 - 0.064i$ computed from the Orr–Sommerfeld equation. Although the numerical results are not as clean as in the temporal evolution problem of figure 6, higher harmonics are nonetheless slaved to the fundamental according to $E_n(x) \sim [E_1(x)]^n$. Note however that the variations of the mean-flow correction energy $E_0(x)$ are algebraic rather than exponential. Presumably, the vortical structures produced in the nonlinear domain generate a *global* mean pressure field which does not simply scale as $[E_1(x)]^2$ with the local linear spatial instability properties. This feature is absent in the temporal evolution case where the waves are strictly streamwise periodic.

With the exception of the mean flow correction, there is no feedback of the fully nonlinear downstream wavetrain on the upstream linear region. A proof of this assertion is obtained by measuring the nonlinear saturation location as a function of the forcing amplitude. The saturation station $x_{n\ell}$ may be precisely defined from the envelope of the fundamental cross-stream velocity component (see figure 9b) along the centreline $y = 0$ as the location where $|v_{(1)}|(x,0)$ reaches a preset value. The resulting variation of $x_{n\ell}$ with $-\log A_f$ displayed in figure 11 is clearly linear with a measured slope of 35.5, which favourably compares with the theoretical value $-\ln 10/k_i^{\ell+} = 36.0$ predicted by linear

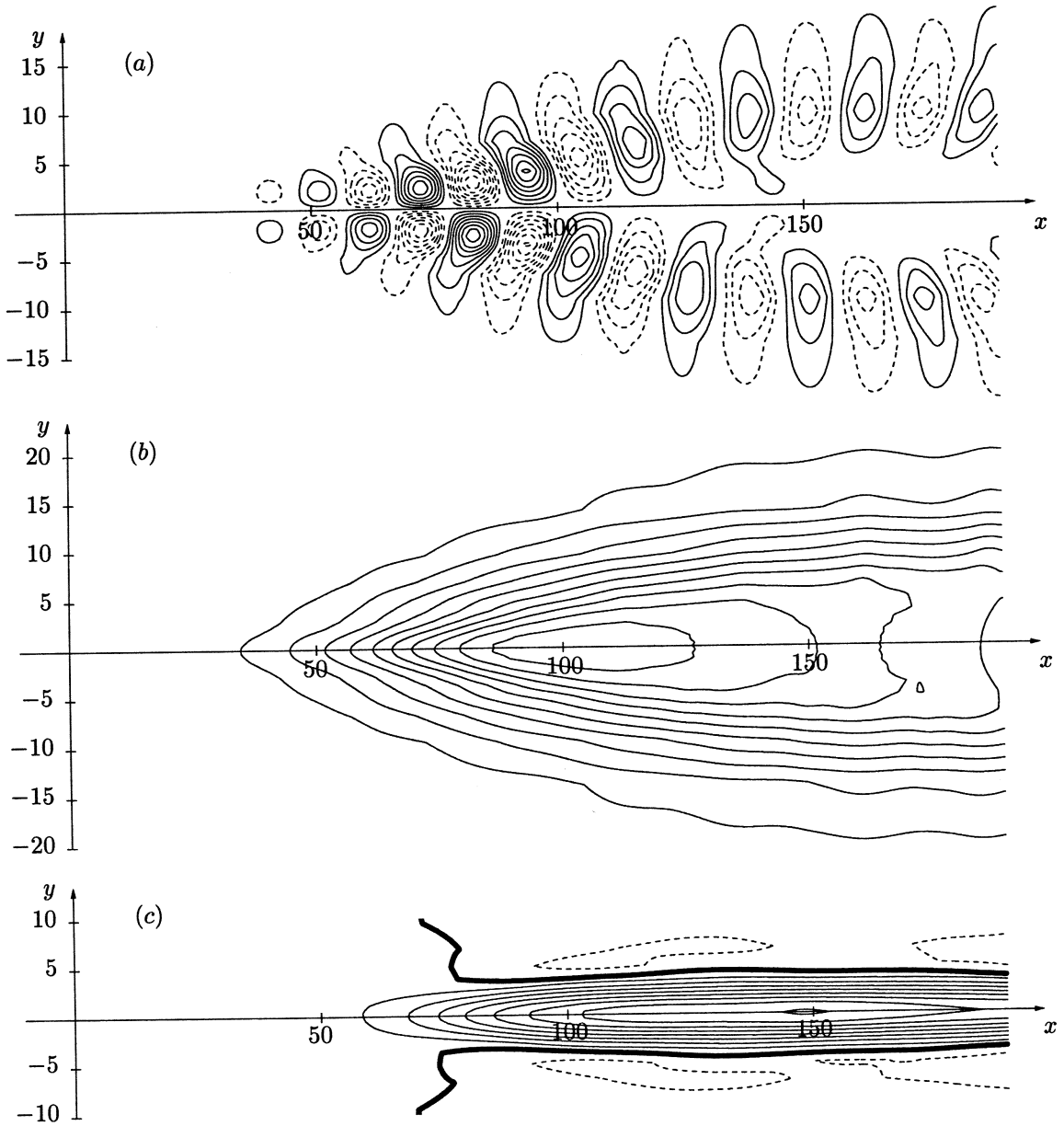


FIGURE 9. Same parallel wake spatial response as in figure 8. (*a*) Snapshot of fundamental streamwise velocity $u_{(1)}(x, y)$. Solid (dashed) lines pertain to 0.02, 0.04, ..., 0.14 (−0.02, −0.04, ..., −0.14) contour levels. (*b*) Contour levels of envelope of cross-stream velocity $|v_{(1)}|(x, y)$ (0.02, 0.04, ..., 0.20). (*c*) Isolevels of nonlinear mean streamwise velocity correction $u_{(0)}(x, y)$. Thick line separates regions of positive (0.05, 0.10, ..., 0.40 solid lines) and negative (−0.05 dashed line) levels.

theory. The nonlinear saturation station is thus solely controlled by the linear growth phase: it depends only on the forcing amplitude A_f and linear spatial growth rate $-k_i^{\ell+}$.

The signalling problem (5.1) may be solved for any forcing frequency ω_f and any station X associated with a given CU wake velocity profile. As the AU threshold at X^{ca} is approached, the receptivity of the flow to forcing at the corresponding real absolute

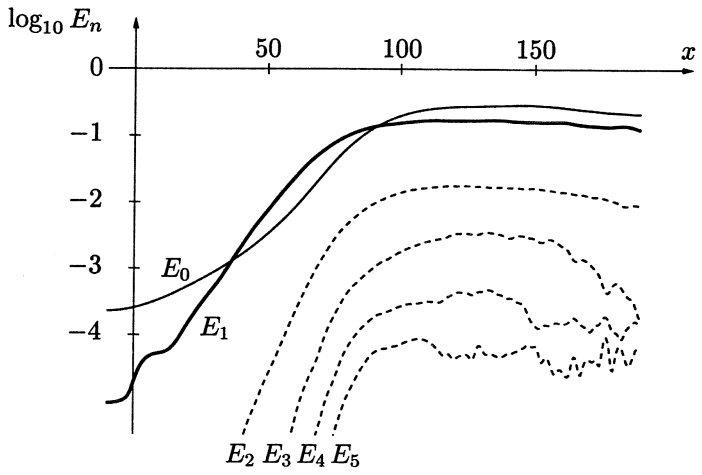


FIGURE 10. Same parallel wake spatial response as in figure 8. Semi-log plots of the streamwise evolution of the energy $E_n(x)$ pertaining to each harmonic component.

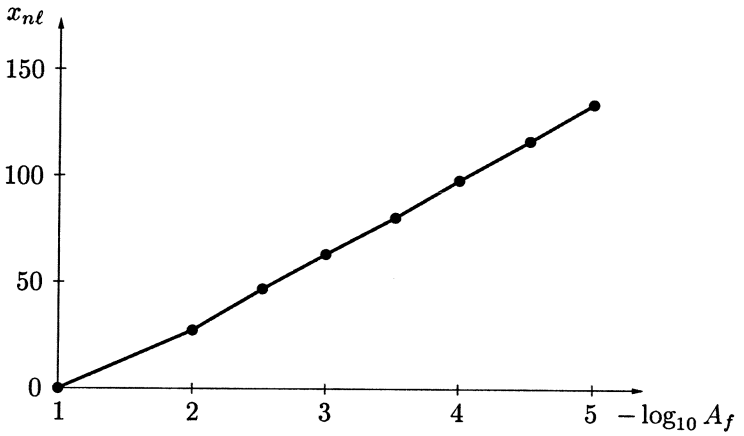


FIGURE 11. Evolution of nonlinear saturation station $x_{n\ell}$ with forcing amplitude A_f in parallel wake. All other parameter settings same as in figure 8.

frequency ω_0^{ca} increases (Pier & Huerre 1999a). At the marginal AU station X^{ca}, upstream and downstream spatial branches pinch, *i.e.*, $k^{\ell+}(X^{ca},\omega_0^{ca}) = k^{\ell-}(X^{ca},\omega_0^{ca}) = k_0(X^{ca}) \equiv k_0^{ca}$ and by definition $\Omega_k^{\ell}(k_0^{ca},X^{ca}) = 0$. Thus, according to (5.3), the spatial response diverges. In other words, the forcing amplitude required to maintain a fixed location of nonlinear saturation $x_{n\ell}$ vanishes as $(X,\omega_f) \to (X^{ca},\omega_0^{ca})$. In this limit, a front structure is obtained connecting a downstream fully nonlinear wavetrain to an upstream decaying tail *without any forcing*. This is precisely the stationary Dee–Langer front living in the marginally AU medium.

A numerical implementation of this strategy is illustrated in figure 12(*a*,*b*). The forcing frequency is kept constant at $\omega_f = 0.19 \simeq \omega_0^{ca}$ and the signalling problem is solved at $X = 0.20$ and $X = 0.22$, all other parameters being kept at the same settings. The resulting perturbation field is seen to only weakly depend on X as the limit $X^{ca} = 0.24$ is approached. The spatial response distribution arising from a forced problem on the CU side of X^{ca} in effect provides a good approximation of the self-sustained front structure prevailing at X^{ca} in the absence of forcing. The fact that resonance takes place at X^{ca} is

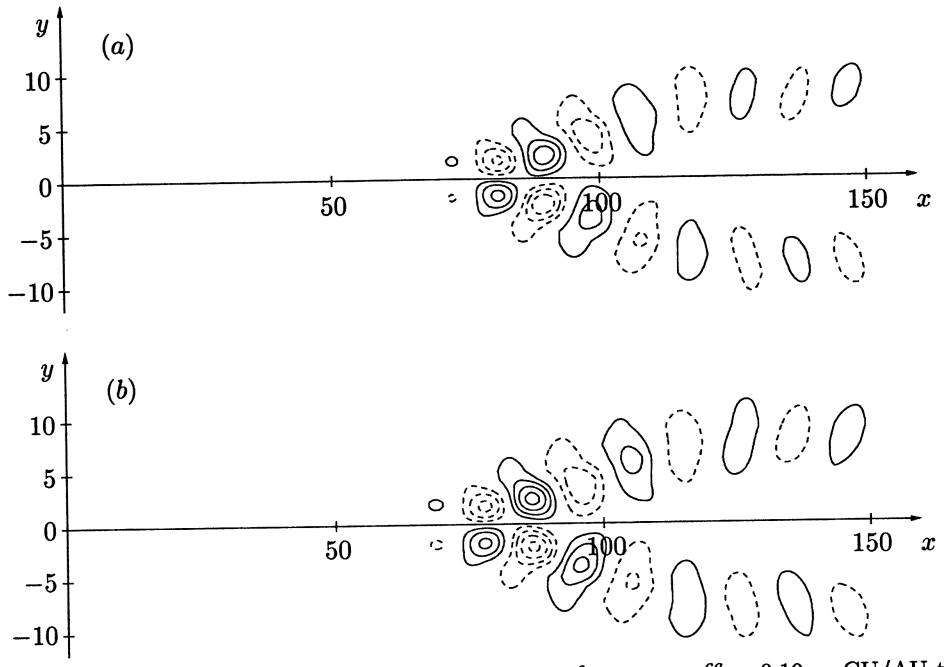


FIGURE 12. Parallel wake spatial response to forcing at frequency $\omega_0^{ca} = 0.19$ as CU/AU transition station $X^{ca} = 0.24$ is approached: Isocontours of fundamental streamwise velocity at (*a*) $X = 0.20$ (*b*) $X = 0.22$ (0.05, 0.10, 0.15, 0.20 solid lines, −0.05, −0.10, −0.15, −0.20 dashed lines).

not associated with any drastic change in the perturbation field. It only manifests itself by pinching of $k^{\ell+}$ and $k^{\ell-}$ branches in the complex k-plane.

It is naturally impractical to perform a numerical simulation at the very CU/AU transition since in this limit the forcing problem becomes ill-defined. However, one may attempt to verify that the spatial response would reach such a self-sustained front-like structure by tracking the nonlinear saturation station $x_{n\ell}$ as $(X, \omega_f) \to (X^{ca}, \omega_0^{ca})$. Accordingly, the station $x_{n\ell}$ is measured for different wake velocity profiles pertaining to $X < X^{ca} = 0.24$, for $\omega_f = \omega_0^{ca} = 0.19$ while keeping the forcing amplitude A_f at a fixed constant value. Results are displayed in figure 13 together with the theoretically predicted curve

$$x_{n\ell} = \frac{\ln\left|\Omega_k^\ell\left(k^{\ell+}(X,\omega_0^{ca}),X\right)\right|}{-k_i^{\ell+}(X,\omega_0^{ca})} + \text{const.}, \tag{5.7}$$

arising from the forced response (5.3). It is straightforward to demonstrate via a Taylor expansion of $\Omega_k^\ell\left(k^{\ell+}(X,\omega_0^{ca}),X\right)$ in the neighbourhood of X^{ca} that $|\Omega_k^\ell| \propto |X - X^{ca}|^{1/2}$. Thus, according to (5.7), the nonlinear saturation station $x_{n\ell}$ scales as

$$x_{n\ell} \sim -\frac{1}{2}\ln|X - X^{ca}| + \text{const.} \quad \text{when} \quad X \uparrow X^{ca}.$$

The constant appearing in the theoretical prediction (5.7) depends on the forcing amplitude A_f and would in principle be determined by calculating the multiplicative constant in (5.3). We are solely concerned here with the functional form of $x_{n\ell}$ versus X and the constant has been adjusted to achieve reasonable fit with the numerical data points. Due to the slow logarithmic divergence and the insufficient accuracy of the measured $x_{n\ell}$ values, the theoretical curve only poorly fits the numerical data. This somewhat mixed

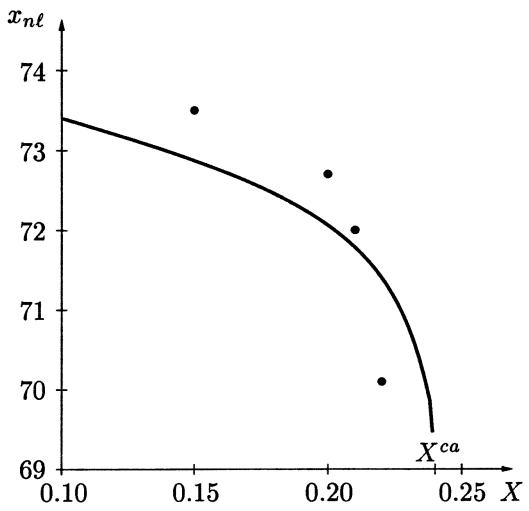


FIGURE 13. Evolution of spatial response nonlinear saturation station $x_{n\ell}$ as the marginal AU wake profile at X^{ca} is approached. Comparison of numerical measurements (dots) and theoretical prediction derived from the linear dispersion relation (solid line).

result is not too surprising: the perturbation field is exponentially growing along the stream, and in order to check the validity of the scaling law (5.7), one must extract from the numerics the prefactor multiplying the exponential term. This process is numerically risky since a small error in the evaluation of the growth rate drastically contaminates the evaluation of the prefactor. It is well known that asymptotic limits are often hard to reach numerically!

6. Self-sustained global structures in spatially developing wake

This part of the study is devoted to the detailed presentation of globally synchronized self-sustained structures, as obtained by direct numerical simulation of the spatially developing wake-flow defined in §2. Their interpretation in terms of the previously identified elements is postponed to the next section.

Numerical simulations are performed in the vorticity/streamfunction formulation

$$\left(\frac{\partial}{\partial t}+U_0(x,y)\frac{\partial}{\partial x}\right)\varpi+U_{0,yy}(x,y)\frac{\partial\psi}{\partial x}+\left(\frac{\partial\psi}{\partial y}\frac{\partial}{\partial x}-\frac{\partial\psi}{\partial x}\frac{\partial}{\partial y}\right)\varpi=\frac{1}{\mathrm{Re}}\Delta\varpi, \qquad (6.1a)$$

$$\Delta\psi=-\varpi, \qquad (6.1b)$$

governing the dynamics of the perturbation fields. Note that the spatial variation of the basic flow is here expressed in terms of $x = X\mathrm{Re}$. The following results pertain to a simulation at $\mathrm{Re} = 100$ over the domain $0 < x < 200$ ($0 < X < 2$). The numerical scheme exactly follows the method implemented for the signalling problem in §5 with the parallel basic flow being replaced by the spatially developing wake. Harmonic forcing is suppressed and perturbations are triggered by a small-amplitude initial impulse close to the inlet. The precise localisation of the impulse is unimportant and it has been checked that the same final state is obtained for a variety of initial conditions. In the initial stage, the impulse wavepacket grows and spreads in space to perturb the entire domain. Perturbations living at each streamwise station slowly synchronize and eventually lead to a global structure tuned at an overall frequency. The following results were obtained at $t = 5000$, with the parameters $n_x = 200$, $\delta x = 1.0$, $n_y = 61$, $l_y = 6$, $\delta t = 0.05$.

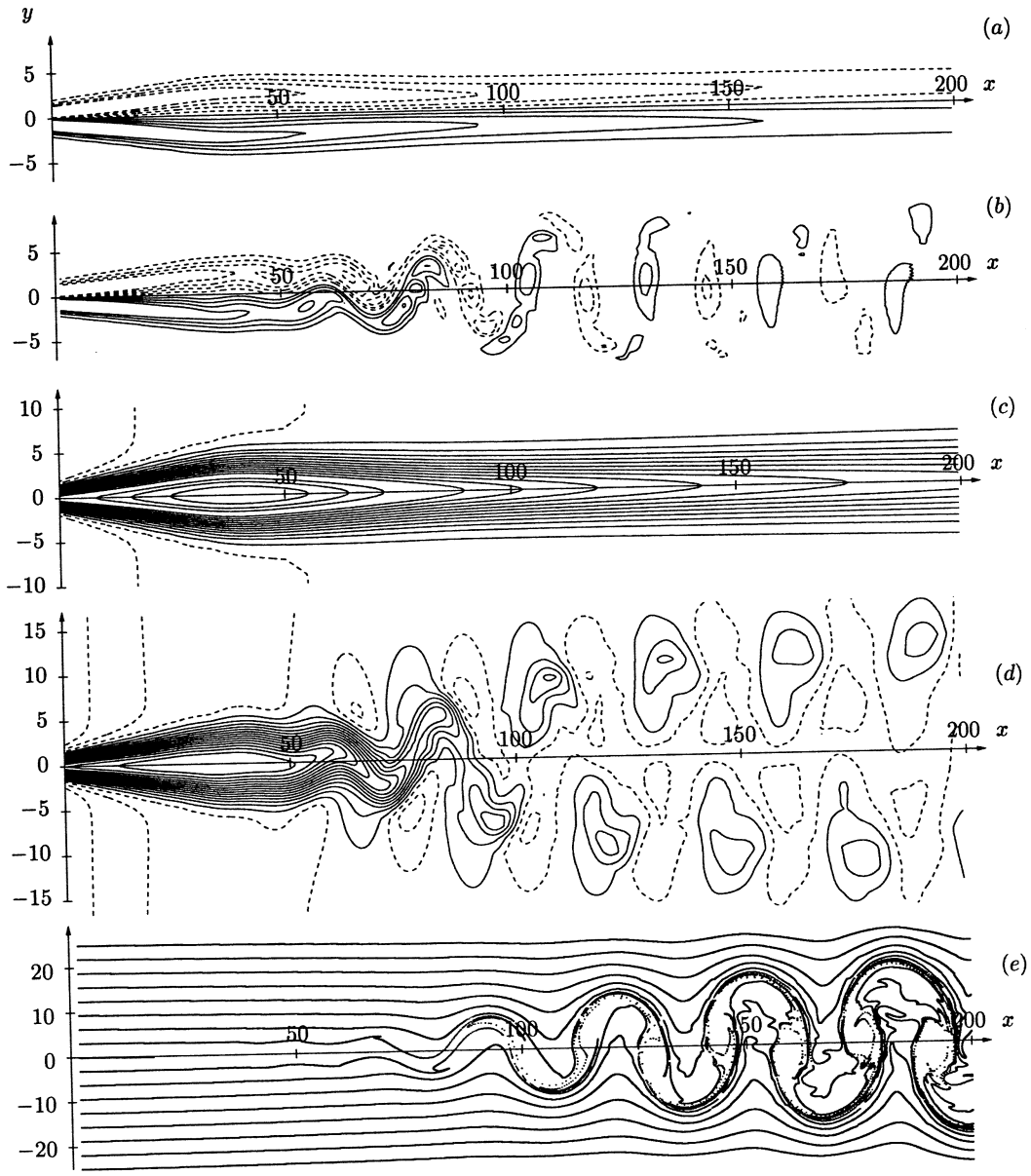


FIGURE 14. Self-sustained global structure at Re = 100 and $t = 5000$ in spatially developing wake flow defined in figure 1. (a, b) Basic and total vorticity contours. Solid lines pertain to positive levels (0.05, 0.10, 0.15, 0.20), dashed lines to negative levels (−0.05, −0.10, −0.15, −0.20). (c, d) Basic and total streamwise velocity. Dashed lines represent the levels 0.95, 0.90, 0.85 above the outlet free-stream velocity, solid lines pertain to the levels 0.80, 0.75, ..., 0.10. (e) Corresponding streaklines.

Isolines of basic and total vorticity are shown in figure 14(a, b), of basic and total streamwise velocity in figure 14(c, d). Comparison of basic and total fields shows that the region close to the inlet is governed by small-amplitude dynamics, whereas a nonlinear wavetrain develops further downstream. In figure 14(b) the two vorticity layers of opposite sign are seen to be unstable and to give rise to periodic vortices which completely mask the underlying basic wake flow. The Kármán-like vortex street is more vividly illustrated

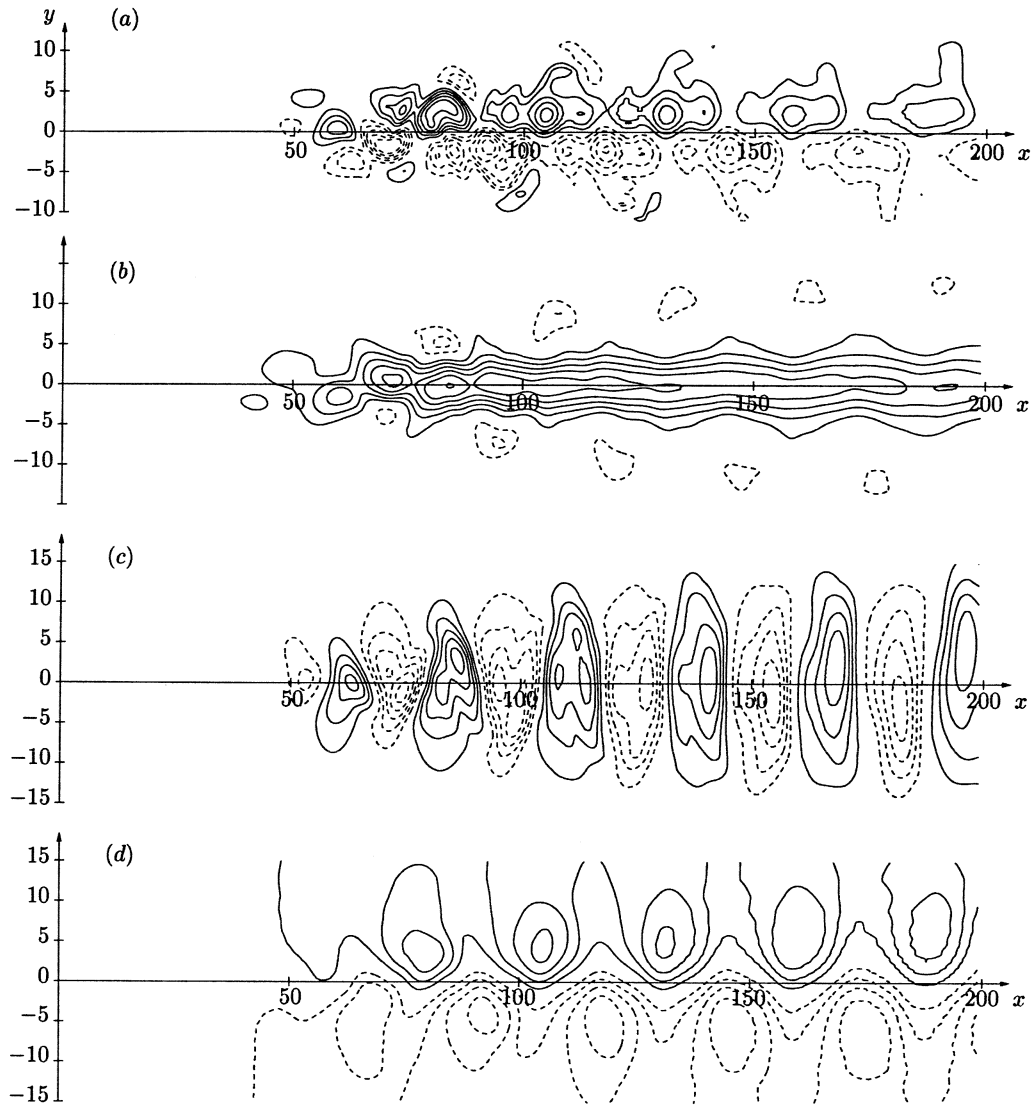


FIGURE 15. Global mode structure: instantaneous perturbation fields. Same conditions as in figure 14. (*a*) Isovorticity contours (0.05, 0.10, ..., 0.25 solid lines, −0.05, −0.10, ..., −0.25 dashed lines). (*b*) Streamwise velocity contours (0.1, 0.2, ..., 0.6 solid lines, −0.1, −0.2 dashed lines). (*c*) Cross-stream velocity contours (0.05, 0.10, ..., 0.25 solid lines, −0.05, −0.10, ..., −0.25 dashed lines). (*d*) Streamlines (0.5, 1.0, 1.5, 2.0 solid, −0.5, −1.0, −1.5, −2.0 dashed).

by the streaklines in figure 14(*e*). Note that in sketches (*a-d*) the cross-stream scale has been magnified for clarity, while x and y coordinates are on the same scale in (*e*).

Snapshots of the perturbation vorticity, u- and v-velocity contours and streamlines are displayed in figure 15(*a-d*). The interpretation of the global mode in terms of an extended nonlinear wavepacket is illustrated by the centreline cross-stream velocity $v(x, 0, t)$ shown in figure 16.

Vorticity time series have been recorded at different locations within the flow in order to ascertain the synchronized behaviour of the global structure. The examination of the associated frequency spectra (figure 17) indicates that all stations are tuned to

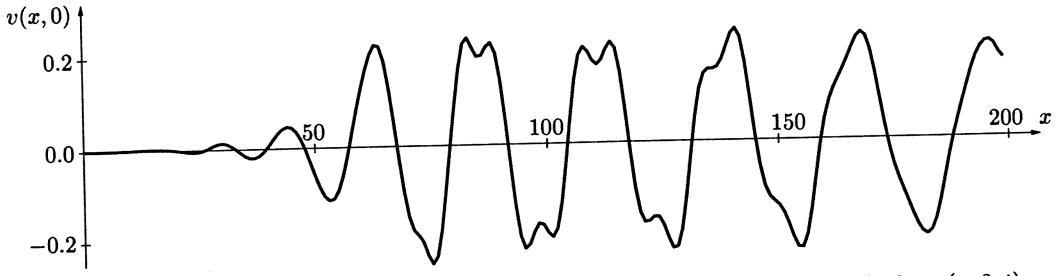


FIGURE 16. Global mode structure: instantaneous centreline cross-stream velocity $v(x,0,t)$. Same conditions as in figure 14.

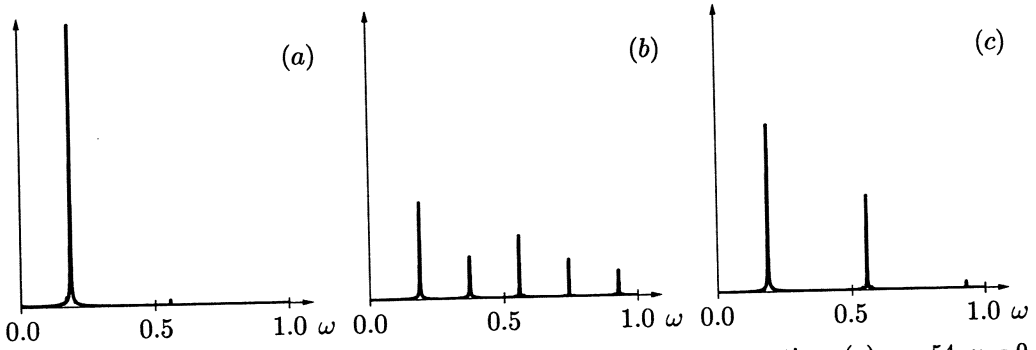


FIGURE 17. Global mode power spectrum of vorticity time series at stations (*a*) $x = 54$, $y = 0$, (*b*) $x = 114$, $y = 5.6$, (*c*) $x = 150$, $y = 0$, based on signal recorded over $5000 < t < 10000$. Same conditions as in figure 14.

the same global fundamental frequency $\omega_g = 0.186 \pm 0.002$ and its harmonics. At the station $(x, y) = (54, 0)$ (figure 17*a*) the fluctuations are seen to be almost sinusoidal. Further downstream on the centreline at $(x, y) = (150, 0)$ (figure 17*c*) higher odd harmonics are excited. Sketch (*b*) at $(x, y) = (114, 5.6)$ shows that off the centerline all harmonics are represented. Following the analysis of Dušek, Le Gal & Fraunié (1994) and Dušek (1996), the spatial distribution of different harmonics may be computed as displayed in figure 18. These graphs clearly demonstrate the wavetrain nature of the global mode in the downstream region. The nonlinear structures sustained by the basic wake flow give rise to a finite meanflow distortion as shown in figure 19. Reynolds stresses are seen to induce a mean flow modification in the form of a pair of counter-rotating large scale vortices (figure 19*a*). The associated streamwise velocity contours displayed in figure 19(*b*) reveal that the velocity defect of the basic wake profiles has been reduced by nonlinearities. The corresponding overall entrainment pattern is displayed in figure 19(*c*). Most of the dominant dynamics are captured by the fundamental and mean-flow components: Superposition of the u-velocity contours pertaining respectively to the fundamental (figure 18*a*) and mean flow distortion (figure 19*b*) yields a pattern which is indeed close to the total perturbation u-velocity contours (figure 15*b*). In the same line of thought as in §5, one may display the streamwise evolution of the energy $E_n(x)$ contained in each harmonic (see equations (5.6)) as shown in figure 20. Higher harmonics ($n > 1$) are seen to reach very low amplitude levels even in the nonlinear region. This observation is also corroborated by the power spectra of figure 17.

It may be concluded that the spatio-temporal development of the vortex street is essentially determined by three components: the imposed unstable basic flow, the funda-

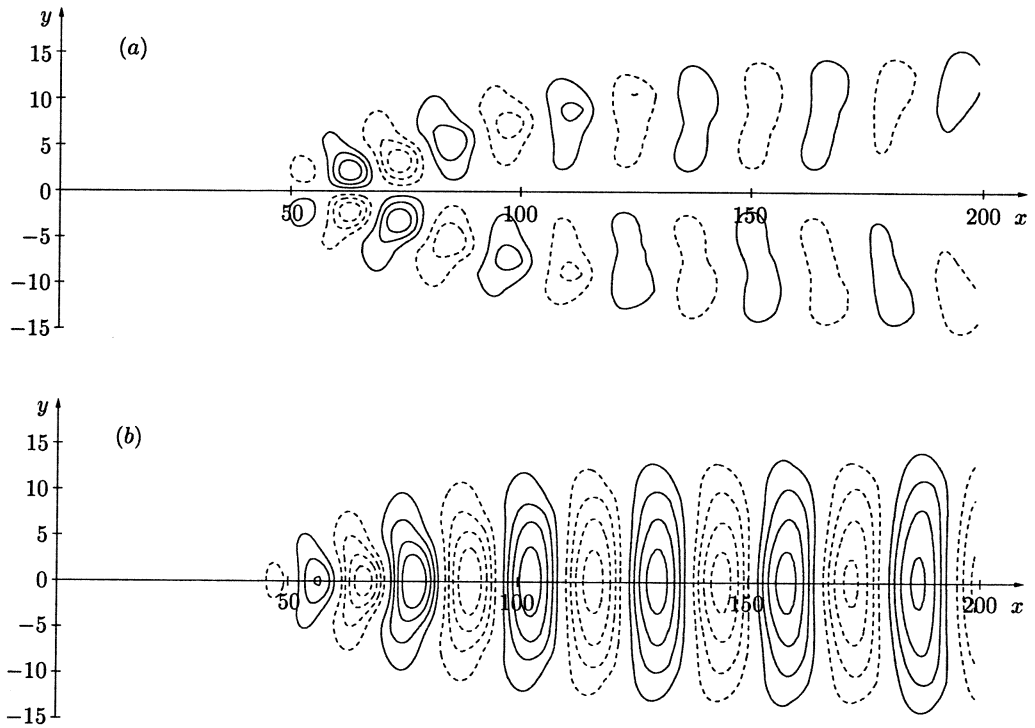


FIGURE 18. Global mode structure: fundamental velocity components. (*a*) Streamwise velocity contours (0.05, 0.10, 0.15 solid lines, −0.05, −0.10, −0.15 dashed lines). (*b*) Cross-stream velocity contours (0.05, 0.10, 0.15, 0.20 solid lines, −0.05, −0.10, −0.15, −0.20 dashed lines). Same conditions as figure 14.

mental wavetrain of frequency ω_g which it sustains and the ensuing mean flow distortion produced by Reynolds stresses.

7. Interpretation of the vortex street as a steep global mode

The objective of this section is to demonstrate that the vortex street observed in the direct numerical simulations of spatially developing wakes in §6 is indeed a steep global mode as defined by Pier *et al.* (1998). In other words, its frequency obeys the marginal stability criterion (1.2) and its spatio-temporal structure is controlled by a front which generates nonlinear travelling wavetrains further downstream.

The application of the steep frequency selection criterion (1.2) to the local absolute frequency $\omega_0(X)$ calculated in §3 and displayed in figure 3 yields

$$X^{ca} = 0.24 \quad \text{and} \quad \omega_0^{ca} = \omega_0(X^{ca}) = 0.190, \tag{7.1}$$

to be compared with the observed global vortex street frequency $\omega_g = 0.186$. The prediction (7.1), which is only a leading-order approximation in $\epsilon = 1/\mathrm{Re} = 0.01$, is seen to be in excellent agreement with the value obtained by direct numerical simulation. The observed frequency should also be compared with the *complex* linear global frequency $\omega_s = 0.143 + 0.008i$ obtained from the linear saddle-point criterion (1.1). The complex ω_s only applies to uniformly linear global mode structures, and does not capture the nonlinear dynamics governing the present vortex street.

The global mode spatial distribution is compared with the associated front structure

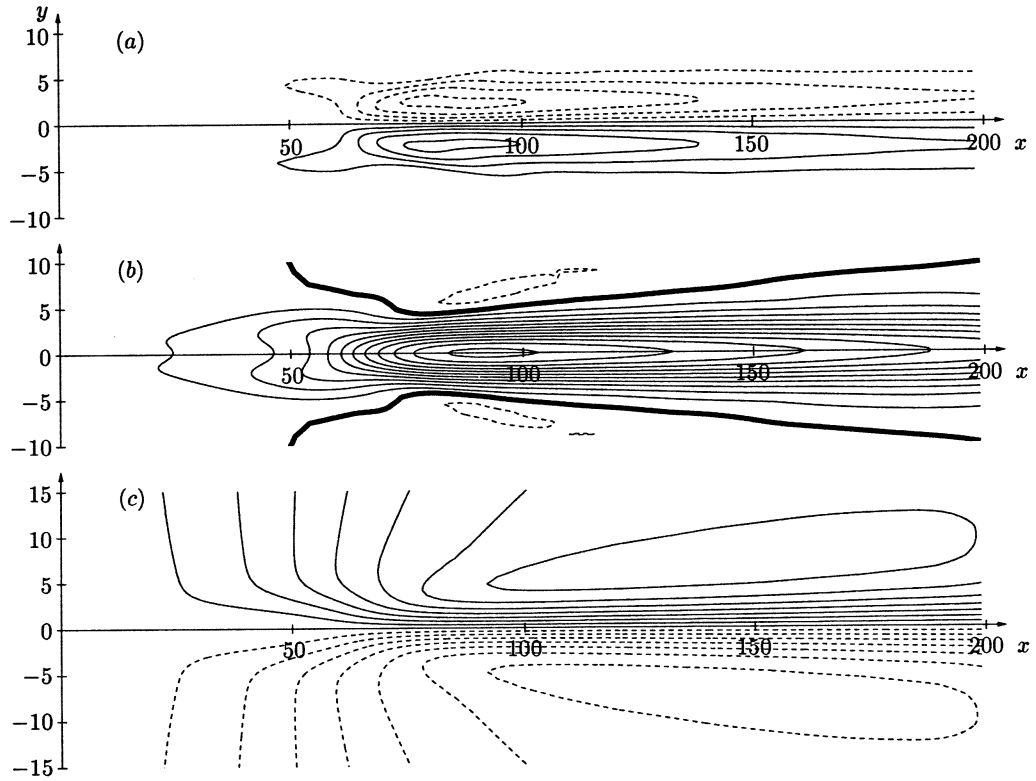


FIGURE 19. Global mode structure: finite-amplitude mean flow correction. (*a*) Isovorticity contours (0.04, 0.08, 0.12, 0.16 solid lines, −0.04, −0.08, −0.12, −0.16 dashed lines). (*b*) Streamwise velocity contours. Thick line separates regions of positive (0.05, 0.10, ..., 0.55 solid lines) and negative (−0.05 dashed line) levels. (*c*) Streamlines (0.2, 0.4, ..., 1.4 solid lines, −0.2, −0.4, ..., −1.4 dashed lines). Same conditions as in figure 14.

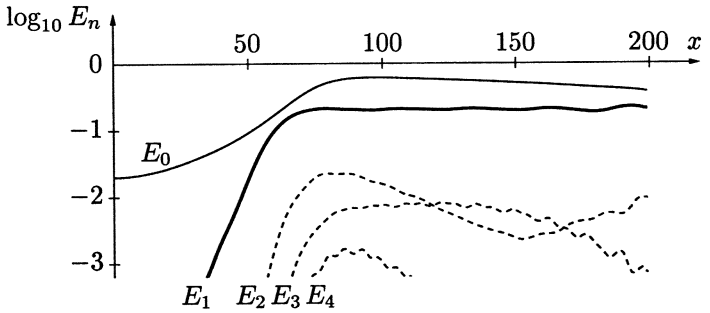


FIGURE 20. Semi-log plot of global mode spatial energy distribution of different harmonics $E_n(x)$. Same conditions as in figure 14.

and local nonlinear travelling wavetrains in figure 21. Contour levels of the fundamental streamwise velocity pertaining to the vortex street (figure 21*a*, already displayed in figure 18*a*) are compared with the same field for the quasi-front of frequency $\omega_0^{ca} = 0.19$ at $X = 0.22$ (figure 21*b*, already displayed in figure 12*b*). The pattern in figure 12(*b*) has been suitably shifted in the streamwise direction and in time so as to adjust amplitude and phase to those of figure 21(*a*). Although this X-station is below the absolute tran-

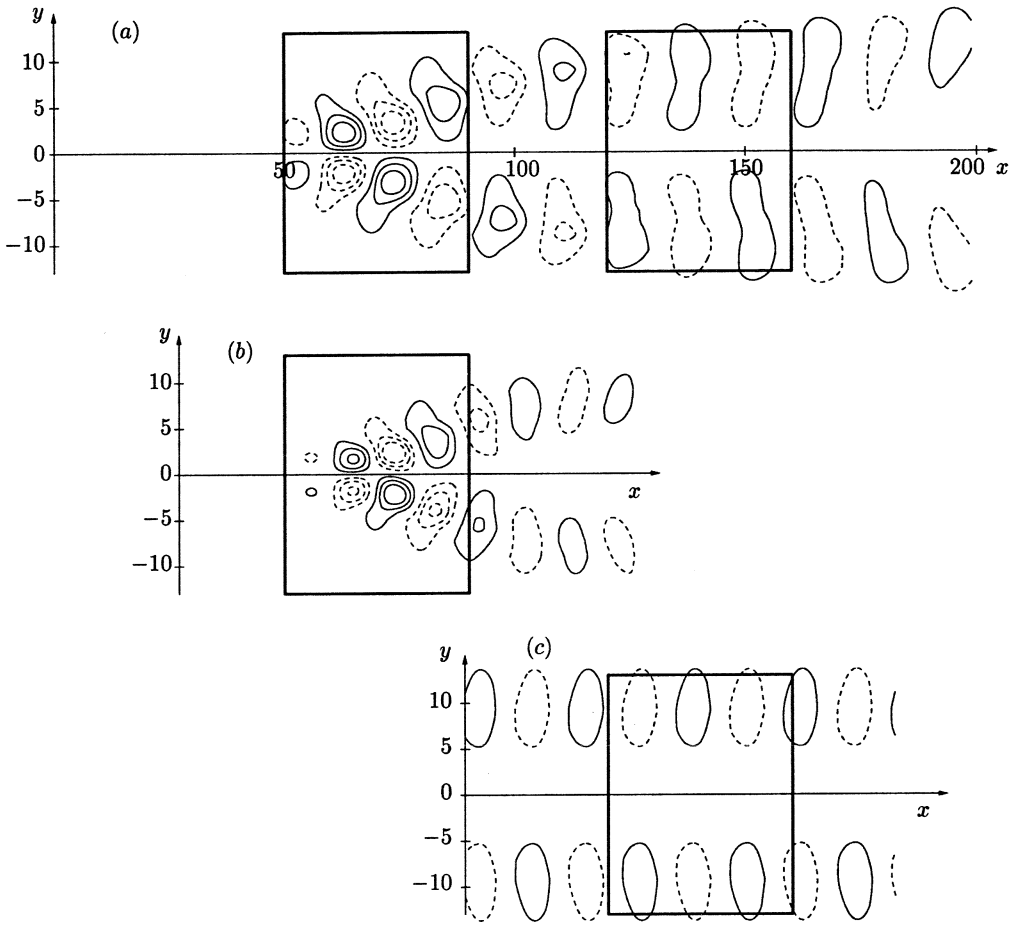


FIGURE 21. Interpretation of global mode structure (a) in terms of a front (b) and fully nonlinear travelling waves (c). Isolevels of fundamental streamwise velocity component are shown (0.05, 0.10, 0.15 solid lines, −0.05, −0.10, −0.15 dashed lines).

sition point $X^{ca} = 0.24$, the structure of the fundamental is seen to be approximately reproduced by the front.

The same vortex street contour levels (figure 21a) are compared with those for a fully nonlinear travelling wave at $X = 1.40$ obtained via temporal numerical simulation (figure 21c). More specifically, the local wave number $k^{nl+} = 0.27$ prevailing at $X = 1.40$ and $\omega_0^{ca} = 0.19$ is determined from the local nonlinear dispersion relation plotted in figure 5(a), and a streamwise periodic temporal simulation is performed as detailed in §4. Here again, the downstream region of the global mode is seen to be approximately represented by nonlinear wavetrains which travel according to the local nonlinear dispersion relation at each streamwise station.

Note however that the characteristic wave lengths of the quasi-front in (b) and nonlinear travelling wave in (c) appear to be somewhat smaller than those of the corresponding global mode structure in (a). This feature may be related to the frequency difference between the two cases: $\omega_0^{ca} = 0.190$ in (b, c) and $\omega_g = 0.186$ in (a). The wavemaker triggering the vortex street is located at the marginally AU station $x^{ca} = \mathrm{Re}X^{ca} = 24$; however, full nonlinearity is only attained about a wavelength downstream of this

location. Thus the region where the global mode structure reaches finite amplitude is actually pushed to the downstream side of the AU region $24 < x < 55$. This result is not all that surprising: the front characterizing the streamwise transition between linear waves and a fully nonlinear wavetrain is known to typically extend over one wavelength (see *e.g.* van Saarloos 1987).

8. Conclusion

This study has demonstrated that the steep global modes previously identified and analysed in one-dimensional CGL evolution equations also arise in spatially developing shear flows exhibiting a region of absolute instability. The self-sustained structures have been shown to be controlled by a front located at the upstream edge of the AU region which acts as a wavemaker to generate nonlinear travelling waves in its wake. Provided that the streamwise variations of the underlying basic flow are sufficiently slow (WKBJ approximation), such wavetrains are governed at each station by the associated local nonlinear dispersion relation obtained from a purely temporal evolution problem on the local shear flow profile considered as parallel. Fast streamwise variations are confined to the front layer where the full Navier–Stokes equations have to be resolved for the wave field on the fast x-scale.

It should again be noted that the stationary fronts identified in the present shear flow framework are of the same nature as the propagating fronts studied in the context of pattern formation: the criterion (1.2) is merely an application of the marginal instability criterion of Dee & Langer (1983) and van Saarloos (1987, 1988). The present findings are also consistent with the nature of the nonlinear impulse response in parallel wakes studied by Delbende & Chomaz (1998). Furthermore, the conjecture put forward by Monkewitz & Nguyen (1987) has been fully confirmed: the first streamwise station X^{ca} of non-negative absolute growth rate indeed supports a front which imposes its frequency ω_0^{ca} to the entire flow.

The present approach constitutes a significant departure from the landmark nonlinear hydrodynamic instability analyses of spatially evolving shear flows developed by Goldstein & Leib (1988) and Goldstein & Hultgren (1988). These investigations require to simultaneously enforce the assumptions of overall small wave amplitude and slow streamwise variations. As a result, finite-amplitude effects arise only within nonlinear critical layers of small cross-stream extent. An asymptotically consistent description of the streamwise development of perturbations of given frequency may then be obtained for convectively unstable shear flows. In the present study, the small-amplitude assumption has been totally relaxed and only the slow streamwise variation hypothesis has been retained. The fully nonlinear evolution of perturbations of order unity may then be captured either for the forced problem in CU flows or for self-sustained structures in flows with an AU region. Nonlinearities then extend over the entire shear region in the cross-stream direction. Whereas critical layer studies succeed in achieving a quasi-analytic formulation of the forced dynamics, the present approach relies on local numerical simulations to identify the various constitutive elements of the dominant WKBJ approximation. It is surmised that the same fully nonlinear theory is applicable to a wide variety of spatially evolving shear flows whether they are in a self-sustained mode or subjected to forcing.

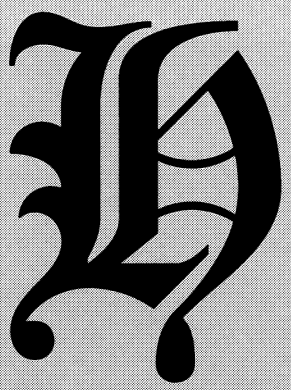
A systematic asymptotic approximation scheme of the kind presented in Pier & Huerre (1999a) has not been attempted here. Furthermore, the Reynolds number has been kept relatively small at $\mathrm{Re} = 100$. Exploratory simulations indicate that secondary instabilities occur for the present basic flow beyond $\mathrm{Re} \sim 200$. It is therefore impractical to push Re up to larger values in order to move closer to the WKBJ limit $\epsilon = 1/\mathrm{Re} = 0$.

It should be emphasized that the steep frequency selection criterion (1.2) which has been demonstrated here to apply to real flows is purely based on the local *linear* dispersion relation, although it pertains to fully *nonlinear* sychronized structures. The saddle-point criterion (1.1) is also linear but it is solely applicable to strictly linear global modes. And indeed, the numerically obtained $\omega_g = 0.186$ is much closer to $\omega_0^{ca} = 0.190$ of criterion (1.2) than to $\omega_s = 0.143 + 0.008i$ of criterion (1.1), which in any case is incompatible with the saturated nonlinear wavetrains observed downstream of the front at X^{ca}. Furthermore, as demonstrated by Pier & Huerre (1999a), steep global modes are triggered as soon as local linear absolute instability appears, while linear global modes become unstable only when the linear AU region is of sufficiently large extent (Chomaz *et al.* 1991). To confirm this argument, the same simulation has been carried out with a spatially developing wake obtained for a pressure gradient designed to yield a minimum centerline velocity of 0.047 instead of 0.010 as in figure 1. The saddle-point frequency is then $\omega_s = 0.155 - 0.001i$, which corresponds to a decaying linear global mode. Nevertheless, there is still a small locally absolutely unstable region $0.34 < X < 0.44$ with $\omega_{0,i}^{max} = 0.001$. In this case, a steep global mode is observed in the direct numerical simulation, whereas no self-sustained structure survives if nonlinear terms are turned off. This result is entirely consistent with the transition scenario outlined in Pier & Huerre (1999a).

It is somewhat paradoxical that the intricate complex X-plane analyses developed over the years to uncover the selection properties of linear global modes are masked in practice by the onset of local absolute instability which immediately prevails and imposes its frequency and the overall structure of the synchronized oscillations.

As a final note of caution, it should be stressed that the present analysis cannot be obviously extended to bluff-body wakes where the AU region lies immediately behind the obstacle. In spite of the fact that the synthetic wake considered here is purely co-flowing, it can nonetheless sustain a synchronized vortex street which qualitatively displays the same features.

The authors are grateful to Jean-Marc Chomaz and Arnaud Couairon for enlightening discussions. The expert advice and suggestions of Carlo Cossu played an essential rôle in the design and validation of the numerical scheme.



Happy End

Ce travail a permis de montrer qu'il existe deux types de structures synchronisées intrinsèques. Les modes de type "chapeau" ont une enveloppe et un nombre d'onde local qui varient continûment partout en espace ; leur fréquence est déterminée par une condition de point-selle appliquée à la relation de dispersion non linéaire locale. Les modes de type "éléphant" sont caractérisés par un front stationnaire tourné vers l'amont ; ce front est associé à un saut de nombre d'onde et d'amplitude et c'est lui qui impose sa fréquence à tout le système. Les mécanismes de résonance ont été identifiés grâce à l'étude du modèle de Ginzburg–Landau à coefficients complexes. En analysant ce modèle simplifié au lieu des équations complètes de la dynamique des fluides, j'ai pu mettre en évidence les paramètres caractéristiques qui contrôlent le comportement global. La première structure synchronisée à laquelle le système non perturbé donne naissance est un mode éléphant. Les modes chapeaux n'existent que plus loin au-delà du seuil d'instabilité globale ; ils sont plus facilement obtenus dans des cas de faible advection.

La généralisation des résultats précédents aux écoulements réels a montré que, une nouvelle fois, le modèle GLC est un outil parfaitement adapté à la dynamique des fluides. En effet, les éléments constitutifs d'un mode global du modèle GLC trouvent chacun leur homologue dans le cadre des équations de Navier–Stokes. C'est ainsi que la fréquence de l'allée tourbillonnaire de Bénard–Kármán a pu être prédite correctement grâce à l'étude des propriétés locales du sillage au sein duquel se forment les tourbillons périodiques.

Un résultat essentiel de ces travaux est que des structures *globales* et *non linéaires* sont déterminées par des effets *locaux* et *linéaires*. Le mode éléphant présente une région non linéaire d'extension finie, mais il est déclenché par un front qui obéit au critère linéaire de stabilité marginale. Ainsi, les effets d'amplitude finie se manifestant en aval ne modifient pas le comportement à l'endroit où le mécanisme de résonance se situe. La généralisation de cette propriété aux écoulements réels est plus surprenante : les non-linéarités induisent une correction de l'écoulement moyen qui aurait pu complètement remettre en cause le critère de stabilité marginale. Mais les vérifications détaillées du dernier chapitre ont montré que dans le cas des sillages aussi, les effets non linéaires ne font qu'arrêter l'amplification des trains d'ondes instables sans conduire à un comportement fondamentalement différent. Ainsi, les instabilités hydrodynamiques rencontrées dans cette étude ont un caractère essentiellement super-critique ; le moteur de l'instabilité se situe au niveau des propriétés linéaires.

Cependant, ce sont les propriétés linéaires *locales* qui l'emportent sur la stabilité linéaire *globale*. En effet, l'instabilité linéaire globale nécessite en général une région AI d'extension finie, alors qu'il a été montré au chapitre $\mathcal{F}$ que les structures non linéaires globales existent dès l'apparition d'un point AI dans le système. Ainsi, l'instabilité absolue locale est une condition nécessaire *et* suffisante pour l'existence de modes globaux. La transition de l'état non perturbé vers un mode éléphant s'effectue par une bifurcation nœud-col et est indépendante du changement de stabilité d'un

mode global linéaire. Ce sont donc les caractéristiques locales qui déterminent le comportement global et qui masquent la déstabilisation du mode global linéaire associée à un point-selle dans le plan des X complexes. Ainsi, la transition *globale* vers des structures non linéaires synchronisées est de nature sous-critique.

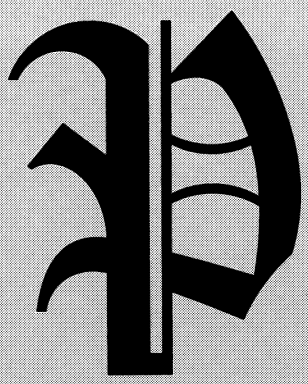
La modification de l'écoulement de base semble jouer un rôle passif. Cependant il a été observé (figure 10 p.156) que, dans les régions linéaires, la correction de l'écoulement de base n'a pas le comportement linéaire attendu. Ceci peut être dû à des effets globaux de pression qui ne suivent pas la décroissance exponentielle linéaire. Ce point mérite d'être approfondi. La condition limite en amont (une branche $k^{\ell-}$) est essentielle, mais une telle branche exponentiellement décroissante semble noyée par la lente décroissance de la perturbation de l'écoulement moyen. Le comportement global n'est pourtant pas modifié.

La correction de l'écoulement moyen est le seul effet propre aux équations de Navier–Stokes, absent du modèle de Ginzburg–Landau. Le problème d'évolution temporelle (section 4 de l'article précédent) permet d'obtenir la relation de dispersion non linéaire. La fréquence est calculée dans le régime quasi-stationnaire où la composante non fluctuante continue à diffuser lentement. Même si la fréquence non linéaire n'évolue plus dans ce régime, il n'est pas évident de choisir l'instant approprié de l'évolution temporelle pour faire la comparaison entre le train d'onde non linéaire de l'allée tourbillonnaire (figure 21*a* p.164) et les ondes locales (figure 21*c*). Une étude détaillée de la variation de l'écoulement moyen le long du courant devrait répondre à cette question.

L'étude s'est affranchie des problèmes liés à la présence d'obstacles pour aboutir à une théorie cohérente de la sélection de fréquence dans des écoulements ouverts se développant le long du courant. Dans les situations expérimentales, l'obstacle se trouve généralement à l'endroit le plus défavorable : au bord amont de la région AI. C'est pourquoi des expériences plus délicates seraient nécessaires pour valider tel quel le critère de sélection de fréquence développé ici ; ou alors, un complément de théorie serait requis pour trouver l'écoulement sans obstacle équivalent à une situation donnée.

Dans le dernier chapitre, l'accent a été mis sur les modes éléphants, qui sont les seuls possibles dans le cadre des sillages. Pour pouvoir être observés, les modes chapeaux requièrent une faible advection. Pour les produire expérimentalement, on pourrait donc imaginer des systèmes de convection de Rayleigh–Bénard avec une différence de température variable.

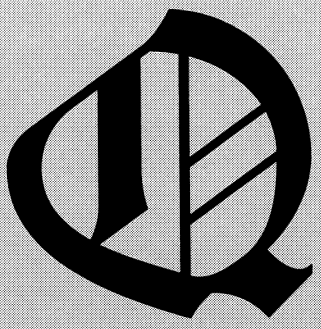
Après avoir contemplé les ondulations fugitives des écoulements cisaillés,
notre balade dans une forêt de tourbillons s'achève.



Post-scriptum

Les logiciels suivants ont été utilisés pour obtenir et présenter les résultats de ce travail. Les textes et les programmes ont été édités avec `vi`. Les parties françaises du mémoire ont été composées à l'aide du système de typographie TEX [46] ; les articles en LATEX ont été insérés à l'impression. Les figures sont entièrement conçues en `PostScript`. Les calculs numériques simples, comme par exemple les branches spatiales pour la relation de dispersion explicite de GLC, sont également effectués en `PostScript`. Les programmes plus élaborés demandant la résolution de problèmes aux valeurs propres ou d'équations aux dérivées partielles sont écrits en `C++`. Les routines auxiliaires de la librairie `Lapack` ont été exploitées pour l'algèbre linéaire.

Les calculs courts (au maximum quelques heures) ont été réalisés sur "tiramisu" (Toshiba Satellite 4000CDS exploité sous `Linux`) et "tomcat" (imprimante QMS 1725). Les simulations de longue haleine (jusqu'à plusieurs semaines) ont été mises en œuvre sur les stations Silicon Graphics "gibi" (SGI Origin 200) et "shadok" (Indigo 2).

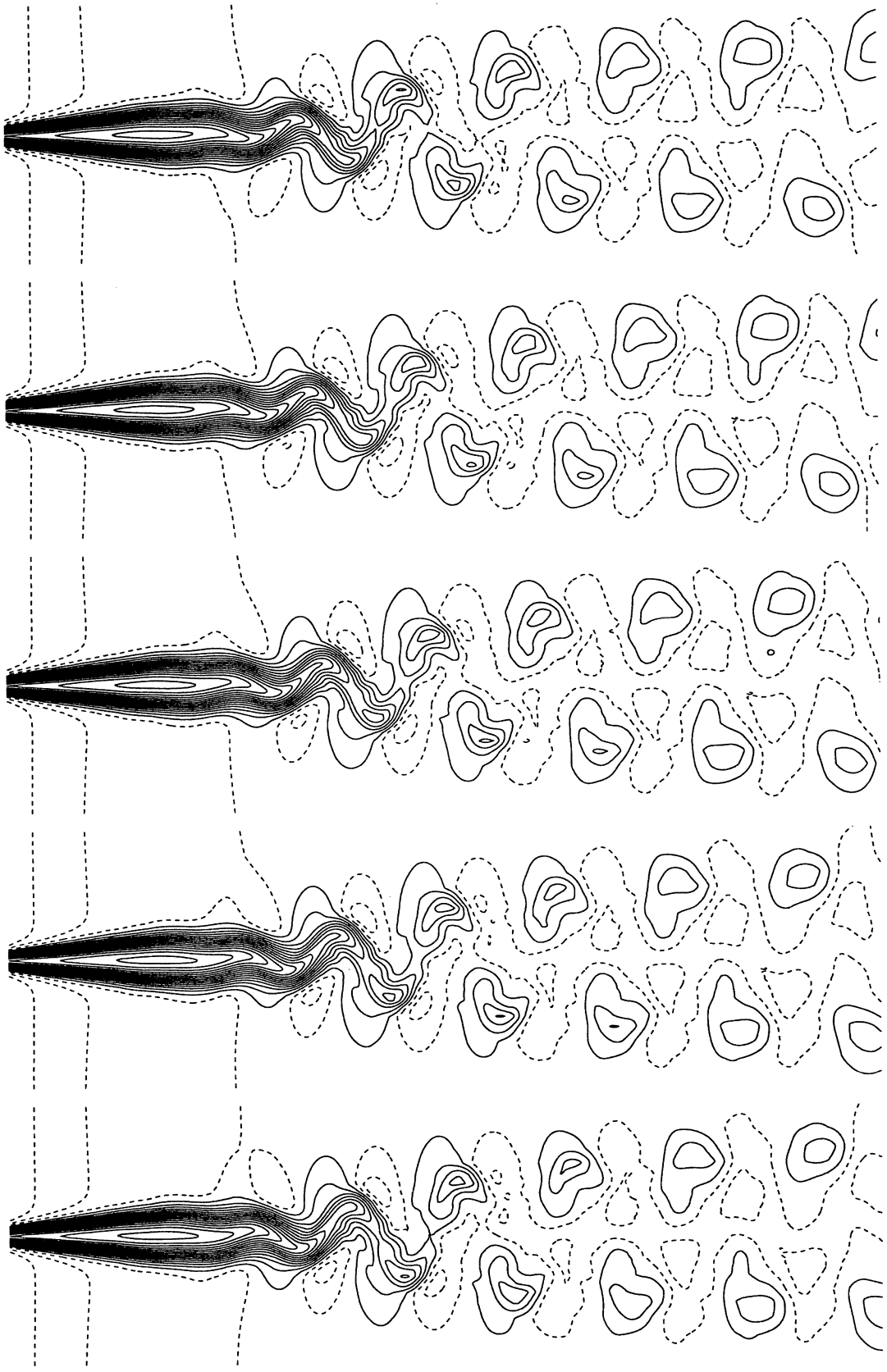


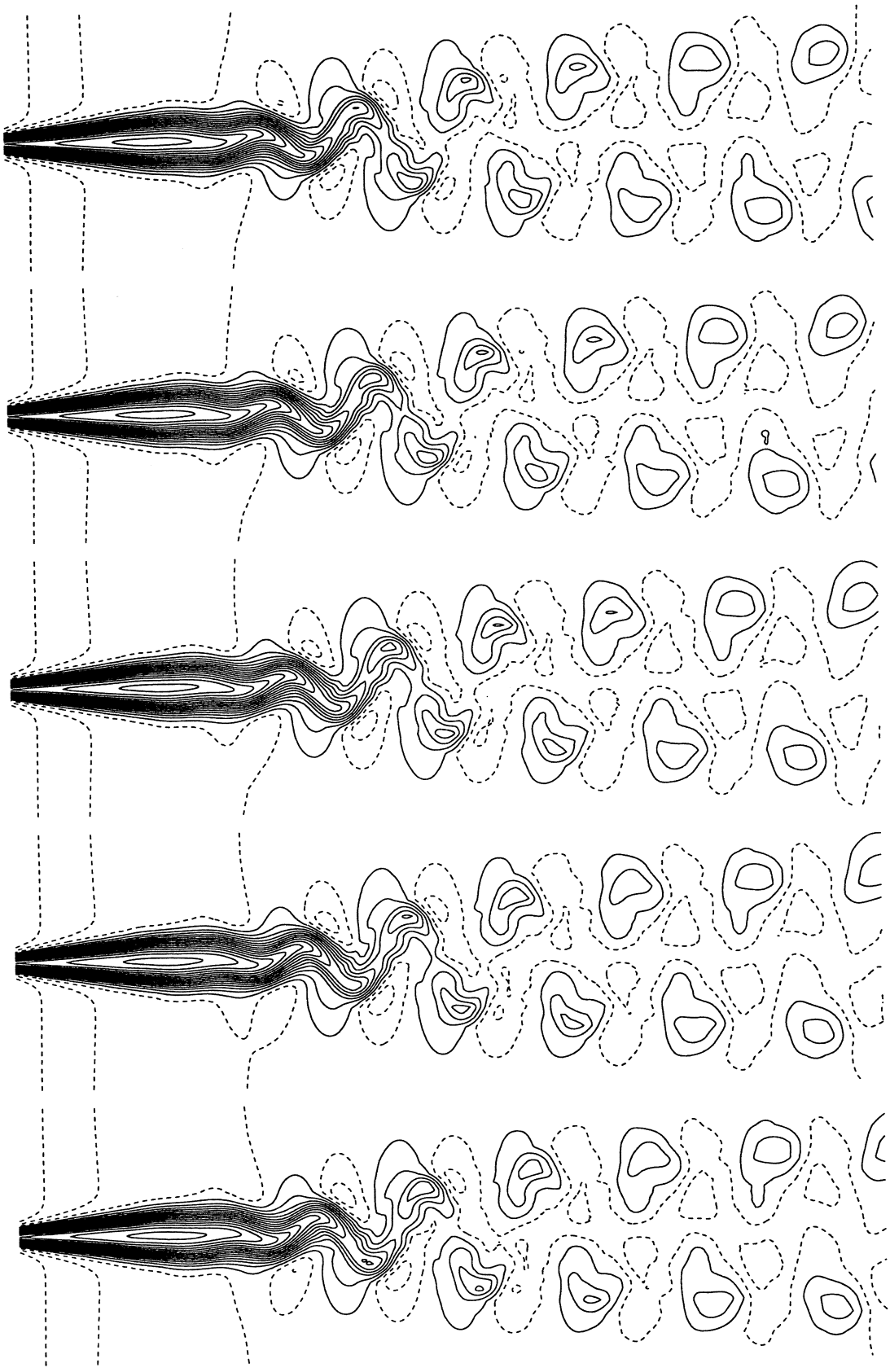
Quatre-quarts

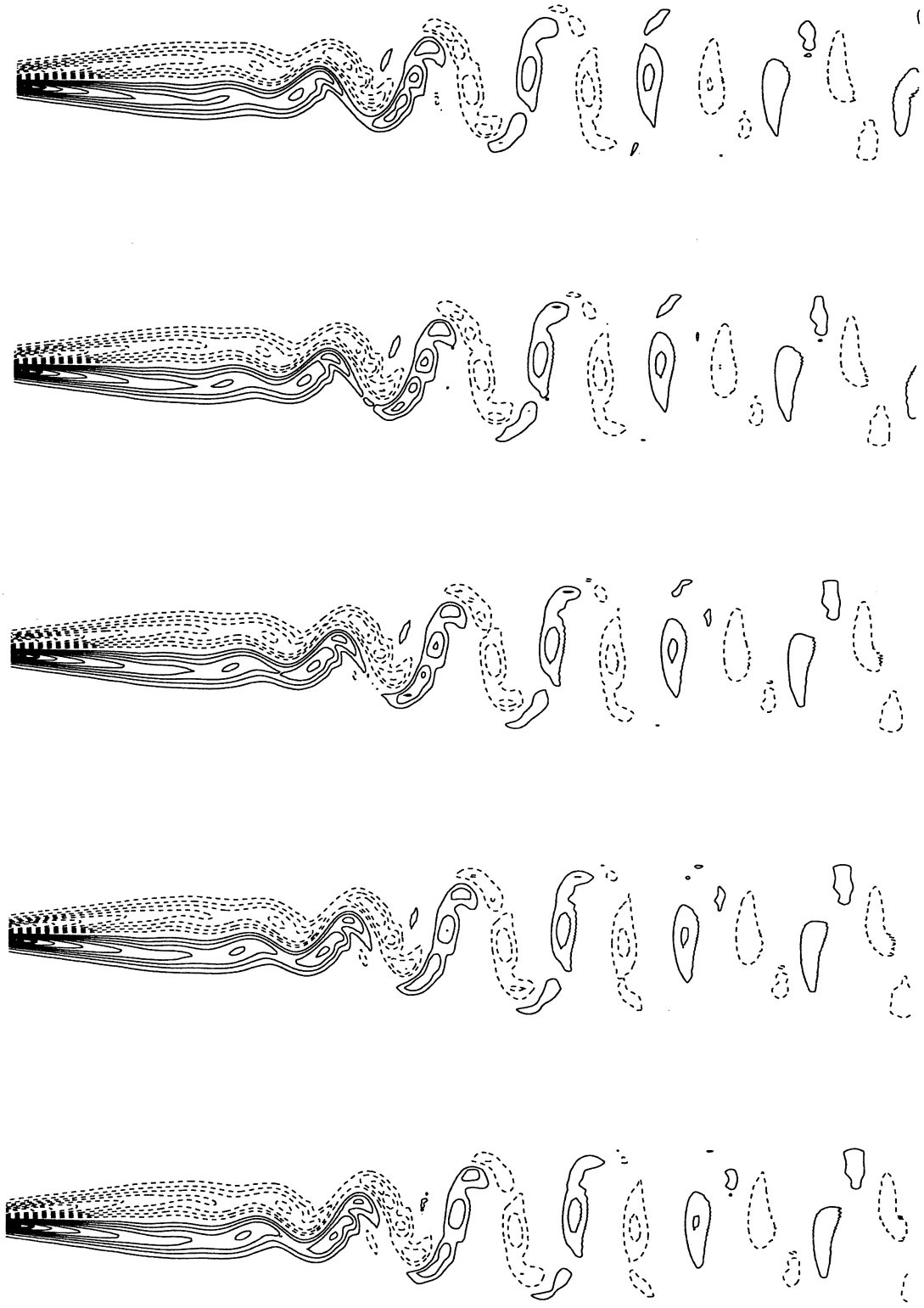
Le comportement synchronisé du sillage étudié au chapitre 6 est illustré ici par des clichés successifs. La configuration étudiée est la même que celle de la figure 14 p.159 et la période d'émission des tourbillons vaut $T = 2\pi/\omega_g = 33.8$. Les clichés sont espacés de $\Delta t = 4$; dix images successives couvrent ainsi un peu plus qu'une période des oscillations globales.

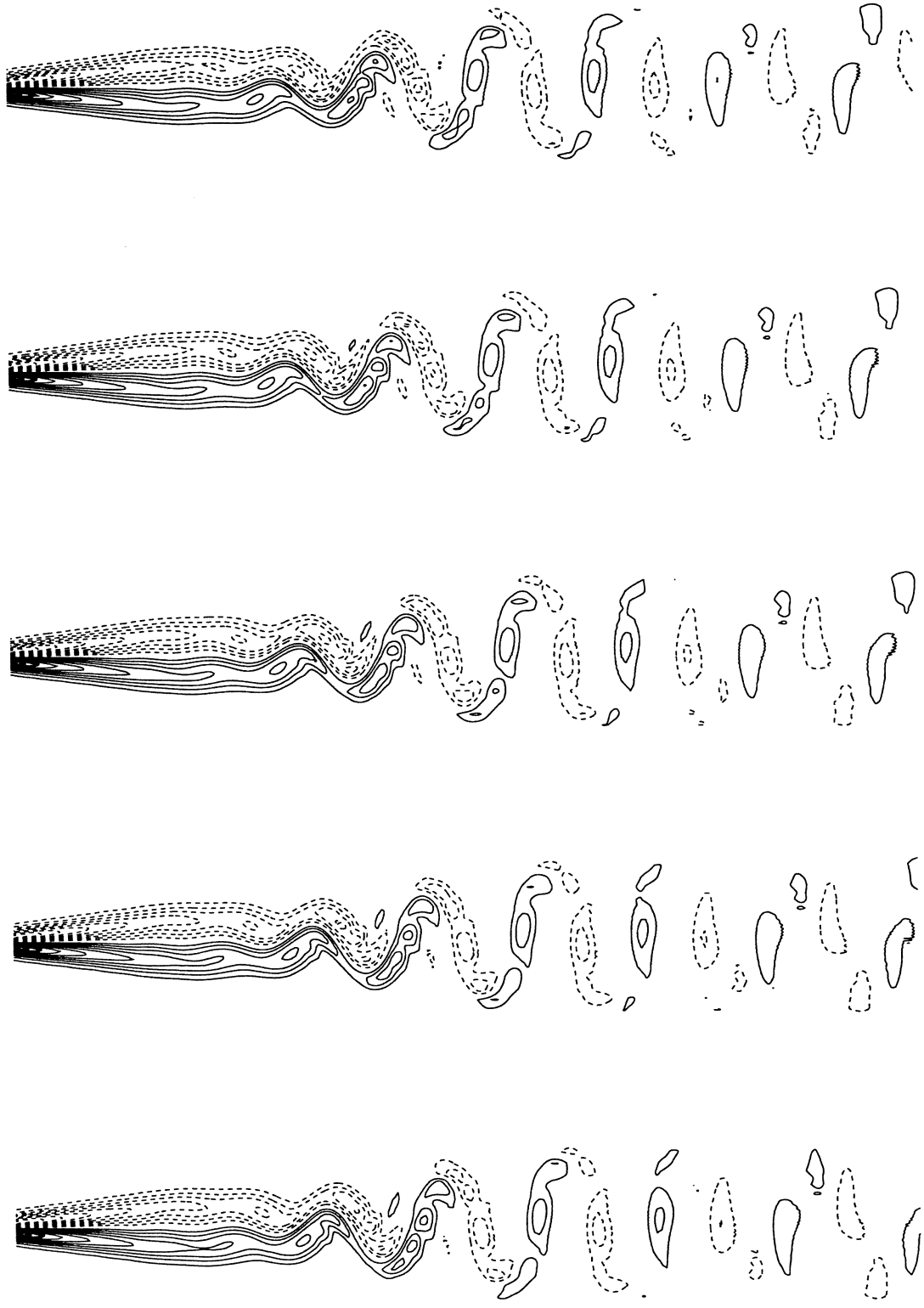
Les champs de vitesse axiale (p.172–173) et de vorticité (p.174–175) montrent la production périodique de tourbillons contrarotatifs. Les champs de vitesse transverse (p.176–177) font ressortir le rôle de source joué par le bord amont de la région absolument instable. Les lignes d'émission (p.178–179) fournissent l'image la plus connue de l'allée tourbillonnaire.

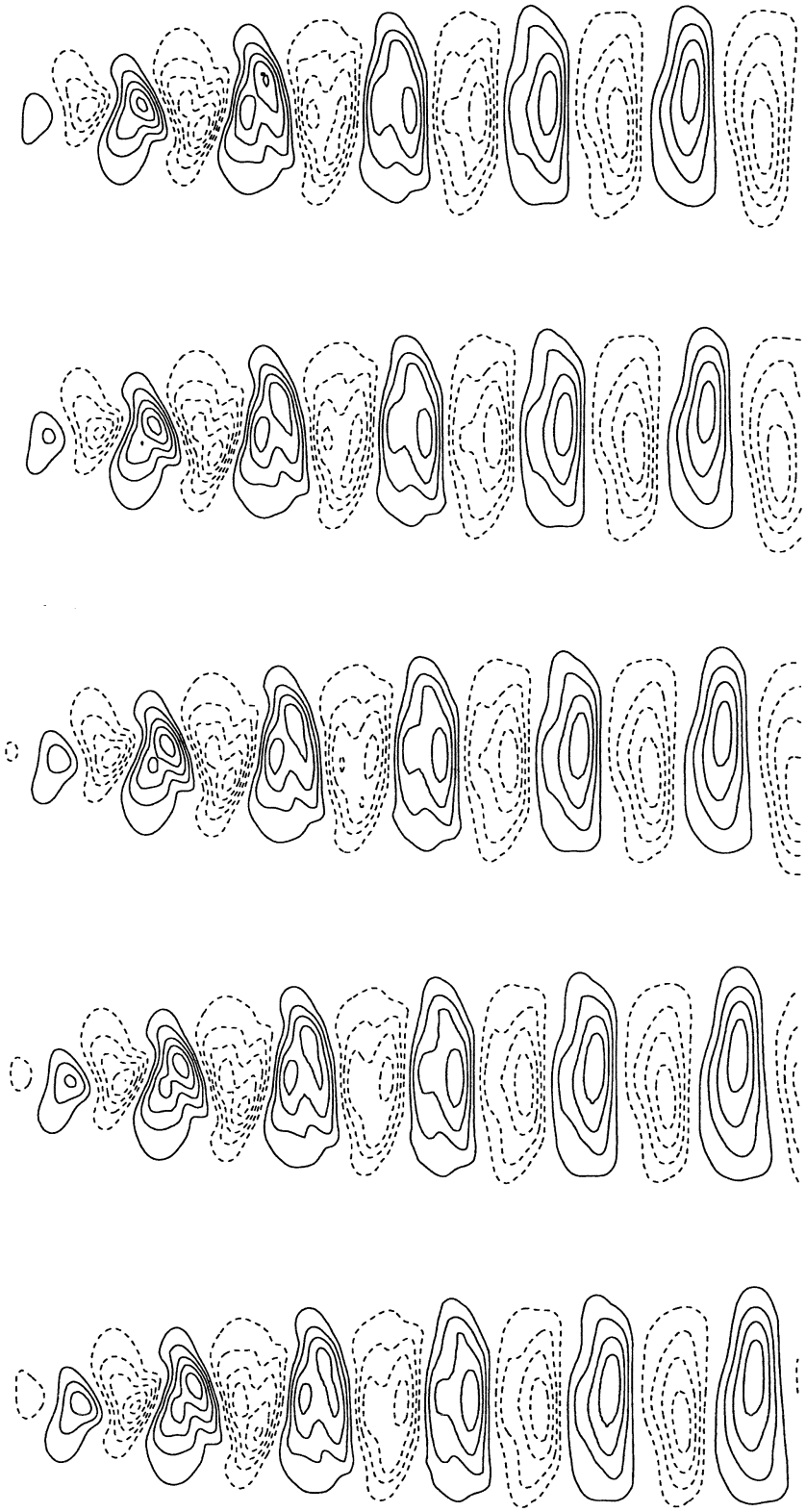
Les courbes indiquées (p.172–177) correspondent aux niveaux définis pour les graphes p.159 figures 14(*d*) et (*b*) et p.160 figure 15(*c*) respectivement.

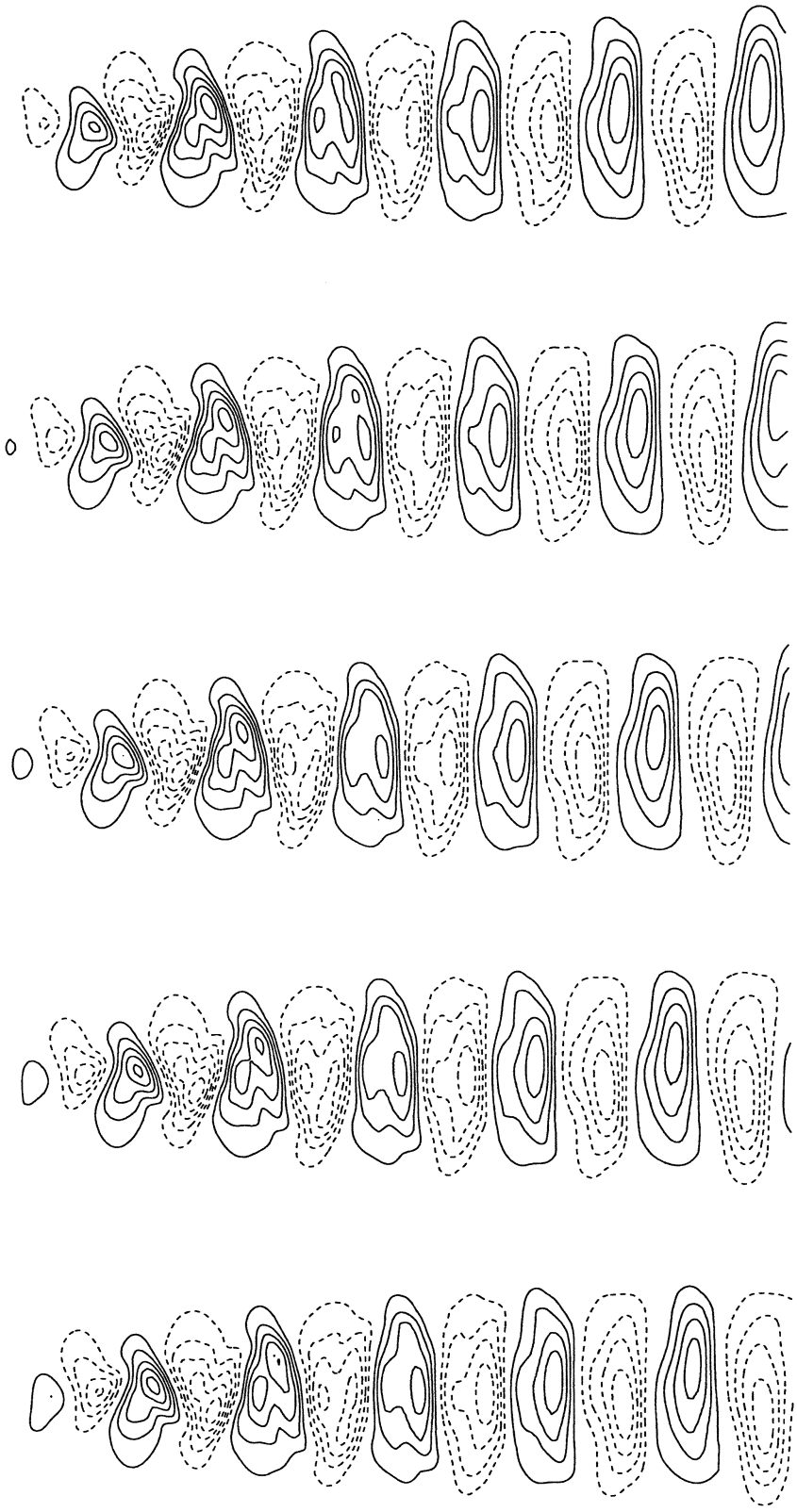


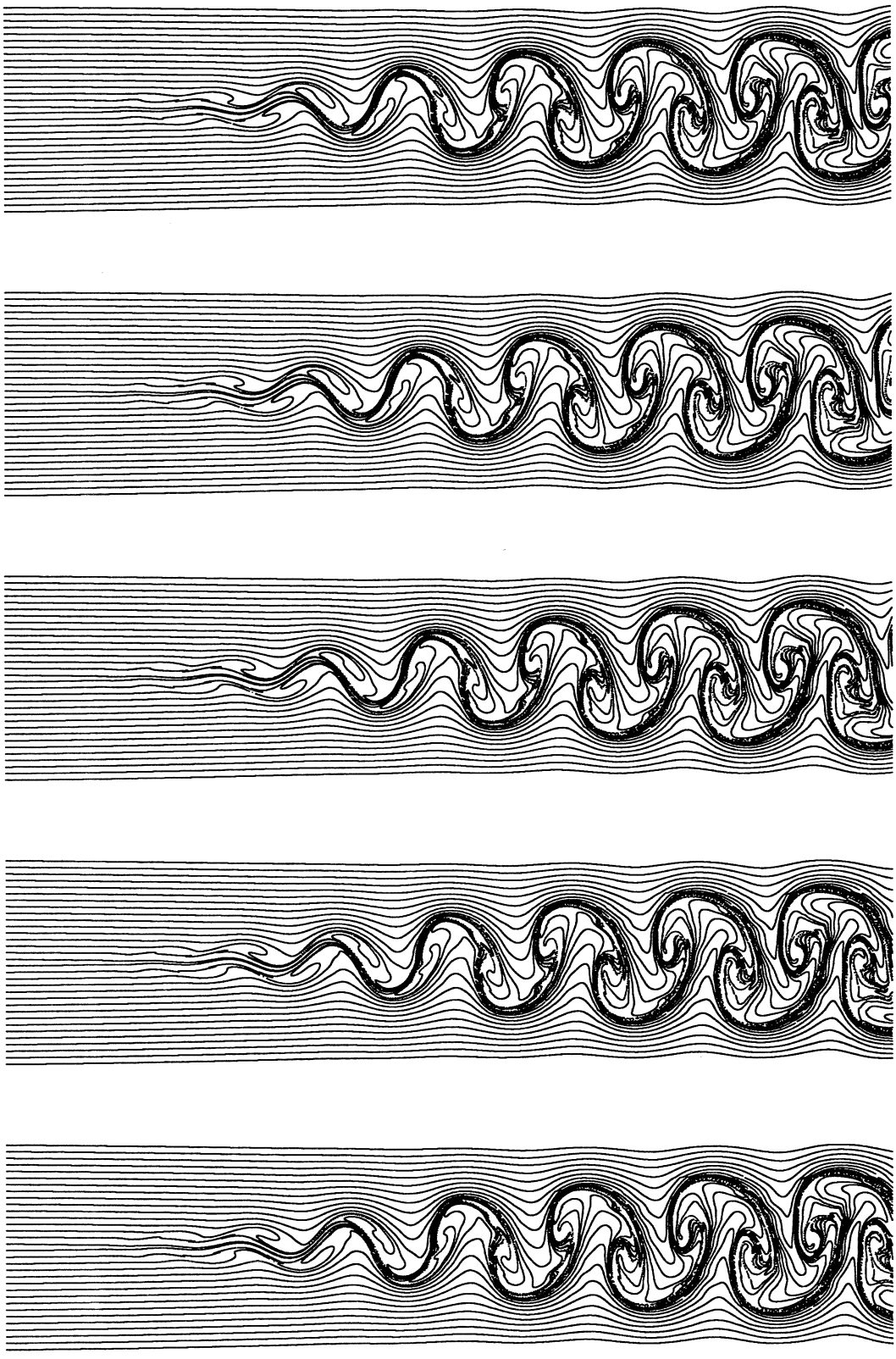


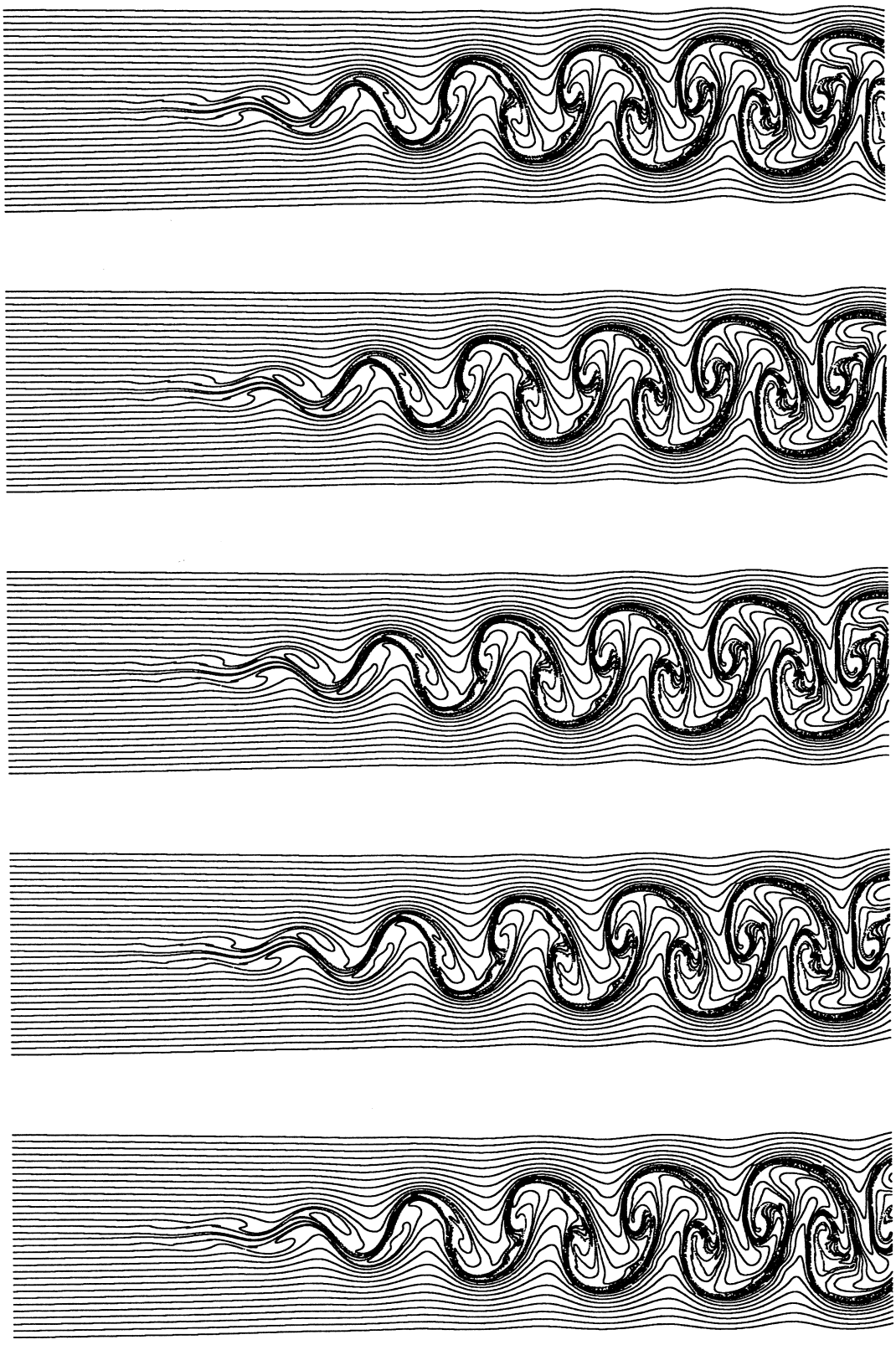


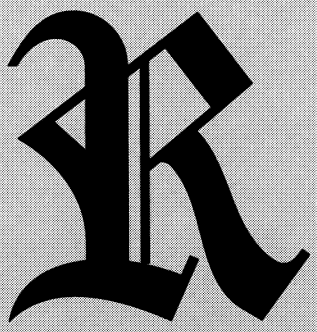












Remerciements

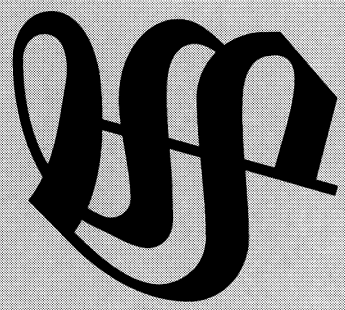
Ce travail est le résultat de quatre années intenses et stimulantes passées sous la direction de Patrick Huerre au LadHyX. Depuis ma première visite de ce laboratoire (en février 1995) jusqu'à aujourd'hui, son enthousiasme indéfectible m'a accompagné dans le monde de la dynamique des fluides. Son ouverture d'esprit, sa vision globale des écoulements, sa parfaite connaissance de la bibliographie ont su me guider très efficacement tout en me laissant libre d'organiser mes recherches selon mes goûts. Sa fascination pour le moindre petit résultat nouveau ou inattendu m'a constamment redonné courage et envie d'aller encore plus loin ou de tout remettre en cause. De surcroît, à son contact j'ai été initié au perfectionnisme dans la rédaction, à l'acharnement allant jusqu'à changer vingt fois un mot pour trouver celui qui exprime parfaitement une idée. Bref, je souhaite à tout thésard d'avoir un tel directeur de thèse.

Je dois à Paul Manneville de m'avoir ouvert les portes du royaume des instabilités et du non-linéaire (il y a sept ans...). Pendant ma thèse, nos nombreuses discussions autour d'un expresso matinal ont été pour moi autant de leçons sur les sujets les plus variés allant de la torréfaction du café jusqu'à l'appendice 𝔇 du TEXbook. Paul est un grand gourou de TEX.

J'exprime ma très vive reconnaissance à Jacques Webert pour sa parfaite gestion de l'équipement informatique du LadHyX, sa constante disponibilité, sa patience à répondre d'innombrables fois aux mêmes questions, son intelligence de `Linux`, son conseil de passer à `bash` parce que c'est "plus pur" que `tcsh`, son art de programmer des `shell scripts`. Saint Jacques, priez pour nous !

Anaël Lemaître, mon co-thésard de bureau, m'a grandement facilité le travail : par ses fous rires chaleureux, sa maîtrise de `C++` et ses goûts culinaires. Sans Carlo Cossu et sa recette virtuelle de tiramisu, j'aurais mis beaucoup plus de temps à simuler les équations de Navier–Stokes, je n'aurais pas trouvé de nom pour mon ordinateur portable et je n'aurais pas regardé la quasi-finale France-Italie. Merci à Jean-Marc Chomaz pour ses réflexions percutantes, pour m'avoir associé à son enseignement. Stéphane Le Dizès et Arnaud Couairon ont accompagné mes premiers pas dans les modes globaux. Tout le monde sait que le LadHyX n'existerait pas sans Thérèse Lécuyer et ses sourires. Antoine Garcia n'a pas ménagé son temps et son talent pour que le théoricien que je suis devienne capable de faire un enseignement expérimental. Mes remerciements s'addressent à tous les ladhyxiens, permanents ou de passage, anciens et nouveaux, qui constamment recréent la magie propre à ce laboratoire et son ambiance familiale, studieuse et détendue — j'ai renoncé à dresser une liste exhaustive, il manquerait toujours des noms.

Je n'oublie pas mes amis et ma famille, qui ont suivi de près ou de loin les différentes étapes de ce travail, m'ont soutenu et ont attendu l'aboutissement avec patience.



Sources bibliographiques

[1] A.P. Bassom, K.M. Kuzanyan & A.M. Soward 1999
A nonlinear dynamo wave riding on a spatially varying background.
Proc. R. Soc. Lond. A **455**, 1443–1481.

[2] H. Bénard 1908
Formation de centres de giration à l'arrière d'un obstacle en mouvement.
Comptes rendus hebdomadaires des séances de l'Académie des sciences **147**, 839–842.

[3] C.M. Bender & S.A. Orszag 1978
Advanced mathematical methods for scientists and engineers.
McGraw-Hill, New York.

[4] A.J. Bernoff 1988
Slowly varying fully nonlinear wavetrains in the Ginzburg–Landau equation.
Physica D **30**, 363–381.

[5] A. Bers 1983
Space-time evolution of plasma instabilities – absolute and convective.
In *Handbook of plasma physics.*
(eds. M.N. Rosenbluth and R.Z. Sagdeev),
North–Holland, Amsterdam, 451–517.

[6] R.J. Briggs 1964
Electron-stream interaction with plasmas.
M.I.T. Press, Cambridge, Mass.

[7] P. Büchel, M. Lücke, D. Roth & R. Schmitz 1996
Pattern selection in the absolutely unstable regime as a nonlinear eigenvalue problem : Taylor vortices in axial flow.
Phys. Rev. E **53**, 4764–4777.

[8] F.H. Busse 1985
Transition to turbulence in Rayleigh–Bénard convection.
In *Hydrodynamic instabilities and the transition to turbulence.*
(eds. H.L. Swinney & J.P. Gollub), Springer, New York, 97–137.

[9] S. Chandrasekhar 1981
Hydrodynamic and Hydromagnetic Stability.
Dover, New York.

[10] J.-M. Chomaz 1992
Absolute and convective instabilities in nonlinear systems.
Phys. Rev. Lett. **69**, 1931–1934.

[11] J.-M. Chomaz & A. Couairon 1999
Against the wind.
Phys. Fluids. **11**, 2977–2983.

[12] J.-M. Chomaz, P. Huerre & L.G. Redekopp 1990
The effect of nonlinearity and forcing on global modes.

In *New Trends in nonlinear dynamics and pattern-forming phenomena.* (eds. P. Coullet & P. Huerre), Plenum Press, New York, 259–274.

[13] J.-M. Chomaz, P. Huerre & L.G. Redekopp 1991
A frequency selection criterion in spatially developing flows.
Stud. Appl. Math. **84**, 119–144.

[14] A. Couairon 1997
Modes globaux fortement non linéaires dans les écoulements ouverts.
PhD thesis, École polytechnique.

[15] A. Couairon & J.-M. Chomaz 1996
Global instability in fully nonlinear systems.
Phys. Rev. Lett. **77**, 4015–4018.

[16] A. Couairon & J.-M. Chomaz 1997*a*
Absolute and convective instabilities, front velocities and global modes in nonlinear systems.
Physica D **108**, 236–276.

[17] A. Couairon & J.-M. Chomaz 1997*b*
Pattern selection in the presence of cross flow.
Phys. Rev. Lett. **79**, 2666–2669.

[18] A. Couairon & J.-M. Chomaz 1999
Fully nonlinear global modes in slowly varying flows.
Phys. Fluids **11**, 3688–3703.

[19] D.G. Crighton & M. Gaster 1976
Stability of slowly diverging jet flow.
J. Fluid Mech. **77**, 397–413.

[20] M.C. Cross & P.C. Hohenberg 1993
Pattern formation outside of equilibrium.
Rev. Mod. Phys. **65**, 851–1112.

[21] M.C. Cross & A.C. Newell 1984
Convection patterns in large aspect ratio systems.
Physica D **10**, 299–328.

[22] G.T. Dee & J.S. Langer 1983
Propagating pattern selection.
Phys. Rev. Lett. **50**, 383–386.

[23] I. Delbende & J.-M. Chomaz 1998
Nonlinear convective/absolute instabilities in parallel two-dimensional wakes.
Phys. Fluids **10**, 2724–2736.

[24] T.M. DelSole & B.F. Farrell 1994
Nonlinear equilibrium of localized instabilities on a baroclinic jet.
J. Atmos. Sci. **51**, 2270–2284.

[25] P.G. Drazin & W.H. Reid 1981
Hydrodynamic Stability.
Cambridge University Press, Cambridge.

[26] J. Dušek 1996
Spatial structure of the Bénard von Kármán instability.
Eur. J. Mech. B/Fluids **15**, 619–650.

[27] J. DUŠEK, P. LE GAL & P. FRAUNIÉ 1994
A numerical and theoretical study of the first Hopf bifurcation in a cylinder wake.
J. Fluid Mech. **264**, 59–80.

[28] M. VAN DYKE 1982
An album of fluid motion.
Parabolic Press, Stanford.

[29] U. EHRENSTEIN & W. KOCH 1989
Nonlinear bifurcation study of plane Poiseuille flow .
DLR Forschungsbericht 89-42.

[30] U. EHRENSTEIN & W. KOCH 1995
Homoclinic bifurcation in Blasius boundary-layer flow.
Phys. Fluids **7**, 1282–1291.

[31] J.H. GERRARD 1981
The mechanics of the formation region of vortices behind bluff bodies.
J. Fluid Mech. **25**, 401–413.

[32] M.E. GOLDSTEIN & L.S. HULTGREN 1988
Nonlinear spatial evolution of an externally excited instability wave in a free shear layer.
J. Fluid Mech. **197**, 295–330.

[33] M.E. GOLDSTEIN & S.J. LEIB 1988
Nonlinear roll-up of externally excited free shear layers.
J. Fluid Mech. **191**, 481–515.

[34] D.A. HAMMOND & L.G. REDEKOPP 1997
Global dynamics of symmetric and asymmetric wakes.
J. Fluid Mech. **331**, 231–260.

[35] K. HANNEMANN & H. OERTEL JR 1989
Numerical simulation of the absolutely and convectively unstable wake.
J. Fluid Mech. **199**, 55–88.

[36] L.N. HOWARD & N. KOPELL 1977
Slowly varying waves and shock structures in reaction-diffusion equations.
Stud. Appl. Math. **56**, 95–145.

[37] P. HUERRE 2000
Open shear flow instabilities.
In *Developments in Fluid Mechanics : A Collection for the Millenium.*
(eds. G.K. Batchelor, H.K. Moffatt & M.G. Worster),
Cambridge University Press, Cambridge, to appear.

[38] P. HUERRE & P. MONKEWITZ 1985
Absolute and convective instabilities in free shear layers.
J. Fluid Mech. **159**, 151–168.

[39] P. HUERRE & P.A. MONKEWITZ 1990
Local and global instabilities in spatially developing flows.
Ann. Rev. Fluid Mech. **22**, 473–537.

[40] P. HUERRE & M. ROSSI 1998
Hydrodynamic instabilities in open flows.
In *Beg-Rohu.* (eds. C. Godrèche & P. Manneville),
Cambridge University Press, Cambridge, 81–294.

[41] R.E. HUNT & D.G. CRIGHTON 1991
Instability of flows in spatially developing media.
Proc. R. Soc. Lond. A **435**, 109–128.

[42] G. JIN & M. BRAZA 1993
A nonreflecting outlet boundary condition for incompressible unsteady Navier–Stokes calculations.
J. Comp. Phys. **107**, 239–253.

[43] Th. VON KÁRMÁN 1912
Über den Mechanismus des Widerstandes, den ein bewegter Körper in einer Flüssigkeit erfährt.
Nachrichten von der königlichen Gesellschaft der Wissenschaften zu Göttingen, Mathematische Physikalische Klasse, 547–556.

[44] G.E. KARNIADAKIS & G.S. TRIANTAFYLLOU 1989
Frequency selection and asymptotic states in laminar wakes.
J. Fluid Mech. **199**, 441–469.

[45] J. KEVORKIAN & J.D. COLE 1981
Perturbation methods in applied mathematics.
Springer, New York.

[46] D.E. KNUTH 1986
The TEXbook.
Addison–Wesley, Reading.

[47] W. KOCH 1985
Local instability characteristics and frequency determination of self-excited wake flows.
J. Sound Vib. **99**, 53–83.

[48] Y. KURAMOTO 1984
Phase dynamics of weakly unstable periodic structures.
Prog. Theor. Phys. **71**, 1182–1196.

[49] L. LANDAU & E.LIFSCHITZ 1989
Mécanique des fluides.
Mir, Moscou.

[50] S. LE DIZÈS, P. HUERRE, J.-M. CHOMAZ & P.A. Monkewitz 1992
Nonlinear stability analysis of slowly-diverging flows : limitations of the weakly nonlinear approach.
In *Proc. IUTAM Symp. on Bluff-Body Wakes, Dynamics and Instabilities.* (eds. H. Eckelmann, J.M.R. Graham, P. Huerre & P.A. Monkewitz), Springer, Berlin, 147–152.

[51] S. LE DIZÈS, P. HUERRE, J.-M. CHOMAZ & P.A. MONKEWITZ 1996
Linear global modes in spatially developing media.
Phil. Trans. R. Soc. Lond. A **354**, 169–212.

[52] R.J. LINGWOOD 1995
Absolute instability of the boundary layer on a rotating disk.
J. Fluid Mech. **299**, 17–33.

[53] R.J. LINGWOOD 1996
An experimental study of absolute instability of the rotating-disk boundary-layer flow.
J. Fluid Mech. **314**, 373–405.

[54] P. MANNEVILLE 1991
Structures dissipatives, chaos et turbulence.
Aléa, Saclay.

[55] C. MATHIS, M. PROVANSAL & L. BOYER 1984
The Bénard–von Karman instability : an experimental study near the threshold.
J. Phys. Paris Lett. **45**, L483–L491.

[56] N. MEUNIER, M.R.E. PROCTOR, D.D. SOKOLOFF, A.M. SOWARD & S.M. TOBIAS 1997
Asymptotic properties of a nonlinear $\alpha\omega$-dynamo wave : period, amplitude and latitude dependence.
Geophys. Astrophys. Fluid Dynamics **86**, 249–285.

[57] P.A. MONKEWITZ 1988
The absolute and convective nature of instability in two-dimensional wakes at low Reynolds numbers.
Phys. Fluids **31**, 999–1006.

[58] P.A. MONKEWITZ, D.W. BECHERT, B. BARSIKOW & B. LEHMANN 1990
Self-excited oscillations and mixing in heated round jets.
J. Fluid Mech. **213**, 611–639.

[59] P.A. MONKEWITZ, P. HUERRE & J.M. CHOMAZ 1993
Global linear stability analysis of weakly non-parallel shear flows.
J. Fluid Mech. **251**, 1–20.

[60] P.A. MONKEWITZ & L.N. NGUYEN 1987
Absolute instability in the near-wake of two-dimensional bluff bodies.
J. Fluids Struct. **1**, 165–184.

[61] P.A. MONKEWITZ & K.D. SOHN 1988
Absolute instability in hot jets.
AIAA J. **26**, 911–916.

[62] H.W. MÜLLER, M. LÜCKE & M. KAMPS 1992
Transversal convection patterns in horizontal shear flow.
Phys. Rev. A **45**, 3714–3726.

[63] A.C. NEWELL, T. PASSOT, J. LEGA 1993
Order parameter equations for patterns.
Ann. Rev. Fluid Mech. **25**, 399–453.

[64] A.E. PERRY, M.S. CHONG & T.T. LIM 1982
The vortex-shedding process behind two-dimensional bluff bodies.
J. Fluid Mech. **116**, 77–90.

[65] B. PIER & P. HUERRE 1996
Fully nonlinear global modes in spatially developing media.
Physica D **97**, 206–222.

[66] B. PIER & P. HUERRE 1999*a*
Bifurcation to fully nonlinear synchronized structures in slowly varying media.
submitted to Physica D.

[67] B. PIER & P. HUERRE 1999*b*
Nonlinear self-sustained structures and fronts in spatially developing wake flows.
in preparation for J. Fluid Mech.

[68] B. PIER, P. HUERRE, J.-M. CHOMAZ & A. COUAIRON 1998
Steep nonlinear global modes in spatially developing media.
Phys. Fluids **10**, 2433–2435.

[69] R.T. PIERREHUMBERT 1984
Local and global baroclinic instability of zonally varying flow.
J. Atmos. Sc. **41**, 2141–2162.

[70] Y. POMEAU & P. MANNEVILLE 1979
Stability and fluctuations of a spatially periodic convective flow.
J. Phys. Lett. **40**, L609–L611.

[71] M. PROVANSAL, C. MATHIS & L. BOYER 1987
Bénard–von Kármán instability : transient and forced regimes.
J. Fluid Mech. **182**, 1–22.

[72] W. VAN SAARLOOS 1987
Dynamical velocity selection : marginal stability.
Phys. Rev. Lett. **58**, 2571–2574.

[73] W. VAN SAARLOOS 1988
Front propagation into unstable states : marginal stability as a dynamical mechanism for velocity selection.
Phys. Rev. A **37**, 211–229.

[74] W. VAN SAARLOOS 1989
Front propagation into unstable states : II. Linear versus nonlinear marginal stability and rate of convergence.
Phys. Rev. A **39**, 6367–6390.

[75] W. VAN SAARLOOS & P.C. HOHENBERG 1992
Fronts, pulses, sources and sinks in generalized complex Ginzburg–Landau equations.
Physica D **56**, 303–367.

[76] A. DE SAINT-EXUPÉRY 1946
Le Petit Prince.
Gallimard, Paris.

[77] C. SCHÄR & R.B. SMITH 1993
Shallow-water flow past isolated topography. Part II. Transition to vortex shedding.
J. Atmos. Sci. **50**, 1401–1412.

[78] A.M. SOWARD 2000
Thin aspect ratio $\alpha\Omega$-dynamos in galactic discs and stellar shells.
In *Advances in nonlinear dynamos.*
(ed. M. Núñez & A.F. Mas), to appear.

[79] A.M. SOWARD & C.A. JONES 1983
The linear stability of the flow in the narrow gap between two concentric rotating spheres.
Q. Jl. Mech. appl. Math. **36**, 19–42.

[80] K.R. SREENIVASAN, S. RAGHU & D. KYLE 1989
Absolute instability in variable density round jets.
Exp. Fluids **7**, 309–317.

[81] K.R. SREENIVASAN, P.J. STRYKOWSKI & D.J. OLINGER 1990
On the Hopf bifurcation and the Landau–Stuart constants associated with

vortex "shedding" behind circular cylinders.
unpublished.

[82] V. STROUHAL 1878
Über eine besondere Art der Tonerregung.
Ann. d. Phys. u. Chem. N. F. (Leipzig) Band 5 Heft 10, 216–251.

[83] P.J. STRYKOWSKI & D.L. NICCUM 1991
The stability of countercurrent mixing layers in circular jets.
J. Fluid Mech. **227**, 309–343.

[84] P.J. STRYKOWSKI & K.R. SREENIVASAN 1990
On the formation and suppression of vortex "shedding" at low Reynolds numbers.
J. Fluid Mech. **218**, 71–107.

[85] M.J. TAYLOR & N. PEAKE 1999
A note on the absolute instability of wakes.
Eur. J. Mech. B/Fluids **18**, 573–579.

[86] S. TOBIAS, M.R.E. PROCTOR & E. KNOBLOCH 1998
Convective and absolute instabilities of fluid flows in finite geometry.
Pysica D **113**, 43–72.

[87] D.J. TRITTON 1988
Physical Fluid Dynamics.
Oxford University Press, Oxford.

[88] G.S. TRIANTAFYLLOU & G. KARNIADAKIS 1990
Computational reducibility of unsteady viscous flows.
Phys. Fluids A **2**, 653–656.

[89] G.S. TRIANTAFYLLOU, M.S. TRIANTAFYLLOU & C. CHRYSSOSTOMIDIS 1986
On the formation of vortex streets behind stationary cylinders.
J. Fluid Mech. **170**, 461–477.

[90] W. WASOW 1985
Linear turning point theory.
Springer, New York.

[91] S. WEIL 1966
Attente de Dieu.
Fayard, Paris.

[92] C.H.K. WILLIAMSON 1996
Vortex dynamics in the cylinder wake.
Ann. Rev. Fluid Mech. **28**, 477–539.

[93] B.M. WOODLEY & N. PEAKE 1997
Global linear stability analysis of thin aerofoil wakes.
J. Fluid Mech. **339**, 239–260.

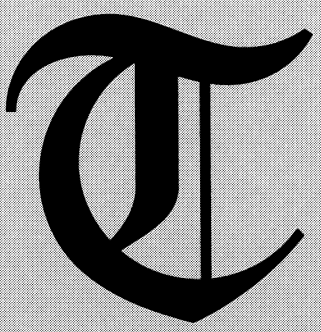


Table des matières

A. Avant-propos 1

B. Balade le long d'une allée de tourbillons 3

1. À propos des écoulements 3
2. Comportement synchronisé 4
3. Un archétype : l'allée tourbillonnaire de Bénard–Kármán 4
4. Quelques principes de sélection 7
5. Objectifs 10
6. Plan 10

C. Courte introduction aux instabilités hydrodynamiques 13

1. Les équations de Navier–Stokes 13
2. Stabilité et instabilités 14
3. Milieux inhomogènes 19
4. Formulation du problème de comportement synchronisé 20
5. Modes globaux linéaires 21
6. Approche faiblement non linéaire 22

D. Doux chapeaux 23

Fully nonlinear global modes in spatially developing media 25
Commentaires 48

E. Éléphants avec un front raide 51

Steep nonlinear global modes in spatially developing media 52
Commentaires 58

F. Formation et déformation des structures synchronisées 61

Bifurcation to fully nonlinear synchronized structures in slowly varying media 63
Commentaires 134

G. Généralisation aux écoulements réels 135

Nonlinear self-sustained structures and fronts in spatially developing wake flows 137

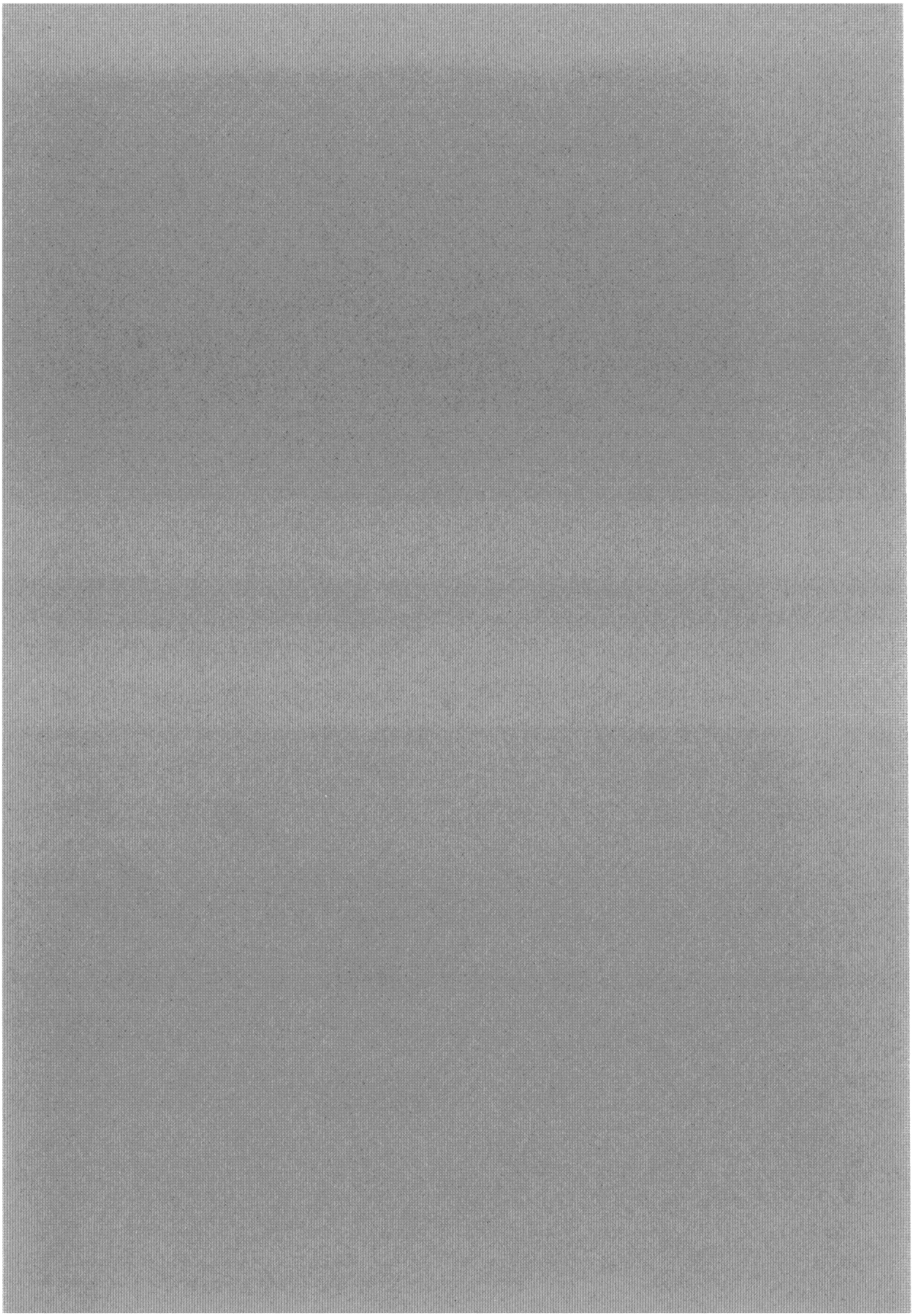
H. Happy End 167

P. Post-scriptum 169

Q. Quatre-quarts 171

R. Remerciements 181

S. Sources bibliographiques 183



Comportement non linéaire synchronisé dans les écoulements cisaillés

Cette étude est consacrée aux écoulements qui se mettent à osciller de façon spontanée. Sans action extérieure, de petites fluctuations aléatoires, inévitables dans tout système physique, sont amplifiées dans certaines régions. Ces perturbations peuvent croître sur place ou être emportées par l'écoulement vers l'aval tout en continuant à se développer. Une croissance transitoire des perturbations peut aboutir à un *mode global* : un régime stationnaire où les fluctuations d'amplitude finie s'installant aux différents endroits sont toutes accordées à une même fréquence.

Les trois premiers chapitres de cette thèse sont consacrés à l'étude de l'équation de Ginzburg–Landau à coefficients complexes et variables en espace afin de simuler les caractéristiques des écoulements ouverts. Deux types de modes globaux non linéaires ont été obtenus : des *modes chapeaux* avec une amplitude évoluant partout lentement le long du courant et des *modes éléphants* avec un front raide au bord amont de la région non linéaire. Dans les deux cas, la fréquence globale ainsi que la forme spatiale associée sont obtenues analytiquement par la méthode des développements asymptotiques raccordés. La transition entre l'état non perturbé et chacun de ces deux modes est étudiée en détail et des paramètres de contrôle globaux sont identifiés.

Dans le dernier chapitre, les résultats précédents sont généralisés aux écoulements réels régis par les équations de Navier–Stokes. Il est montré que le comportement synchronisé des sillages présentant une zone absolument instable entourée par des zones convectivement instables prend la forme d'un mode global de type éléphant. La fréquence globale et la forme spatiale de l'allée tourbillonnaire sont déduites des relations de dispersion locales calculées à partir de l'écoulement de base. Ces prédictions théoriques sont en excellent accord avec des simulations numériques directes des équations de Navier–Stokes.

Mots-clefs : écoulements ouverts, modes globaux, comportement synchronisé, sillages, instabilités absolue et convective, modes chapeaux et éléphants.

Nonlinear synchronized behavior of open shear flows

In this study, open shear flows that sustain intrinsic oscillations are investigated. Without external perturbations, small fluctuations, always present in physical systems, develop in certain regions of the flow. These fluctuations may grow in place or be carried away in the downstream direction while being amplified. Beyond a transient growth phase, a *global mode* may be observed, *i.e.*, a steady state where finite-amplitude fluctuations at each station are all tuned at the same frequency.

The first three chapters of this dissertation are devoted to the Ginzburg–Landau equation with complex space-dependent coefficients in order to mimic the characteristics of open flows. Two types of nonlinear global modes are identified: *hat modes* with a slowly varying amplitude everywhere and *elephant modes* with a sharp front at the upstream boundary of the nonlinear region. In both situations, the global frequency and associated spatial structure are analytically obtained via matching asymptotic expansion techniques. The transition scenario between the unperturbed state and both global modes is analysed in detail and global control parameters are identified.

In the last chapter, the previous results are generalised to real flows governed by the Navier–Stokes equations. The synchronized behavior of wakes displaying an absolutely unstable region embedded within convectively unstable regions is shown to take the form of an elephant mode. The global frequency and spatial structure of the vortex street are derived from the local dispersion relations pertaining to the basic flow. The theoretical predictions are in excellent agreement with direct numerical simulations of the Navier–Stokes equations.

Keywords: open shear flows, global modes, synchronized behavior, wakes, absolute and convective instability, hat and elephant modes.